University of Southampton

Faculty of Engineering, Science and Mathematics

School of Chemistry

An Investigation of Electrochemical Techniques in Acoustic Environments

by

Jekaterina Kuleshova

A thesis submitted for degree of
Doctor of Philosophy

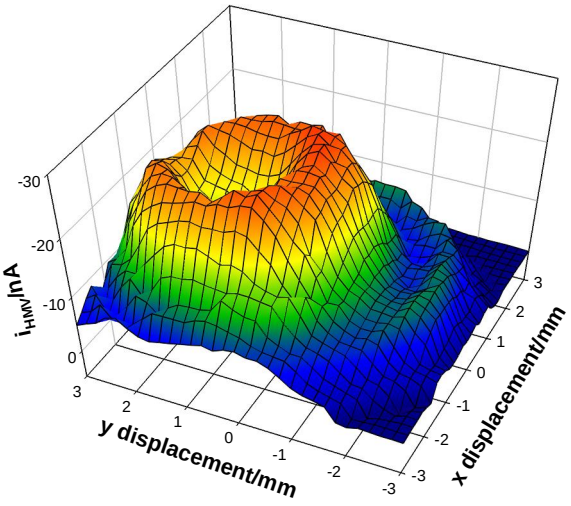

December 2008

UNIVESITY OF SOUTHAMPTON

ABSTRACT

Faculty of Engineering, Science and Mathematics
School of Chemistry

Doctor of Philosophy

An Investigation of Electrochemical Techniques in Acoustic Environments

by Jekaterina Kuleshova

A new system for the generation of hydrodynamic modulation voltammetry (HMV) is presented. This system consists of an oscillating jet produced through the mechanical vibration of a large membrane/piston. The structure of the cell is such that a relatively small vibration is transferred to a large (~ 1 m s^{-1}) fluid flow at the jet outlet. High-speed imaging of the system shows vortex behaviour of the flow at the exit of the jet. Positioning of an electrode over the exit of this jet enables the detection of the modulated flow of liquid. The periodic character of the signal recorded at the electrode allows a "lock-in" approach to be employed. This enables discrimination of the background processes signal from the mass transport component. This is demonstrated for $Fe(CN)_6^{3-/4-}$. Here "lock-in" to the modulated hydrodynamic signal is achieved through the deployment of bespoke software. The apparatus and procedure is shown to produce a simple and efficient way to obtain the desired signal. In addition the spatial variation of the HMV signal, phase correction and time averaged current with respect to the jet orifice is presented. The detection limit for the analysing system is shown to be 45×10^{-9} mol dm^{-3}.

The HMV method is employed to study the reduction of molecular oxygen at high surface area (*H_I-Pt*) modified electrodes. The successful elimination of background signals is achieved for the 0.5 mm diameter nanostructured Pt electrode with roughness factor (RF) of 42.4. Employment of higher roughness factors (>50) *H_I-Pt* electrodes revealed an anomalous "drop off" effect characterising these electrodes. It is demonstrated that the "drop off" is not caused by the hydrogen peroxide production at the electrode or pH change near the electrode surface. However, a clear dependence of the current deflection on the roughness factor of the electrodes is observed. The shape of the "drop off" followed the shape of the hydrogen adsorption region. It is suggested that the surface characteristics of the electrodes are important in these investigations. It is proposed here, that the capacitance of the electrode influences the HMV signal.

Another type of hydrodynamic modulation method, specifically a vibrating 50 μm diameter Pt or Au wire or "tight-rope" electrode was studied. High frequency modulation (80 Hz) is employed. FFT data processing was employed to extract the desired signal from the total current. This technique was applied to study reduction of molecular oxygen at the modulated electrodes. A current "drop off" in hydride region was again observed. This is shown to be related to the uncompensated resistance of the cell. In particular, the resistance of the reference electrode is demonstrated to contribute to this effect

Contents

Acknowledgements

My heartfelt thanks go to my supervisor, Dr Peter Birkin. There are no real words to express my gratitude to him not only for his excellent supervision but also for the friendship developed through my PhD years. His enthusiasm and optimism always inspired me, offering encouragement through example. I am very grateful to him for giving me the opportunity to expand my scientific knowledge by going to conferences and by organising an industrial placement. I would like to thank him for his constant support, advice and understanding, for listening to me and caring about my interests.

I also would like to thank my second supervisor, Dr Joanne Elliott, for her help during my PhD years; discussions with her and general comments have been invaluable. I am also very grateful to her for giving me opportunity to discover the "magic" world of synchrotron, providing me with unforgettable experience.

Huge thanks go to my friends without who these years would not be the same.
Here in university: Raya, Matt, Phil, Hannah, Chris, Maria, Pan, Yasu, Yuki, Doug, Laura, Jyo, Xiaohong, Camilla, Remik, Maciej, Matt L., Alla, Andy, Ken. Thank you for providing abiding friendship and putting up with my occasional "katienism".

Ma olen tänulik minu headele sõbradele: Enel, Piret, Monika, Ben ja Martin; kes toetasid mind esimesest päevast Inglismaal. Suur äitah teile et olete alati valmis jagada minuga kas mure või õnn.

Особую благодарность хочу выделить своей семье: маме, папе, Тане и Юле. Спасибо вам за понимание, доброту, безграничную любовь и веру. Ваша поддержка и советы всегда являлись для меня источником воодушевления и уверенности в себе.

I want to apologise to all those I forgot to mentioned but still deserve to be here.

Symbols and Abbreviations

Symbols

Symbol	Meaning	Units	Section
A	electrode surface area	m^2	1.2
A	zero to peak acceleration amplitude derived from the accelerometer output	V	3.1
a	hydrodynamic radius	m	5.5
a_0	dc level		1.7
a_n	amplitude		1.7
C	concentration of electroactive species in solution	mol dm^{-3}	1.2
C_{dl}	double layer capacitance	F	7.1
C_{H^+}	proton concentration	mol dm^{-3}	1.4.1
C_ϕ	pseudocapacitance	F	1.4.1
C^∞	the bulk solution concentration	mol dm^{-3}	1.2
D	diffusion coefficient of species	cm^2 s^{-1}	1.2
d	width of a channel flow cell	m	1.3.2
D_{bot}	lower cone diameter	m	4.1
d_n	diameter of a capillary used in RFMRE	m	1.3.2
d_r	diameter of vortex ring	m	4.2
D_{top}	cone upper diameter	m	4.1
E	electrode potential	V	1.3
F	Faraday constant; charge on one mole of electrons	C	1.2
F	applied force	N	Appendix B
f	modulation frequency	Hz	3.1
f_0	fundamental frequency	Hz	1.7
h	cone height	m	4.1
$H(f)$	frequency domain	Hz	1.7
$h(t)$	time domain	s	1.7
h	half the distance between the plane bearing the electrode and the roof of the cell	m	1.3.2
I	current	A	1.2
i/i^c_{max}	normalized current; HMV current divided by the maximum cathodic HMV current	none	5.4
I_{2e}-	current for 2-electron process	A	5.8
I_{4e}-	current for 4-electron process	A	5.8
I_{av}	time averaged current	A	3.1
I_{col}	current of collector-electrode in RRDE	A	5.8
I_{dif}	current difference between initial current and phase corrected current	A	5.8
I_{disc}	current recorded at disk electrode	A	2.2.3, 5.8
I_{FFT}	current obtained through the FFT data processing	A	6.1
$I_{FFT\,(2f)}$	FFT current at twice the fundamental frequency	A	6.3

I_{gen}	current of generator-electrode in RRDE	A	5.8
I_{HMV}	HMV (in-phase) current	A	3.1
i_{lim}	mass transport limiting current	A	1.3.1
$I_{Lock\text{-}in}$	lock-in current	A	6.4
$I_{original}$	initial HMV current	A	5.5
$I_{phase\ corrected}$	phase corrected HMV current	A	5.5
I_{ring}	current recorded at ring electrode	A	2.2.3, 5.8
Δi	peak-to-peak current	A	1.3.1
i_{ω_0}	current at central rotation frequency	A	1.3.1
J	flux of species	mol cm^{-2} s^{-1}	1.2
K	wall and inertial correction	none	2.1.7, 5.6
K_{ad}	surface equilibrium constant	none	5.7
k_m	mass transport coefficient	cm s^{-1}	5.8
l	length of a channel (pipe)	m	1.2
L	length of a tube (channel)	m	6.3
n	number of electrons	none	1.2
N	collection efficiency	none	2.2.3, 5.8
Q	charge	C	7.1
q_1	the charge for monolayer deposition	C	1.4.1
R	gas constant	J mol^{-1} K^{-1}	1.4.1
Re	Reynolds number	none	1.2
Re_{crit}	critical Reynolds number	none	6.3
R_f	faradaic resistance	Ω	7.1
r_j	jet radius	m	3.1, 4.1
r_m	the membrane radius	m	3.1
r_p	radius of piston	m	4.1
R_u	uncompensated resistance	Ω	7.1
t	time	s	1.2
T	temperature	K, °C	1.4.1
U	velocity of vortex	m s^{-1}	4.2
V	velocity of liquid	m s^{-1}	1.2
V_1	volume displaced by the piston	m^3	4.1
V_2	volume of the displaced liquid in the funnel neck	m^3	4.1
V_{ap}	cell voltage	V	7.1
V_f	volume flow rate	m^3 s^{-1}	1.3.2
V_o	orbital velocity of vortex	m s^{-1}	4.2
V_T	velocity of toroid	m s^{-1}	4.2
x	distance from electrode	m	1.2
X	displacement amplitude of the membrane centre	m	3.1
x_e	length of a band electrode	m	1.3.2
υ	kinematic viscosity	cm^2 s^{-1}	1.2
ω	rotation rate	r.p.m.	1.3.1
ω_0	central rotation frequency	r.p.m.	1.3.1
$\Delta\omega$	peak-to-peak rotation amplitude	r.p.m.	1.3.1

w	width of a band electrode	m	1.3.2
θ_H	the site fractional occupancy	none	1.4.1
v_{jet}	jet zero to peak amplitude velocity	m s^{-1}	3.1, 4.1
ϕ_n	phase angle	rad	1.7
ρ_f	the density of the ball	g ml^{-1}	2.1.7
ρ	density of liquid	g cm^{-3}	2.1.7
μ	dynamic viscosity of fluid	cP	2.1.7
n_{app}	average number of electrons exchanged during the ORR	none	5.8
θ	is the fraction of molecular oxygen converted to H_2O_2	none	5.8
$\chi_{H_2O_2}$	fractional hydrogen peroxide yield in ORR relative to the total amount of O_2	none	5.8
$\dot{x}$	electrode velocity	m s^{-1}	6.5

Abbreviations

Abbreviation	Meaning
AC	Alternating Current
ADC	Analogue-to-digital conversion
AES	Auger Electron Spectroscopy
CF	Chopped Flow
CF	Current Follower
CF-MJE	Chopped Flow-Microjet Electrode
CSFM	Channel Stopped Flow Method
CTAB	hexadecyltrimethylammonium bromide
CV	Cyclic Voltammetry
DC	Direct Current
EQCN	Electrochemical Quartz-Crystal Nanobalance
FFT	Fast Fourier Transform
FG	Function Generator
FT	Fourier Transforms
FTHMV	Fourier Transform Hydrodynamic Modulation Voltammetry
FT-IR	Fourier Transform Infrared Reflection
HCPA	hexachloroplatinic acid
H_I	hexagonal
HMRDE	Hydrodynamic Modulated Rotating Disk Electrode
HMV	Hydrodynamic Modulation Voltammetry
H-UME	Hydrodynamic Ultramicroelectrode
LC	Liquid Crystals
LLC	Lyotropic Liquid Crystals
LLD	Lower Limit of Detection
MCM-41	Mobil Composition of Matter 41
MJE	Microjet Electrode
ML	Molecular Layer

MMS	Mercury-Mercurous Sulfate Reference Electrode
NHE	Normal Hydrogen Electrode
ORR	Oxygen Reduction Reaction
PZC	Potential of Zero Charge
RDE	Rotating Disk electrode
RF	Roughness factor
RFMRE	Radial Flow Microring Electrode
RFMRE-HME	Radial Flow Microring Electrodes-Hydrodynamic Modulation Voltammetry
RHE	Reference Hydrogen Electrode
RRDE	Rotating Ring-Disk Electrode
SCE	Saturated Calomel Electrode
SECM	Scanning Electrochemical Microscopy
SG/TC	Substrate Generation/Tip Collection
UME	Ultramicroelectrode
UPD	Underpotential Deposition

Chapter 1

Introduction

Electroanalytical techniques ideally provide the sensitivity desired in a variety of situations, and for many practical (clinical, environmental or technological) problems offer a promising methodology (*1-7*). Hydrodynamic modulation voltammetry (HMV) is one particular electroanalytical method that has been used over the years in trace detection analysis (*8, 9*). This technique is also of interest to the current work. The development of a new HMV method and its applications are described in this thesis. A literature review of the previous HMV techniques is presented in Chapter 1. In addition this chapter also gives a brief introduction to the electrochemical processes investigated within this thesis.

1.1 Electrode Processes

Electrode processes are chemical reactions involving the transfer of electrons across the interface normally between a solid and an adjacent solution phase. In the simplest systems, a potential is applied to a working electrode (WE, where the reaction of interest occurs) with respect to a reference electrode (RE) and a current is measured. In order to drive this process an appropriate potential, should be applied. For example, driving the electrode to more negative potentials can result in electron transfer from the electrode to the reactant, resulting in the *reduction* of the reactant. Similarly, in case of imposing more positive potential the electron transfer process can proceed from the reactant to the electrode, causing *oxidation* of the reactant

A schematic representation of a typical electrode reaction, $O + ne \leftrightarrow R$, composed of a series of steps that cause the conversion of the dissolved oxidized species, O, to a reduced, R, is shown in figure 1.2.

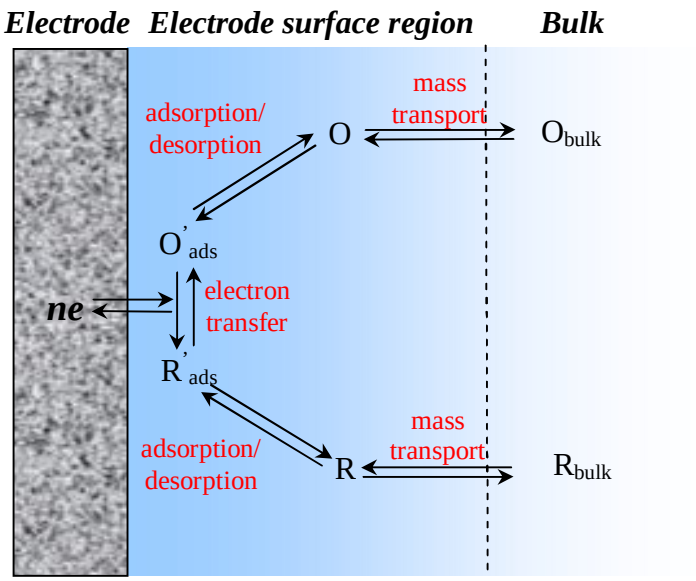

Figure 1.2. Schematic representation of a typical electrode reaction (*10*).

The simplest reaction involves only electron transfer at the electrode and mass transport of a reactant to the electrode and the product to the bulk solution. More complex reactions may involve chemical reactions before or after electron transfer, and surface processes, such as adsorption or desorption (*10*). The rate of the electrochemical reaction, and hence the current response at the WE, is determined by the rate of the overall sequence. In turn this will be limited by the rate of the slowest step. In some cases the electron transfer occurs faster than the transport of the electroactive species to and from the electrode. Here, the current response is limited by the rate of mass transport. Alternatively if the rate of mass transfer is rapid then the rate of the electrode reaction becomes limiting.

Measurement of changes in mass transfer is employed throughout this work. This topic will now be discussed in more detail.

1.2 Mass Transport

Mass transfer can be regarded as the mechanisms by which material in a system moves from one place to another. There are three modes of mass transfer: diffusion, convection and migration (*11*).

Diffusion relies on the random motion of the material within the phase. Transfer of material is trigged by a concentration gradient (*e.g.* from areas of high concentration to areas of low concentration). A mathematic representation of the diffusion process is

described by Fick's laws. Fick's first law states that the flux, *J* is proportional to the concentration (*c)* gradient with respect to distance (*x*) and is given by:

$$J = -D\frac{dc}{dx} \tag{1.1}$$

where *D* is the diffusion coefficient of the species. The minus sign in the equation ensures that species move from concentrated to dilute solution (*11*). Under steady state conditions the concentration gradient does not change with time. However, many experiments are carried out under conditions of non-steady state mass transfer. In this case the concentration profile will depend on time. Fick's second law can be used to interpret the results for these types of experiments. This describes how the concentration (*c*) of a species changes with time (*t*) and hence variation of the flux to the surface with time.

$$\frac{\partial c(x,t)}{\partial t} = \frac{D\partial^2 c(x,t)}{\partial x^2} \tag{1.2}$$

The flux of material can be related to the current flowing at an electrode by the employment of concentration gradient at the electrode/electrolyte interface. Figure 1.3 shows a schematic representation of a typical concentration gradient.

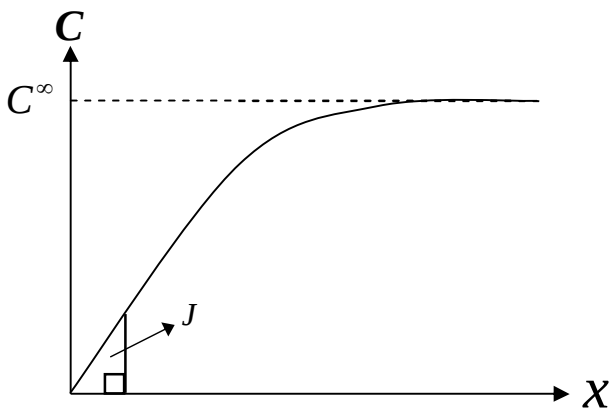

Figure 1.3. Concentration profile in the diffusion layer. *J* represents the rate of diffusion (flux), C^{∞} is the bulk solution concentration of analyte. *C* is the electrode surface concentration at different potentials and *X* is the distance from the electrode surface.

The flux, *J* , can be then directly related to current, *I,* through equation 1.3:

$$I = nFAJ \tag{1.3}$$

Hence,

$$I = nFA\left(- D\left(\frac{\partial c}{\partial x} \right)_{X=0} \right) \tag{1.4}$$

Clearly an understanding of how J varies with time and conditions allows one to calculate the resultant current.

Another mode of the mass transport is migration. *Migration* is the movement of charged particles due to a potential gradient. However, this effect is normally minimized by adding a large concentration of inert electrolyte and hence will be ignored from this point on.

Finally, the movement of the bulk solution is called *convection*. This can be achieved by mechanical agitation, pressure, temperature and potential gradients. In the presence of both diffusion and convection a steady state system may be envisaged. Here a thin layer close to the electrode surface (Nernst diffusion layer) across which the concentration of the electroactive species changes with distance from the electrode. Increasing the convection rate in the system will decrease the boundary layer. This change in diffusion layer leads to a change in the rate of mass transport and hence current. Also convection helps to remove the small random contribution from natural convection which can complicate measurement performed in stagnant solution. Forced convection can be produced in a number of ways. For example, (i) modulating the motion of the electrode with respect to the solution, e.g., rotating disk electrode (*12*, *13*) or vibrating electrode (*14-18*) or (ii) varying the solution flow rate over a static electrode (*19-22*).

It is desirable to have a well-controlled system. Therefore it is important to be able to define the fluid flows within the employed set-up. One type of the fluid flow is termed *laminar*. In this case the flow is smooth and steady, occurring as if in layers. Two examples of laminar flow are shown in figure 1.4a. In uniform flow (case 1) the velocity is constant in all points within the fluid. For example if a liquid enters a pipe, the friction between the fluid and flow will slow down the layer adjacent to the surface. This results in the non-uniform distribution of solution velocities with the maximum velocity, V_{max}, in the centre of the pipe and a minimum at the wall/solution interface. A parabolic velocity profile (figure 1.4, case 2) will develop. This parabolic flow is called Poiseuille flow. If the solution velocity becomes too large, then the flow can become unsteady and chaotic. This flow type is termed *turbulent*. For example, a

barrier placed in a pump would result in the beginning of the turbulent flow (see figure 1.4b).

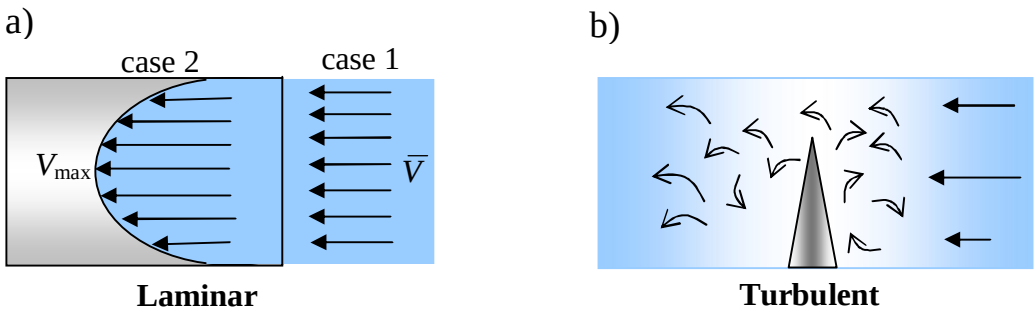

Figure 1.4. Types of fluid flow: a) laminar: case 1-uniform flow, case two- Poiseuille flow; and b) turbulent (*10*).

A dimensionless number characterising to what extent the flow of solution will be laminar or turbulent is called the "*Reynolds number*", *Re*. In general, it is given by:

$$\mathrm{Re} = \frac{Vl}{\nu} \qquad \text{eq. 1.5}$$

where *l*, *V* and *v* are characteristic length, velocity and kinematic viscosity, respectively (*10*).

Methods involving convective mass transport of species to the electrode surface are called hydrodynamic methods. One particular method, which is of interest to this thesis, is hydrodynamic modulation voltammetry (HMV). This will be discussed in the next section.

1.3 Hydrodynamic Modulation Voltammetry

Hydrodynamic modulation voltammetry (HMV) has shown significant promise for trace analysis, because it reduces interference from background processes normally encountered in electrochemical analysis. These background interferences can include solvent decomposition, double layer charging, irreversible surface reactions and transformations of the surface layer. HMV uses the fact that the analytical current for a solution species is mass transport controlled, whereas that for the background processes is not. Therefore only the mass transport limited component of the current will respond to the periodic modulation of the electrode or solution with respect to the electrode. The detection limits for the technique can be increased if the modulated

current is a significant fraction of the total current recorded. In the next subsections we discuss the available literature related to HMV methods.

1.3.1 Modulation of the electrode

The rotating disk electrode (RDE) produces efficient and well-defined mass-transport behaviour. This is also one of the few techniques for which the hydrodynamic equations and the convective-diffusion equation are well defined. Therefore a portion of the literature was focused on the employment of this electrode in HMV studies. In the simplest approach, the rotation rate of an RDE can be stepped between two selected rotation speeds. The difference in current at the two well-separated speeds and at the constant potential was measured (*23-26*). Using this approach, a high signal-to-noise ratio was obtained. The detection limits for the technique has been reported to be around 10^{-8} mol dm^{-3} (*23, 24*). In order to increase the difference between the measured currents, high surface area rotated porous-carbon disk electrodes were employed (*25, 26*). However, one of the disadvantages of the modulation technique is the long time needed to achieve the complete relaxation of the concentration boundary layer after the hydrodynamic step. In addition the modulation frequency is also limited by the response of the motor employed in the RDE assembly and the response time of the diffusion layer.

Bruckenstein and Miller were the first to report sinusoidally modulated RDE in HMV experiments (*12, 27-29*). The technique involves the sinusoidal modulation of the speed of rotation of a RDE about a fixed central rotation frequency (*8*). The in-phase current component of the modulated signal from a RDE was investigated for a variety of different electrode materials (for example, silver, platinum, gold, amalgamated gold, graphite) and electroactive species (*e.g.* nitrobenzene, sulphide, Fe^{2+}, Tl^{+}, Hg^{2+} and hydroquinone). The detection limits for some of the species were as low as 5×10^{-8} mol dm^{-3} (*12*). As an example, the DC RDE and in-phase Hydrodynamic Modulation Rotating Risk Electrode (HMRDE) response for the detection of 2.0×10^{-7} mol dm^{-3} Tl^{+} in 0.01 mol dm^{-3} $HClO_4$ at a Hg modified gold (Au amalgam) disk electrode shown in figure 1.5.

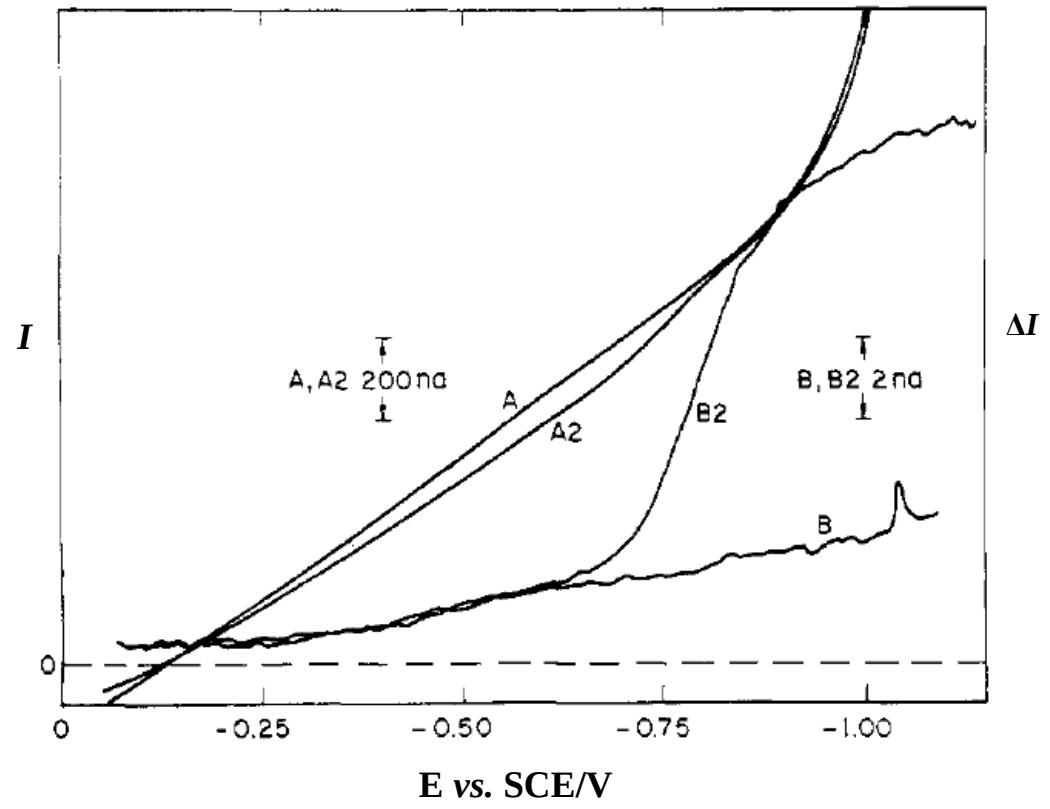

Figure 1.5. Controlled potential cathodic scans of Tl^{+} at an amalgamated gold disk. All A scans are RDE curves, all B scans are in-phase HMRDE curves. The plots A and B for the 0.01 mol dm^{-3} $HClO_4$ solution; A2 and B2 – for 2.0×10^{-7} mol dm^{-3} in 0.01 mol dm^{-3} $HClO_4$ solution. Current sensitivities indicated by double-ended arrows, zero current for all curves is the dashed line. For all curves the central rotation speed of the RDE is 3600 rpm. For HMRDE (B) the rotation speed was modulated ± 6 rpm at a frequency of 3 Hz about the central speed. The averaging time constant is 3 s and the scan rate is 2 mV s^{-1}. (Taken from reference (*12*).)

Figure 1.5 shows that the background current in the HMRDE analysis was significantly reduced and a *S*-shape voltammogram (see figure 1.5, B2 scan) for the redox species employed was obtained compared to the ill-defined signal recorded with a conventional RDE. In the conventional experiments the background current is clearly dominant (see figure 1.5, A2 scan). According to Levich theory the current at a RDE can be calculated from equation 1.4:

$$i_{\lim} = 0.62nFAD^{2/3}\omega^{1/2}\nu^{-1/6}C\,, \qquad (1.4)$$

where i_{lim} is the mass transport-limited current, n the number of electrons transferred per redox event, F Faraday's constant, C the bulk concentration of the electroactive species of interest, A the electrode surface area, ω the rotation rate (rad s^{-1}), D is the diffusion coefficient and ν the kinematic viscosity. In the HMRDE sinusoidal modulation of the rotation speed ω near the central rotation frequency (ω_0) with peak-

to-peak amplitude of ($\Delta\omega$) is employed. Therefore the Levich equation for the HMRDE will be given by (*8, 10, 13, 30*):

$$i(t) = 0.62nFAD^{2/3}\nu^{-1/6}C[\omega_0^{1/2} + \Delta\omega^{1/2}\sin(\sigma t)] \quad (1.5)$$

and the current peak-to-peak response as:

$$\Delta i = i_{\omega_0}(\Delta\omega/\omega_0)^{1/2} \quad (1.6)$$

However, one of the obligatory conditions of the HMRDE experiments is that the modulation amplitude ($\Delta\omega$) should be only 1-10% of the central rotation frequency (ω_0). The modulation frequency is dependent on the motor response time and should be small (3-6 Hz or 18.8-37.7 rad s^{-1}) (*30*). The theory and experiments were improved for higher amplitudes and modulation frequencies (up to 12.5 Hz), where the limiting current cannot be predicted by the Levich equation (*30-33*).

The concept of the hydrodynamic-modulated RDE was further extended by Deslouis and Tribollet and co-workers under the name of electro-hydrodynamic impedance (*34-38*). This technique was applied to study reaction kinetics (*39*), investigate the evolution of the surface roughness on an electrode (*40-42*), characterise surface films (*43*) and examine films formed on metallic surfaces during corrosion phenomena (*44-46*).

An alternative method of producing hydrodynamic modulation is by vibrating an electrode. The first mention of the application of a vibrating electrode for analytical voltammetry was as early as 1948 in work carried out by Harris and Lindsay (*47-49*). They used vibrated electrodes in titrametric analysis. The history of analytical and synthetic utilization of the vibrating electrodes is summarised in literature by different authors (*9, 50, 51*). The attention of many researchers was turned to this type of hydrodynamic modulation because of the simplicity of the technique. The results of some of the investigations will be discussed here. Pratt and Johnson used a flow-injection system vibrating wire electrode in their HMV studies (*51, 52*). The detection limit of I^- species in solution at concentrations as low as 5×10^{-10} mol dm^{-3} was quoted for the technique. In these experiments the Pt wire (0.31 mm diameter and 5.19 mm length) was vibrated at a frequency of 240 Hz with a peak to peak amplitude of 0.48 mm. However, the modulation efficiency, at the frequency employed was significantly less than 100 %. This fact was further investigated by Schuette and McCreery (*53*). They showed that the experimental modulation efficiency depends on the electrode geometry. It was demonstrated that for the relatively high frequency modulations (160

Hz), an increase in the diameter of the wire results in a drop in efficiency (see figure 1.6).

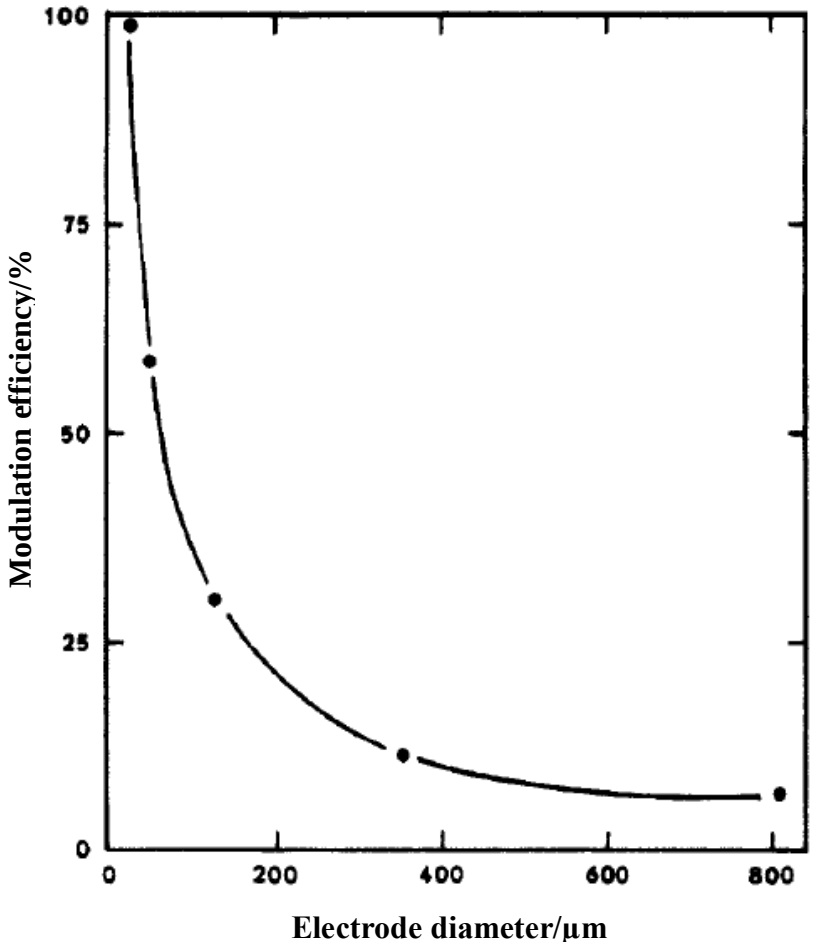

Figure 1.6. Experimental modulation efficiency *vs.* diameter of vibrating microcylinder electrode: modulation frequency, 160 Hz; 0.91 mmol dm^{-3} ferrocene/0.1 mol dm^{-3} TBAP in acetonitrile. Taken from reference (*53*).

It was proposed that this effect is due to the high Reynolds numbers characterising the hydrodynamic modulation of large diameter wire electrodes. The effect of electrode geometry was the subject of a number papers (*52-54*). Schuette and McCreery used a vibrating microcylinder electrode (Pt wire, 25 µm diameter and 3 mm in length) in their investigations. In order to extract the desired signal from the total current a lock-in approach was used. The detection limits for the technique approached 10^{-8} mol dm^{-3} for ferrocene in acetonitrile.

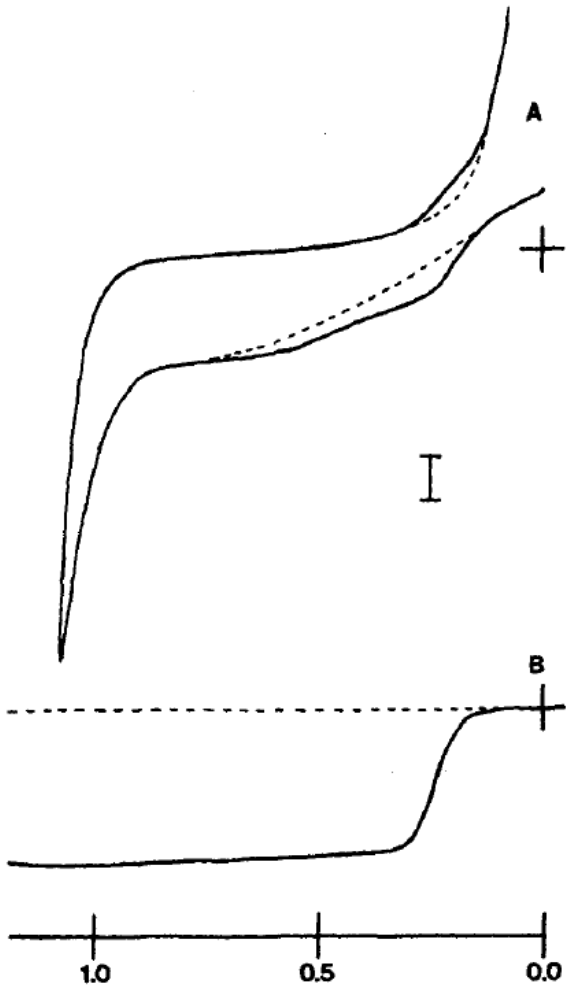

Figure 1.7. Comparison of a cyclic voltammogram using a conventionally size Pt disk electrode with a hydrodynamic modulation voltammogram using a microcylinder Pt electrode. Solid lines were obtained from 0.17×10^{-3} mol dm^{-3} bis(hydroxymethyl)-ferrocene in pH 7 citric acid/phosphate buffer, while the dashed lines are of the blank buffer solution; scan rate 50 mV s^{-1}. A) Conventional voltammogram from a 1.5 mm diameter Pt disk electrode, scale 1 μm. B) In-phase HMV from a 25 μm diameter microcylinder electrode vibrating at 80 Hz, scale 50 nA. (Taken from reference (*53*).)

In addition the methodology was found to provide excellent background signal rejection, as shown in figure 1.7. In the example presented the modulation frequency employed was 80-160 Hz. Schuette and McCreery extended this technique by developing a double modulation method. The method was based on the simultaneous sinusoidal modulation of the electrode potential and vibration of the electrode. The detection limit of 4×10^{-7} mol dm^{-3} for 1,1'-bis(hydroxymethyl)ferrocene was observed (*55*). Another type of vibrating electrode, microband electrodes, have been used by Williams *et al.* for the detection of chlorine in water (*56*). The modulation zero-to-peak amplitude and signal enhancement for these electrodes was shown to be smaller than

those characteristic for a vibrating microwire (*53*) but larger than those from large diameter wires (*52*). The modulation frequency range of the microband electrode was 2-50 Hz with a peak-to-peak amplitude in the range of 1-2 mm. A detection limit of approximately 3×10^{-7} mol dm^{-3} was determined.

The HMV techniques described in this section rely on the modulation of the electrode. Alternatively a periodic motion of flow can be used as a type of hydrodynamic modulation. This is the subject of the next section.

1.3.2 Modulation of the solution flow

Early studies of HMV using flow modulation were concentrated on pulsating the flow rate of the solution through a tubular or channel-shaped electrochemical cell. The difference in current (in DC mode only) as result of the modulation was measured (*57-59*). Detection limits of 1×10^{-7} mol dm^{-3} were achieved. Blaedel and Wang combined a stopped rotation approach with a flow-through rotating porous disk electrode (*58*). The employing of the high surface area electrode allowed further increase in the sensitivity up to 1×10^{-9} mol dm^{-3} for $Fe(CN)_6^{4-}$. However, the main disadvantage of this system is the long response time, often tens of seconds, because of the relatively low mass transport rates. In an effort to overcome the problem, various thin-layer cells were designed which reduced the relaxation distance of the concentration boundary layer when the flow was pulsed (*60, 61*). However, a maximum modulation frequency of 2 Hz was employed. Further development of this technique led to the channel stopped flow methods (CSFM) (*9*). This used a channel microband electrode with an appropriate flow cell (*62-64*). Figure 1.8a shows a schematic representation of the microelectrode. The position of the electrode inside the channel was chosen so that flow over it would be fully developed, laminar and Poiseuille in nature (*63*). Under these conditions the mass transport limited current can be derived from the Levich equation, which for the current system takes the form of (*63, 64*):

$$i_{\lim} = 0.925nFC\left(\frac{Dx_e}{h}\right)^{2/3}\left(\frac{V_f}{d}\right)^{1/3} w \ , \qquad (1.7)$$

where x_e and w are the length and width respectively of the band electrode, d is the width of the channel flow cell, $2h$ is the distance between the plane bearing the electrode and the roof of the cell and V_f is the volume flow rate.

a)

b)

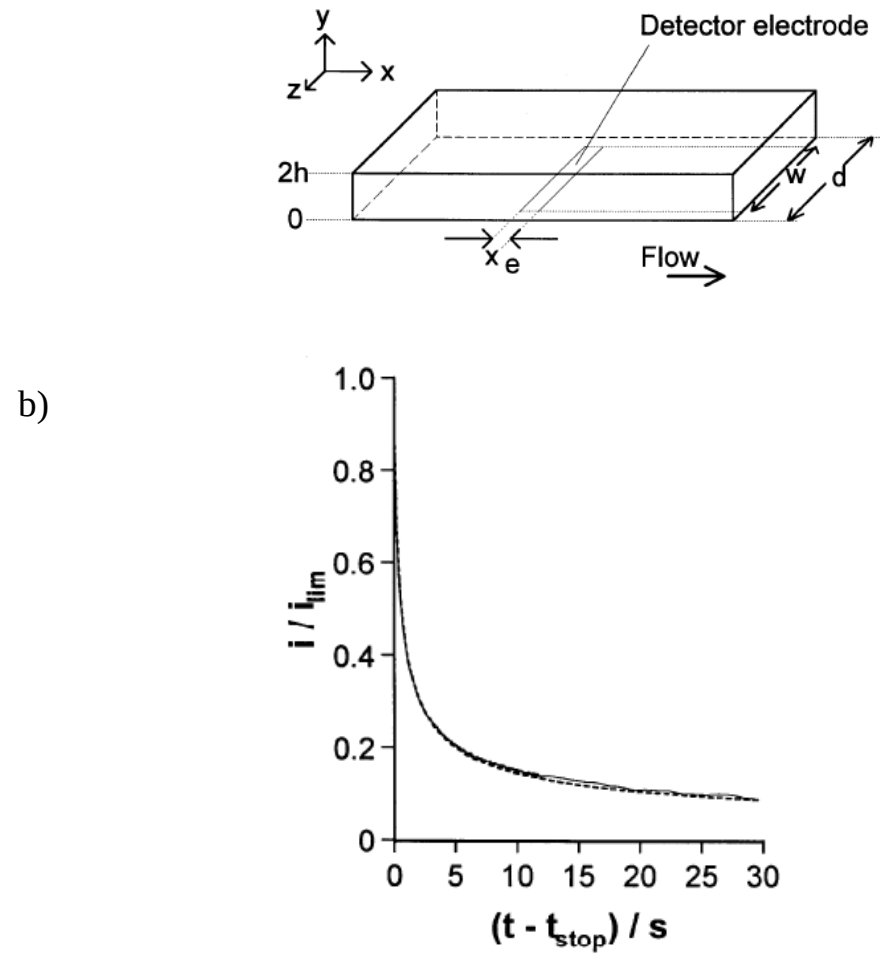

Figure 1.8. **a)** Schematic diagram showing the geometry of a typical channel flow electrode. **b)** Experimental (**—**) and theoretical (**▪▪▪**) chronoamperometric response for the diffusion-limited oxidation of 2×10^{-3} mol dm^{-3} $Fe(CN)_6^{4-}$ in 0.1 mol dm^{-3} KCl at a rectangular electrode, 2.5 mm long and 6.25 mm wide, in a 0.5 mm high channel flow cell under channel stopped flow conditions. The initial volume flow rate of the solution was 0.197 cm^3 s^{-1}, which gave a limiting current at the channel electrode, defined as i_{lim}. At time, t_{stop}, solution flow was retarded. (Taken from reference (*9*).)

This hydrodynamic set-up was used to find the diffusion coefficient (*D*) of the electroactive species employed. Figure 1.8b shows the experimental results used to measure the *D* value for the $Fe(CN)_6^{4-}$ species, independent of the knowledge of its concentration. The results obtained showed a good agreement between the experimental data and theoretical predictions.

a)

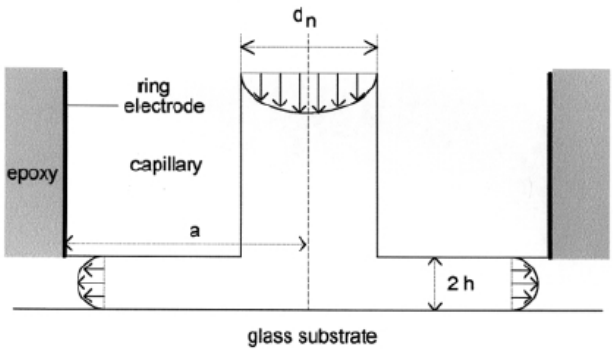

b)

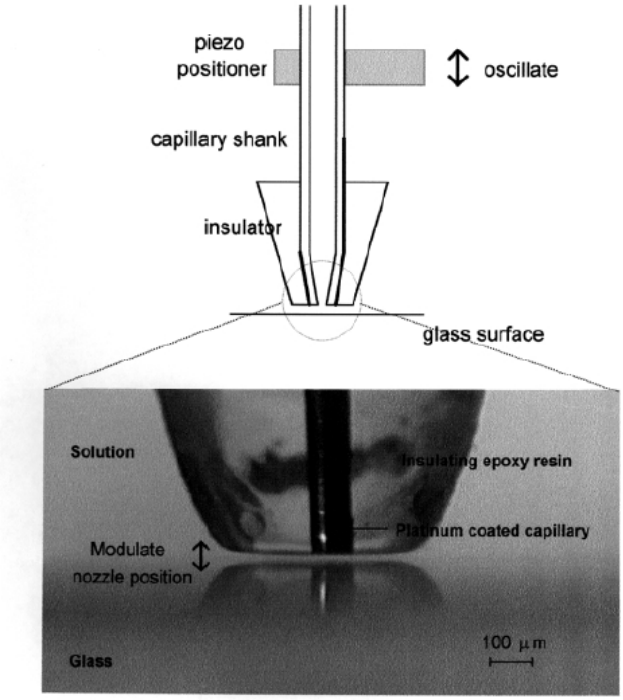

Figure 1.9. **a)** Schematic cross-section of the RFMRE arrangement, *a* is the inner radius of the ring electrode and d_n is the nozzle diameter. The ring electrode is placed on the outer side of the nozzle and is exposed at the end. The epoxy coating provides electrical insulation and completes the formation of a thin channel with the glass substrate through which solution radially flows. **b)** Video microscopy image of the hydrodynamically-modulated RFMRE. In this configuration, the capillary shank of the ring electrode is attached to a piezoelectric positioner which modulates the position of the nozzle with respect to the underlying glass substrate. Typical modulation frequencies and nozzle-substrate half-height modulation amplitudes of 1-5 Hz and 1-4.5 µm, respectively, are employed. (Taken from reference (*65*).)

Recently another type of hydrodynamic ultramicroelectrode (H-UME) has been developed by Macpherson *et al.* Here, a Radial Flow Microring Electrode (RFME) has been employed (*64-67*). A schematic of the electrode design is shown in figure 1.9a. The solution flows down a central capillary (diameter d_n), which is positioned close to a glass substrate forming a thin-layer radial flow cell. As the fluid leaves the capillary, it is forced between the nozzle-substrate gap and flows over the ring-electrode. Mass-

transfer coefficients up to 2 cm s^{-1} have been achieved using this technique. This is the highest mass transfer rate of any HMV techniques reported (*66*). As for the flow channel cell (see figure 1.8) the limiting current here can be predicted by the Levich equation 1.7. However, in this case w is equivalent to *d*, the equation 1.7 can be simplified to:

$$i_{\lim} = 0.925nFC\left(\frac{Dx_e w}{h}\right)^{2/3} V_f^{1/3}. \qquad (1.8)$$

According to equation 1.8, modulation of the current can be achieved in two ways: modulation of V_f or *h*. The easiest way is to vary the distance between the capillary nozzle and the glass substrate (see figure 1.9b). The Radial Flow Microring Electrode-Hydrodynamic Modulation Voltammetry (RFMRE-HME) with variable height, combined with in-phase electrochemical detection, was described by Macpherson and Unwin (*65*).

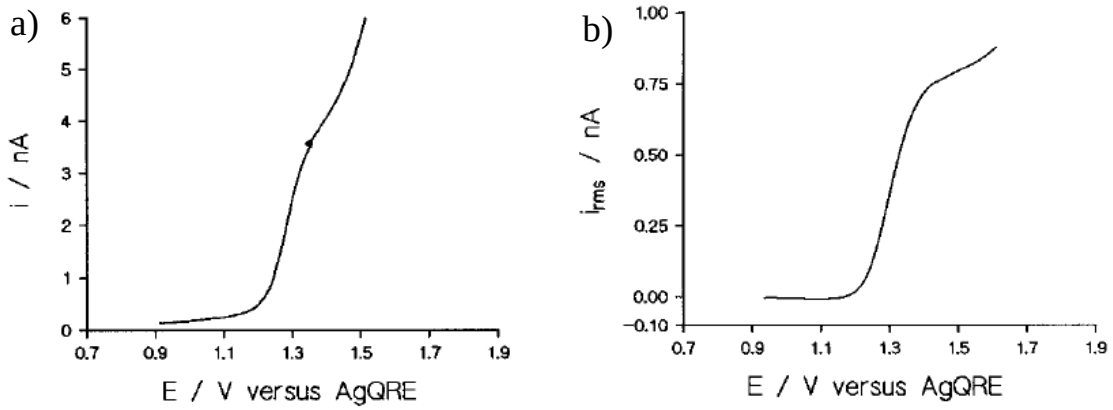

Figure 1.10. Steady-state linear voltammograms recorded for the oxidation of 5 × 10^{-5} mol dm^{-3} $Ru(bipy)_3^{2+}$ in 0.1 mol dm^{-3} KNO_3 at **a)** a constant nozzle-substrate half-height separation, h = 13.8 μm, and **b)** HMV current-voltage response for a modulated nozzle-substrate half height separation, h = (13.8 ± 4.5) μm, at a frequency of 1 Hz. In both cases the RFMRE configuration was characterized by d_n = 110 μm, a = 74 μm, x_e = 0.40 μm and V_f = 1.67 × 10^{-2} cm^3 s^{-1}. (Taken from reference (*65*).)

An example of the HMV analysis for the oxidation of $Ru(bipy)_3^{3+}$ in 0.1 mol dm^{-3} KNO_3 is shown in figure 1.10. Solvent decomposition distorts the electrochemical data recorded at the electrode in the steady flow system (see figure 1.10a), whereas the HMV data shows excellent rejection of the background signal (see figure 1.10b).

The microjet electrode (MJE) is another example of the H-UME (*68-71*). In the MJE, a jet of solution was fired at high velocities (up to 25 m s^{-1}) from a nozzle onto ultramicroelectrode UME. Modulation of the mass transport rate was achieved by oscillation of the position of the jet, in a plane parallel to the electrode surface, between

two positions: 1) jet impinges electrode and 2) jet misses the electrode (*70*). The system is characterised by high mass transport rates and the short time with which the diffusion and hydrodynamic boundary layers relax. This enabled relatively high frequency of modulations (up to 20 Hz) to be employed.

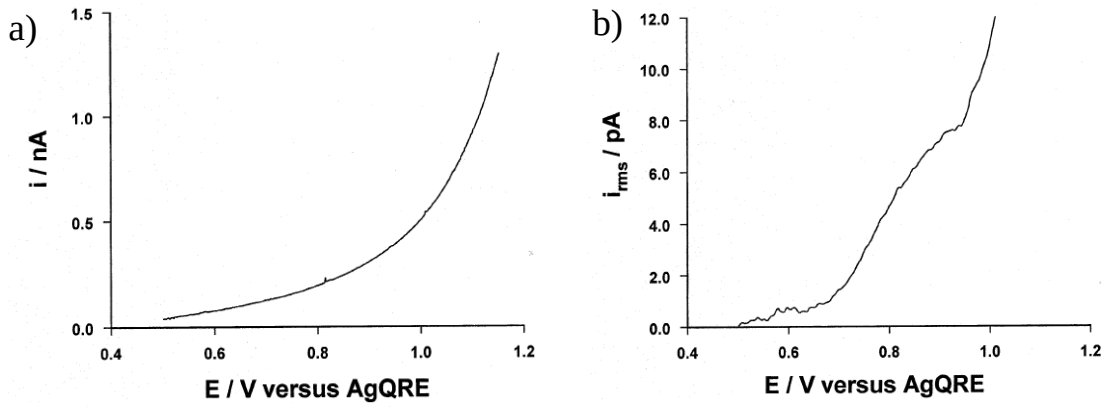

Figure 1.11. **a)** Steady-state linear sweep voltammogram for oxidation of aqueous 50×10^{-9} $IrCl_6^{3-}$ in 0.2 mol dm^{-3} KNO_3 in the MJE arrangement. **b)** The HMV current obtained at the UME, when the jet nozzle was periodically oscillated at frequency of 1 Hz. In both cases the MJE configuration was characterized by d_n = 42 μm, H = 100 μm and V_f = 3.33×10^{-2} cm^3 s^{-1}. The HMV measurement employed a ± 30 μm sinusoidal (1 Hz) perturbation of the lateral nozzle position, with one limit of the motion corresponding to the position of maximum mass transport limited current and the other limit the minimum. (Taken from reference (*70*).)

An example of the trace analysis using the technique is presented in figure 1.11. The analysis show excellent rejection of background noise and detection limits as low as 10^{-9} mol dm^{-3}. In further developments the MJE method was simplified by introducing the chopped flow modulation (CF) (*64, 72*). In this case a rotating blade was positioned between a nozzle of the jet and the UME probe and was used to periodically interrupt flow to the electrode. This resulted in modulation of the mass transfer rates. The method again showed good ability to discriminate against background noise, which may complicate the interpretation of the measurements at low analyte concentrations.

An alternative method used to produce hydrodynamic modulation is the employment of ultrasound. The concept of the use of ultrasound as a method of introducing convection into a system is not new and was investigated as long ago as 1963 by Bard (*73*). Dewald and Peterson (*74*) were the first to introduce hydrodynamic modulation using an ultrasonic field. In these investigations a 20 kHz ultrasound horn was positioned above the electrode and hydrodynamic modulation was achieved by the pulsation of the ultrasonic probe. A detection limit for $[Fe(CN)_6]^{4-}$ in the order of 10^{-7} mol dm^{-3} was determined. In other studies Coury and co-worker (*75*) used continuous ultrasound to

produce modulation of the mass transport to an electrode. The working electrode was positioned 1 cm above the ultrasonic horn (operated at a frequency of 20 kHz). The operation of the horn induced hydrodynamic modulation. The detection limit quoted for the system was 1×10^{-7} mol dm^{-3} for ferrocene in acetonitrile (*75*). Here, flow which was attributed to the collapsing bubbles, induced by the ultrasonic field, near the electrode surface, results in the modulation of the limiting current recorded at the electrode (*76, 77*).

All these techniques described above show the significance of the HMV technique as an electroanalytical tool. Despite the variety of techniques available some improvements in this area (speed, sensitivity, selectivity etc.) are still desirable. The work presented here will introduce a novel HMV technique specifically an oscillating jet. Its design (Chapter 2), characteristics (Chapter 3 and 4) and applications (Chapter 5) will be presented. The HMV technique will be used to study electrochemical processes at mesoporous and polished Pt electrodes. The next section will discuss the plethora of electrochemistry describing these electrodes.

1.4 Surface Electrochemistry of Platinum

1.4.1 Platinum in Acid

Platinum is known to have rich surface electrochemistry. One of the examples is adsorption and desorption of hydrogen and oxygen on the platinum surface from an aqueous solution. The nature of these surface processes was the subject of many studies (*78-82*). A typical cyclic voltammogram in acid is presented in figure 1.12. The potential region between +0.6 and +1.3 V *vs.* RHE corresponds to the oxide formation/reduction zone. The voltammetry shows that the anodic sweep is quite different from the cathodic sweep. Three peaks O_{A1}, O_{A2} and O_{A3} followed by a broad region (see figure 1.12) characterise the oxide formation zone while a single peak O_c for oxide reduction is observed. Conway *et al.* (*83*) referred to this kind of irreversibility as an "intrinsic irreversibility" (*84, 85*). This suggests that there are different types of species or states on the surface during the anodic and cathodic sweeps. It has been proposed that the oxide formation process is based on a place exchange mechanism (*86*).

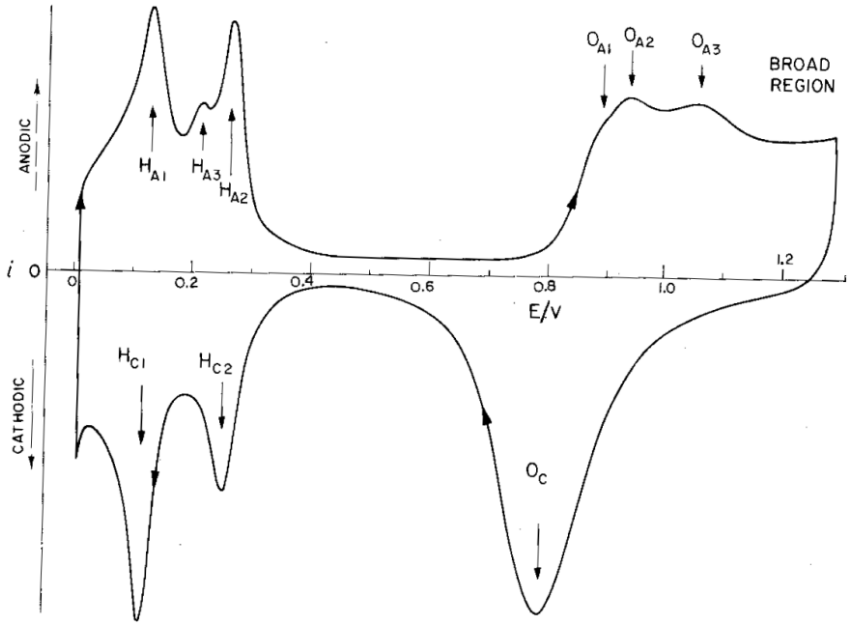

Figure 1.12. Cyclic voltammogram for polycrystalline Pt surface in high purity 0.5 mol dm^{-3} sulphuric acid solution (25 °C). Sweep rate = 0.1 V s^{-1}. (Taken from reference (*80*).)

Several studies have been reported of investigations of this process. It is known that a Pt surface is covered with an adsorbed O, or an oxide layer, before oxygen evolution starts (*87, 88*). Studies of the oxide layer have also contributed to the understanding of the mechanism of electrocatalysis of certain anodic reactions (*89, 90*). The main contributions in this subject were made by Reddy (*91, 92*), Damjanovic (*93-95*), Conway (*80, 96*) and Vetter and Schulze (*90*). At present, it is well known that the crystallographic orientation of the surface and the electrolyte composition play a significant role in the formation of the interface. This in turn gives rise to metal-anion interactions which affect the potential at which the oxide growth takes place (*97*). The mechanism for oxide formation can be summarised as follows (*80, 98, 99*):

1) $Pt + H_2O \rightarrow Pt - OH_{ads} + H^+ + e^-$ (*E = 0.85-1.10 V*)

2) $Pt - OH_{ads} \xrightarrow{place\ldots exchange} (OH - Pt)_{quasi-3D\ldots lattice}$

3) $(OH - Pt)_{quasi-3D\ldots lattice} \rightarrow (Pt - O)_{quasi-3D\ldots lattice} + H^+ + e^-$ (*E =1.10-1.40 V*)

Mechanism A

Here, the first step in the mechanism corresponds to the oxidation of H_2O molecules producing an adsorbed hydroxide group (OH_{ads}). This occurs in a potential region between 0.85 and 1.10 V *vs.* RHE. The surface coverage of the OH_{ads} in this potential region is thought to be low and do not form a lattice. The second step in Mechanism A

represents the place exchange between OH_{ads} and surface Pt atoms. This causes the formation of a quasi-3D lattice. This step is regarded as being rate-determining. Finally oxidation of OH groups is proposed.

More recently Jerkiewicz and co-workers (*97, 100*) re-examined the mechanism of surface-oxide growth using the combined cyclic voltammetry (CV), electrochemical quartz-crystal nanobalance (EQCN) and Auger electron spectroscopy measurements (AES). They proposed revisions of the mechanism.

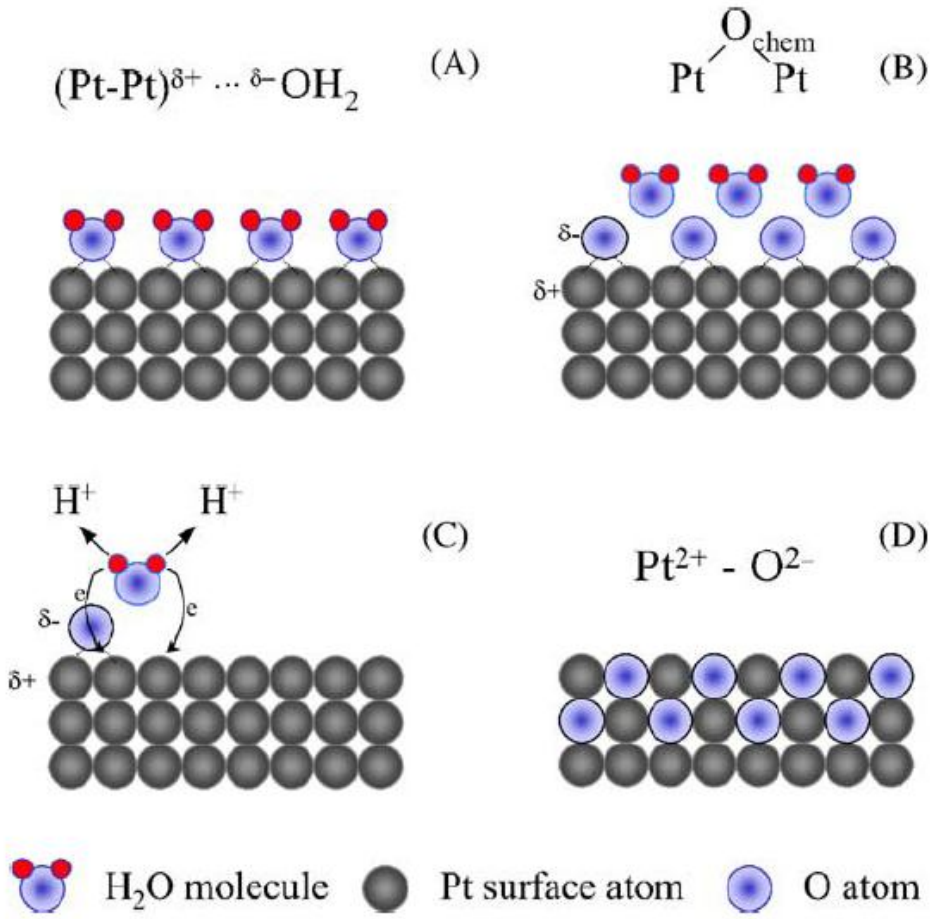

Figure 1.13. **Mechanism B.** Visual representation of the platinum-oxide growth (taken from reference (*97*)).

According to these investigations the first step involves interaction of H_2O molecules with the Pt surface (see figure 1.13A). The potential region for this process is between +0.27 and +0.85 V *vs.* RHE (positive to the pzc). In this region the Pt is positively charged and hence attracts the negatively charged oxygen end of the water molecules. In the second step (figure 1.13B), a monolayer of bridging Pt-O-Pt molecules occurs and this results in formation of 0.5 monolayer (ML) of chemisorbed oxygen (O_{chem}) and the departure of protons. This process takes place at potentials between +0.85 and

+1.15 V *vs.* RHE and is accompanied by Faradaic charge transfer. In the third step (see figure 1.13C), PtO is formed and a complete monolayer of O is produced at the surface (already covered by ~0.5 ML of O_{chem}). As this complete monolayer of O_{chem} begins to build up, strong dipole-dipole lateral repulsive interactions occur. In order to minimize the repulsions, some of the O_{chem} adatoms undergoes an interfacial place-exchange process producing the PtO lattice. The place exchange is accompanied by completion of the charge transfer from Pt to O_{chem}. This results in the formation of a quasi-3D surface lattice comprising Pt^{2+} and O^{2-} (see figure 1.13D).

From the cyclic voltammetry (figure 1.12) it is clear that the oxide reduction occurs at a potential more negative compared to the adsorption process resulting in the formation of a hysteresis between the anodic and cathodic sweeps (*84*, *85*).

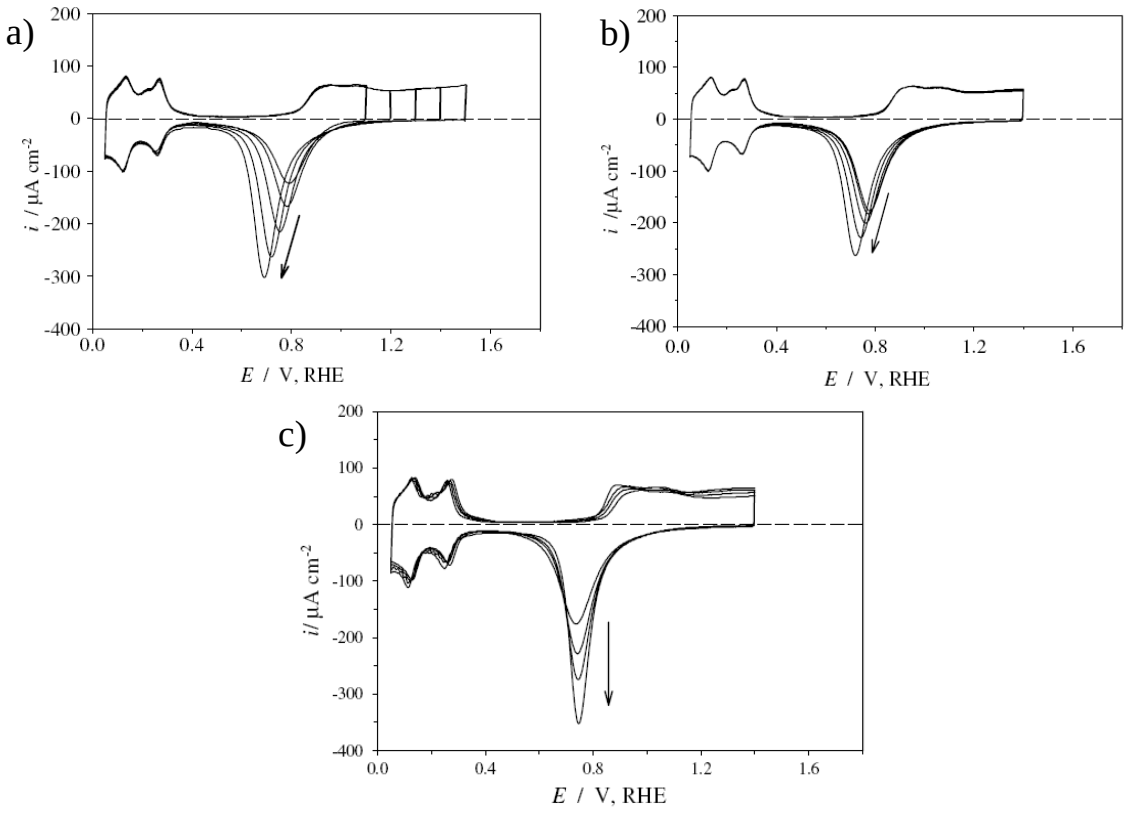

Figure 1.14. Series of CV profiles for Pt in 0.5 mol dm^{-3} aqueous sulphuric acid at sweep rate of 50 mV s^{-1} showing the effect of: **a)** increased E_p from 1.10 to 1.50 V for t_p = 10^4 s and T = 293 K; **b)** increased t_p from 1 to 10^4 s at E_p = 1.4 V and T = 293 K; **c)** increased T from 278 to 323 K at E_p = 1.4 V and t_p = 10^4 s on the oxide growth behaviour. (Taken from reference (*100*).)

This was attributed to a rearrangment of a surface phase with lower free energy compared to that of the species deposited in the anodic sweep (*80*). Investigation of the processes as a function of different conditions (temperature, potential and time) revealed more details on the effect (*80, 100*). Platinum oxide formed at higher

potentials (see figure 1.14a) and/or for longer times (see figure 1.14b) presumably provides surface films that are more stable and reduce at more negative potentials compared to those formed at short time and low potentials. On the other hand, an increase in temperature does not lead to any significant shift in the reduction potential. However, an increase in the peak density with increasing temperature indicates thicker films are formed at higher temperatures (*100*).

In contrast to the many problems associated with the understanding of the oxygen adsorption mechanism, it has been accepted (*81*) that a monolayer of hydrogen is adsorbed on Pt a potentials about 0.3 V more positive to the reversible hydrogen electrode (hence it may be called "underpotential" deposition, UPD (*101*)). Formally, the UPD of H can be represented as shown in eq. 1.9:

$$\begin{array}{cccccc} H_3O^+ + Pt & & + e^- & \leftrightarrow & MPt_{ads} + H_2O \\ C_{H^+} & 1-\theta_H & E & & \theta_H & \end{array} \qquad (1.9)$$

where E is potential, C_{H^+} is proton concentration, θ_H is the site fractional occupancy for H_{ads} and $(1-\theta_H)$ represents the vacant sites fraction ($0<\theta_H<1$). The Nernst equation for this process will take form of:

$$E(\theta_H) = \frac{RT}{F}\ln K_H C_{H^+} - \frac{RT}{F}\ln\frac{\theta_H}{(1-\theta_H)} \qquad (1.10)$$

The capacitance can be given by:

$$C_\phi = \frac{q_1 F}{RT}\cdot\theta_H(1-\theta_H) = \frac{q_1 F}{RT}\cdot\frac{K_H C_{H^+}\exp[-EF/RT]}{(1+K_H C_{H^+}\exp[-EF/RT])^2} \qquad (1.11)$$

where q_1 is the charge for monolayer deposition of H (*102*).

This capacitance (C_ϕ) is called *pseudocapacitance* because the charge consumed does not stay directly in the electrode, but transports producing a faradaic change (*103, 104*). In turn the pseudocapacitance is associated with the potential dependence of θ_H (as shown in eq. 1.11).

Typical hydrogen waves are shown in figure 1.12 in the potential region between +0.4 and 0 V *vs.* RHE. The anodic (ionisation) and cathodic (deposition) waves are symmetrical, indicating a very rapid rate of reaction. Eucken and Weblus (*105*) using impedance measurements and later Will and Knorr (*106*) in the studies involving linear cyclic voltammograms were the first to recognise that there are two states for hydrogen adsorption (see figure 1.12, H_1 and H_2). Later studies were based on the investigation

of hydrogen adsorption on single crystal Pt with different orientations (*107-110*). However, the main problem in the studies was to have pure Pt surface, as it is known to be an excellent adsorbent for impurities. The best results in this area were achieved by Clavilier (*111*).

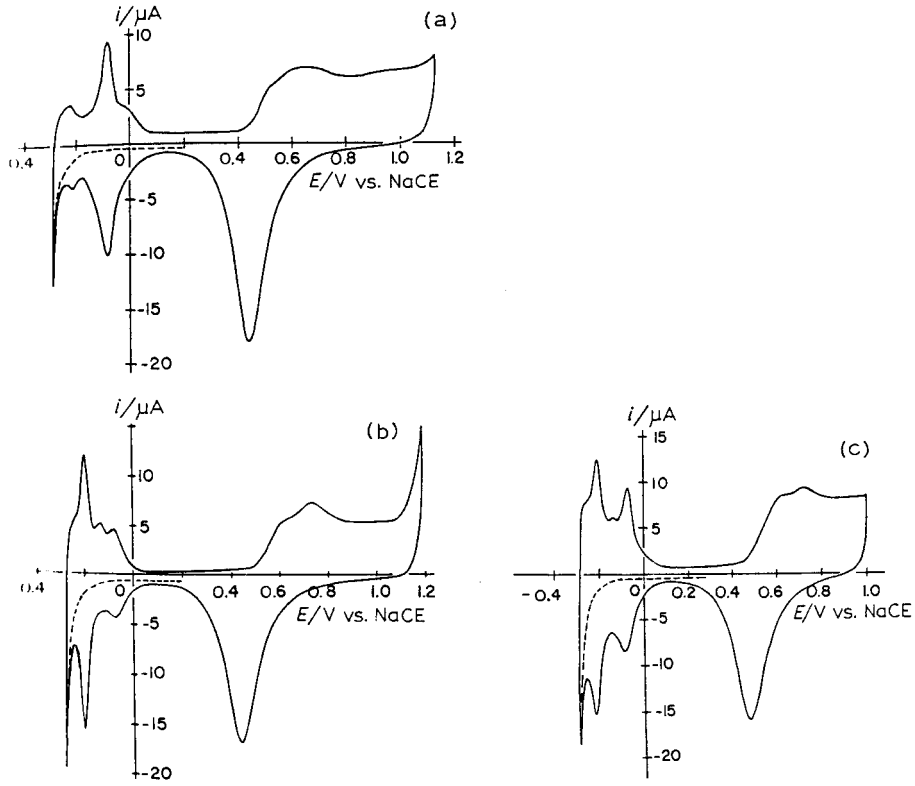

Figure 1.15. Cyclic voltammograms for Pt electrodes in 1 mol dm^{-3} sulphuric acid solution **a)** Pt (100) single crystal, **b)** Pt (111) single crystal and **c)** polycrystalline Pt electrode. Sweep rate 10 mV s^{-1}. Electrode area: a) 0.622, b) 0.579, c) 0.800 cm^2. (Taken from reference (*112*).)

Now it is generally agreed that the multiple peaks correspond to different types of surface sites. These surface sites have different surface free energies. All studies clearly showed that in cyclic voltammetry of polycrystalline platinum there is a prominent peak for the Pt(111) surface corresponding to the "weakly adsorbed hydrogen" and one for the Pt(100) surface corresponding to the "strongly adsorbed hydrogen" (*113*). Formation of the third anodic peak sometimes could be seen (see figure 1.12, peak labelled H_3). The third "anomalous" peak is attributed to HSO_4^- ion adsorption (*107*). The specific adsorption is known to play a significant role in platinum surface electrochemistry. Therefore, such processes certainly deserve more detailed consideration.

1.4.2 Effect of anions adsorption on the platinum electrochemistry

Pt electrochemistry significantly depends on the purity of the system. However, it is not always possible to remove all factors what would influence the surface electrochemistry of Pt. In particular, the adsorption of electrolyte anions to varying degrees, will always be present at the surface. Detailed studies of the influence of ion adsorption have been made by a number of researchers (*114-120*).

As an example of specific anion adsorption, figure 1.16 shows the effect of addition of chloride to the voltammogram in perchloric acid solution obtained by Breiter (*115*). The investigations showed that as the concentration of Cl^- ions increases, the strongly bonded UPD hydrogen becomes more inhibited and three peaks occur in the hydrogen desorption region.

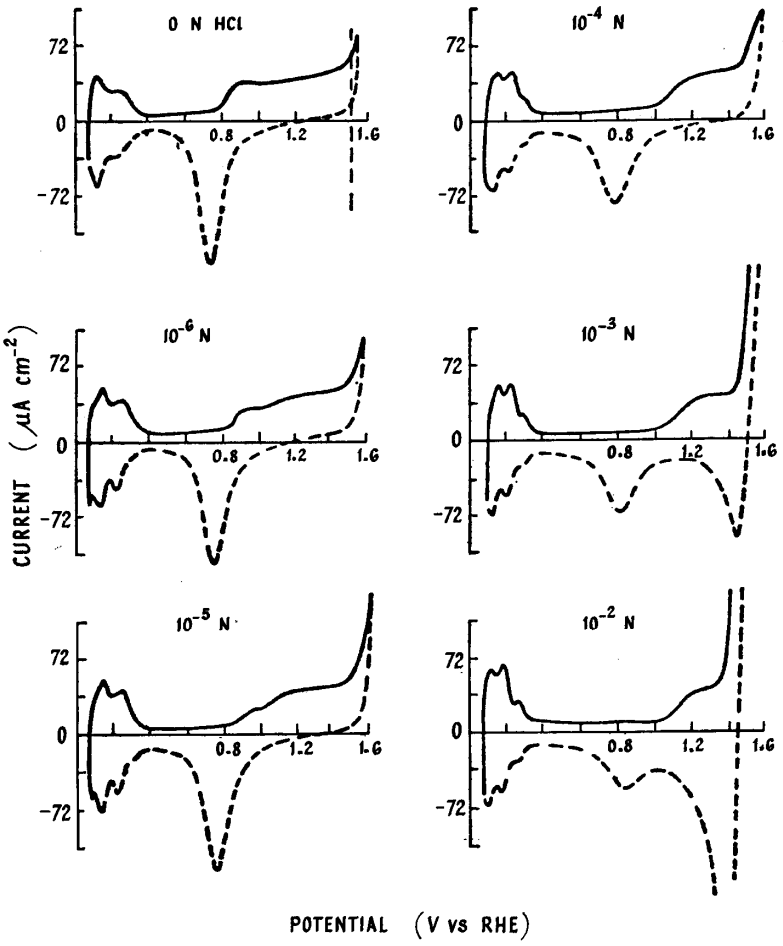

Figure 1.16. Effect of various additions of HCl on the voltammogram of Pt in 1 mol dm^{-3} $HClO_4$ at 30 mV s^{-1}. (—) anodic, (— —) cathodic scans. (Taken from reference (*115*)).

In this case competitive adsorption of H atoms and halide ions takes place (*121, 122*). In addition the formation of Pt oxide starts at increasingly more positive potentials. Breiter suggested that chloride ions begin to adsorb in the hydrogen region during the anodic sweep. The adsorption increases in the double layer region and causes a shift in the oxide formation region to more positive potentials. In this potential region some of the adsorbed ions are replaced by oxygen atoms. In contrast desorption of Cl^- ions is triggered during the cathodic sweep extending down into the Pt H_{UPD} region.

It has also been shown that the type of anions adsorbing on the surface will strongly depend on the potential of the electrode, the electrode material and the pH of solution. For example, Kunimatsi *et al*. (*123*) used Fourier transform infrared reflection (FT-IR) absorption spectroscopy to study the adsorption of bisulphate and sulphate ions on Pt in sulphuric acid by observing their asymmetric S-O stretching vibrations. It was found that the two anions are co-adsorbed over the potential range studied.

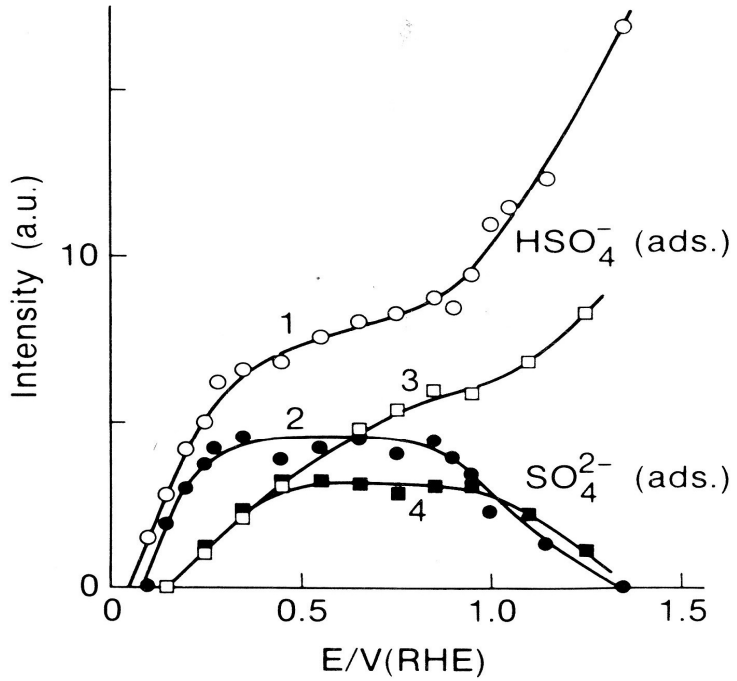

Figure 1.17. Potential dependence of integrated band intensity of HSO_4^- and SO_4^{2-} adsorbed on Pt in 0.05 (□, ■, ×) and 0.5 mol dm^{-3} H_2SO_4 (○, ●). Taken from reference (*123*).

Figure 1.17 shows the potential dependence of the asymmetric S-O stretching bands of HSO_4^- and SO_4^{2-}, adsorbed on polycrystalline Pt electrode in 0.05 mol dm^{-3} and 0.5 mol dm^{-3} sulphuric acid. The intensities of both bisulphate and sulphate ions increase

with potential in the hydrogen region and then tend to saturate in the double-layer region. However, as the potential increases into the oxide region, the sulphate band loses its intensity rapidly, while the bisulphate band gains intensity.

Similarly, the specific adsorption of phosphate anions as a function of pH and potential using the FTIR method was examined and reported in the literature (*124-127*). Phosphoric acid is triprotic with acid dissociations constants (pK_a values) 2.14, 7.2 and 12.4, for H_3PO_4, $H_2PO_4^-$ and HPO_4^{2-}, respectively. Using these dissociation constants the concentration ratios for different pH values can be calculated. The concentration ratios are presented in Table 1.1.

pH	Species	Concentration Ratio
12.6	$[PO_4^{3-}]/[HPO_4^{2-}]$	1/0.62
8.0	$[HPO_4^{2-}]/[H_2PO_4^-]$	1/0.17
6.8	$[HPO_4^{2-}]/[H_2PO_4^-]$	1/2
4.4	$[HPO_4^{2-}]/[H_2PO_4^-]$	1/131
2.0	$[H_2PO_4^-]/[H_3PO_4]$	1/1.45

Table 1.1. Concentration ratios of phosphate ions at different pH of solution (*124, 126*).

Ye *et al.* (*126*) observed spectra of polycrystalline platinum electrodes in phosphate media at pH 6.8 and 12.6. The potential dependences of the spectra at the electrode are shown in figure 1.18.

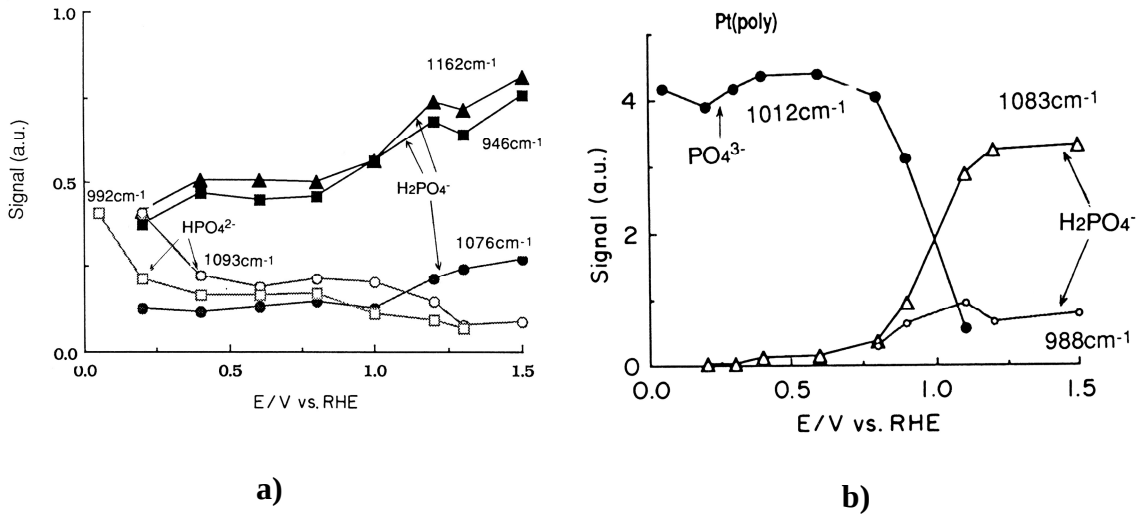

a) **b)**

Figure 1.18. Potential dependence of the bands for adsorbed phosphate species at polycrystalline platinum electrodes at a) pH = 6.8 and b) pH = 12.6 (*126*).

At pH 6.8 the species HPO_4^{2-} and $H_2PO_4^-$ are expected to exist at a ratio of 1:2 (see Table 1.1). Figure 1.18a shows that intensities of the adsorbed HPO_4^{2-} are constant in the potential range between +0.4 and +0.8 V *vs.* RHE (here the hydride and double layer region). However, when the potential exceeds +0.9 V *vs.* RHE (*e.g.* oxide region), the band due to the protonated $H_2PO_4^-$ increases while that of HPO_4^{2-} decreases. At pH 12.6 the species PO_4^{3-} and HPO_4^{2-} are expected to exist at a ratio of 1:0.62 (see Table 1.1). The potential dependences of the spectra at pH 12.6 show that at low potentials, (E < +0.8 V *vs.* RHE), the PO_4^{3-} species dominate. At higher potentials (E > 0.8 V *vs.* RHE) the band intensity of PO_4^{3-} begins to decrease while that of HPO_4^{2-} increases. This clear change in ion adsorption occurs as the Pt electrode enters the oxide region.

All the above investigations suggest that changing of experimental conditions (*e.g.* electrolyte type, concentration, pH) will affect the surface electrochemistry of the Pt electrode. These factors will be taken into account in the investigations of Pt electrochemistry (see Chapter 5) discussed in this thesis.

The previous sections have focused on the general electrochemistry of polycrystalline (polished) Pt. However, a significant part of work presented in this thesis employs modified Pt electrodes (specifically mesostructured Pt). The preparation and characterisation of these materials is the topic of the next section.

1.5 Mesoporous Materials

Mesoporous materials are materials containing pore size within the range of 2-50 nm according to the IUPAC notation (*128*). These materials have found applications in many different scientific areas. Examples include capacitors, membranes, batteries, catalysts, sensors and molecular sieves (*129-135*). Natural porous materials, aluminosilicate form an extensive class of materials known as zeolites. These materials generally consist of a periodic three-dimensional crystalline framework structures with a pores sizes usually around 10 Å (*136*). These synthetic materials are widely used for selective catalysis or the separation of gases or liquids (*137*). However, the small size of the pores, and therefore low accessibility, restricts the number of applications of these materials. Hence new methods of fabrication with the ability to create larger pore

size were required. This was completed by employing surfactants (*e.g.* Brij 56, polyoxyethylene glycols, pluronics, CTAB) to act as structure directing aids and templates. The properties of these surfactants (*138*) allow the formation of a liquid crystal mesophase. Liquid crystals (LC) are substances that have properties between those of the liquid state (they flow as a liquid) and those the of solid state (molecules arranged in crystal-like manner) (*139*).

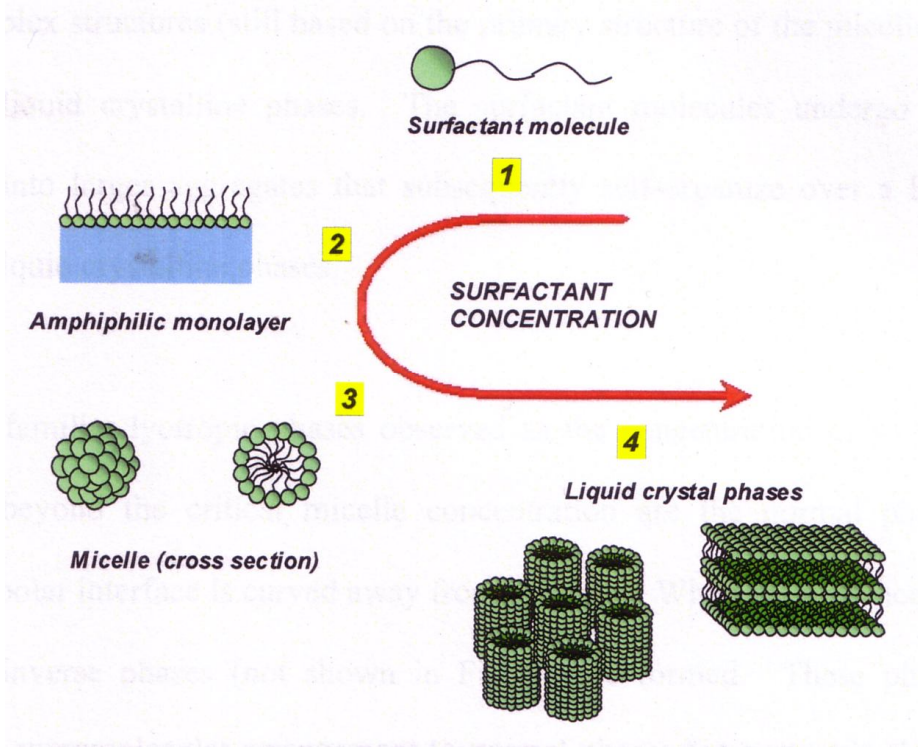

Figure 1.19. Schematic representation of formation of liquid crystal phases. (Taken from reference (*140*).)

The ability of surfactants to produce LC comes from the chemical structure of the compounds. Surfactants are normally long chain molecules and combine two very well differentiated parts: a hydrophilic 'head' and a hydrophobic 'tail'. Increasing the surfactant concentration in solution allows various LC phases to be formed as illustrated in figure 1.19. The driving force for all these arrangements is to minimize the energy of the system with respect to the interaction of the aqueous environment with the hydrophobic portion of molecule and therefore create the most thermodynamically stable assembly. Figure 1.19 shows that at low concentration the most favourable form is the amphiphilic monolayer (2), which will rearrange into a micelle form as the concentration of surfactant is increased (3). If the concentration keeps increasing the arrangement of the molecules will change into more complex

structures forming other lyotropic liquid crystalline (LLC) phases (for example, hexagonal, cubic, lamellar structures).

Temperature and concentration are two important factors in the self-assembly of LC mesophases. By varying the temperature and concentration a phase diagram can be obtained, which would allow prediction of the LC phase at the current conditions (see figure 1.20).

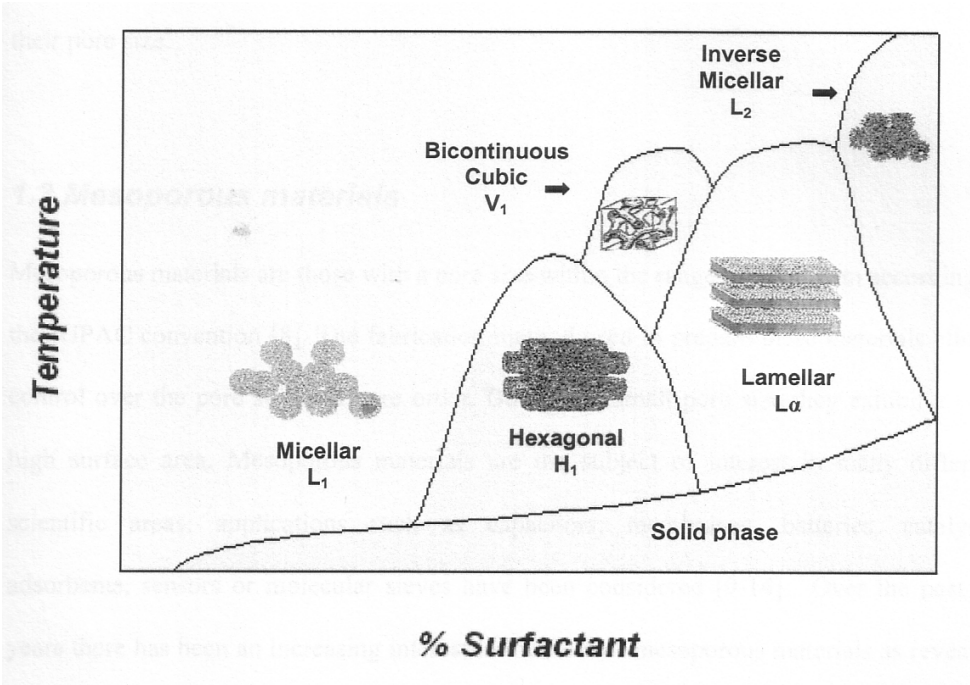

Figure 1.20. Schematic of surfactant phase diagram showing some of the liquid crystal phases formed. (Taken from reference (*140*).)

It is clear that the possibility of predicting the phase present would be one of the advantages in utilisation of LLCs for templating materials.

Kresge *et al.* (*141*) was first to use a liquid crystal template mechanism for synthesis of inorganic mesoporous materials M41S (*142*) are a family of silicate/aluminosilicate mesoporous molecular sieves what have been produced using the templating method. In this technique low concentrations of surfactant were used. The templating mechanism involved the interaction between an alkaline colloidal silica precursor and an ionic amphiphile specifically hexadecyltrimethylammonium bromide, CTAB. A variety of different materials were synthesised using this technique. The most studied of these materials is MCM-41 (Mobil Composition of Matter 41), containing a hexagonal arrangement of channels with a diameter in the range of 16 Å to 100 Å (*141*). Other members of the family are MCM-48, with a complex interconnecting, 3-

dimensional, channel system and MCM-50 consisting of a lamellar structure (*143, 144*).

An alternative route to produce an ordered mesoporous materials is to use "true lyotropic liquid crystalline phases" as a structure directing media. In this case the synthesis of the inorganic material takes place within the ordered environment of a bulk surfactant. This method was reported by Attard *et al.* (*145*) in 1995 for synthesis of mesoporous silica. The resulting silica had pores with diameter of *ca.* 30 Å and surface area of *ca.* 1400 m^2 g^{-1}. Varying the lyotropic liquid crystalline phases it was possible to obtain different architecture silicas (H_I-SiO_2, *Ia3d*-SiO_2, and L_α-SiO_2). In contrast to the syntheses of MCM mesoporous materials, the surfactant concentration used in these experiments was high, typically >30 wt %. This was necessary to ensure that a homogenous liquid crystalline phase was obtained and that the phase remained unchanged throughout the progress of the reaction and the calcination process (*146*).

Attard *et al.* (*147, 148*) used hexagonal (H_I) liquid crystalline phase as a template for the synthesis of mesoporous platinum powders and films (H_I-Pt) via the reduction of hexachloroplatinic acid (HCPA). Figure 1.21 is showing the 3D structure of the hexagonal liquid crystalline phase and the expected nanostructure of the material produced within this template environment.

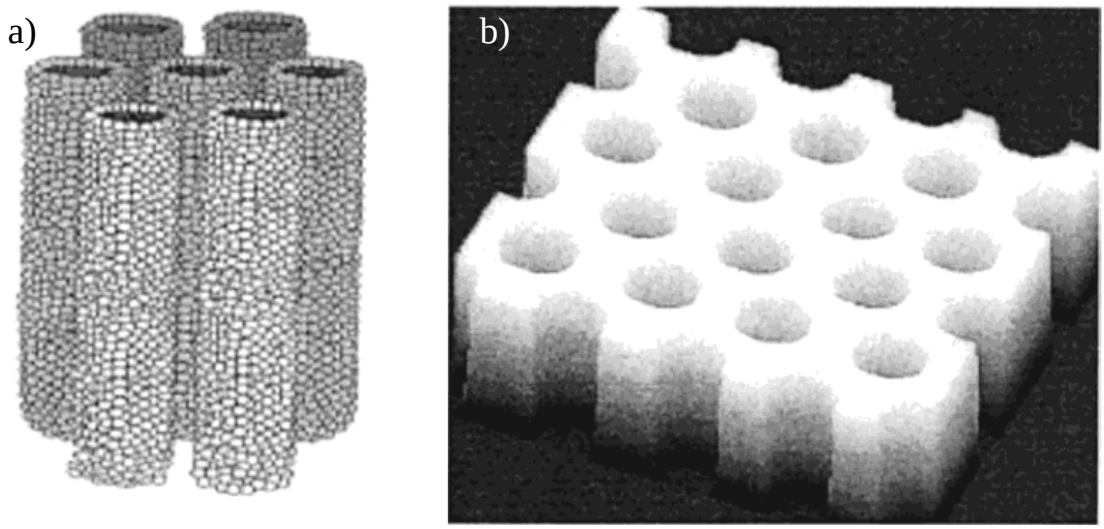

Figure 1.21 Schematic of (a) the 3D structure of a hexagonal liquid crystalline phase and (b) the expected nanostructure of a material produced in its presence. After (*146*).

The resulting films were adherent and shiny, but were shown to have a nanostructure as well as the H_I-Pt powders. For films from mixture containing $C_{16}EO_8$, the pore diameter was found to be 25 ± 1.5 Á. The wall thickness between the pores was also found to be 25 ± 2 Á. The studies also showed that the diameters of the pores could be

controlled either by using surfactants with shorter or longer chains than $C_{16}EO_8$, or by swelling the phase with hydrocarbon additive.

Electrodeposition of the mesoporous platinum directly onto an electrode surface provides the necessary control over the conditions to create the film and the possibility to predict the thickness of the deposited film (*149*). Attard *et al.* demonstrated that the electrode potential and the temperature during the electrodeposition had an influence on the uniformity and surface area of the nanostructured films produced (*146*).

In this thesis Pt electrodes modified with H_I-Pt films will be employed to study oxygen reduction in an HMV system. Hence the next section outlines the electrochemistry of molecular oxygen.

1.6 Electroreduction of Molecular Oxygen

The reduction of molecular oxygen at the surface of an electrode is of considerable importance to many fields of research (*150-153*). The mechanism for the reduction of molecular oxygen is known to be complex and dependent on the substrate employed. The literature discussing the oxygen reduction reaction (ORR) is broad and has been reviewed on several occasions (*99, 154-156*). The rotating ring-disk electrode (RRDE) (*157*) has been widely used to study complex electrochemical reactions involving intermediate compounds. Mueller and Nekrasov (*158*) were first to use the RRDE to study oxygen reduction. In this case the oxygen reduction was carried out on the disk while the H_2O_2 was monitored on the ring (note the ring was held at a potential sufficient to oxidize hydrogen peroxide back to O_2). More recently the substrate generation/tip collection (SG/TC) mode of scanning electrochemical microscopy (SECM) coupled with linear voltammetry was proposed as a method to study the ORR (*159*). The SECM method is able to achieve higher collection efficiency and sensitivity compared to the RRDE and does not employ convection.

According to the mechanisms discussed in the literature (*154, 159-165*), the general scheme of the oxygen electroreduction process can be presented as:

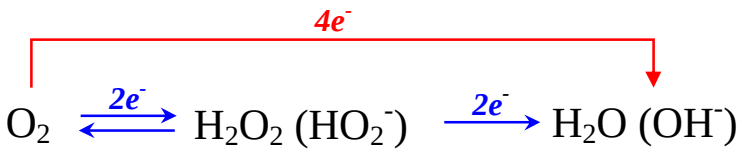

Figure 1.22. Schematic pathway mechanism proposed for electrochemical reduction of oxygen (*164*).

The electrochemical reduction of oxygen involves two parallel pathways: a direct 4-electron reduction to produce H_2O or OH^-, and an indirect 2-electron reduction to produce H_2O_2 and subsequent reduction of H_2O_2 to H_2O or OH^- via a second 2-electron process. Despite the apparent simplicity, these reactions (figure 1.22) combine complex electrocatalytic networks involving several elementary steps. Two groups of substrate can be identified, those reducing oxygen to hydrogen peroxide through a 2 electron pathway and those reducing oxygen to water through the 4 electron pathway (*10, 162, 164, 166-168*) .

The oxygen reduction reaction (ORR) occurs as the cathodic process in energy conversion systems. The occurrence of the 4-electron pathway is the most desirable for the production of electrical energy. Therefore, the conditions to achieve the 4-electron pathway have been long investigated using a variety of different electrode materials and within a multitude of electrolytes (*169-172*). The electrochemical reduction of oxygen has been also investigated using the mesoporous platinum microelectrodes. Kucernak *et al.* (*173, 174*) reported electron transfer numbers of *ca.* 4 in acidic media. However, at this stage it was concluded that there is no real improvement in ORR what could be attributed to the mesoporous characteristics of the electrodes. Birkin *et al.* (*172*) reported that Pt mesoporous modified electrodes have significantly altered oxygen reduction characteristics when compared to polished platinum electrodes of the same dimensions within a phosphate buffer. However, increasing the surface area of the deposit further did not shift the reduction wave to more positive potentials. In this case it was proposed that the influence of adsorbed species (probably PtO) inhibited the ORR reaction and therefore increasing the surface area did not introduce further beneficial kinetic effects.

In this thesis results obtained from a HMV investigation of ORR are presented. In some of these investigations, data analysis has been performed with a Fast Fourier Transform (FFT) approach. Hence the next section outlines Fourier Transforms (FT) and Fast Fourier Transforms (FFT) data analysis.

1.7 FFT Analysis

In the work presented in this thesis the FFT approach will be applied to analyse some of the HMV data collected (see Chapter 6). The general idea of the technique is to be able

to obtain multiple frequency data from a single measurement. This can be achieved by employment of a FFT approach to data analysis. Therefore in this section a brief outline required for understanding the FFT procedure and its applications to the analysis of the electrochemical data gathered will be discussed.

Any periodic waveform can be represented as a sum of simple sinusoidal components comprising of a fundamental frequency and its harmonics. Figure 1.23 shows an example of how a square wave can be approximated with a series of sine waves. This could be presented as:

$$y(t) = \frac{a_0}{2} + \sum_{n=1}^{\infty} [a_n \cos(2\pi n f_0 t) + b_n \sin(2\pi n f_0 t)] \tag{1.12}$$

or, alternatively,

$$y(t) = A_0 + \sum_{n=1}^{\infty} A_n \sin(2\pi n f_0 t + \phi_n) \tag{1.13}$$

where a_n, b_n, A_n are the amplitudes of the component with frequency nf_0 (f_0 - fundamental frequency) and ϕ_n is its phase angle, a_0, A_0 is the dc level. This series is called a *Fourier series* (*10*).

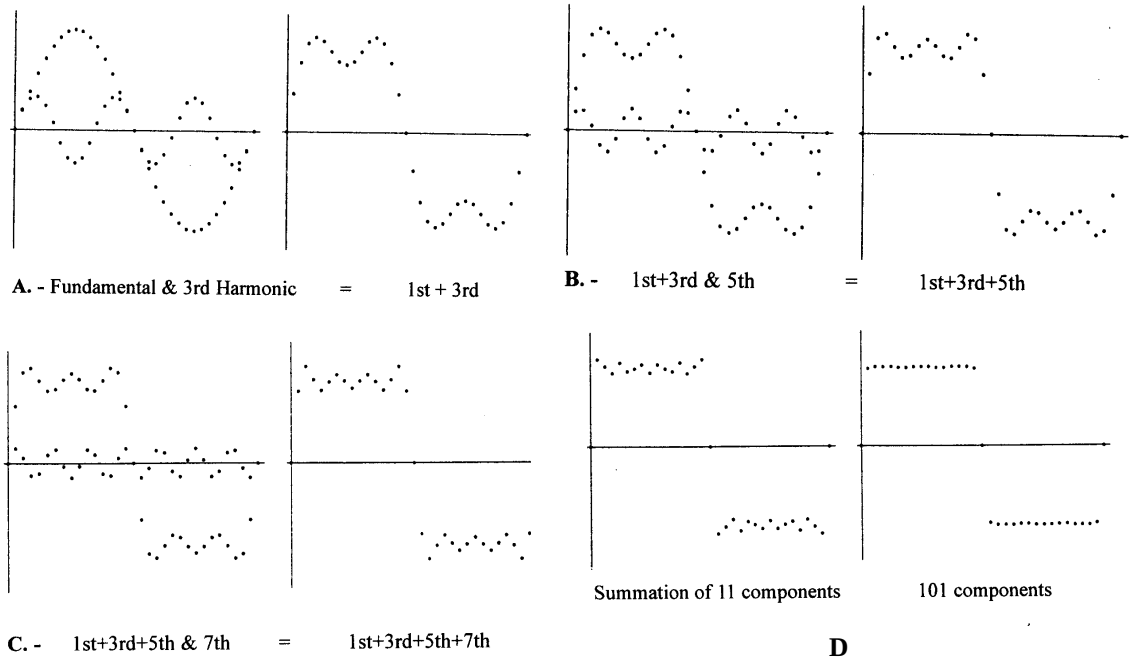

Figure 1.23. Construction of a square wave. (Taken from reference (*175*).)

Fourier series allow transformation of signal from the *time domain h(t)* (showing how the signal changes over time) to the *frequency domain H(f)* (a set of amplitudes and phase angles of the components sinusoids) and inversely. A given signal can be

converted between the time and frequency domains using the operation called *Fourier transform (10, 175)*:

$$H(f) = \int_{-\infty}^{\infty} h(t) e^{-j2\pi f t} dt \tag{1.14}$$

$$h(t) = \int_{-\infty}^{\infty} H(f) e^{j2\pi f t} df \tag{1.15}$$

In most electrochemical applications the signal of interest are digitized (sampled) at a constant rate. In the work presented here, the signal of interest is current represented as a series of data points taken at evenly spaced time intervals. Therefore, the numeric algorithm would be created using the Fourier transform eq. 1.12 to generate the frequency domain information. The result would consist of a lists of amplitudes and phase angles (*10*).

The Fourier transform (FT) technique is central to many frequency response measurements used in analytical chemistry. FT techniques have found their applications in numerous different research fields including infrared spectroscopy (FTIR) (*176, 177*) and electrochemical impedance spectroscopy, where FT processing methods are routinely used (*10, 178*). Fourier transforms have also been employed in HMV analysis (FTHMV). Schwartz (*31, 32*) *et al.* used this data analysis method to study electrochemistry at a rotating disc electrode. The FTHMV technique was used to study the frequency response characteristics of the mass-transfer limited reduction of 2 mmol dm^{-3} ferric ion. The method was shown to be fast and accurate. The technique was also used to study nonlinear behaviour of convective systems. This allowed the employment of the HMRDE system at higher frequencies (12.5 Hz) when compared to conventional HMV RDE.

In this thesis a FFT approach will be adopted to analyse current oscillations from a vibrating wire experiment (see Chapter 6). It will be shown that this approach enables relatively high modulation frequencies (> 80 Hz) and scan rates (500 mV s^{-1}) to be employed.

In the majority of HMV systems described in the literature and here, mass transfer modulation is achieved through some form of hydrodynamic flow variation. Clearly understanding the flow characteristics is important in these systems. One method to achieve this understanding is to use flow visualisation within the system employed. In

the next section a discussion of some relevant flow visualisation techniques is presented.

1.8 Flow Visualisation

Flow visualisation is a process by which the physics of fluid flows (liquids, gases) are made visible. There are many methods of flow visualization (*179, 180*). These may be images of dye or smoke injected into the flow field, particles which have been added into the flow, or electrochemically generated hydrogen bubbles.

One of the oldest methods of fluid observations employs smoke or dye. For example in 1883 Osborne Reynolds used a dye to show the transition from laminar flow to turbulent flow within a pipe (*181*). The technique is inexpensive and easy to apply. Food dye, laundry brightener, milk or fluorescent materials are the most commonly used colouring indicators (*180, 182, 183*). Here, two examples of dye application in flow visualisation are presented.

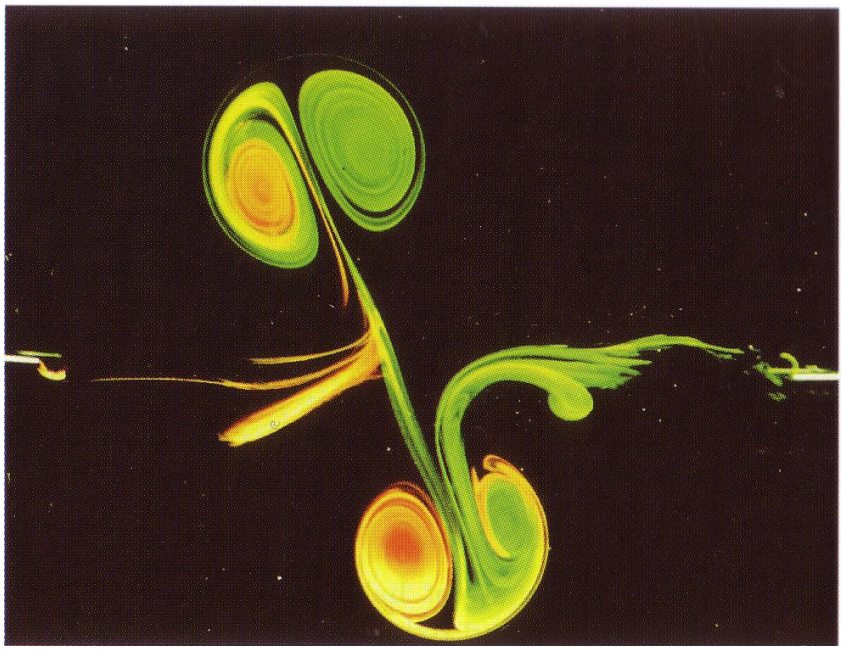

Figure 1.24. Collision of the two vortices. (Taken from reference (*184*).)

Figure 1.24 shows the collision of two vortices. As a result of the collision each ring of the original vortices splits into two forming two new rings. Here, the "exchange mechanism" was observed using two dyes (green and yellow). Another example is shown in figure 1.25. Again the employment of a dye allows the flow patterns of a

round jet to be visualised. The dye marks the jet shear layer, which rolls up producing distorted ring vortices.

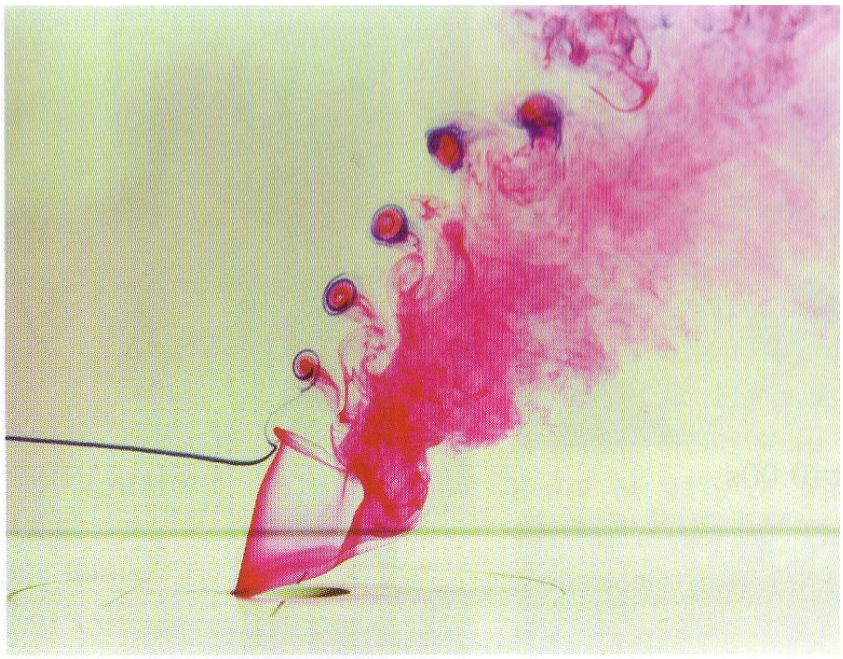

Figure 1.25. A round jet in cross flow. (Taken from reference (*185*).)

Another example of flow visualisation is the hydrogen bubble method. Hydrogen bubbles are electrochemically generated on a fine wire placed in the flow. The technique is often used to capture the flow structure of turbulent boundary layers (*186, 187*). An example of such an investigation is presented in figure 1.26.

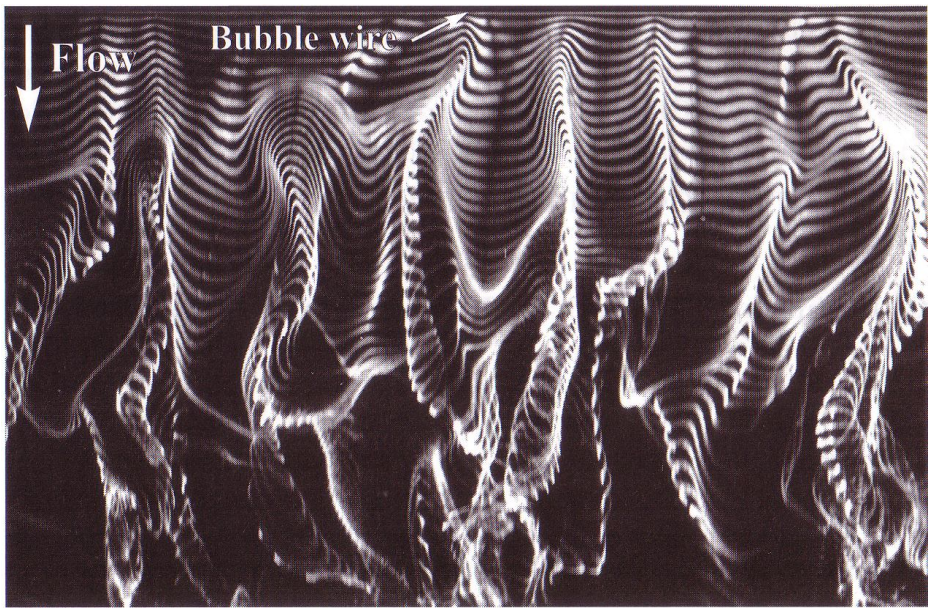

Figure 1.26 Turbulent low-speed streak pattern visualized by horizontal bubble time-lines in the near wall region of a turbulent boundary layer. Time-line generation frequency of 30 Hz. Taken from (*180*).

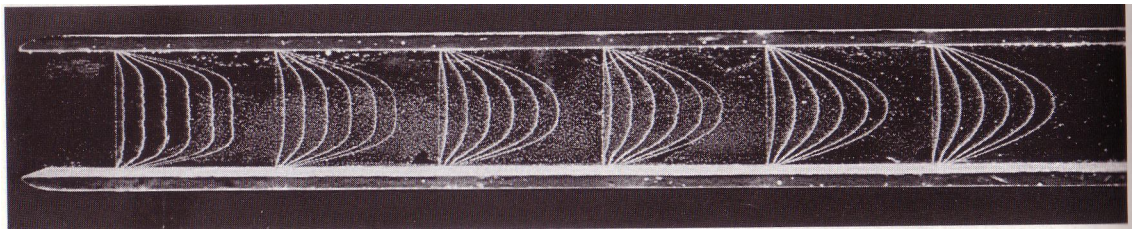

Figure 1.27. Flow in an inlet region between parallel plates (water, flow velocity 3.2 cm s^{-1}, distance between two plates 20 mm, *Re* = 640). Taken from (*179*).

In this case the bubble generation was periodically interrupted (pulsed) to produce the time lines which could be use in quantitative or qualitative analysis. The time lines of hydrogen bubbles were also used to record the flow between the parallel plates as shown in figure 1.27. The clear formation of parabolic or Poiseuille flow can be observed as result of this visualisation method.

1.9 Summary of Work Presented

The overall aim of this thesis was to develop novel hydrodynamic modulation techniques and use them to investigate analytically important modified electrodes.

Chapter 2 describes the experimental techniques and procedures used throughout the work.

Chapter 3 introduces a novel hydrodynamic modulation technique - an oscillating jet system. A lock-in approach is used as a method allowing discrimination between the signal of interest and other background signals. The application of the HMV apparatus in combination with the lock-in approach to trace detection is demonstrated.

Chapter 4 details further characterisation of the technique. Here high-speed imaging is used to give valuable insights into the behaviour of the oscillating jet. The results are compared with electrochemical experiments presented in chapter 3.

Chapter 5 investigates molecular oxygen reduction at polished and nanostructured platinum electrodes using the HMV technique described in chapters 3 and 4. The results obtained at different roughness factor mesoporous electrodes are reported.

Chapter 6 considers the application of vibrating tight-rope electrodes as a hydrodynamic modulation method. The analysing procedure used in the experiments is based on the FFT analysis.

Chapter 7 proposes a possible explanation for the pulsed behaviour observed in HMV experiments.

Finally, Chapter 8 summarises the conclusions drawn and areas of further investigations.

Chapter 2

Experimental

This chapter gives details of the experimental procedures, which were used during this thesis, including the apparatus and reagents used.

2.1 Electrochemical Measurements Using the Oscillating Jet System

2.1.1 General experimental set-up

The oscillating jet apparatus used in this work is shown in figure 2.1. This consisted of a ~3.5 cm radius membrane/piston attached to the base of an inverted funnel (see figure 2.2). The funnel neck was then pulled into a 2 mm diameter jet orifice. The cell was fitted with a glass tube of 28 mm inner diameter glued with epoxy resin to the funnel. During the electrochemical measurements an electrode was positioned inside the tube and above the jet orifice. Another glass tube (with a diameter of 1 cm) was added to the side of the funnel to make it easier to fill cell with a solution. Two different types of mechanical shakers were employed in this work. These were a LDS type V101 mini shaker and Gearing & Watson Electronics Ltd (Data Physics) mechanical shaker Model V4. The shakers were driven by either a stereo integrated amplifier Model AX-220 (JVC) or a Gearing and Watson Electronics Ltd Signal Force 30 W power amplifier (Model PA 30E). The power amplifier was supplied with a suitable signal by a function generator (TGA 12101, 100 MHz, TTi). The mechanical shaker was attached to the centre of membrane/piston with a mechanical coupling incorporating a single axis accelerometer (Model 3100B, Dytran Instruments, Inc., sensitivity 99.3 mV g^{-1}).

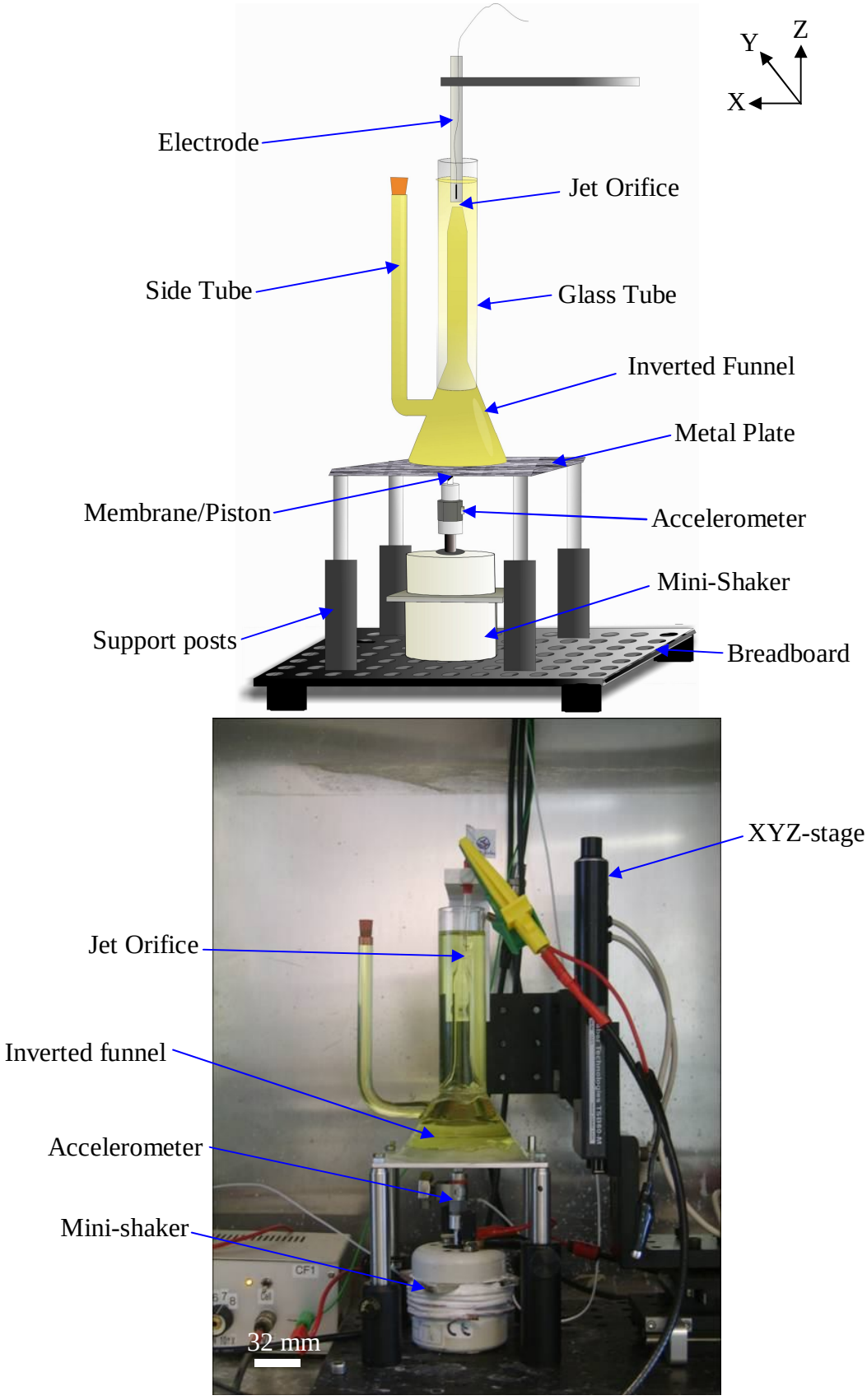

Figure 2.1. Experimental set-up of oscillating jet apparatus.

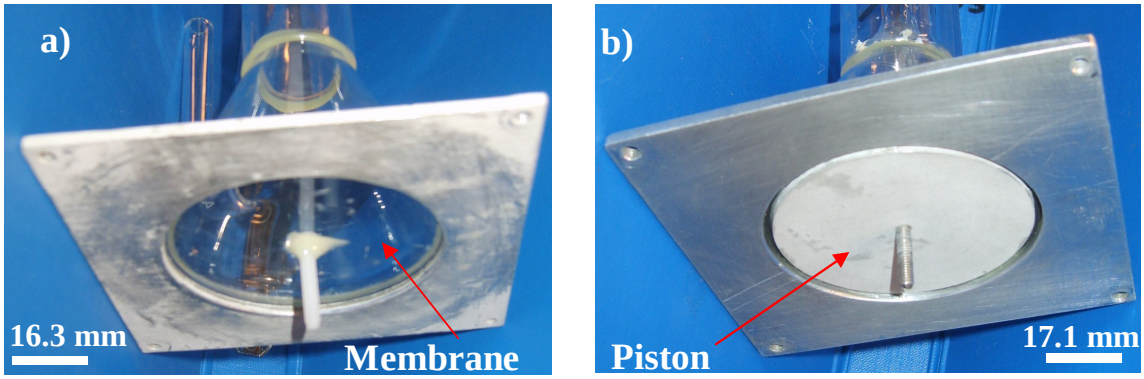

Figure 2.2. Underneath images of **a)** acetate membrane and **b)** piston oscillating jet cell.

The sensor was connected to a battery-powered current source and amplifier model 4105C (Dytran Instruments, Inc.). In order to avoid mechanical vibration of the apparatus, the cell was fitted with a metal plate (110×110 mm) and four posts attached with help of post holders to a breadboard (Thorlabs). The frequency of oscillation of membrane was 16 Hz (unless otherwise stated). Positioning of the electrode with respect to the jet orifice was controlled using XYZ stage (Zaber, 60 mm travel, resolution 0.1 µm, TLA 60A actuators connected to TSB 60-M stages).

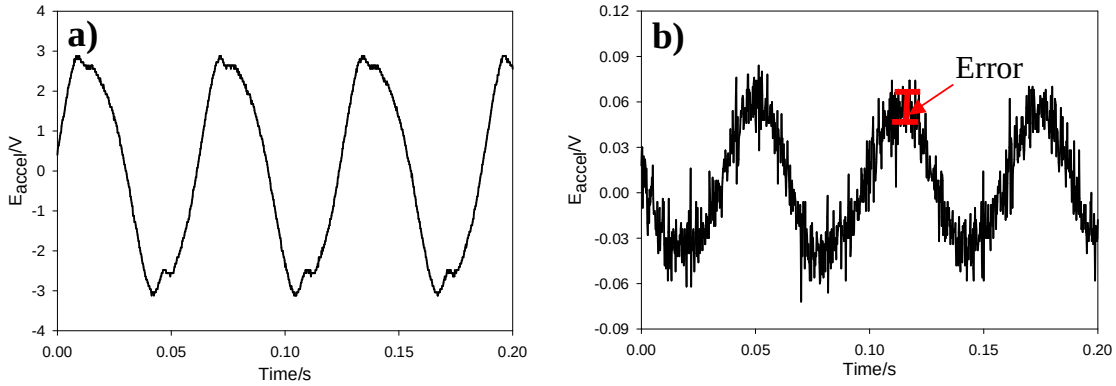

Figure 2.3. Accelerometer signal recorded for empty **(a)** and filled with a liquid cell **(b)**. The piston was modulated at 16 Hz. The accelerometer amplifier gain was set to x100. The noise level (**I—I**) was used to calculate the error of the measurement.

Figure 2.3 shows typical accelerometer signals recorded for the piston cell without (**a)** and with water (**b**). These demonstrate the dramatic decrease in amplitude as the cell was filled with a solution. For example, figure 2.3b indicates zero-to-peak amplitude of 0.0085 mm while figure 2.3a shows 0.2911 mm amplitude. The extra load (see Appendix B) is responsible for this change. The data was obtained using a Tektronix TDS2014 (1GS/s, 100 MHz) oscilloscope and transferred to the PC using commercially available software. However, it should be noted that because of the small amplitude of

the signal and the high level of noise (see figure 2.3b), averaging of the signal was often employed. The reduction of the noise as a result of this signal averaging obtained using the oscilloscope average function is shown in figure 2.4.

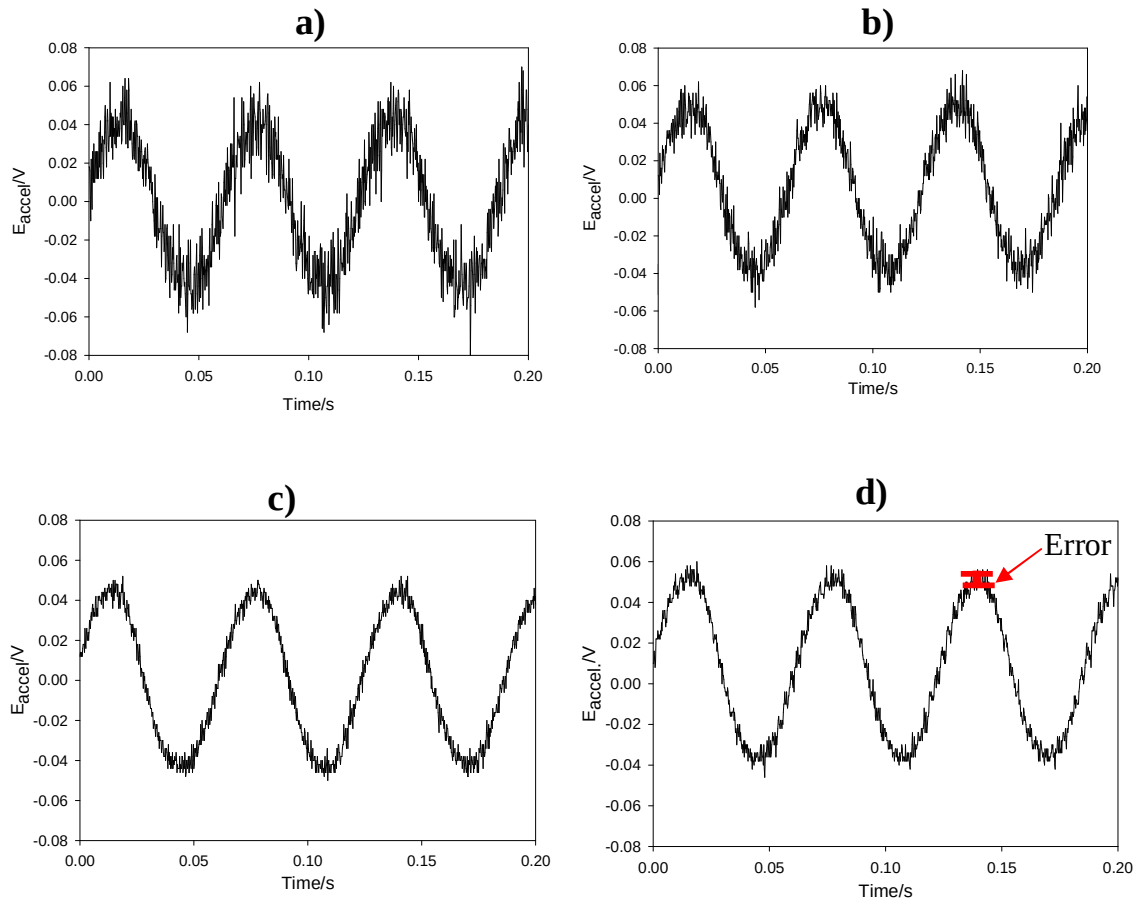

Figure 2.4. Plots showing the averaged signals of raw gathered from the accelerometer. Signals for **a)** 4, **b)** 16, **c)** 64 and **d)** 128 averages are shown. The noise level (**I—I**) was used to calculate the error of the measurement.

The oscillating frequency in most cases was 16 Hz. In order to calculate an error of the measurement a signal noise was measured as shown in figure 2.3b. In this case the error was determined to be ~30% of the measured signal. However, by employment of the averaging procedure reduced the error in this measurement to ~ 5 %.

2.1.2 Associated equipment

Two electrochemical workstations were used mainly throughout the work reported in this thesis. In the experimental measurements studying the electrochemistry of $[Fe(CN)_6]^{3-/4-}$ (under conditions when the generated current was <10 μA cm^{-2}), a two-

electrode cell was employed. In this arrangement a silver wire pseudo reference/counter electrode was used. In this case a system composed of a triangular wave generator (manufactured by T.W. Young) and an in-house built current follower (with a gain range from 1×10^4 V A^{-1} to 1×10^8 V A^{-1}) were used. In oxygen reduction experiments or voltammetry of high surface area electrodes, because of the higher currents generated at the modified electrodes, a three-electrode cell was utilised. Here a T.W. Young three-electrode potentiostat was employed (gain from 1×10^1 V A^{-1} to 1×10^8 V A^{-1}). In this case the reference electrode was a home made Hg/Hg_2SO_4 saturated K_2SO_4 (MMS) electrode and a Pt mesh counter electrode was employed.

The electrochemical data was recorded using a Computer Boards PCI-DAS1602/16 card. All cyclic voltammograms, current time plots or the HMV signal, were performed using in-house written software unless otherwise stated.

All electrochemical experiments were conducted in a Faraday cage to reduce electrical noise unless otherwise stated.

2.1.3 Polycrystalline Pt polished electrodes

The electrodes employed (Pt, 0.5 mm and 25 μm diameters) were fabricated in-house and were sealed in glass (diameter 5.0 mm for 0.5 mm electrode and 2 mm or 5.5 mm for the 25 μm electrode). The electrodes were hand polished to a mirror like finish, in a conventional manner, using alumina powder slurries (Struers, alumina 0.3 μm diameter) on microcloth (Buehler) polishing pads. This type of polished electrode was mainly used in the scanning analysis and detection limits determination measurements.

2.1.4 Nanostructured Pt electrodes

Templating Mixture Preparation

All liquid crystalline mixtures were prepared in a 25 ml glass sample vial where the surfactant, octaethylene glycol monohexadecyl ether ($C_{16}EO_8$), was added to an aqueous solution of chloroplatinic acid hexahydrate (H_2PtCl_6). The mixture was then placed into an oven for 15 minutes at a temperature between 35 and 50 °C to allow better mixing and, thus, better homogeneity of the phase domains. The sample then was removed from the oven and mixed manually for 5-10 minutes before returning to

the oven for a further 10 minutes. The same operation was repeated three to four times per sample. The resultant mixtures were analysed under an Olympus polarising microscope (BH-2) fitted with a heating stage (Linkam, TMS) to identify the resultant liquid crystalline phases.

Electrodeposition

A three-electrode commercial potentiostat (eDaq) with an eCorder 201 interface module was used for electrode deposition. Cyclic voltammograms and deposition transients were recorded using commercial eDaq chart and eChem v2.0.9 software respectively.

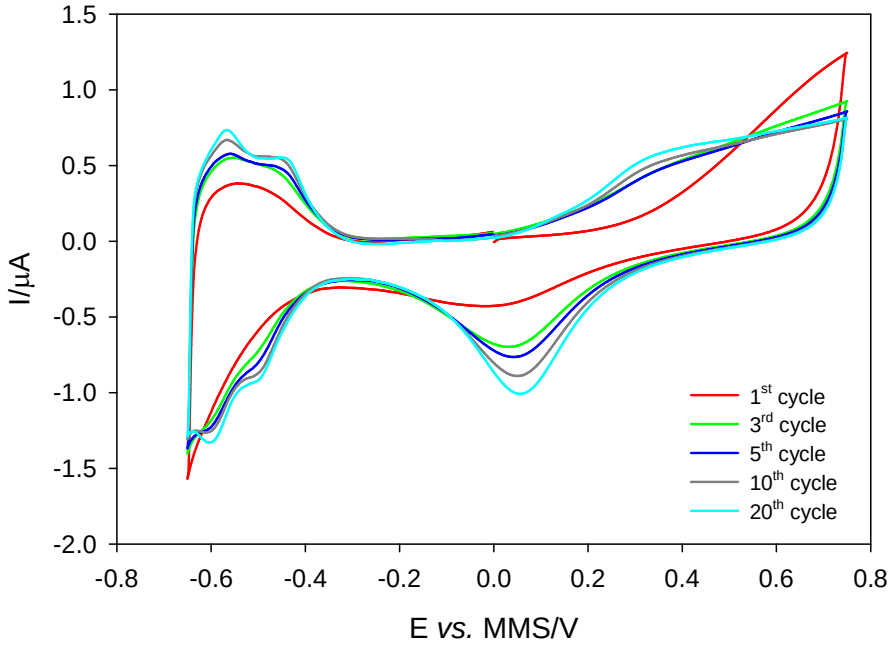

Figure 2.5. Plot showing a series of cyclic voltammograms recorded at the polished Pt electrode of 0.5 mm diameter in 1 mol dm^{-3} sulphuric acid at sweep rate of 200 mV s^{-1}. The measurements were performed at room temperature of 20-25 °C under aerobic conditions.

A set of 0.5 mm diameter Pt electrodes sealed in glass were modified with the nanostructured films. Prior to use, each electrode was polished using alumina powder (0.3 µm diameter). Each electrode was then electrochemically cleaned by cycling in 1 mol dm^{-3} aqueous sulphuric acid between +0.7 V and -0.65 V *vs.* MMS at a scan rate of 200 mV s^{-1}. An example of the cleaning process is shown in figure 2.5.

Electrodes were allowed to dry in air before further use. Different thicknesses films were electrodeposited at -0.5 V *vs.* MMS (25 °C) from the templating mixtures made of 1:1:1.5 w/w/w parts of water, H_2PtCl_6 and $C_{16}EO_8$. The thickness of the films was

controlled by measuring the charge passed during electrodeposition. An example of a current transient recorded at a Pt disk electrode during the electrodeposition of *H_I-Pt* is presented in figure 2.6. The final charge density for this particular example was 6.74 C cm^{-2}.

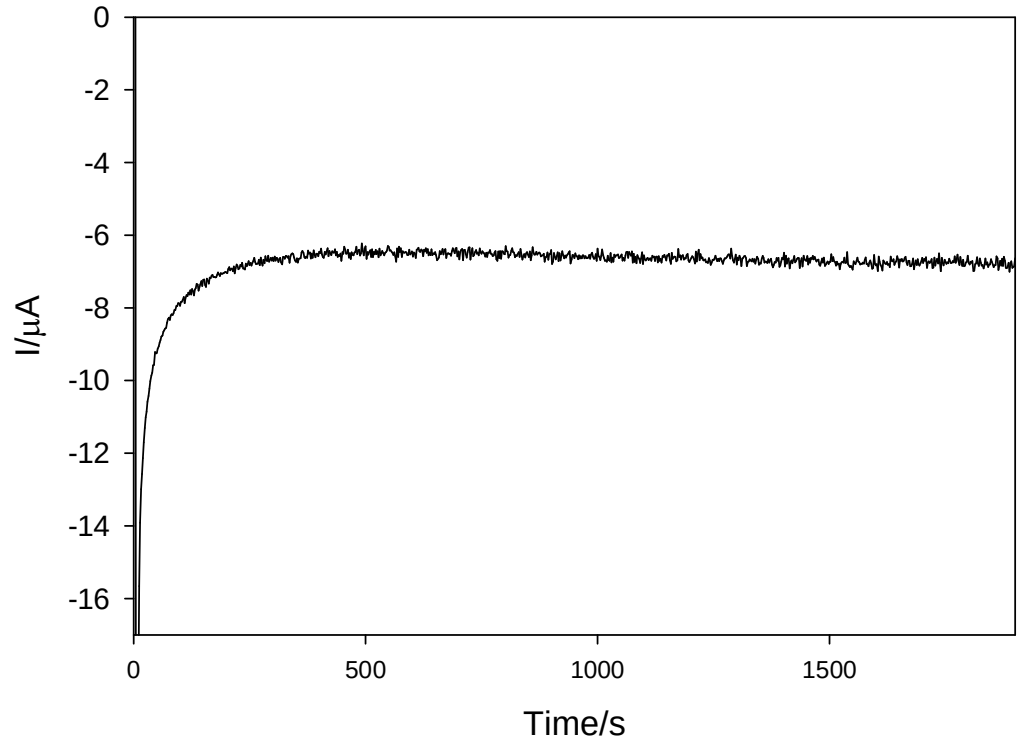

Figure 2.6. Current time transient for the electrodeposition of *H_I-Pt* on a 0.5 mm diameter Pt disk electrode carried out at potential of -0.5 *vs.* MMS. The deposition was performed at temperature of 25 °C.

After deposition the mesoporous electrodes were soaked for a period of 24 to 48 hours in a 250 ml beaker filled with pure water. During this period the water was regularly replaced, every 3 hours (except overnight).

Electrode Characterisation

The mesoporous platinum electrodes were electrochemically characterised by cyclic voltammetry from +0.7 to -0.65 V *vs.* MMS in 1 mol dm^{-3} sulphuric acid solution at a scan rate of 200 mV s^{-1}. The real surface area of the electrode was determined by integrating the current passed during the reverse scan within the range -0.25 to -0.65 V *vs.* MMS (*e.g.* the H_{UPD} region).

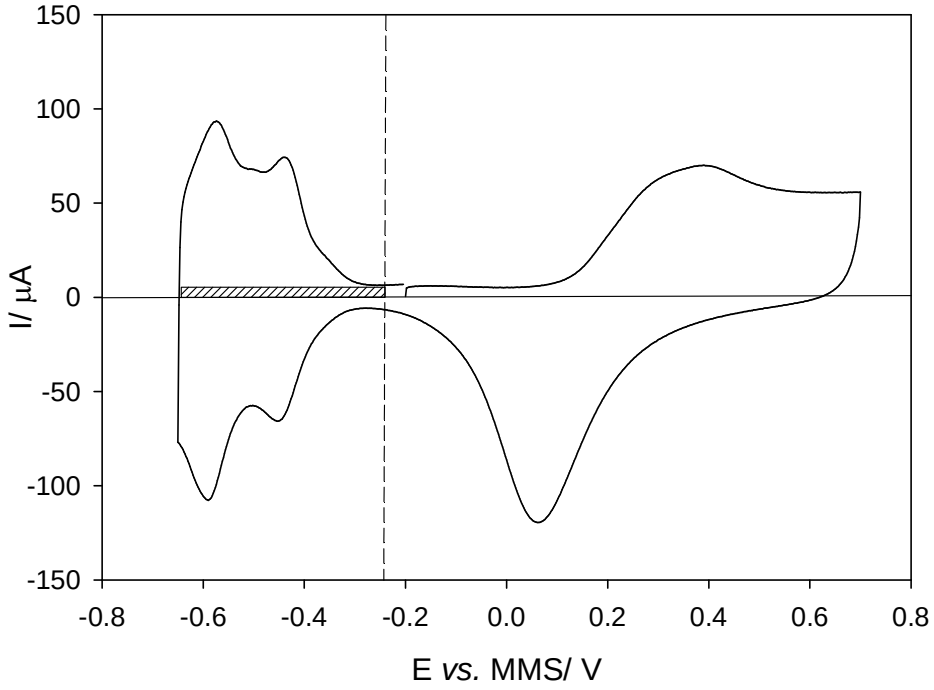

Figure 2.7. Cyclic voltammogram recorded at a 0.5 mm nanostructured Pt electrode in 1 mol dm^{-3} H_2SO_4 solution at a sweep rate of 100 mV s^{-1}. The shaded area on the graph shows the double layer charge. A roughness factor of 420.8 was calculated for this particular electrode.

The appropriate double layer charge (because the integration was carried out over the reverse cycle only) was subtracted (see figure 2.7, shaded area). A conversion factor of 210 μC cm^{-2} was then used to calculate the real surface area (*188*). This surface area measurement was divided by the geometric area of the electrode to produce an estimated roughness factor value (RF).

2.1.5 Scanning experiments

Scanning experiments were performed in the experimental cell described in section 2.1.1.

The experiments were carried out in a solution containing 5 mmol dm^{-3} $[Fe(CN)_6]^{3-}$ with 0.1 mol dm^{-3} $Sr(NO_3)_2$ supporting electrolyte (*189*). The electrodes employed in these measurements were polished Pt electrodes described in section 2.1.3. Positioning of the electrodes was achieved with a XYZ stage.

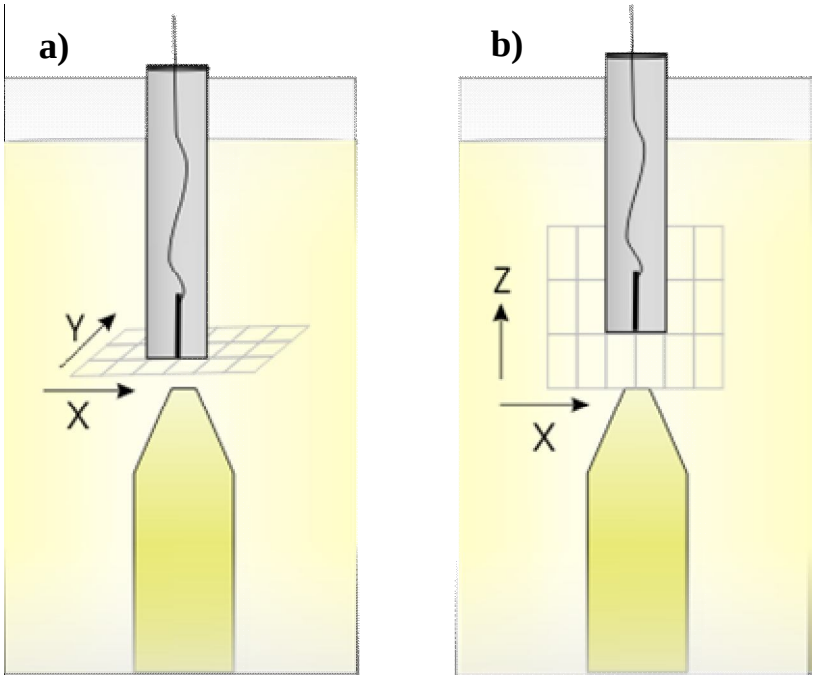

Figure 2.8. Schematic showing the **a)** XY and **b)** XZ planes of scanning experiments

Scanning experiments in the XY- (figure 2.8a) and XZ- (figure 2.8b) plane were under taken. In all experiments the electrode was initially placed in the centre of the jet orifice. The electrode was then brought slowly down until it would touch the mouth of the jet (observed by eye). The coordinates of this position were assigned as (0,0,0) and all further measurements were taken with respect to this point. In XY scanning the Z displacement was set to 1 mm and in the XZ measurements; the Y position of the electrode was equal to 0 mm. The potential of the electrode was held at -0.2 V *vs.* Ag which corresponds to the mass transfer limited potential of the redox system employed. However, it should be noted that aerobic solutions were used in these experiments. Therefore a contribution from oxygen reduction should also be considered. The combination of software (VB6), to control the position of the electrode and to determine either conventional cyclic voltammetry or the appropriate HMV signals, was developed in-house.

2.1.6 Detection limit measurement

In order to determine the detection limit of the HMV oscillating jet system the experimental set-up presented in figure 2.1.1 was slightly modified. A micropump (TCS, Model M100-S) was added to the set-up to allow mixing of the solution inside the glass cell. A schematic of the pump used is presented in figure 2.9a. The inlet of

the pump was connected using flexible tubing to the side tube of the funnel (see figure 2.9b, IN). Another plastic tube was attached to the outlet of the micropump. Liquid transferred from the inlet of the pump to its outlet and returns back to the experimental cell (see figure 2.9b, OUT).

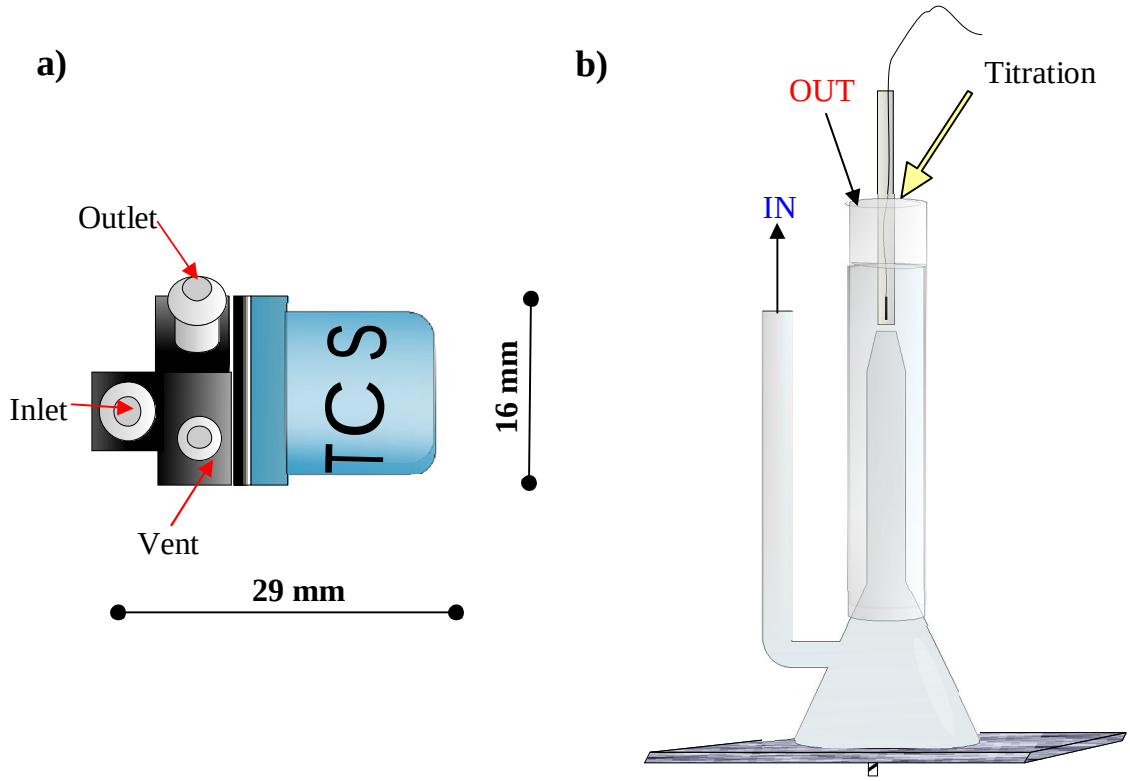

Figure 2.9. **a)** Schematic of the micropump used in the titration experiments. **b)** Experimental cell used in these measurements. Arrows (IN, OUT) show direction of flow to and from the pump. The thick arrow indicates the titration point.

The micropump was connected to a DC power supply (Maplins, Model N93CX). The input voltage used was between 3.0-4.0 V. This voltage range allowed flow rates between 250-350 ml min^{-1} to be achieved. A sample of the titrant was added to the electrolyte solution in the upper part of the experimental cell with an Acura adjustable volume micropipette (capacity 5-50 µl) followed by an appropriate mixing time to allow adequate equilibrium of the entire cell volume.

2.1.7 Oxygen electroreduction

The study of molecular oxygen reduction employed a variety of electrodes including high surface area nanostructured Pt electrodes described in section 2.1.4. Molecular oxygen reduction was carried out mainly in a solution of 1 mol dm^{-3} H_2SO_4. In the

experiment where oxygen saturated solutions were used, pure oxygen gas was sparged through the solution for ~10 minutes.

Oxygen electroreduction was also studied in aerobic 0.1 mol dm^{-3} and 1 mol dm^{-3} phosphate buffer solutions (pH 7) made from KH_2PO_4 and K_2HPO_4. The pH of solution was measured using the Hanna Microprocessor pH Meter (HI 9321). The viscosity of the buffer solutions was measured using a falling sphere viscometer (Gilmont). The experimental apparatus consisted of a cylindrical glass tube and a glass ball. The tube was filled with a solution and the ball was allowed to descend through the liquid. The time taken for the ball to pass two marks on the tube was measured. The viscosity of the fluid was then calculated using Stokes' law:

$$\mu = Kt(\rho_f - \rho) \tag{2.1}$$

where ρ_f represents the density of the ball (2.53 g ml^{-1} for the glass ball employed), the time (min) and K 0.3 (the dimensionless wall and inertial correction). The density of liquid ρ was 1.0201 and 1.1263 g ml^{-1} (calculated by measuring mass and volume of the liquids) for 0.1 and 1 mol dm^{-3} buffer solutions respectively. Each solution was tested five times and an averaged of these measurements used in further calculations. These measurements showed that the viscosity of 0.1 mol dm^{-3} phosphate buffer solution was 0.925 ± 0.019 cP and of 1 mol dm^{-3} was 1.663 ± 0.021 cP.

2.2 Rotating Ring Disk Electrode Measurements

2.2.1 Experimental set-up and equipment

The experimental apparatus used in the rotating ring disk electrode (RRDE) measurements is presented in figure 2.10. A commercial, Perkin-Elmer Ring-Disk Electrode system (Model 636), was used in this work. The rotation speed was controlled by a Perkin-Elmer control unit. The RRDE measurements were carried with an electrochemical bi-potentiostat (Oxford electrodes). An electrochemical cell was specially constructed for the RRDE investigations. A schematic representation of the cell is shown in figure 2.11. This cell allowed efficient removal of molecular oxygen from the solution. Note, the employment of conventional glass cells resulted in only ~75 % of the oxygen being removed despite relatively long degassing time. The electrochemical cell consisted of a main glass body diameter of 70 mm (slightly bigger

than the RRDE motor housing). The body was fitted with a glass t-piece. Exits B (with a glass frit) and A (figure 2.11) where directly connected to the upper and lower part of the cell respectively. The third, exit C, was attached to the Ar gas supply.

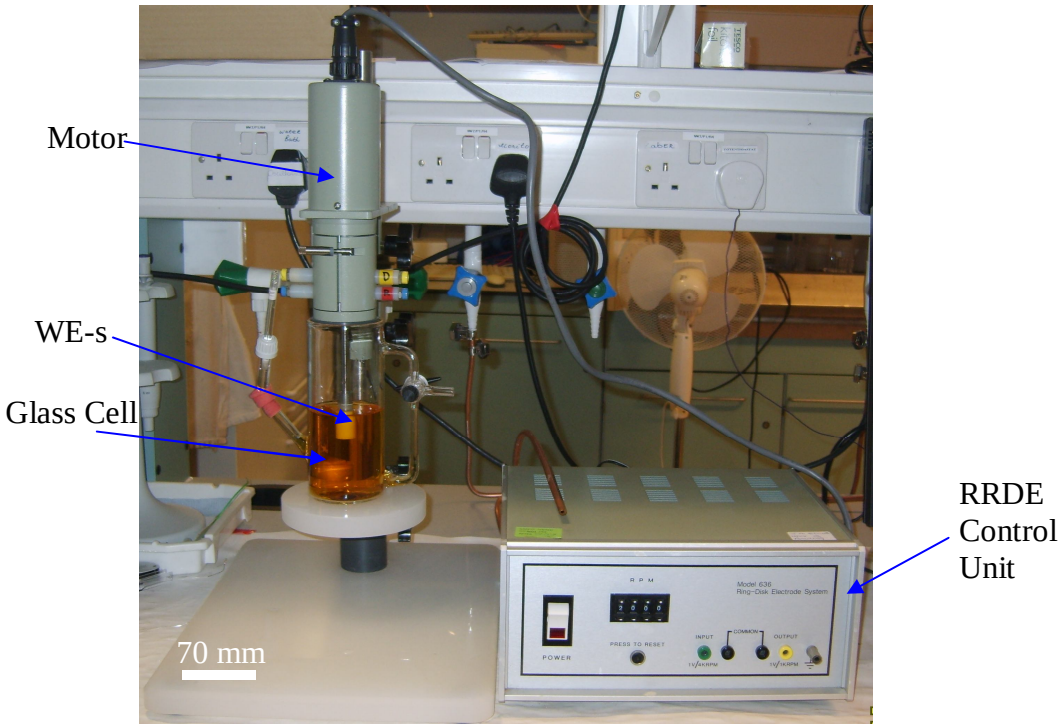

Figure 2.10. Experimental set-up used in the rotating ring disk (RRDE) experiments.

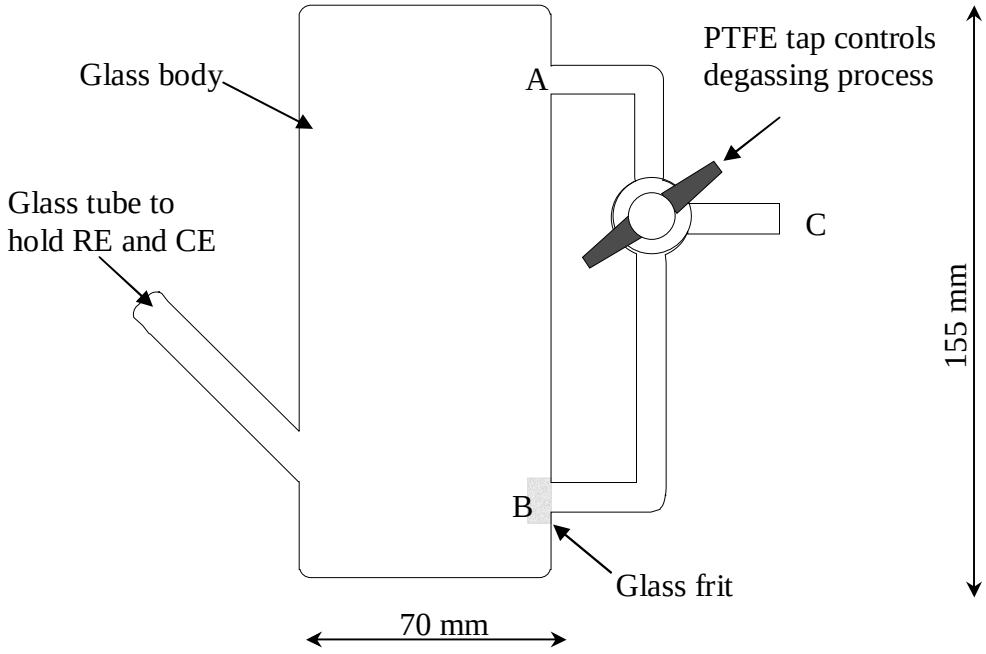

Figure 2.11. Experimental glass cell designed for the use in RRDE experiments.

The overall degassing process was controlled by a three-position PTFE tap. During the degassing the tap was positioned so that gas would flow simultaneously from exits A and B. During the electrochemical measurements the position of the tap was chosen so the only A tube will be open allowing gas flow on top of the solution. The electrochemical cell was also supplied with a side glass tube to hold the reference and counter electrodes. A gas tight seal was provided by a Suba-Seal through which the reference and counter electrodes were inserted. The electrochemical experiments were not conducted in a Faraday cage.

2.2.2 Electrodes

Rotating electrodes (MT 28 Series) were supplied by Pine Instruments, and included a Au disk-Pt ring electrode, and a Pt disk–Pt ring electrode. The dimensions of the electrodes (supplied by manufacturer) were 4.57 mm diameters for disks and 5.38 mm outer and 4.93 inner diameters of the rings. Templating mixture preparation, electrodeposition of the nanostructured platinum and further characterisation of the deposited films were performed as for conventional electrodes described in section 2.1.4. An example of current time transient for electrodeposition of H_I-*Pt* on the Au disk electrode is presented in figure 2.12. The deposition charge density for the disk was 1.82 C cm^{-2}. The deposition charge density for both ring electrodes was 1.61 C cm^{-2}. The charge densities and roughness factors of the RRDE electrodes are presented in Table 2.1.

Electrode		Charge density, C cm^{-2}	Roughness Factor
Au/Pt	Pt ring	1.61 C cm^{-2}	94.4
	Au disk	1.82 C cm^{-2}	53.7
Pt/Pt	Pt ring	1.61 C cm^{-2}	79.0
	Pt disk	-	1.0

Table 2.1. Charge densities and roughness factors for the RRDE-s.

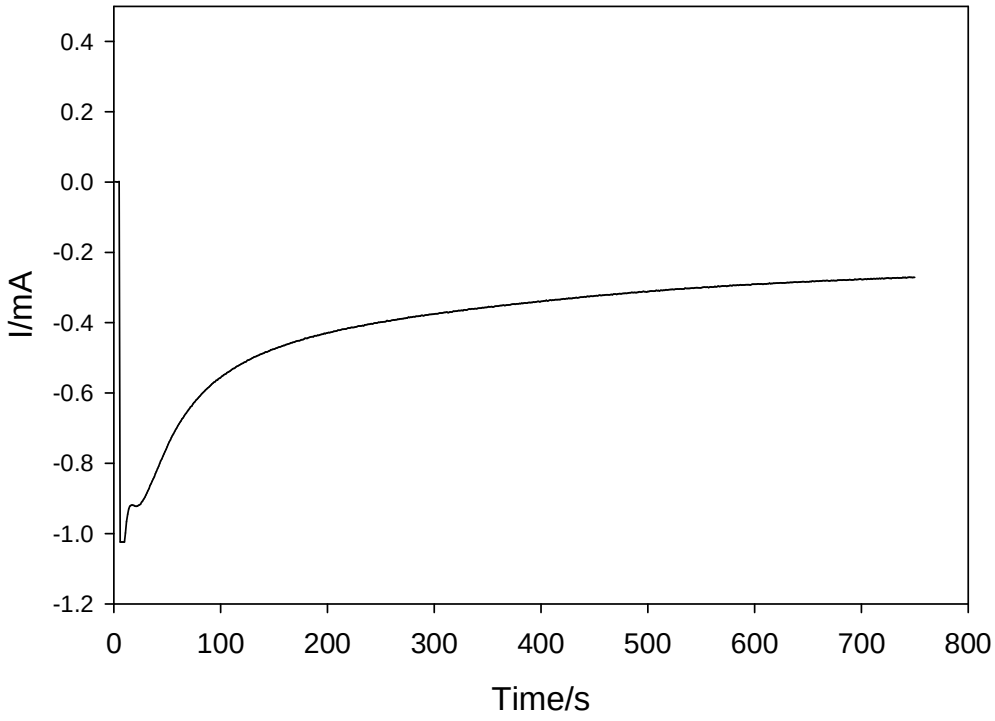

Figure 2.12. Current time transient for the electrodeposition of H_I-Pt on Au of 4.57 mm diameter carried disk electrode out at potential of -0.5 *vs.* MMS.

2.2.3 Collection efficiency determination

Collection efficiency, *N*, defined as the fraction of completely stable, solution soluble intermediate produced by the disk, I_{disc}, which is detected as a ring current, I_{ring} (*11*) is given by:

$$N = -\frac{I_{ring}}{I_{disc}} \tag{2.2}$$

The collection efficiency of the nanodisk-nanoring RRDE apparatus used in this thesis was determined using a 5 mmol dm^{-3} $[Fe(CN)_6]^{3-}$ redox couple (in 1 mol dm^{-3} $Sr(NO_3)_2$).

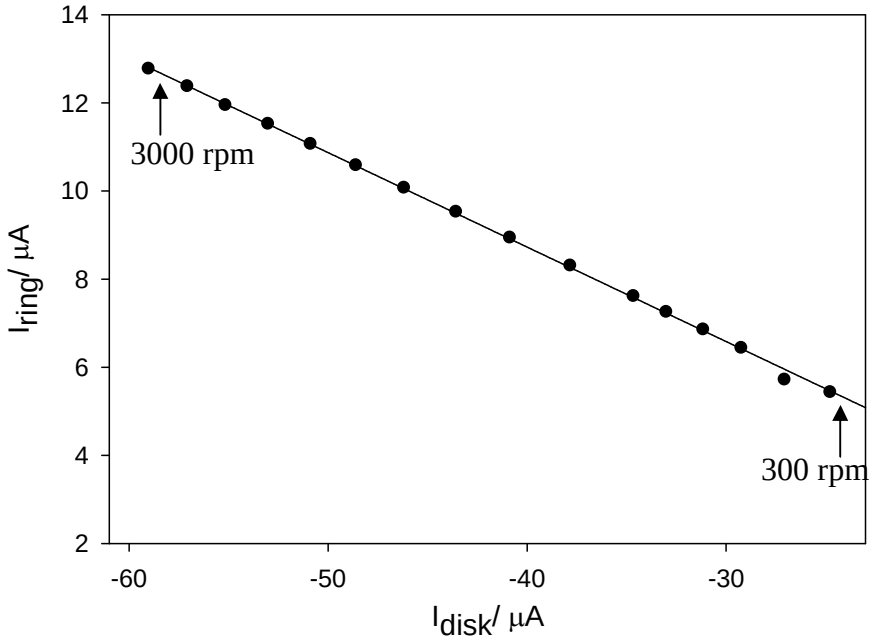

Figure 2.13. Plot showing current recorded at the ring electrode recorded as a function of current recorded at the disk electrode at different electrode rotation speeds (from 300 to 3000 rpm). Solution employed was 5 mmol dm^{-3} $[Fe(CN)_6]^{3-}$ in 0.1 mol dm^{-3} $Sr(NO_3)_2$. The potential of disk was -0.2 V *vs.* Ag and of ring was +0.5 V *vs.* Ag.

Here, the potential of the disk electrode was held at potential of -0.2 V *vs.* Ag where the $[Fe(CN)_6]^{3-}$ reduction is mass transport controlled. The potential of the ring was +0.5 V *vs.* Ag corresponding to the mass transport limited oxidation of $[Fe(CN)_6]^{4-}$. The limiting currents were then recorded as a function of rotation rate. Figure 2.13 shows the ring and disk currents as the speed of rotation was varied from 300 to 3000 rpm. Using a regression analysis of the plot the collection efficiency for the system was found to be 0.2143. This is in a good agreement with a theoretical value (Appendix C) of 0.2158 for the employed electrode with dimensions presented above.

2.2.4 High-speed camera imaging

A schematic of the experimental set-up used in the high-speed camera experiments is presented in figure 2.11. A Photron APX RS high-speed camera (8 GB onboard memory) with a Navitron lens (12x Zoom, with lens attachment (0.5x)) was used to capture the fluid motion within the HMV cell. The camera is capable of recording at up to 250,000 frames per second (fps) depending on the resolution. The maximum frame rate used in the experiments was 2000 fps. In order to acquire the images, the

apparatus was back lit by High bright white LED source (PHLOX-LEDW-BL-50 x 50-S-Q-1R-24V). Image analysis was achieved through the use of Photron Motion Tools Software.

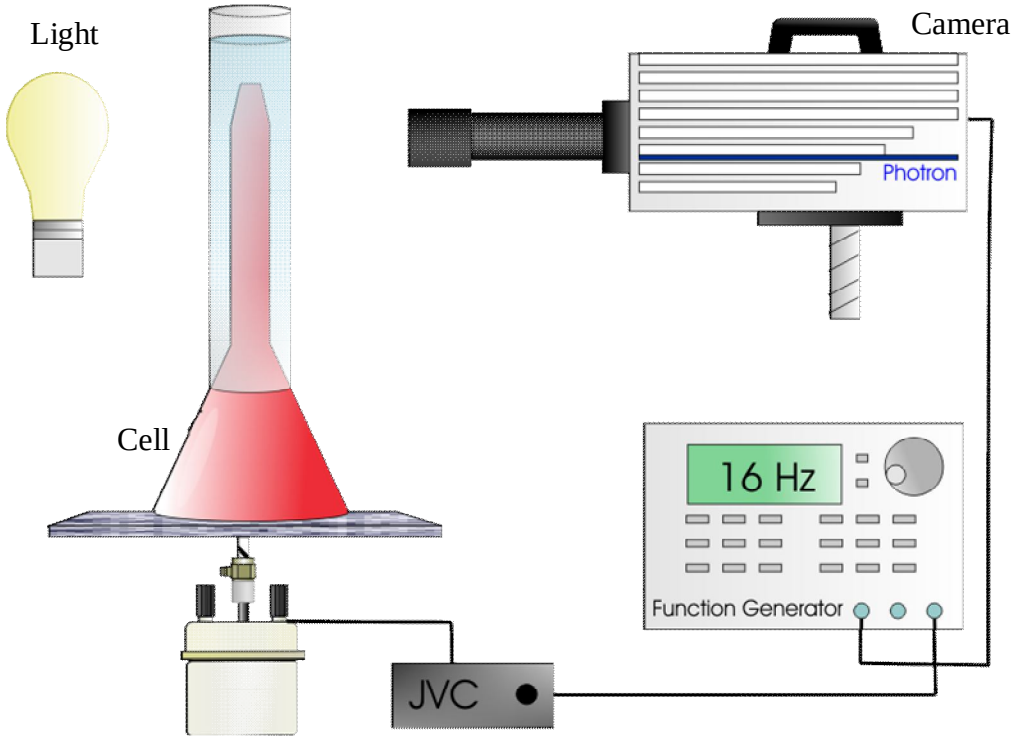

Figure 2.14. A schematic of experimental arrangement used in the high-speed camera investigations.

A function generator (TGA 12101, 100MHz, TTi) was added to the set-up (see figure 2.14) to trigger the camera and mini-shaker simultaneously in the experiments where it was required (*e.g.* dye experiments).

2.2.5 Method using dye

Red food dye was used to monitor fluid motion inside the jet apparatus. In order to monitor fluid motion inside the neck of the inverted funnel (see figure 2.1) the funnel was half filled with red coloured water. The top part of the cell was filled with heptane. In order to monitor the fluid motion at the exit of the jet, the cell was filled with water and dye was syringed into the mouth of the inverted funnel. The shaker and camera were simultaneously triggered. The ejected dye would colour the liquid as it was expelled from the jet orifice. Images of this process could then be acquired. The

coloured water was removed from upper portion of the cell with a help of a syringe. The cell was then topped with fresh water/dye as appropriate.

In both jets of dye experiments the images were captured at 500 fps with a resolution of 1024 ×1024.

2.2.6 Method using hydrogen bubbles

Hydrogen bubbles were produced at a Pt (50 µm diameter) stretched across the neck of the funnel 14 mm away from the exit of the jet. Figure 2.15 shows the schematic of the position of the wire inside the funnel.

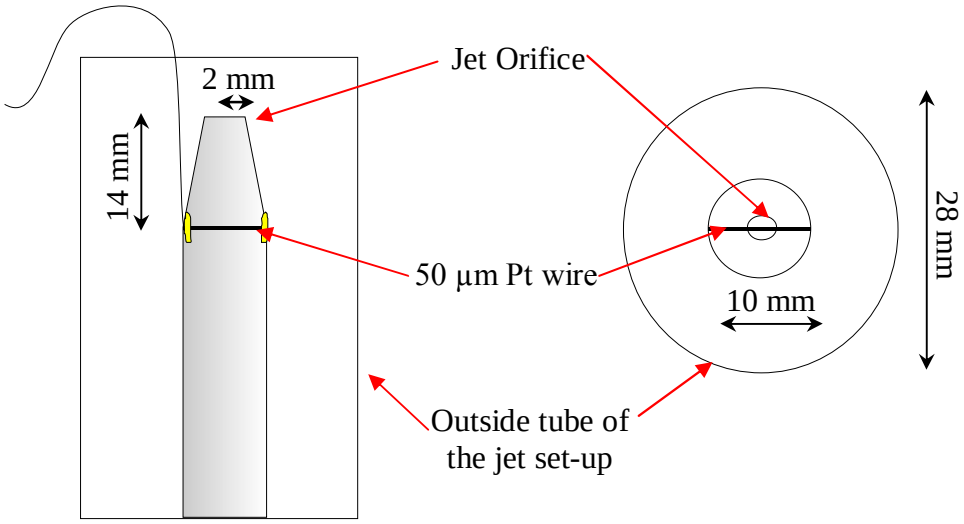

Figure 2.15. Schematic showing position of the Pt wire with respect to the jet exit.

The hydrogen bubbles were produced by the applying negative potential using a DC power supply (Maplins, Model N93CX) to the Pt wire electrode. The images were taken at 2000 fps.

2.3 Electrochemical Measurements Using the Vibrating Wire

2.3.1 Experimental set-up and equipment

The vibration apparatus, illustrated in Figure 2.16, consisted of a mini-shaker Model V101 (Lyng Dynamic Systems LTD) connected to an appropriate electrode housing. An accelerometer Model 3100B (Dytran Instruments, Inc.) with sensitivity of 99.3 mV g^{-1} was included into the construction to monitor electrode vibrations. The sensor was

driven by a battery-powered current source model 4105C (Dytran Instruments, Inc.) with voltage gains of ×1, ×10 or ×100. To record the response of the accelerometer the output of this unit was connected directly to an oscilloscope (a Tektronix TDS2014 (1GS/s, 100 MHz)).

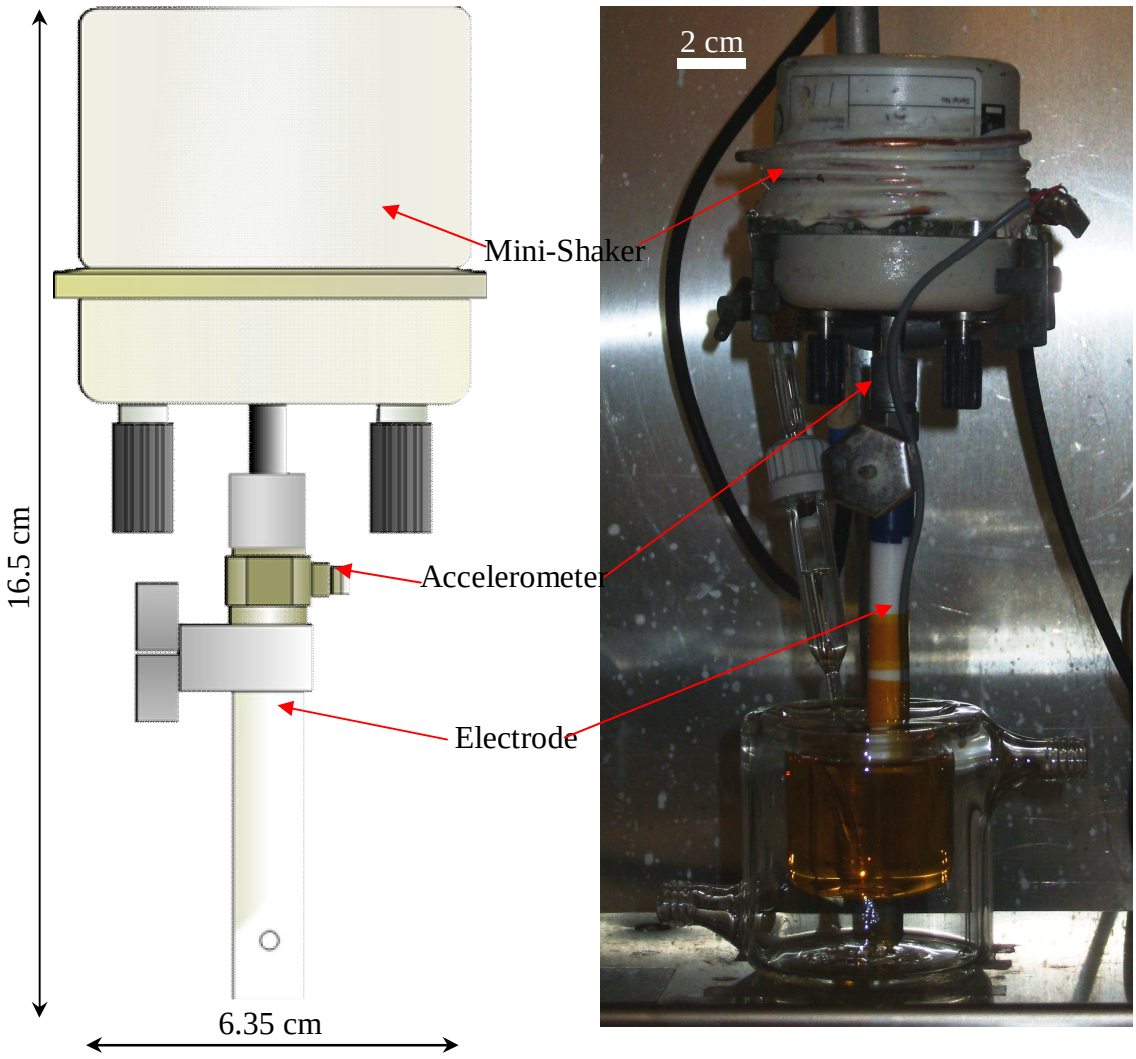

Figure 2.16. Schematic **(a)** and picture **(b)** of an experimental arrangement used in a vibrating "tight-rope" electrode.

The mini-shaker was driven with a stereo integrated amplifier Model AX-220 (JVC) which was used to vary the amplitude of vibration of the electrode. The amplifier in turn was driven by a function generator (TGA 12101, 100MHz, TTi). The vibration frequency was varied from 10 to 150 Hz. The electrochemical workstation used in the experiments was the same as that described in section 2.1.2. In experiments where the removal of oxygen was necessary the cell presented in figure 2.11 was employed.

2.3.2 Electrodes

Figure 2.17 shows a "tight-rope" electrode designed for use in the vibrating wire investigations. A Teflon rod (1 cm diameter; 6 cm or 8 cm in height for Pt and Au electrodes respectively) were employed as an electrode body. A channel (4 cm height; 4 mm diameter) was drilled down the centre of the rod. A hole ("exit") was drilled through the channel 4 cm above its entry. A Pt or Au of wire (both 50 µm diameter) was attached to an insulated wire (coaxial cable to reduce background electrical noise). The insulated wire was the fixed to the Teflon rod with polyamide tape. The Pt or Au microwire was then stretched across the channel and glued to the Teflon rod with fast setting epoxy resin. Enough resin was employed to cover the ~2 cm of insulated wire. The electrode assembly was then left to set at room temperature for ~30 minutes.

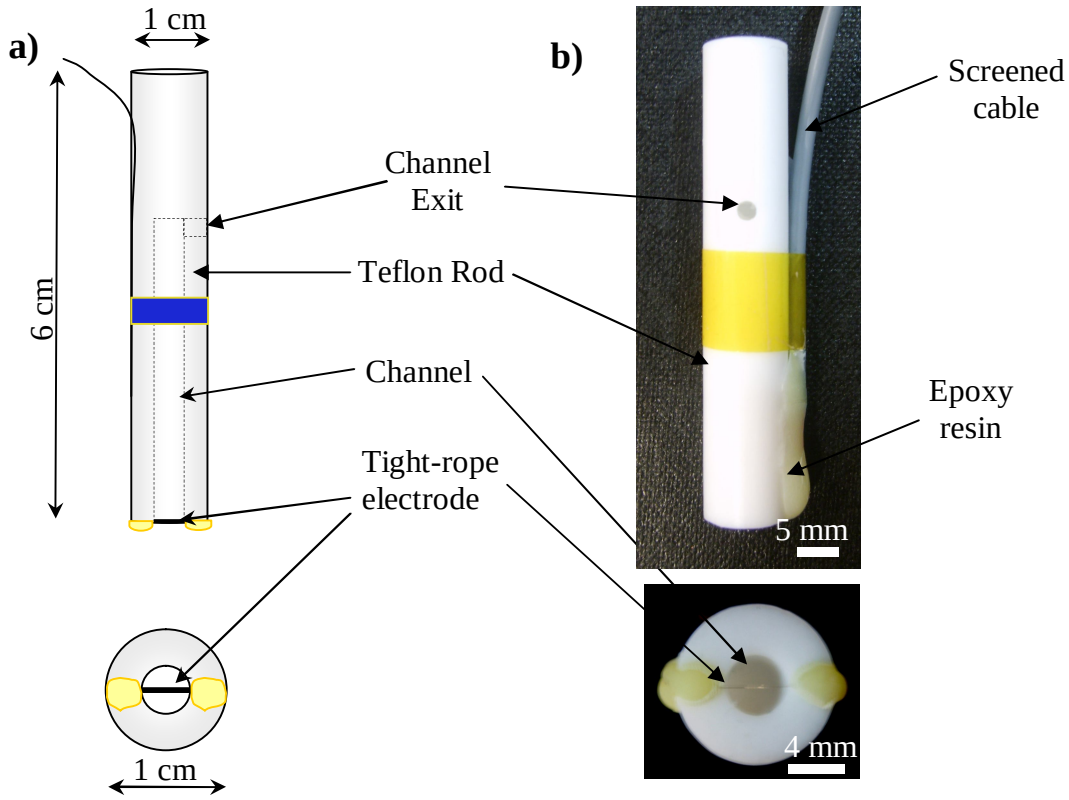

Figure 2.17. **a)** Schematic of the Pt "tight-rope" electrode. **b)** Pictures of the resultant electrode and housing.

The electrodes were electrochemically cleaned by cycling in 1 mol dm^{-3} sulphuric acid between potentials +0.7 and -0.65 V *vs.* MMS at sweep rate of up to 500 mV s^{-1}. It was

previously reported (*190*) that an edge effect could affect the signal recorded from a vibrating wire electrode. Therefore the electrodes with and without insulated edges were constructed and tested. However, no significant difference between the performances of the two electrode constructions could be observed.

Figure 2.18 shows voltammetry of both the Au and Pt tight rope electrodes in 5 mmol dm^{-3} $Fe(CN)_6^{3-}$ solution. This shows that the active areas of the two electrodes do differ as expected considering the method of construction.

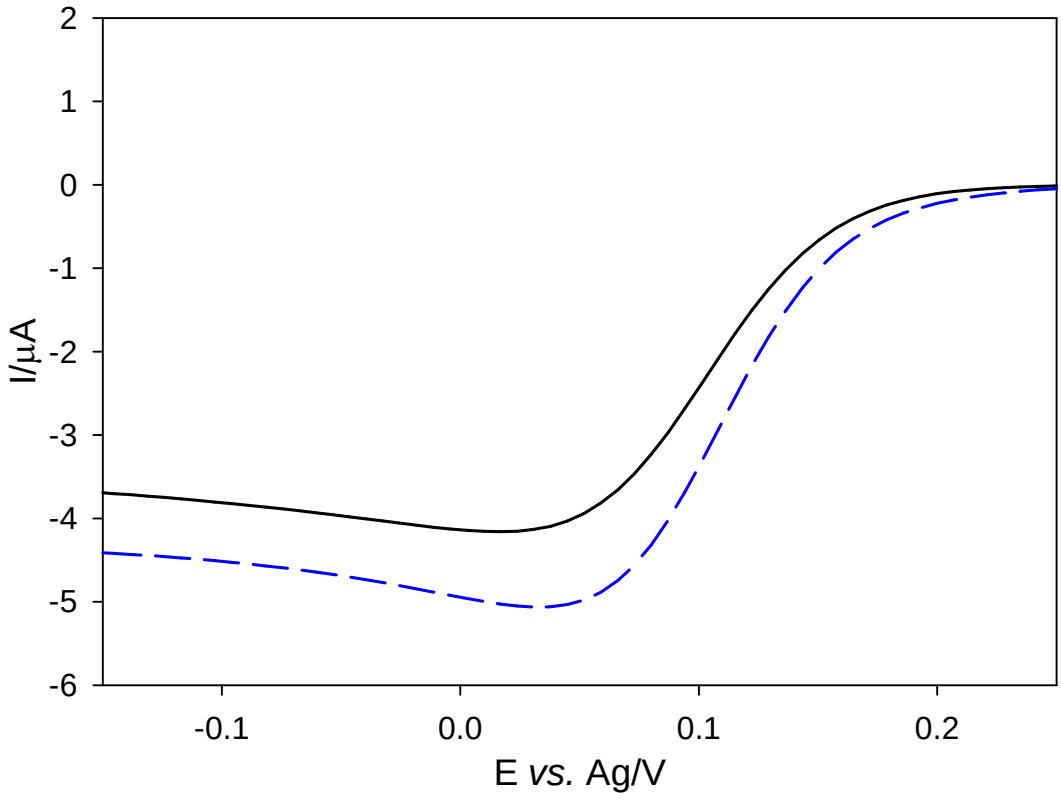

Figure 2.18. Plots showing voltammetry of Au (—) and Pt (– – –) "tight-rope" 50 μm diameter electrodes in 5 mmol dm^{-3} $[Fe(CN)_6]^{3-}$ in 0.1 M $Sr(NO_3)_2$ at sweep rate of 20 mV s^{-1}.

2.4 Solutions

All solutions were prepared using water from a Purite Select Fusion 160 (Ondeo) water purification system (resistivity 18.2 MΩ cm). The concentrations of the species employed in various experiments are given in the appropriate figure legend. A list of chemicals employed, suppliers and purity (no further purification was carried out) is shown in Table 2.2. The electrodes were prepared using wires supplied by Advent.

The purity was as follows: Au (50 µm diameter) 99.996 %, Pt (50 µm diameter) 99.99 %, Ag (0.5 mm diameter) 99.99 %.

Chemical	Supplier	Purity/Grade
H_2SO_4	Fisher-Scientific	Laboratory reagent grade, 98%
H_3PO_4	Fisher-Scientific	Laboratory reagent grade
$HClO_4$	Fisher-Scientific	Laboratory reagent grade, 60%
KCl	Fisher-Scientific	Analytical reagent grade
$Sr(NO_3)_2$	Sigma-Aldrich	A.C.S. reagent, 99+%
$C_{16}EO_8$	Sigma	
H_2PtCl_6	Aldrich Chemical Co.	99.9+%
H_2O_2	Fisher-Scientific	Laboratory reagent grade
Heptane	Aldrich Chemical Co.	99%
Na_2HPO_4	Timstar laboratory suppliers	Laboratory reagent grade
$NaH_2PO_4{\cdot}2H_2O$	Fisher-Scientific	99+%
$K_4Fe(CN)_6$	Fisher-Scientific	Laboratory reagent grade
$K_3Fe(CN)_6$	Sigma-Aldrich	A.C.S. reagent, 99+%
Red food dye	Super Cook	N/A
$NaIrCl_6{\cdot}6H_2O$	Aldrich Chemical Co.	99.9%
O_2	BOC	Pure
Ar	BOC	Pure
Fast setting epoxy resin	Araldite	N/A

Table 2.2. List of chemicals employed, purity and suppliers.

Chapter 3

Oscillating Jet System as a New HMV Technique

Hydrodynamic modulation voltammetry (HMV) is a powerful analytical tool for detecting electrochemically active solution species. This technique relies on periodically altering the mass transfer regime. The method is based on using the lock-in approach to target the mass transfer dependent signal. Other processes, such as charging of the double layer and surface processes are hence eliminated from the system. In this way the voltammetric response of a system is refined to focus only on the mass transfer dependant components.

Chapter 3 introduces a novel hydrodynamic modulation voltammetry (HMV) technique-an oscillating hydrodynamic jet.

3.1 Oscillating Jet in Work

The experimental system deployed is illustrated in figure 2.1. This shows a "minishaker" connected to a membrane via a mechanical coupling incorporating an accelerometer. The inclusion of an accelerometer into the design enabled calibration and monitoring of the motion of the membrane during the experiments. In order to calculate the displacement of the centre of the membrane (coupled to the mechanical shaker), the motion was assumed (see later data) to be largely sinusoidal in nature. Hence it was possible to calculate the zero to peak amplitude of the membrane centre from the accelerometer output. In order to do this, the zero to peak acceleration amplitude derived from the accelerometer output (A, m s^{-2}) was converted to the displacement amplitude of the membrane centre (X, m) by the employment of equation (3.1):

$$X = A/(2\pi f)^2 \tag{3.1}$$

where f represents the frequency (Hz) of oscillation of the shaker employed in the experiment. The motion of the membrane was assumed to be ideal (so that at maximum extension a conical section was developed), allowing the fluid velocity in the neck, or at the jet orifice itself, to be calculated. Using this assumption the volume displaced (V) by the shaker motion (in this case over a complete oscillation of the membrane) is given by equation (3.2),

$$V = \tfrac{2}{3}\pi r_m^{\,2} X \qquad (3.2).$$

where r_m represented the membrane radius (in this case 35 mm). This volume displacement can be related to the velocity amplitude at the jet exit through the equivalent volume at this point. Hence the jet zero to peak amplitude velocity (v_{jet}) is given by equation (3.3),

$$v_{jet} = \omega\left[\frac{\tfrac{1}{3} r_m^2 X}{r_j^{\,2}}\right] \qquad (3.3).$$

where r_j represents the jet radius (in this case 1 mm) and ω the angular frequency ($\omega = 2\pi f$, where f represents the frequency in Hz of the membrane vibration) of membrane vibration. Considering the membrane displacement amplitudes typically employed (measured by the accelerometer at ~ 0.3 mm) and the frequency and dimensions of the system employed, the jet amplitude velocity was of the order of 12.3 m s^{-1}. Note that ideal behaviour of the membrane was assumed in these calculations. See Chapter 4 for more details on the membrane motion where a high-speed camera was employed to test the above assumption.

In order to analyse the motion of the fluid at the exit of the jet, a series of experiments were performed using an electrode to measure the mass transfer limited current for the reduction of $Fe(CN)_6^{3-}$. In order to maintain mass transfer limited conditions the potential of the electrode was held at -0.2 V vs. Ag during this experiment.

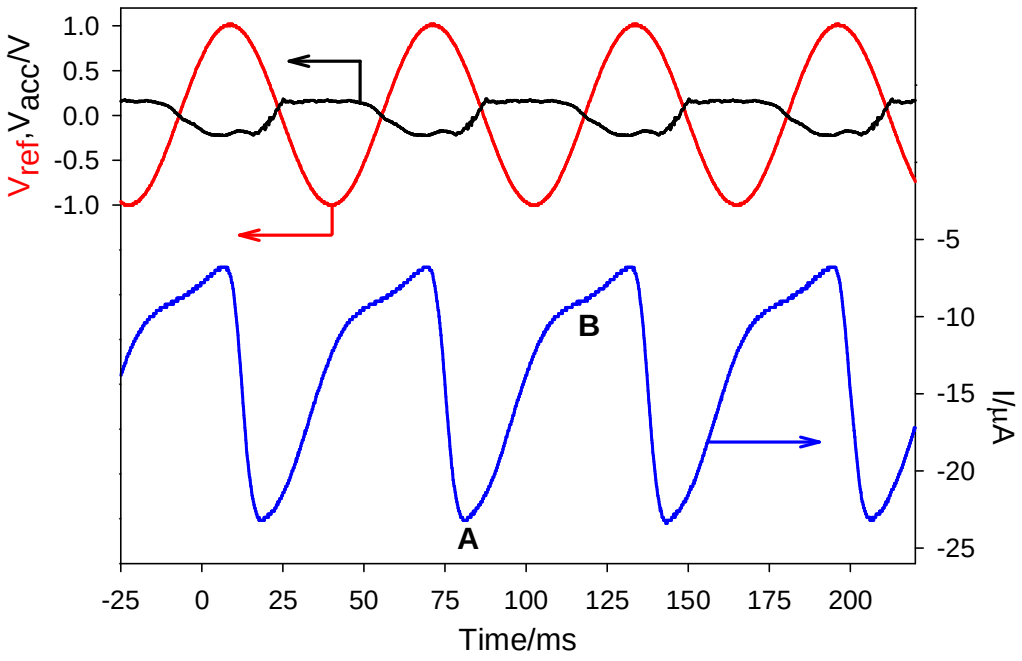

Figure 3.2. Plot showing the current time history (—) of a 500 μm diameter Pt electrode positioned at a distance of 1 mm (X = 1 mm) from the jet centre (Z = 1 mm). The solution contained 5 mmol dm^{-3} $[Fe(CN)_6]^{3-}$ in 0.1 mol dm^{-3} $Sr(NO_3)_2$ electrolyte. The electrode was held at -0.2 V vs. Ag. Included on the figure is the reference signal (V_{ref} —) and corresponding accelerometer signal (V_{acc} —).

Figure 3.2 shows the current time history for a 500 μm diameter Pt electrode positioned above the jet outlet under conditions of oscillation. Included on the figure is the signal from the function generator which is used as a reference signal for lock in measurements (see later discussion) and the output from the accelerometer. First, note that the pulsating motion of the liquid at the funnel mouth was detected as a transient enhancement (in this case mass transport coefficient 2.5 x 10^{-2} cm s^{-1}) in current which was largely asymmetric in nature but occurs at the same frequency as the pulsation driven by the shaker (here 16 Hz). Clearly, as the fluid flows out and into the jet mouth, one would expect current enhancement as a result of fluid flow in the two directions. Indeed the current time transients shown in figure 3.2 have a large cathodic transient (labelled 'A') followed by a smaller ridge in the decay of this transient (see label 'B') Hence, for this relatively large electrode it appears that the current was dominated by one of the flow directions. As a result of this, the pulsation frequency of the current recorded at the electrode was the same as the membrane driver. Interestingly, when an identical experiment was performed with a 25 μm diameter Pt microelectrode, evidence for both flows providing enhanced current time transients was gathered (see figure 3.3).

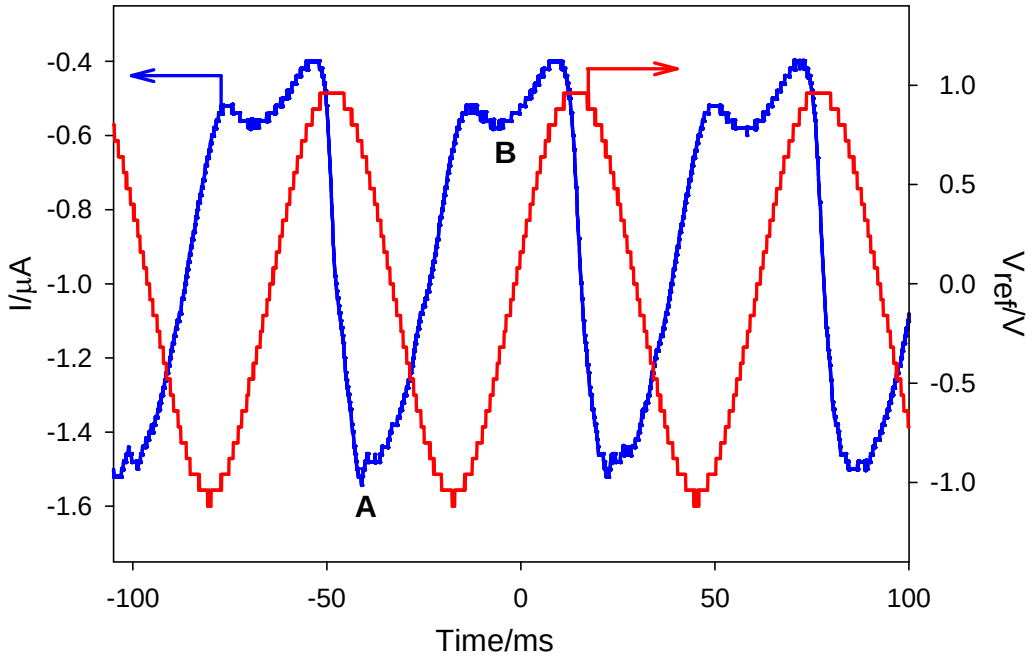

Figure 3.3. Plot showing the current time history (—) 25 μm diameter Pt electrode positioned at a distance of 1 mm (X = 1 mm) from the jet centre (Z = 1 mm). The solution contained 5 mmol dm^{-3} $[Fe(CN)_6]^{3-}$ in 0.1 mol dm^{-3} $Sr(NO_3)_2$ electrolyte. The electrode was held at -0.2 V vs. Ag. Included on the figure is the reference signal (V_{ref} —).

However, one of the flows was still found to play a more significant role. Second, a significant phase difference between the reference signal (here a 1 V amplitude supplied to the amplifier prior to the minishaker) and the peak of the current time data was found. Lastly, figure 3.2 shows that the accelerometer data, although largely sinusoidal in nature, contains non-idealized motion. It should be noted that this non-ideality was found to be highly dependent on the mechanical integrity of the coupling between the minishaker and the membrane and framework used to construct the cell. However, despite the non-ideality of the set-up the periodical character of the signal obtained allows for HMV analysis to be employed on the system. In particular HMV analysis for the electrochemical reduction of $Fe(CN)_6^{3-}$ was performed and the results of these investigations are presented in the next section.

3.2 HMV Analysis for Oscillating Jet Using the Lock-in Approach

In order to characterize the electrochemical HMV signal obtained from the pulsating jet apparatus described above, bespoke software was developed to capture the data and

extract the amplitude of the HMV signal as a function of the electrode potential, time or 3D position of the electrode with respect to the jet mouth. This software relied on an ADC card (sampling in this case at 10 kHz over a 0.5 s time window) and then signal processing of the data (correcting for phase shifts etc.) to extract the relevant data (*191*). This approach is similar to the deployment of a conventional lock in amplifier but with the advantage of introducing dynamic phase correction, DC background current subtraction and integration of the HMV analysis with the electrochemical experiments employed. Figure 3.4 shows a schematic representation of the procedure adopted to capture and analyse the data.

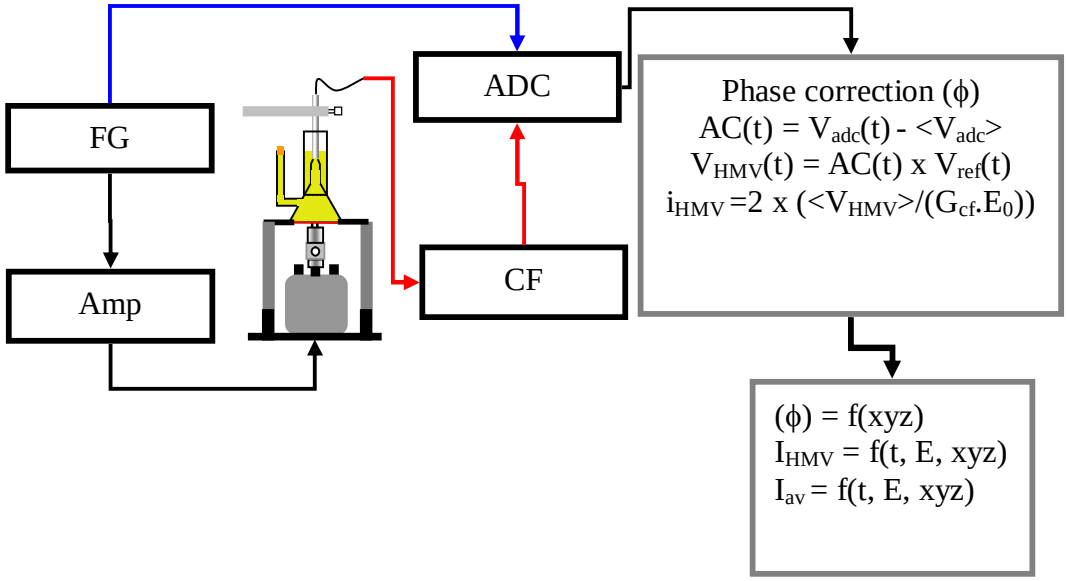

Figure 3.4. Schematic showing the progress of data acquisition and treatment. Here FG represents the function generator, AMP the amplifier supplying the mini shaker, CF the current follower and ADC the interface card. The grey boxes represent the software driven section of the approach while the black boxes the hardware employed. Note V_{adc} represents the data collected by the ADC card as a function of time, $<V_{adc}>$ represents the time averaged ADC data, $V_c(t)$ represents the signal corrected for DC offset as a function of time, $V_{cf}(t)$ represents the result of multiplication of the dc corrected signal by the reference signal (corrected for phase shift) as a function of time, $<V_{cf}>$ represents the time averaged signal, G_{cf} represents the gain of the current follower and E_0 represents the amplitude of the reference signal (here always 1 V).

This 'virtual lock in' procedure (run in VB on a PC with an ADC card) relied on two basic procedures. In the first procedure the electrode was held at the mass transfer limited potential for the redox species in question and a set of data was captured over a 0.5 s period. In order to avoid DC offsets, the data set was averaged to attain the time averaged signal ($<V_{adc}>$ or I_{av}) which was then subtracted from the raw data to leave an AC component. At this stage the phase angle was determined by varying the temporal

position of the reference signal (gathered at the same time as the experimental data) until a maximum or minimum in the data analysis was determined. This phase shift, which was found to be constant as long as the electrode was maintained in one position in the cell, was then used to determine the HMV signal as a function of electrode potential. In the second procedure (where the electrode position was varied while the electrode potential was held at the mass transfer limited potential for the redox system employed) a different analysis routine was deployed. Here, the data was gathered and the time averaged current calculated and subtracted from the raw experimental data. The phase angle to give the maximum HMV signal was then determined. Hence three experimental parameters were determined as a function of the electrode position. These were the time averaged current, the phase angle to give the maximum HMV amplitude (in the case of the $[Fe(CN)_6]^{3-}$ redox species, the most negative) and the HMV amplitude itself. The electrode could then be moved to a different position and the process repeated. An example of how the HMV signal can be determined as a function of electrode potential is shown in figure 3.5. This shows the cyclic HMV signal recorded for a 5 mmol dm^{-3} solution of $[Fe(CN)_6]^{3-}$ solution recorded at a 500 μm diameter Pt electrode. Clearly the HMV signal correlates closely[1] with the amplitude of the current oscillation (see figure 3.2) as expected. However, at this concentration level the DC (time averaged) signal directly from the electrode shows a clear response to the flow of liquid as a result of the pulsating jet. Figure 3.5 also shows that the response of the electrode is markedly different in the absence of jet action. The time averaged signal (I_{av}) shows a clear classic cyclic voltammetric response of a macroelectrode while the lock in signal (I_{HMV}) shows no activity over the entire voltage range investigated. This demonstrates the ability of the lock in approach to discriminate between the desired signal and other components not at the reference frequency. Clearly this shows the potential advantage of using this type of analysis under the conditions employed and highlights the use of HMV in the study of mass transfer dependant reactions at conventional electrodes.

[1] Note the value of the HMV signal will not match exactly the amplitude of the current transient induced by the jet as this analysis is based on matching sinusoidal signals. Here the transient is clearly not sinusoidal. However, the amplitude is ~ 80-90 % (see figure 5 for cyclic HMV data) of that expected considering a pure sinusoidal response of the electrode as 100 %.

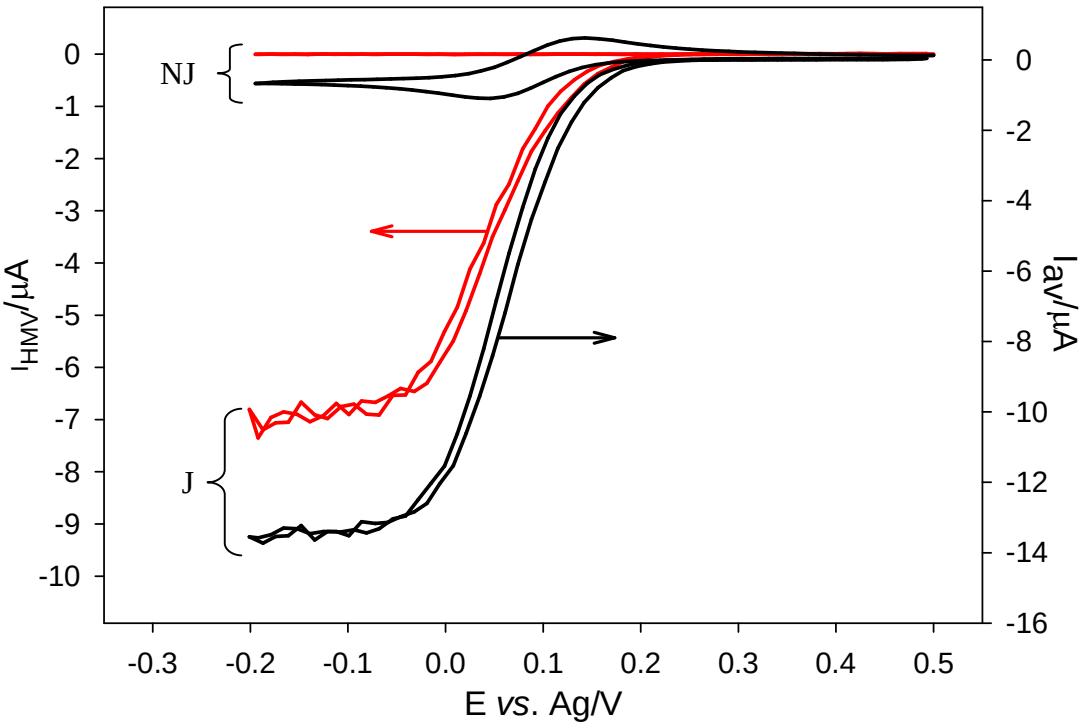

Figure 3.5. Plot showing the HMV signal (I_{HMV}, —) and average current signal (I_{av}, —) as a function of electrode potential recorded at a 500 µm diameter Pt electrode positioned at a distance of 1 mm (X = 1 mm) from the jet centre (Z = 1 mm). The solution contained 5 mmol dm^{-3} $[Fe(CN)_6]^{3-}$ in 0.1 mol dm^{-3} $Sr(NO_3)_2$ electrolyte. The sweep was performed at 20 mV s^{-1}. Included in the figure is the data with the jet running (labelled J) and without the jet running (labelled NJ).

In the previous discussions the position of the electrode was kept constant. However, the effect of electrode position with respect to the jet exit was also investigated and the details of this analysis are now presented.

3.3 Study of the Fluid Motion at the Jet Exit in Current Mapping Experiments

As well as the conventional detection of mass transfer dependant redox active species within a solution, it is possible to use the HMV approach, described here, to study the fluid motion through the jet mouth itself (as a function of the position of the electrode with respect to the jet orifice). Here a number of different experiments were performed with a range of electrode sizes (with variable active geometric electrode areas and support dimensions). Two active electrode areas were deployed: a set of 25 µm diameter Pt electrodes and a 0.5 mm diameter Pt electrode. For these experiments two programs (the software driven lock-in and a XYZ – stage controller) were combined.

This combination enabled the position of the electrode to be controlled while simultaneously recording the experimental HMV signal. However, it should be noted that as the electrode moved with respect to the jet, the phase angle between the reference signal and the electrochemical signal was observed to change. Finally it was also possible to calculate the time averaged DC signal (I_{av}) at each electrode position. Figure 3.6 shows a set of results for a 25 μm diameter Pt electrode as the electrode was scanned over the region above the jet in a raster like fashion. Note that the HMV signal (I_{HMV}) and the phase angle used to obtain this value were recorded as a function of position of the electrode employed in the XY plane above the jet orifice (at a constant z displacement of 1 mm). Figure 3.6a shows that moving the electrode away from the centre of the jet altered the phase angle between the reference and experimental signals. Indeed the phase angle is closely associated to the size of the jet itself and showed a phase angle close to zero within this zone. The diameter of this zone was ~ 3 mm. This matches the sum of the diameter of the jet (2 mm) and the radius of the electrode support (1 mm). It seems that when the electrode centre moved out of this zone, a major shift in the phase angle was detected. The electrode surround clearly influences the detected phase (and as will be shown subsequently, the spatial resolution of the HMV signal). This suggests that the liquid from the jet is 'deflected' across the surface of the electrode support. Hence, even if the electrode (here a 25 μm diameter Pt disk) is outside of the jet, deflection of fluid along the surface of the glass body results in a detectable signal. Figure 3.6b supports this conclusion as it shows that the amplitude of the HMV signal is greatest around the mouth of the jet (in this case 2 mm in diameter) but the signal can be seen to extend to greater distances before returning to the background level. Clearly figure 3.6 a and b show that outside of the jet, both the phase angle and the HMV signal change dramatically. Far from the jet the HMV signal falls to ~-2 nA from a peak value of approximately -23 nA. It is also apparent that the microelectrode shows an increased response around the edge of the mouth of the jet. In these positions a ring of maximum HMV signal, which surrounds a central circular area where the experimental signal is slightly lower, was observed. A similar effect has been previously reported by Macpherson *et al.* when investigating the signal from a wall tube electrode arrangement (*69, 192*). They suggested that as an electrode is moved from the centre of the jet, convective flow in the stagnation region has contributions from both axial and radial velocity components.

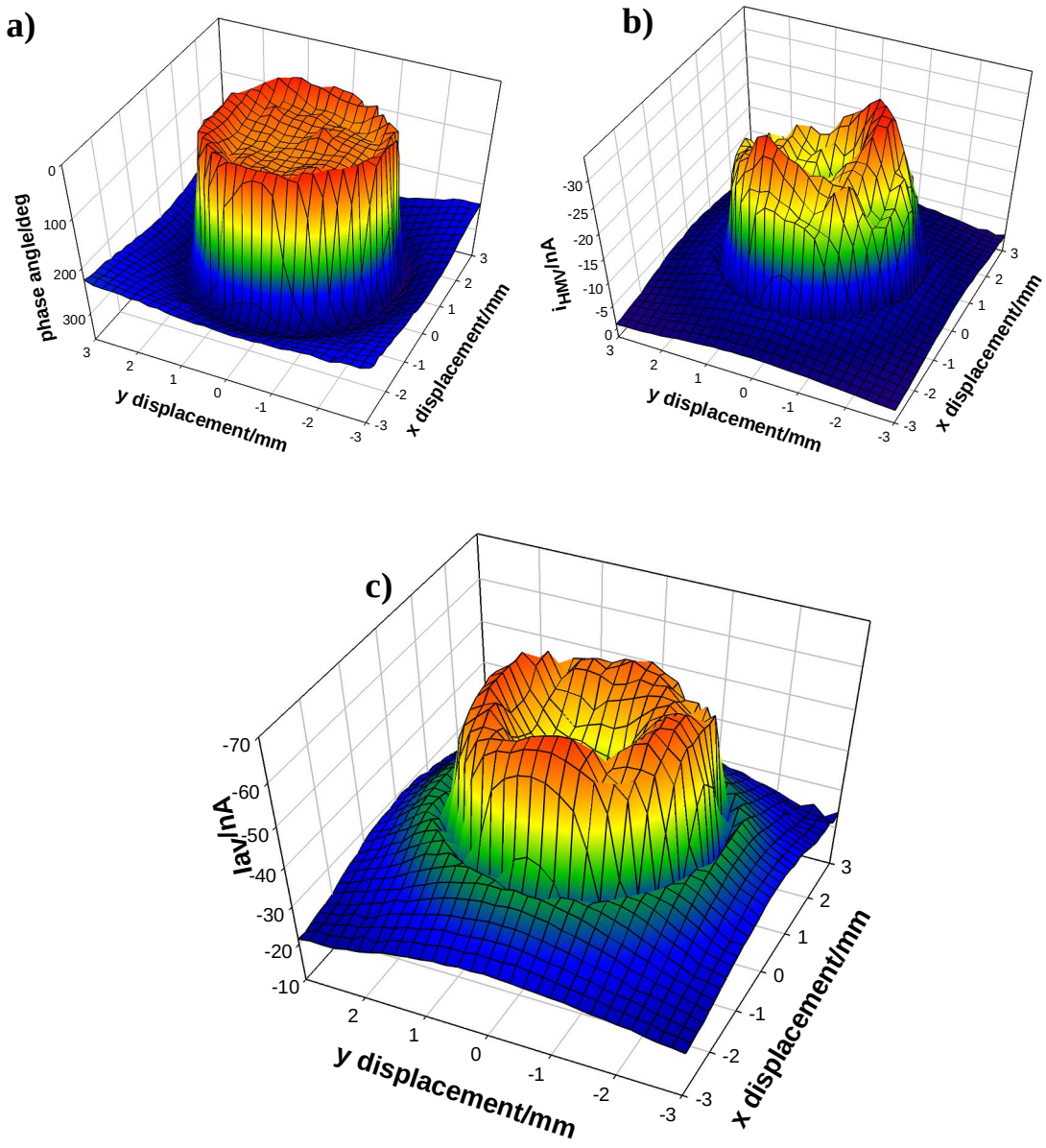

Figure 3.6 **a)** Plot showing the phase correction employed through the automated data collection software as a function of position. **b)** Plot showing the mass transport-limited HMV signal (I_{HMV}) at a 25 μm diameter Pt electrode with an insulating glass sheath (diameter = 2 mm) in a 0.1 mol dm^{-3} $Sr(NO_3)_2$ electrolyte containing 5 mmol dm^{-3} $[Fe(CN)_6]^{3-}$ recorded as a function of electrode position in the XY plane at a distance Z = 1 mm from the funnel mouth. **c)** Plot showing the time averaged dc current (I_{av}) as a function of electrode position. The electrode was held at -0.2 V vs. Ag at all times. Note each plot is a composite of 960 points (200 μm resolution) and is an average of 5 (2.5 s of data) measurements.

However, it should be noted that the experimental system employed here and that of Macpherson *et al.*, although both hydrodynamic in nature, are very different. Here we

employ a pulsating flow where the periodicity and flow direction is governed by the vibration of a diaphragm. However, Macpherson *et al.* employed a modulated flow from a fine capillary positioned over a microelectrode. Hence, direct comparisons are not appropriate. However, the increased HMV signal observed around the mouth of the jet wall, in the experiments reported here, would also suggest that this region is of significance for this pulsating system. One further note should be highlighted; in this pulsating system (and the associated HMV approach) the phase angle detected does not seem to detect this 'dimple' zone in the centre of the jet. This indicates that it is the amplitude of the signal that varies in this region alone rather than a combination of effects. Lastly the time averaged signal is presented in figure 3.6c. Again a clear enhancement in the current detected at the microelectrode is seen. However, the definition around the jet using this averaged signal is less than that observed using the HMV lock in mode. Hence the current does not drop directly to the background level when the electrode moves out of the flow driven directly by the pulsating jet. This is understandable as general forced convection will contribute to the time averaged (I_{av}) signal detected by the microelectrode.

In order to show the influence of the electrode support on the HMV signal detected at a microelectrode, an electrode with a larger support was employed. In this case a 25 μm diameter Pt microelectrode with an insulating sheath radius of 5.5 mm (significantly larger than the size of funnel mouth) was used. Figure 3.7a shows the phase angle measurement determined in this experiment where the electrode was scanned over the mouth of the pulsating jet at a constant height of 1 mm in the XY plane. Again the centre of the jet appears as a phase angle (to generate the highest amplitude of the HMV signal) close to zero degrees. However, at greater distances a 'halo' effect was observed. Again it appears that the radius of the electrode support (here 2.75 mm) in combination with the jet radius (1 mm) contributes to the ring of phase activity (radius 3.75 mm) seen in the image. It would appear that this effect is the result of the flow profiles generated by the pulsating flow and its interaction with the body of the electrode (see Chapter 4). Figure 3.7b shows the HMV amplitude as a function of the XY position of the electrode with respect to the jet orifice (here located at Y ~ 2 mm, X ~ 0 mm). Again a ring like HMV signal was observed around the funnel mouth.

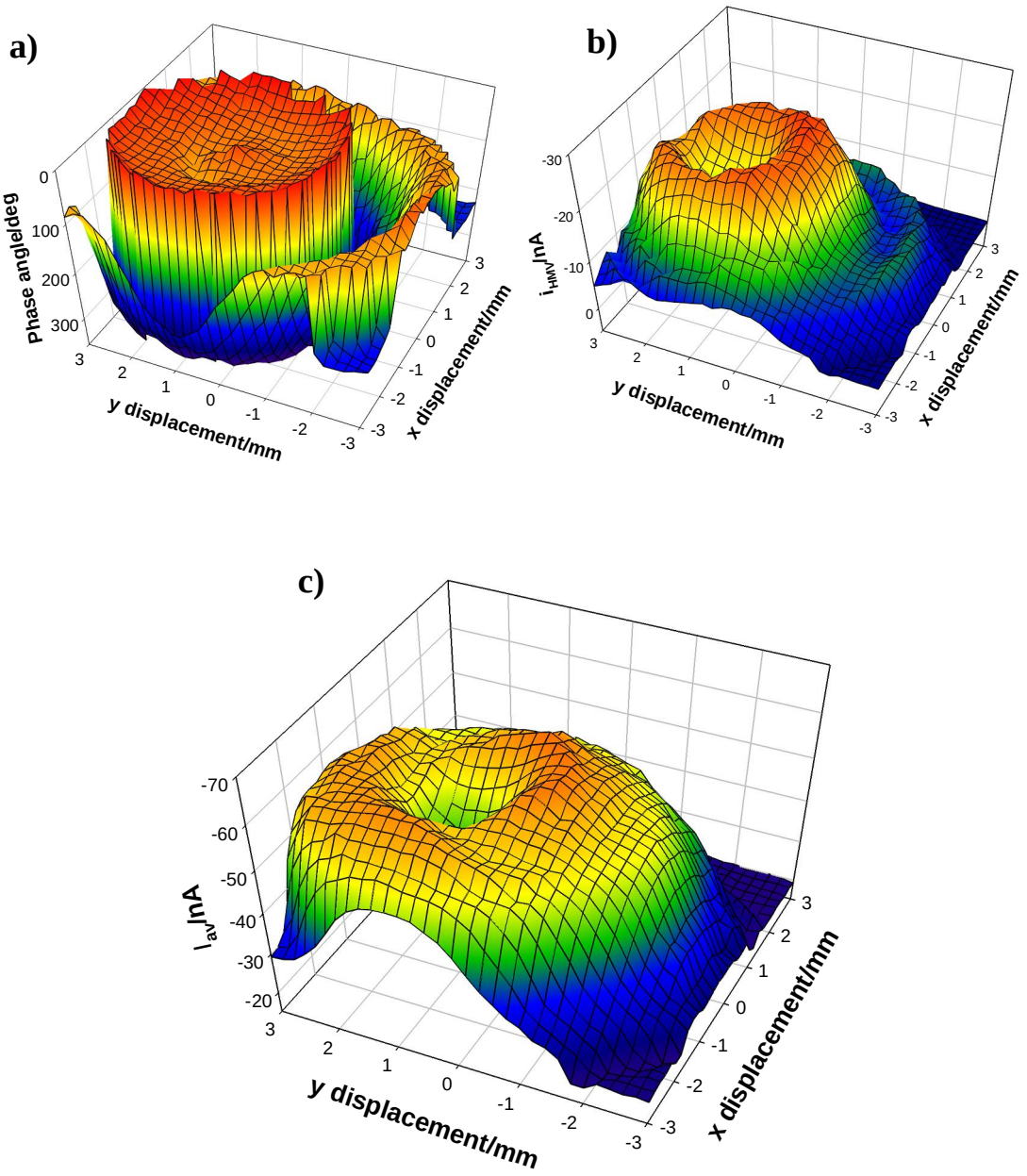

Figure 3.7. **a)** Plot showing the phase correction employed through the automated data collection software as a function of position. **b)** Plot showing the mass transport-limited HMV signal (I_{HMV}) at a 25 µm diameter Pt electrode with an insulating glass sheath (diameter = 5.5 mm) in a 0.1 mol dm^{-3} $Sr(NO_3)_2$ electrolyte containing 5 mmol dm^{-3} $[Fe(CN)_6]^{3-}$ recorded as a function of electrode position in the XY plane at a distance Z = 1 mm from the funnel mouth. **c)** Plot showing the time averaged dc current (I_{av}) as a function of electrode position. The electrode was held at -0.2 V vs. Ag at all times. The Z displacement was maintained at 1 mm from the tip of the funnel mouth. Note each plot is a composite of 960 points (200 µm resolution) and is an average of 5 (2.5 s of data) measurements.

However, figure 3.7 also shows that with this bigger electrode surround, a second ring of increased current appears outside the funnel mouth. The radius of this 'ridge' is ~ 3.75 mm closely matching the sum of the radius of the electrode support and jet. This suggests that even after crossing the boundary of the funnel mouth, flow from the jet is

deflected to the microelectrode surface, where it is detected as an increased electrochemical signal. Interestingly this deflection is seen as a current ridge for this size of electrode support whereas the smaller electrodes (see figure 3.6) does not show this phenomena. Lastly the time averaged current response is plotted as a function of XY position in figure 3.7 (c). This again demonstrates that the resolution of this approach is less than that found when employing the HMV analysis (which shows enhances definition around the jet mouth, see figure 3.7b). Figures 3.7b and 3.7c show the clear 'dimple' effect at the centre of the jet exit. However, the enhanced activity around the jet mouth is only shown clearly with the HMV lock in data analysis approach (see figure 3.7b).

While the experimental results shown in figure 3.6 and 3.7 clearly show the spatial extent of the signals detected in the XY plane, they give no indication of the extent of this enhanced jet edge effect as a function of the vertical distance away from the jet mouth. Hence further experiments were performed to investigate this behaviour. Figure 3.8 shows the vertical extent of the jet edge effect and the influence of the size of the electrode support. Here the current profile is mapped while the microelectrodes were moved in the vertical (XZ) plane (note the y position was manually adjusted prior to the scan to ensure that the electrode mapped the region of interest bisecting the diameter of the jet mouth). Figure 3.8 clearly indicates that the maximum current enhancement is smallest when Z (vertical) displacement is greatest as expected if the flow from the jet dissipates into the solution. However, this decrease in current for the smaller diameter electrode support (see figure 3.8a) is more dramatic when compared to the larger electrode support (see figure 3.8b). This supports the assertion that the electrode surround has a significant effect on the experimental results. The larger the electrode surround, the greater the interaction with the fluid flow from the jet (and subsequent reduction in spatial resolution of the electrode) towards the 25 μm diameter microelectrode is observed. In addition figure 3.8 shows jet edge effects as two zones of high activity extending away (up to ~1 cm) from the edge of the jet. This supports the results presented in figure 3.6 and 3.7 which indicate that the HMV signal was greatest at the edge of the jet mouth.

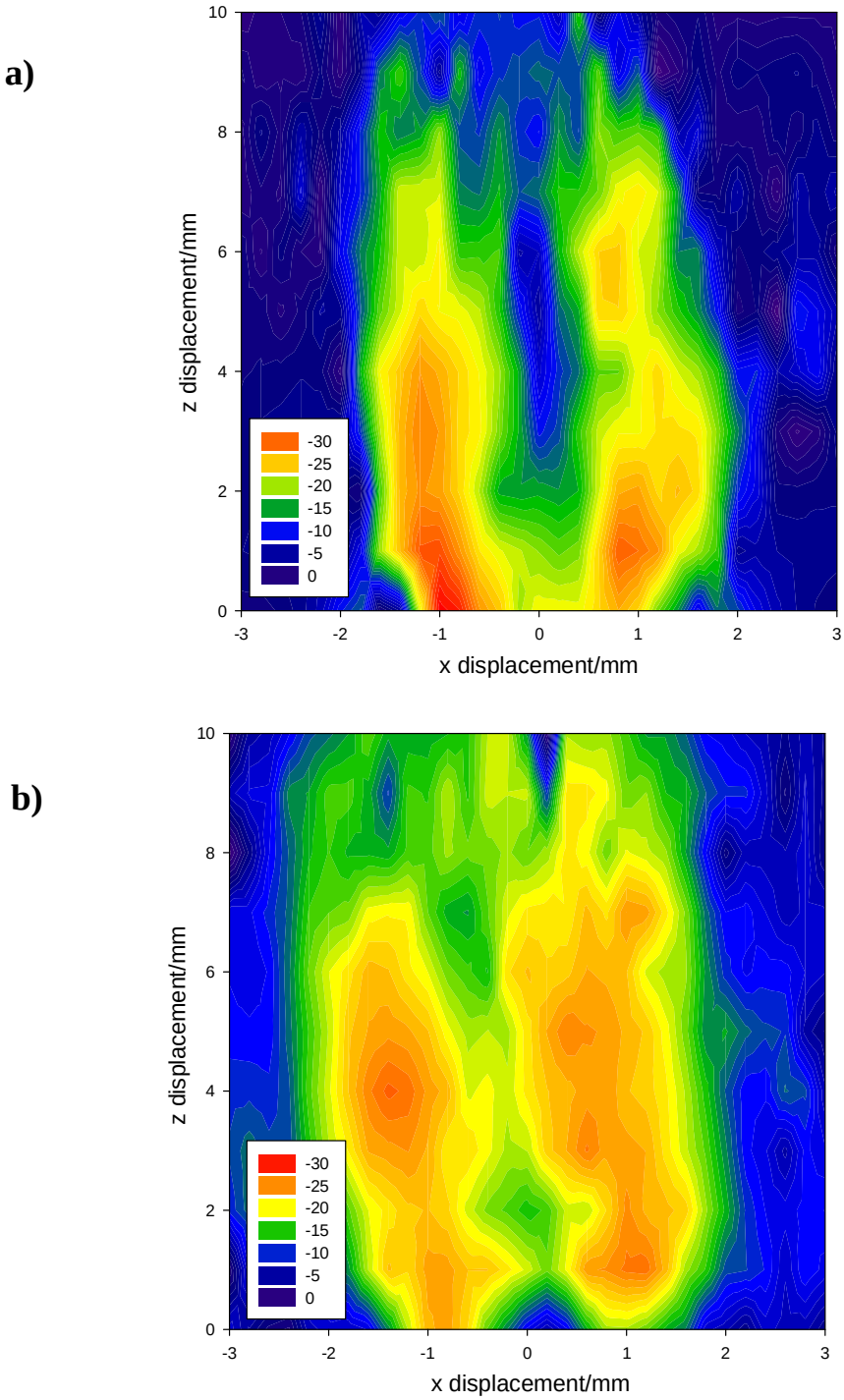

Figure 3.8. Plots showing the transport-limited HMV signal (I_{HMV}) as a function of position of an electrode in the XZ plane, where X is the horizontal and Z the vertical displacement. Here Y = 0 (centre of the funnel mouth). The data were recorded with 25 µm diameter Pt electrodes (insulating glass sheath diameter of **(a)** 2 mm and **(b)** 5.5 mm). The solution consisted of 0.1 mol dm^{-3} $Sr(NO_3)_2$ electrolyte containing 5 mmol dm^{-3} $[Fe(CN)_6]^{3-}$. The electrodes were held at -0.2 V vs. Ag at all times. Note each plot is a composite of 960 points (200 µm resolution) and is an average of 5 (2.5 s of data) measurements.

Similar scanning experiments have been performed using a 500 µm diameter Pt electrode sealed in a 5.0 mm diameter glass support. Figure 3.9 a, b and c show the

phase angle, HMV and time averaged signal respectively as a function of the XY position of the electrode (note in this case the centre of the jet of X ~ 0 mm and Y ~ 0 mm). Figure 3.9a shows the phase correction (to maintain the highest HMV amplitude) plotted as a function of the XY position as the electrode was scanned in the XY plane at constant Z displacement (1 mm). This shows a distinct relationship between phase angle and the location of the electrode. At the centre of the jet the phase correction is ~200^{o}. This is significantly greater than that observed for the microelectrode (see figure 3.6 and 3.7). However, this is to be expected as the response time of this 500 μm diameter electrode is larger than that of the 25 μm diameter microelectrode. Figure 3.9b clearly shows that the 500 μm diameter electrode produces a well defined HMV signal from the pulsating jet with the added consequence of the larger electrode producing an enhanced current signal. As expected, due to both temporal and spatial resolution issues, the current enhancement around the lip of the jet exit is very regular and does not show the variation detected by the 25 μm diameter Pt electrode employed previously (see figure 3.6 and 3.7). Presumably the smaller electrode can detect greater variation in the flow pattern emanating from the jet orifice. Lastly the average current, although still showing evidence of the 'dimple' in the centre of the jet, has a significantly poorer spatial resolution with the enhanced current zone extending completely across the area scanned (see figure 3.9 (c)). This is to be expected as the time averaged signal has none of the temporal information captured in the HMV data. In turn any flow from the jet is detected as an enhanced current signal due to forced convection in the cell. The HMV signal shown in figure 3.9 (a) is clearly well defined and very symmetrical in nature. Indeed, more so than the corresponding microelectrode experiments (see figure 3.6 and 3.7). However, this may be a consequence of the size of the electrode smoothing out any flow variations produced by the jet action itself. Finally the results presented in figures 3.6, 3.7 and 3.9 indicate that, depending on the choice of measurement criteria (HMV, average current or phase angle) selected, the spatial resolution and information gathered by the experiments can vary dramatically.

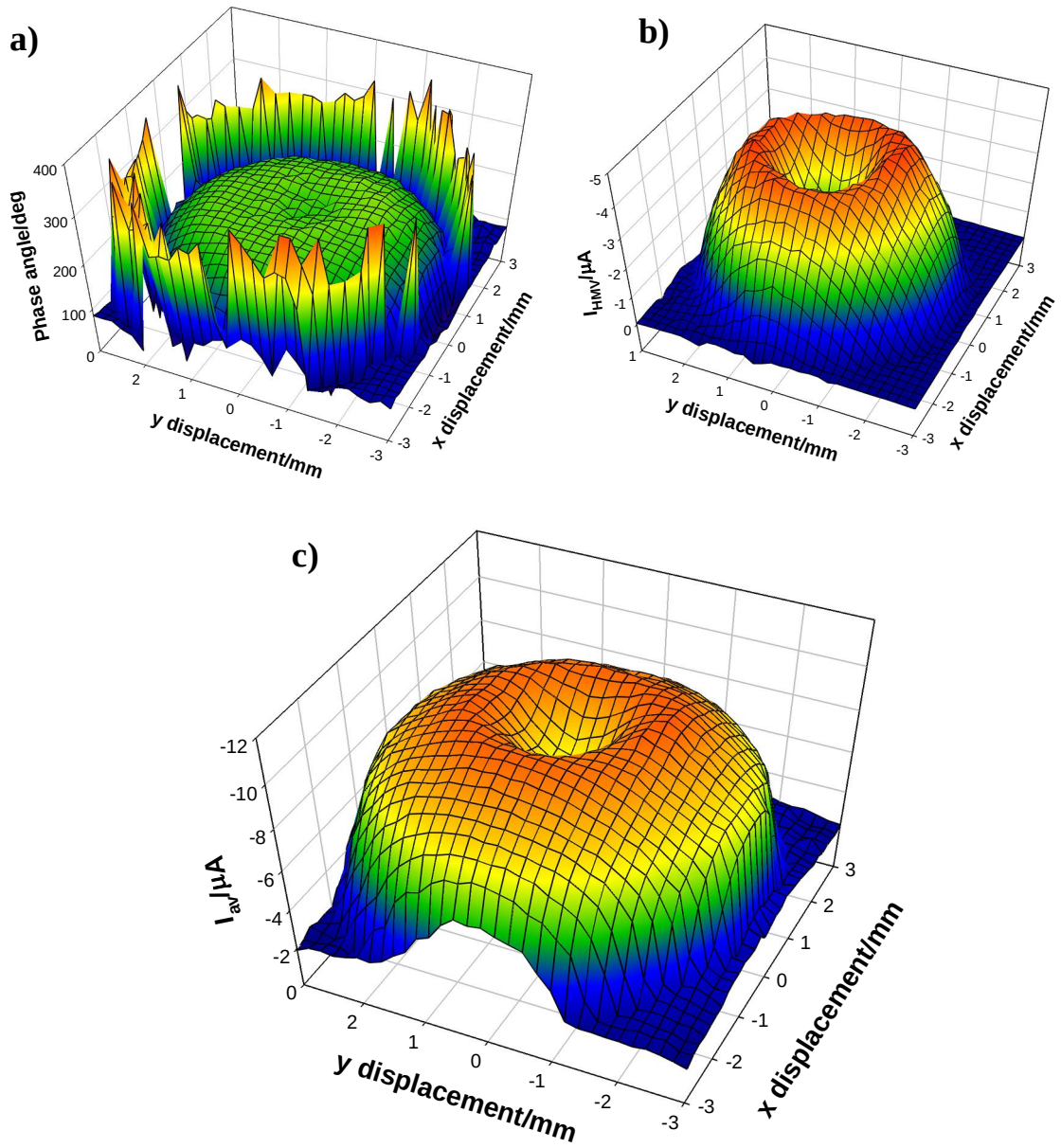

Figure 3.9. **a)** Plot showing the phase correction employed through the automated data collection software as a function of position. **b)** Plot showing the mass transport-limited HMV signal (I_{HMV}) at a 500 μm diameter Pt electrode with an insulating glass sheath (diameter = 5.0 mm) in a 0.1 mol dm^{-3} $Sr(NO_3)_2$ electrolyte containing 5 mmol dm^{-3} $[Fe(CN)_6]^{3-}$ recorded as a function of electrode position in the XY plane at a distance Z = 1 mm from the funnel mouth. **c)** Plot showing the time averaged dc current (I_{av}) as a function of electrode position. The electrode was held at -0.2 V vs. Ag at all times. The z displacement was maintained at 1 mm from the tip of the funnel mouth. Note each plot is a composite of 960 points (200 μm resolution) and are an average of 5 (2.5 s of data) measurements.

The HMV analysis clearly shows the 'ring' effect from the jet edge most clearly while the averaged current gives the poorest resolution. Interestingly the phase angle correction data shows no evidence for the ring effect from the jet edge although still showing evidence for the influence of the electrode support.

In the above investigations it was demonstrated that the oscillating jet could be successfully used in the HMV analysis. This could be now applied in detection of trace species within the solution phase. The results of such a study are reported in the next section.

3.4 Detection Limit Determination for $[Fe(CN)_6]^{4-/3-}$ in the Oscillating Jet System

HMV relies on introducing a modulation in the convective flow of redox species to an electrode surface (*9*). Under appropriate conditions the extraction of the component at the same frequency as the reference signal enables an improvement in the signal to noise ratio. This results in extreme enhancements in detection limits. As an example previous studies (*9, 51*) have determined detection limits for ions in solution as being 0.5 nmol dm^{-3} using HMV (see Chapter 1 for more details). In order to find the detection limit for the oscillating jet system $[Fe(CN)_6]^{4-}$ was employed and its oxidation was monitored. However, it should be noted that to facilitate better mixing of the solution within the cell the apparatus design was slightly changed (see Chapter 2 for more details). In particular, a mini-pump was added to the set-up. The free flow rate of the pump is 300 ml min^{-1} at input voltage of 3.5 V. According to the pump characteristic the time required to pump through 150 ml (~volume of the liquid inside the apparatus) of liquid in order to complete solution mixing (including the large "dead" volumes of the cone) is ~30 s. This time would be used in further experiments as a minimum mixing time.

In order to test performance of the set up a relatively large concentration of the analysing compound was added to the electrolyte solution (see figure 3.10). In this case the cell was filled initially with aerobic electrolyte solution 0.1 mol dm^{-3} $Sr(NO_3)_2$ and a Pt electrode was positioned above the exit of the jet (X~1 mm from the centre of the mouth, Z~1 mm). The signal for molecular oxygen reduction was used to set the phase angle required for lock-in measurements.

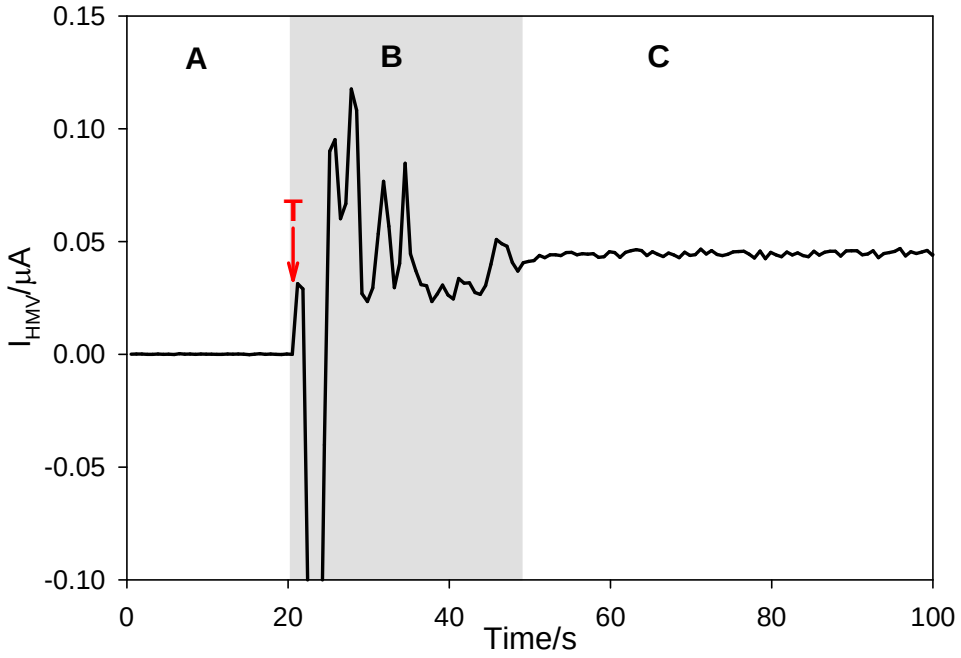

Figure 3.10. Plot showing HMV current as a function of time before titration (section A), after titration T and mixing with a mini-pump (section B). Section C illustrates the region of the stable current. The grey box corresponds to the time required for the full mixing of the liquid within the cell. The concentration of the $[Fe(CN)_6]^{4-}$ in solution was changed from 0.00 mmol dm^{-3} in region A to 0.25 mmol dm^{-3} in region C. The electrolyte used was aerobic 0.1 mol dm^{-3} $Sr(NO_3)_2$ solution. The working electrode employed was polished 500 μm diameter Pt. The electrode was held at +0.5 V *vs.* Ag. The oscillating jet was modulated at 16 Hz with membrane displacement amplitude of (0.022 ± 0.001) mm. Pump input voltage was 3.5 V. The experiments were performed at room temperature 18-22 °C.

Initially the electrode potential was held at -0.4 V *vs.* Ag corresponding to mass transfer limited molecular oxygen reduction. The current time data was used to calculate the phase angle under these conditions. The electrode potential was then changed to +0.5 V *vs.* Ag (at this potential the oxidation of $[Fe(CN)_6]^{4-}$ is mass transfer controlled) and the current was monitored as a function of time. Figure 3.10, section A corresponds to the period of time when no redox species were present in the solution. As expected no current was observed in this region. After titrating an amount of $[Fe(CN)_6]^{4-}$ (labelled as a 'T' in figure 3.10) the pump was switched on. Figure 3.10 (zone C) shows that as the pump was switched off a current increase corresponding to the oxidation of 0.25 mmol dm^{-3} of $Fe(CN)_6^{4-}$ was recorded. These investigations showed that the employed apparatus performed well and could be used in trace analysis.

Figure 3.11 illustrates the result of the titration experiments. The phase angle (between the reference and data signal) here was obtained using the molecular oxygen reduction signal at potential of -0.4 V *vs.* Ag. The electrode potential was then changed to +0.5 V *vs.* Ag and the current was monitored as a function of time. The concentration of the

$[Fe(CN)_6]^{4-}$ ions in $Sr(NO_3)_2$ solution was varied from 0.0 nmol dm^{-3} (see section A), to 30 nmol dm^{-3} (in section B) and to 60 nmol dm^{-3} (in section C). T1, T2, T3 illustrate the titration points and the grey areas correspond to the pumping time.

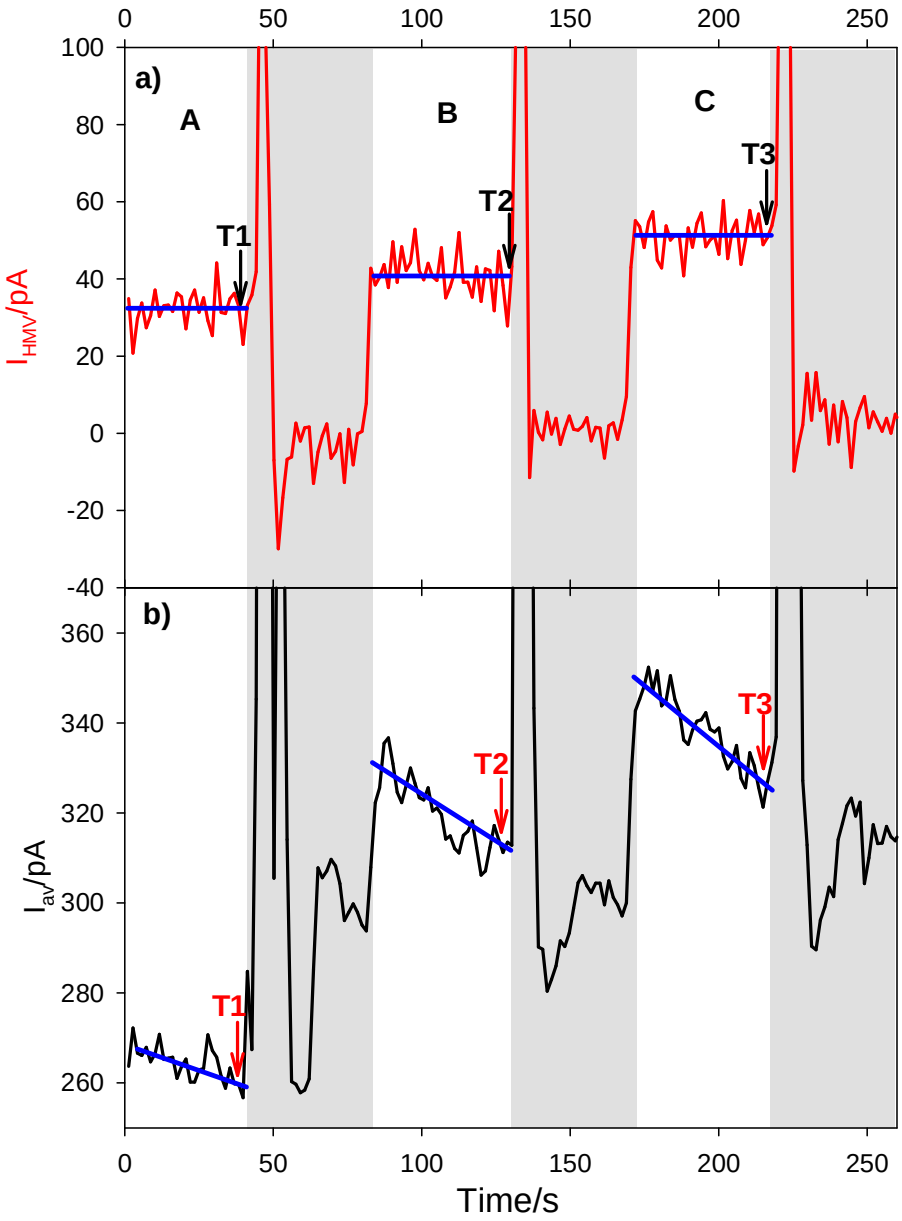

Figure 3.11. Plots showing the results of the titration experiments. T1, T2, T3 correspond to the titration points. I_{HMV} and I_{av} are HMV and time averaged current respectively recorded as a functions of time. The working electrode employed was a polished 500 µm diameter Pt. The electrode was held at potential of +0.5 V *vs.* Ag. The concentration of $[Fe(CN)_6]^{4-}$ was changed from 0.0 nmol dm^{-3} in section A, to 30.0 nmol dm^{-3} in section B and to 60.0 nmol dm^{-3} in section C. The electrolyte solution used was aerobic 0.1 mol dm^{-3} $Sr(NO_3)_2$. The grey areas on the graph illustrate the mixing time. The experiments were performed at room temperature 18-22 °C.

Figure 3.11 shows that after each titration, an increase in current was recorded for both HMV and time averaged current (see figure 3.11 sections A, B and C). However, the

HMV current stabilizes very quickly and stays stable over time while the time averaged current showed a completely different behaviour. In this case continuous decay in current was observed due to the contribution of the background signals to the current. This experiment shows a clear advantage of the HMV technique over the conventional time averaged method. Further interesting observations can be made. It was noticed that as the pump was switched on the HMV current dropped to zero (see figure 3.11a). This suggests that the pumping process completely suppressed the flow modulation from the oscillating jet. However, the effect is expected as the flow modulated by the pump action was moving in the opposite direction to the flow modulated by the motion of the jet apparatus.

It was possible to calculate the lower limit of detection (LLD) for the system employed. LLD was estimated as the mean of the background sample (see figure 3.11, section A) plus 3 times the SD obtained on the background signal (*193, 194*). The detection limit was found to be ~45 nmol dm^{-3}.

3.5 Summary and Conclusion

This chapter presented a novel HMV technique- a mechanically oscillated pulsating jet. The amplified periodic current response was recorded at the electrode as result of the jet modulation. The pulsation of the jet was successfully employed with a software based "lock-in" approach to capture HMV signals of a simple redox system. The technique showed the impressive ability to extract the desired mass transport dependent signal from the total current. Improved spatial resolution of the orifice was observed in the HMV and phase angle mapping measurements of the pulsating jet compared to the direct measurements of time averaged current for the same modulated jet system. The detection limits for the analytical technique was shown to be ~ 45 nmol dm^{-3}.

In the next chapter the characterization of the HMV technique will be further studied. A High-Speed Camera was employed in order to validate the motion of the components (for example the fluid motion and the action of the membrane and shaker) within the experimental apparatus employed.

Chapter 4

Flow Motion Inside the Oscillating Jet

Chapter 3 introduced a novel HMV technique-oscillating jet system. Its characteristics were studied using electrochemical measurements. In particular, the flow of the liquid inside the set up was monitored as a function of the electrode position with respect to the exit of the jet. The current modulation was recorded as the jet was oscillated. Several interesting observations were made when the electrode was scanned across the XY- and XZ- plane above the pulsating jet. It was noticed that a ring of maximum current occurred close to the edge of the mouth of the jet with a significant decrease in the middle. It was proposed that the reason for the behaviour could be a flow motion of the liquid as it leaves the jet. This chapter will focus on characterisation of the HMV system using a high-speed camera. The results obtained will be compared to the electrochemical investigations described previously in Chapter 3.

4.1 High-speed Observations of the Membrane-Jet Performance

In these investigations the high-speed camera has been used in order to monitor the fluid motion within the cell. Because of the transparency of the fluid their flow patterns are invisible to the viewer without some special methods making them visible. In these studies two different methods were employed in order to observe flow patterns. These are the use of a dye or hydrogen bubble tracers. These techniques are widely used in visualization of fluid mechanics (*180*). The details of the experimental set up are reported in Chapter 2. However, in order to aid the reader, a schematic of the apparatus is also presented in figure 4.1. This shows that the investigations were mainly concentrated on two regions: the inner part of the funnel (labelled as “Image 1” in figure 4.1) and the outlet of the jet (see figure 4.1, “Image 2”).

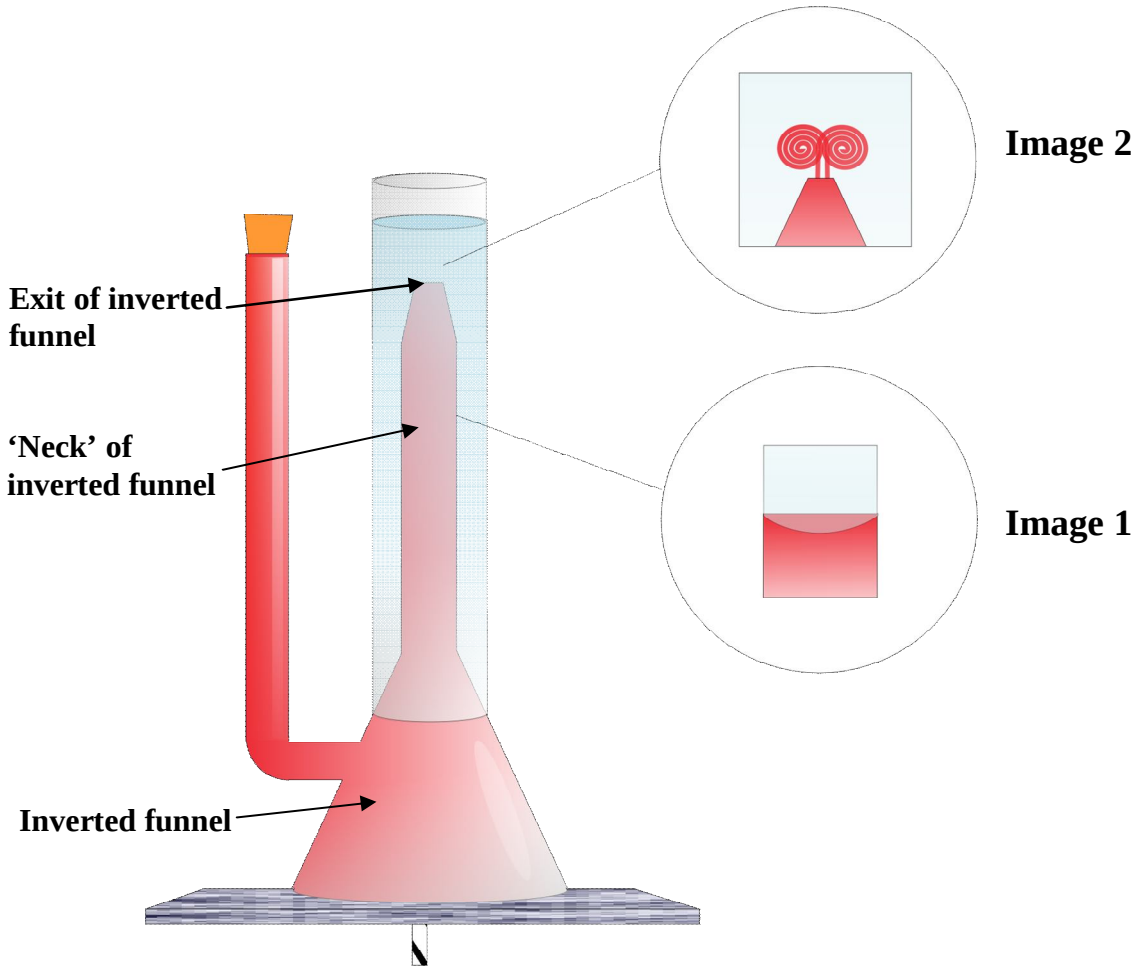

Figure 4.1. Schematic of the apparatus used in the High Speed imaging experiments. Image is not to scale.

Figure 4.2a shows a sequence of frames recorded at 500 fps as the membrane of the cell was vibrated at 16 Hz. In this case the motion of the fluid within the neck of the funnel is shown. In order to do this the lower section of the funnel was filled with water containing a red dye while the upper section was filled with heptane. This produced a liquid/liquid interface in the neck of the funnel which could be easily followed using the high-speed camera. Note that attempts to monitor the fluid motion in the absence of the heptane layer proved unsuccessful as the liquid/air interface broke up during oscillatory motion at the higher amplitudes employed. In chapter 3 the calculation of the liquid velocities were based on the accelerometer measurements (see equations 3.1-3.3). Clearly this calculation assumed ideal behaviour from the membrane. Figure 4.2b shows the actual amplitude of oscillation of a liquid/liquid interface within the neck assuming that the shape of the meniscus can be approximated as an oblate

spheroid (*195*). In addition the predicted displacement amplitudes are shown using the accelerometer to predict the motion of the membrane.

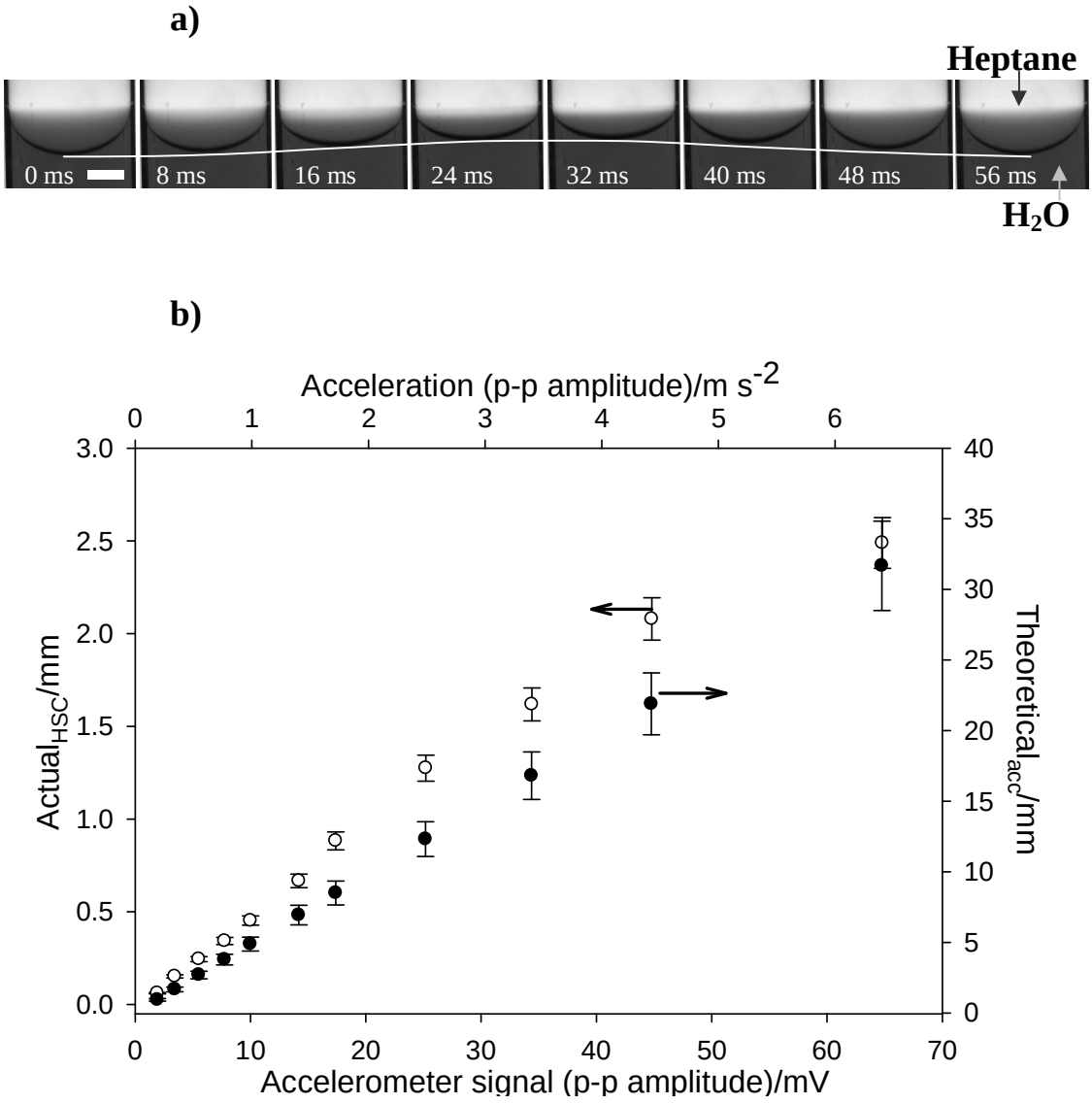

Figure 4.2 **a)** Images obtained from high-speed camera investigation of the motion of the fluid within the neck of the funnel. Note in this experiment the liquid phase consists of water with a red food dye (lower) and heptane (upper) at 20-23 ^{o}C. The images were taken at 500 fps while the shaker was driven at 16 Hz. Every 4th frame is shown with the appropriate time added to each individual frame with respect to the first frame in the sequence. The scale bar represents 2 mm. **b)** Plot showing the analysis of the actual displacement determined from the high-speed images (○) and the theoretical displacement from the accelerometer data (•) considering an oblate correction for the shape of the liquid/liquid interface.

Under the conditions employed, displacement amplitudes of ~30 mm are expected in the neck of the inverted funnel. However, the high-speed camera experiments clearly show that the actual displacement was of the order of 2.5 mm. This is clearly significantly less than expected. This suggests that the assumption of ideal behaviour of the membrane is not maintained under the conditions employed. This cannot be

accounted for by errors associated with the accelerometer measurements. Indeed the motion predicted by the accelerometer was validated by measuring the displacement amplitude of this component with a high-speed camera (see figure 4.3) and then comparing this value (0.82 mm) to the displacement amplitude predicted by the accelerometer output (0.88 mm).

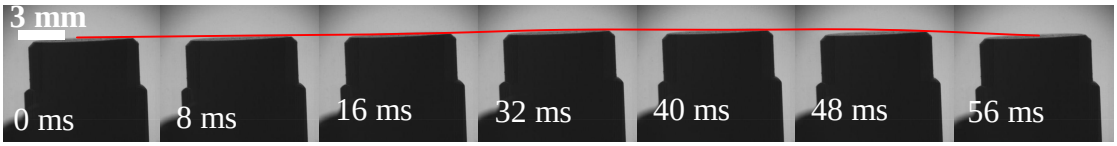

Figure 4.3. Video sequences showing the motion of the accelerometer. The images were taken at 500 fps while the shaker was driven at 16 Hz. Every 4th frame is shown with the appropriate time added to each individual frame with respect to the first frame in the sequence.

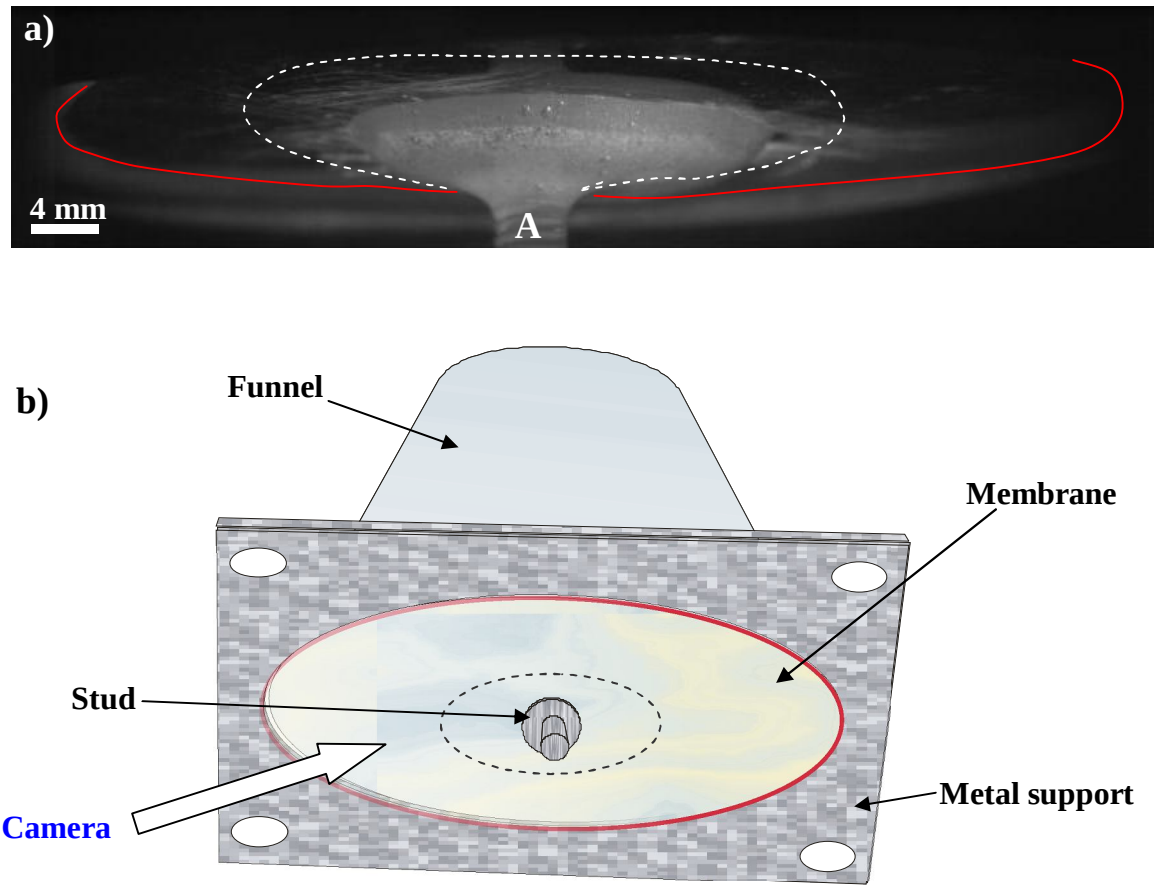

Figure 4.4. **a)** A single frame of the high-speed recording taken from the underneath of the jet focused on the membrane. The Red line highlights the edges of the membrane; the dashed line indicates the main area what is affected by the displacement of the shaker. A is the stud connecting the centre of the membrane with the shaker. **b)** Schematic representation of the experimental set-up.

Clearly this cannot account for the observed deviation in figure 4.2b. However, imaging the membrane (see figure 4.4 and 4.5) provides strong evidence that the

deviation between the predicted and measured displacements shown in figure 4.2b was as the result of non-ideal motion of the membrane. The single frames of the video recordings are shown in figures 4.4a and 4.5a.

a)

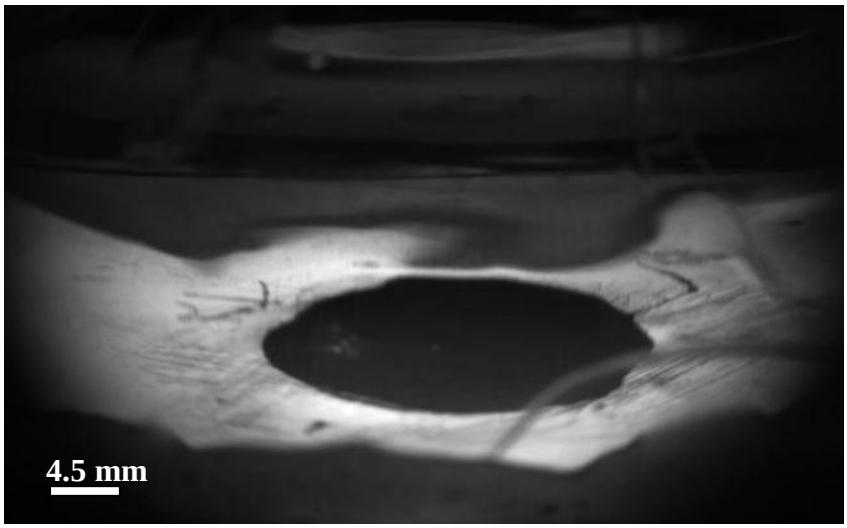

b)

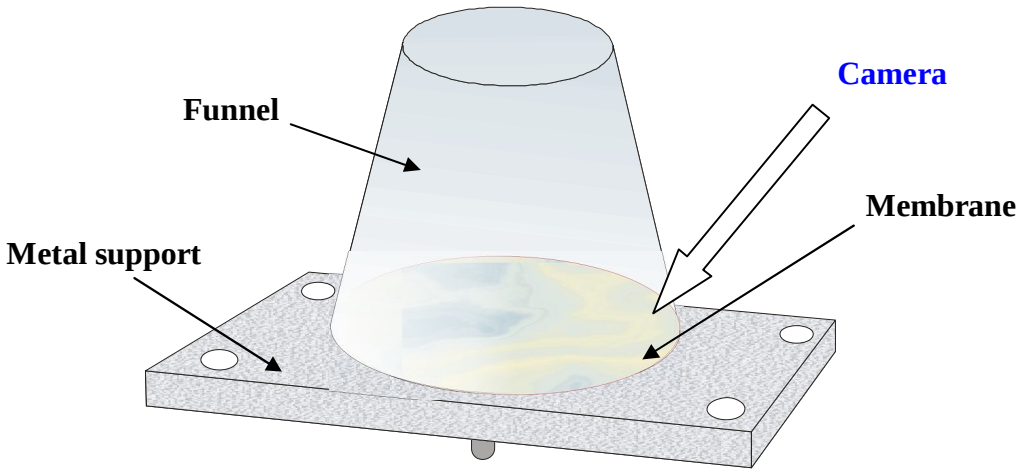

Figure 4.5. **a)** A single frame taken from the high-speed video recording when the motion of the membrane was monitored. **b)** Schematic representation of the experimental set-up.

These images revealed that as the centre of the membrane is displaced by the transducer, the outer section of the circular membrane moves down (presumably due to the forces resulting from the fluid inertia and back pressure associated with flow (*196*) through the jet). This significantly reduces the displaced volume, which in this case appears to be an order of magnitude lower than expected. Despite this disadvantage of the membrane set-up this arrangement produced significant periodic flow rates. Hence the apparatus could be used in the HMV investigations. This was previously demonstrated in Chapter 3. However, attempts to improve performance of the jet were undertaken. In this case the membrane system was replaced with a piston-like set-up (see figure 2.2).

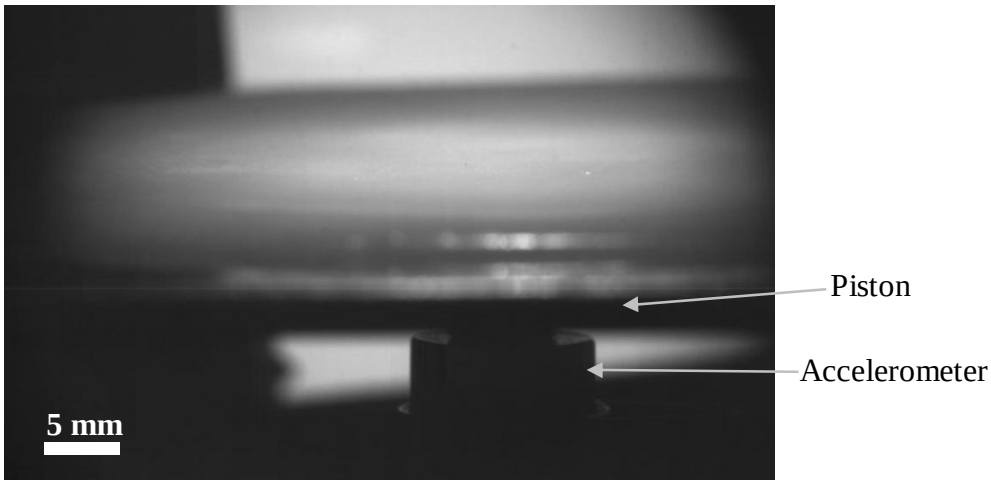

Figure 4.6. A single frame taken from the high-speed video recording when the motion of the piston was investigated.

Figure 4.6 shows a single frame of the video footage monitoring the motion of the piston as the result of the vibration of the mini-shaker. Inspection of the video recordings showed that the whole area of the piston was moving as result of modulation of the shaker. The performance of the setup was further investigated by employing the high-speed camera to monitor the flow of liquid within the neck of the HMV apparatus. In this case visualization of the flow was realized by employing hydrogen bubble tracers (electrochemically generated at a Pt wire stretched across the neck of the funnel). This technique is well known in the art of flow visualisation (*179*, *180*). This method gave reliable information on the flow patterns produced within the system. Hence an understanding of the flow field produced by the device was obtained. Figure 4.7 shows two images taken from a high-speed video recording. The solid line (**——**) on the images indicates the position of the wire inside the funnel neck. The dashed line (**— —**) indicates the displacement of the liquid inside the neck as the jet was modulated. Figure 4.7a illustrates the displacement of the fluid as the piston moved up and figure 4.7b – down. The timescale between the images is 31 ms in agreement with the experimental settings (16 Hz) applied to the system.

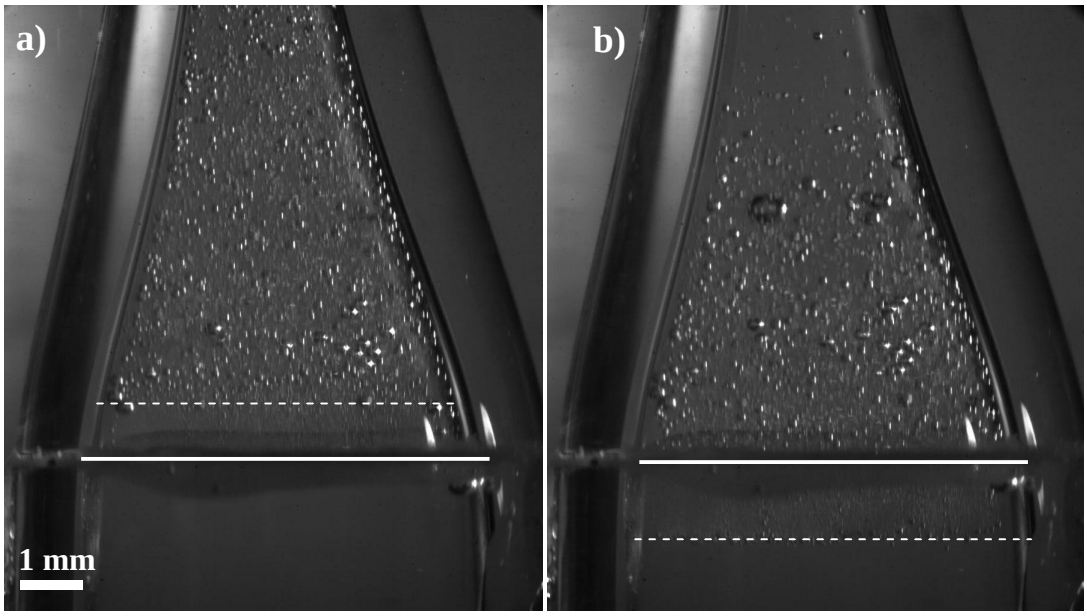

Figure 4.7. Frames showing the displacement of the liquid inside the neck of the funnel (— —) as a result of modulation of the piston recorded using the high-speed camera. The timescale between the images is 31 ms. The piston was modulated at 16 Hz. The flow within the funnel was visualized using the hydrogen bubbles electrochemically generated at the Pt wire stretched across the neck of the funnel (shown as ——).

In this case a peak-to-peak displacement amplitude of the piston was equal to 0.0155 mm (measured by the accelerometer). However, the displacement amplitude of liquid inside the neck of the inverted funnel was 1.73 mm. This can be compared to the predicted displacement values. In order to calculate the expected displacement of the liquid inside the neck the following equations were employed. First, the volume of the displaced liquid, V_2, in the funnel neck is equal to the volume displaced by the piston, V_1.

$$V_2 = V_1 . \tag{4.1}$$

Second, the motion of the piston could be interpreted as a cylinder and its volume calculated according to the equation:

$$V_1 = \pi r^2 X , \tag{4.2}$$

where r is the radius of the piston (in this case 33.5 mm) and X – the peak-to-peak displacement of the piston centre (here 0.0155 mm).

Third, the V_2 could be found according to the partly filled cone volume equation:

$$V_2 = \frac{\pi h}{12}(D_{bot}^2 + D_{bot}D_{top} + D_{top}^2) , \tag{4.3}$$

where D_{bot} is the lower cone diameter, D_{top} is the cone upper diameter and h is the cone height (in this case the displacement of the liquid inside the neck). In these particular

calculations the D_{top} and D_{bot} were 5.78 and 6.78 mm respectively. Hence the expected displacement would be ~1.76 mm. This closely matches the data obtained experimentally (1.73 mm) showing an almost ideal performance of the apparatus. These investigations clearly illustrate the advantages of the piston set-up over the membrane apparatus (see figure 4.2).

It would be also useful to calculate the velocity amplitude at the jet exit. For the piston jet system this could be given by:

$$v_{jet} = \omega\left[\frac{r_p^2 X}{r_j^2}\right] \tag{4.4}$$

For the zero-to-peak displacement of the piston centre of 7.75×10^{-3} mm employed in the experiment presented above (see figure 4.7) the jet amplitude velocity was shown to be 0.87 m s^{-1}. These calculations suggest that a minute motion of the piston results in significant flow of the liquid at the exit of the jet.

The above investigations concentrated on monitoring flow motion inside the inverted funnel. However, it is necessary to visualise the flow distribution at the exit of the jet where the electrochemical measurements are made. This is the region where the electrode interacts with the flow. Hence, this event results in the electrochemical signal recorded at the electrode. The high-speed camera observations in this particular region of the set-up will be presented in the next section.

4.2 Motion of the Liquid at the Exit of the Jet-Vortex Formation

Experiments described in this section were concentrated on monitoring the flow patterns at the exit of the jet (see figure 4.1, Image 2). In the first set of experiments the flow patterns were imaged by injecting the dye into the flow field. Here, the funnel was filled with water and the dye was injected into the water near the edge of the nozzle. The jet was then activated and the displacement of the liquid as a result of this motion was recorded with a high-speed camera. Figure 4.8 shows a sequence of frames recorded at 500 fps as the flow in the cell was modulated at 16 Hz. These images illustrate how the fluid jet leaves the funnel mouth as a function of time. The boundary layer formed at the exit of the jet separates from the edge of the jet mouth (see figure

4.8, F1) and rolls up forming a vortex. A magnified image of a set of developed vortex rings is shown in figure 4.9.

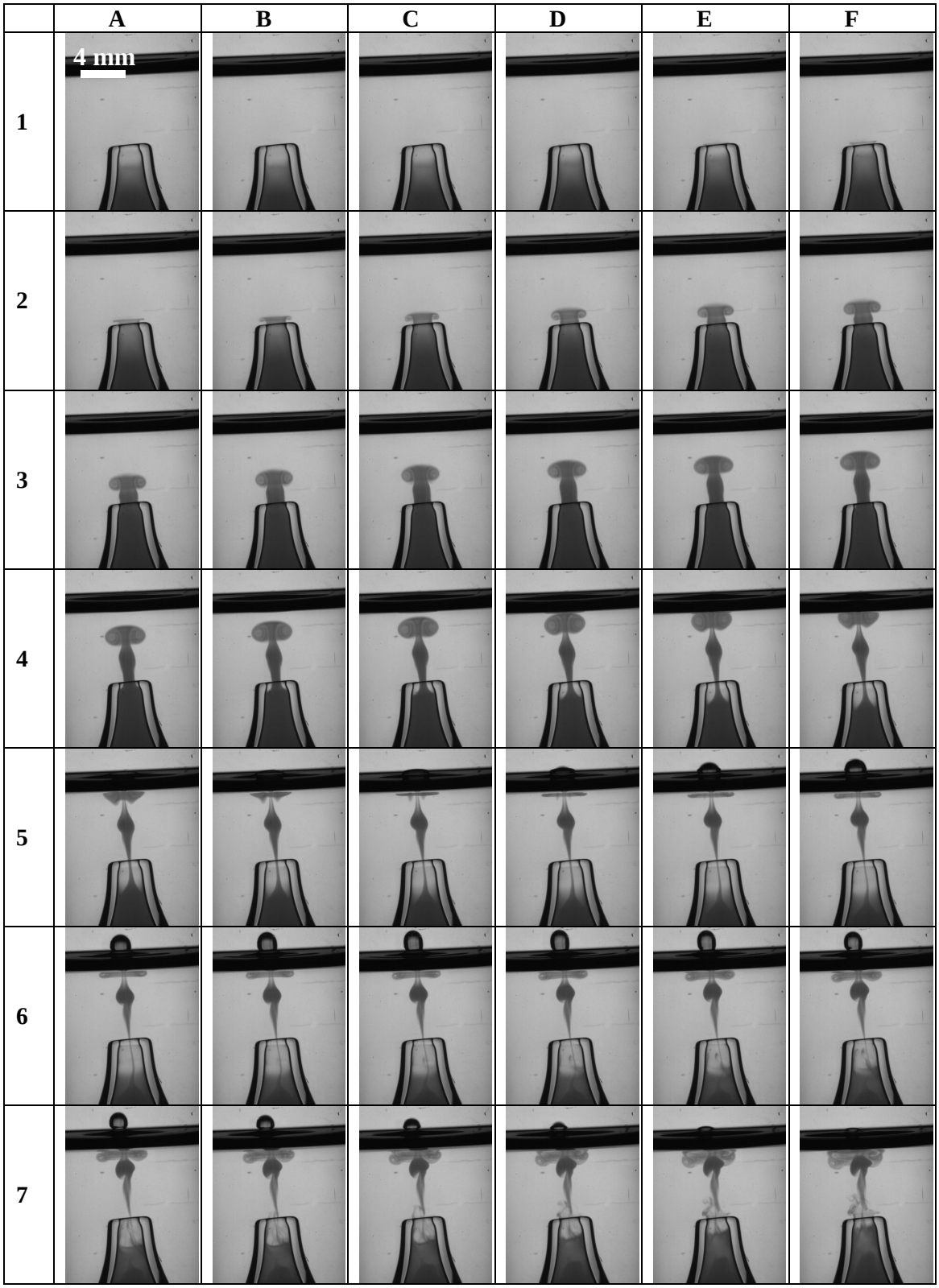

Figure 4.8. Video sequences showing the vortex rising during the jet oscillation. In all cases the capture rate was 500 fps. The interframe time is 2 ms and the first frame is at t = 0 ms. The frames read left to right (A to F) and top to bottom (1-7). The jet was oscillating at 16 Hz. The membrane cell was employed in these experiments. Zero to peak displacement amplitude of 0.178 ± 0.001 mm was employed.

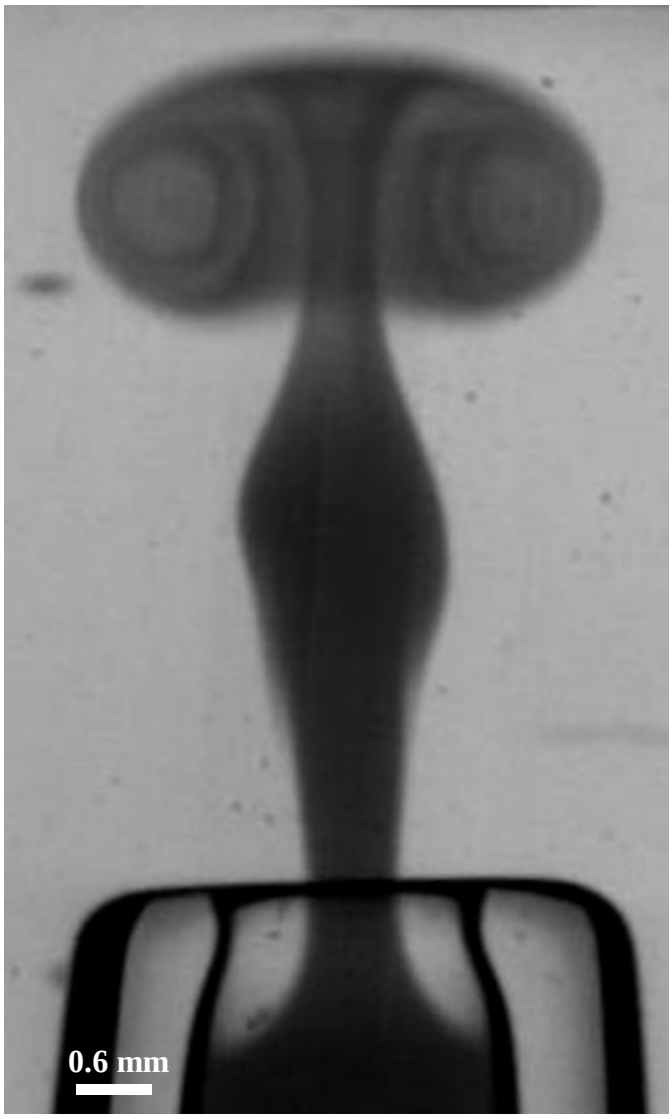

Figure 4.9. The image of the developed vortex rings as the result of the membrane oscillation. The frame is taken from the video sequences presented in figure 4.8 and was labelled as C4. The jet was oscillated at 16 Hz and the zero to peak displacement amplitude of the membrane was 0.178 ± 0.001 mm.

Examples of similar experiments on visualization of the flow of a pulsating jet system can be found in literature (*197-199*). Figure 4.10 are images reported by M. Gühler who monitored the development of the vortex ring in water at a nozzle of the jet. The water was expelled from a tube with the aid of a piston. The flow patterns were visualized by injecting a dye at the edge of the nozzle (*197*). These observations are very similar to the results obtained in this work and presented in figures 4.8 and 4.9. Using analysis of the images shown in figure 4.8, the speed with which the vortex travels through the liquid can be calculated. It was observed that the velocity of the vortex varied with time from 0.042 m s^{-1} close to the exit of the jet to 0.025 m s^{-1} for a

fully developed vortex. This deceleration is related to loss of energy through friction (viscous) effects.

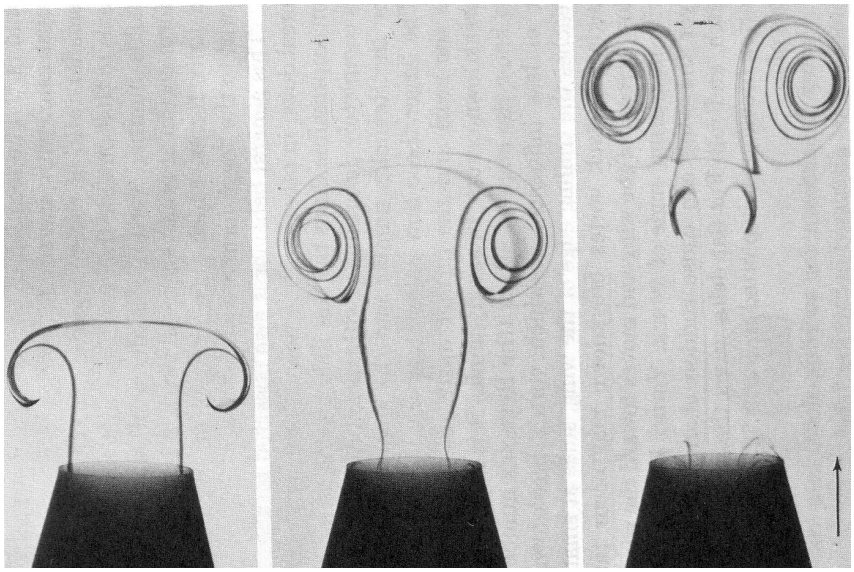

Figure 4.10. Development of a vortex ring in water at a nozzle, made visible by dyed streak lines. Scale is not known. The images are taken from reference (*197*).

However, the diameter of the rings also affects the speed of the vortex. As the vortex rises the diameter of the ring increases through entrainment of fluid from the surroundings.

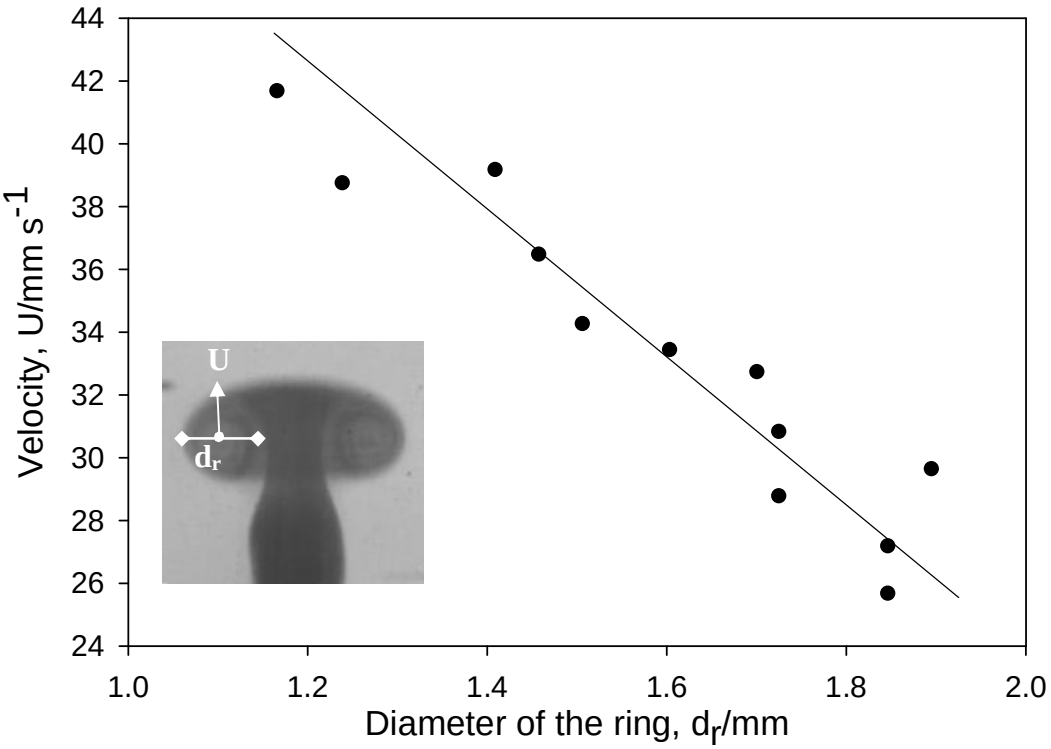

Figure 4.11. Plot showing the Velocity of the centre of the ring as a function of the diameter of the ring. Note the solid line is added as a visual aid only.

This fluid, which is entrained over the whole surface of the ring, must be set into rotation and increases the size of the rings (*200, 201*). The increase of the diameter of the rings in turn results in the loss of the velocity of the vortex (*197, 202*). (Figure 4.11 shows this effect.) In order to illustrate this effect the results obtained from the dye experiments were analysed. Figure 4.11 shows a plot of the vortex diameter (d_r) as a function of the velocity (U). This shows that as the d_r increases the U decreases.

It is possible to compare the electrochemical data with these high-speed camera results. In chapter 3 the flow of the liquid at the exit of the jet was measured electrochemically. The XZ scanning experiments showed that there are two regions of maximum current extending ~ 1 cm away from the mouth of the jet. These results can now be compared to the tracking analysis from high-speed camera investigations. Figure 4.12 shows combination of the electrochemical and high-speed camera measurements. Note these are two different experiments therefore a slight deviation between them is to be expected.

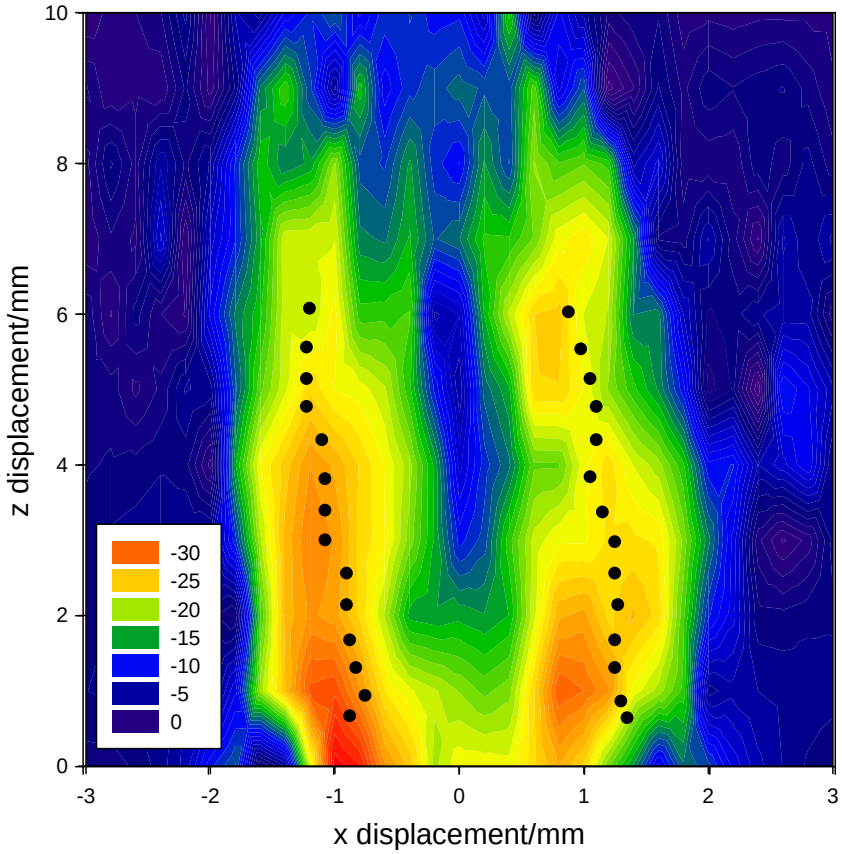

Figure 4.12. Plot showing combination of the scanning and high-speed camera analysis. For experimental details for the electrochemical measurements see figure 3.8. The black dots (●) represent the high-speed camera analysis results. The last were obtained from the video sequence presented in figure 4.8.

The centres of the vortex rings were taken as an object for tracking analysis. These are presented as black dots (●) in figure 4.12. The plot shows that the zones of maximum current coincide with the position of the vortex rings. This suggests that formation of the rings plays the most significant role in the mass transport enhancement obtained from the pulsating jet apparatus. The fact that the current decreases as the electrode moves further away (in the Z direction) from the jet exit can also be related to the deceleration and dying out of the vorticity of the flow as it travels through the liquid.

While the dye experiments are useful, only one 'vortex' can be visualized and the experiments are laborious. To avoid these problems another technique was used to visualize the vortex behaviour of the flow; this was the use of electrochemically generated hydrogen bubbles (see figure 4.13). This method has already been presented, when the displacement of the liquid inside the neck of the jet was studied (see figure 4.7). In these particular experiments, the flow visualisation mode is expected to give more information on the velocity of different parts of the vortex rings. Note, in these investigations the piston design flow cell was used to modulate the flow at the jet.

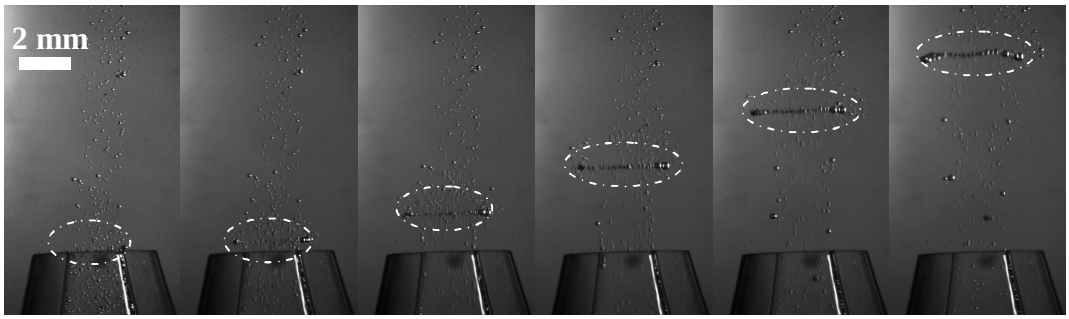

Figure 4.13. High-speed video images. Recorded at 2000 frames s^{-1} with shutter speed of 1/2500 s. The time shown is with respect to the first frame. Hydrogen bubbles were generated using DC power supplier at voltage of 5.1 V and current 0.01 A. The electrochemical cell used in the experiments consisted of 50 μm diameter platinum wire electrode and gauze platinum electrode. The solution employed was 0.1 mol dm^{-3} $Sr(NO_3)_2$. The oscillating frequency was 16 Hz and the zero to peak piston displacement amplitude was 7.75 x 10^{-3} mm. The white annotation arrows show the position of the vortex rings. The timescale between the frames is 5 ms.

A magnified image of the developed vortex is presented in figure 4.14. The white annotations (arrows) on the image show the vertical V_v, and the orbital, V_o, motion of the vortex within the image. Considering the zero to peak piston displacement amplitudes typically employed (measured by the accelerometer at ~7.75x10^{-3} mm), the exit jet amplitude velocity is of the order of 0.86 m s^{-1} (see eq. 4.4). This theoretical velocity was compared to the velocities recorded in the high-speed imaging/bubble tracer experiments (see figure 4.15).

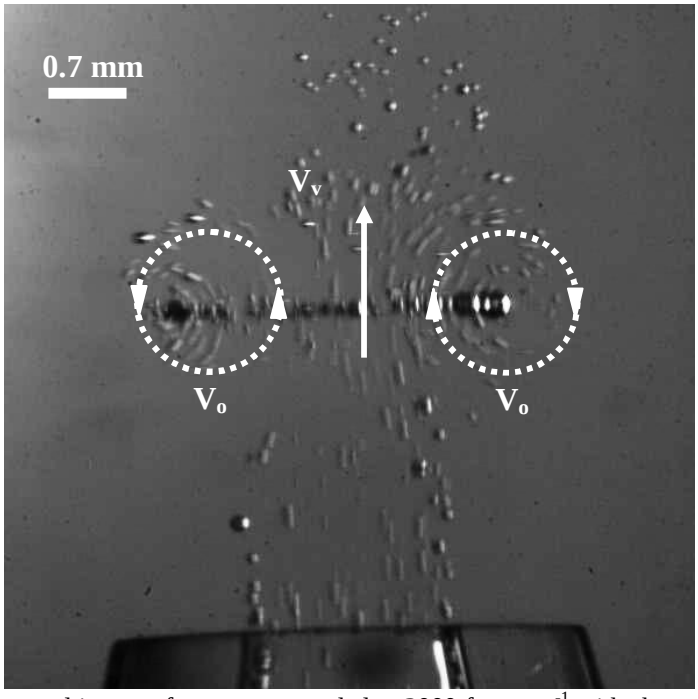

Figure 4.14. High-speed image of a vortex recorded at 2000 frames s^{-1} with shutter speed of 1/2500 s. Oxygen bubbles were generated using DC power supplier at voltage of 5.1 V and current of 0.01 A. The electrochemical cell used in the experiments consisted of 50 µm diameter platinum wire electrode and gauze platinum electrode. The solution employed was 0.1 mol dm^{-3} $Sr(NO_3)_2$. The oscillating frequency was 16 Hz and the zero to peak piston displacement amplitude was 7.75 x 10^{-3} mm. The white annotation arrows show the motion of the toroid and vortex within the image.

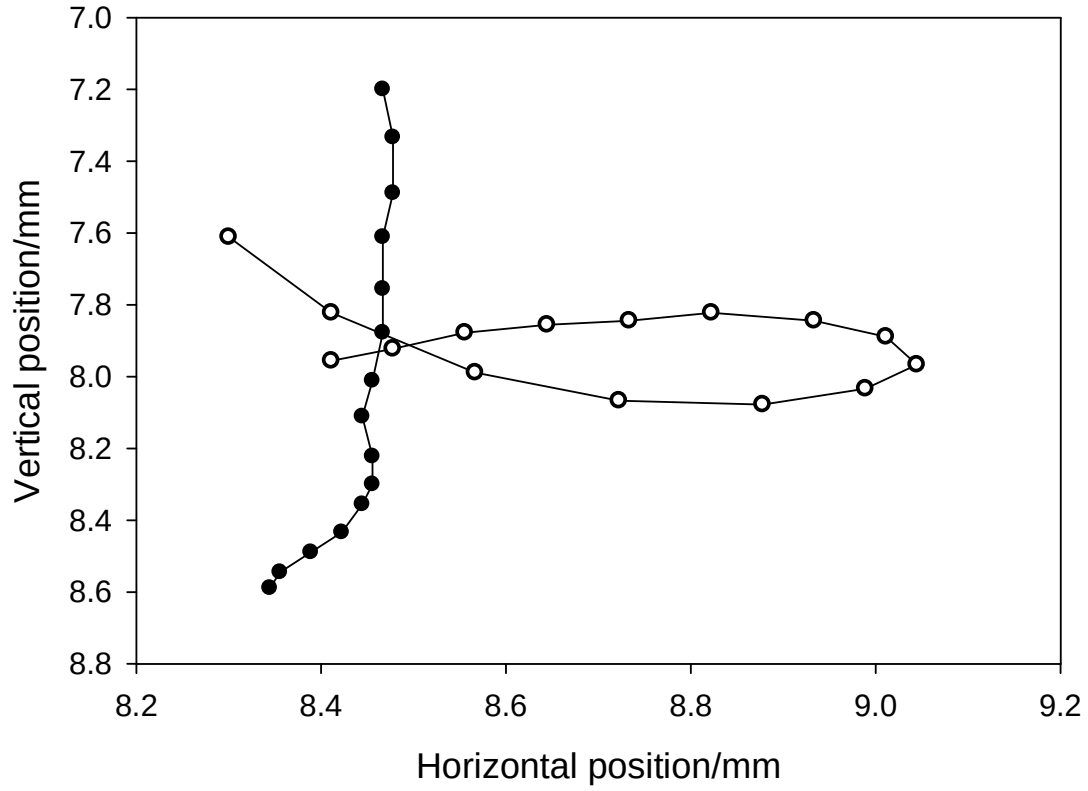

Figure 4.15. Plot showing orbital V_0 (—○) and vertical V_v (—●) positions of the vortex and toroid respectively. The oscillating frequency was 16 Hz and the piston zero to peak displacement amplitude was 7.75 x 10^{-3} mm.

This analysis showed that the toroid travels through the solution with a velocity (V_T) of ~0.3 m s^{-1}. This is significantly less than the jet exit speed. However, the bubble tracking experiment showed that the 'orbital' velocity of the vortex (V_O) is of the order of ~0.7 m s^{-1}. This experiment suggests that the predicted velocity in this system is always going to be higher than that achieved experimentally because both the vortex behaviour of the jet and the orbital fluid movement need to be taken into account.

In order to create the condition close to the conditions for the electrochemical experiments the electrode was positioned above the jet. A high-speed camera was employed to monitor the flow motion as it reaches the electrode. The results are presented in figure 4.16. The electrode was positioned ~3 mm above the jet exit and the dye was then injected into the jet nozzle. As the jet was modulated the rise of the vortex was observed. Note that when the vortex rings impact on the surface of the electrode, vorticity of opposite sign is created (see figure 4.17). Similar effects were observed when a vortex impacted on the surface of the water/gas interface (see figure 4.8, series of images F5-B7).

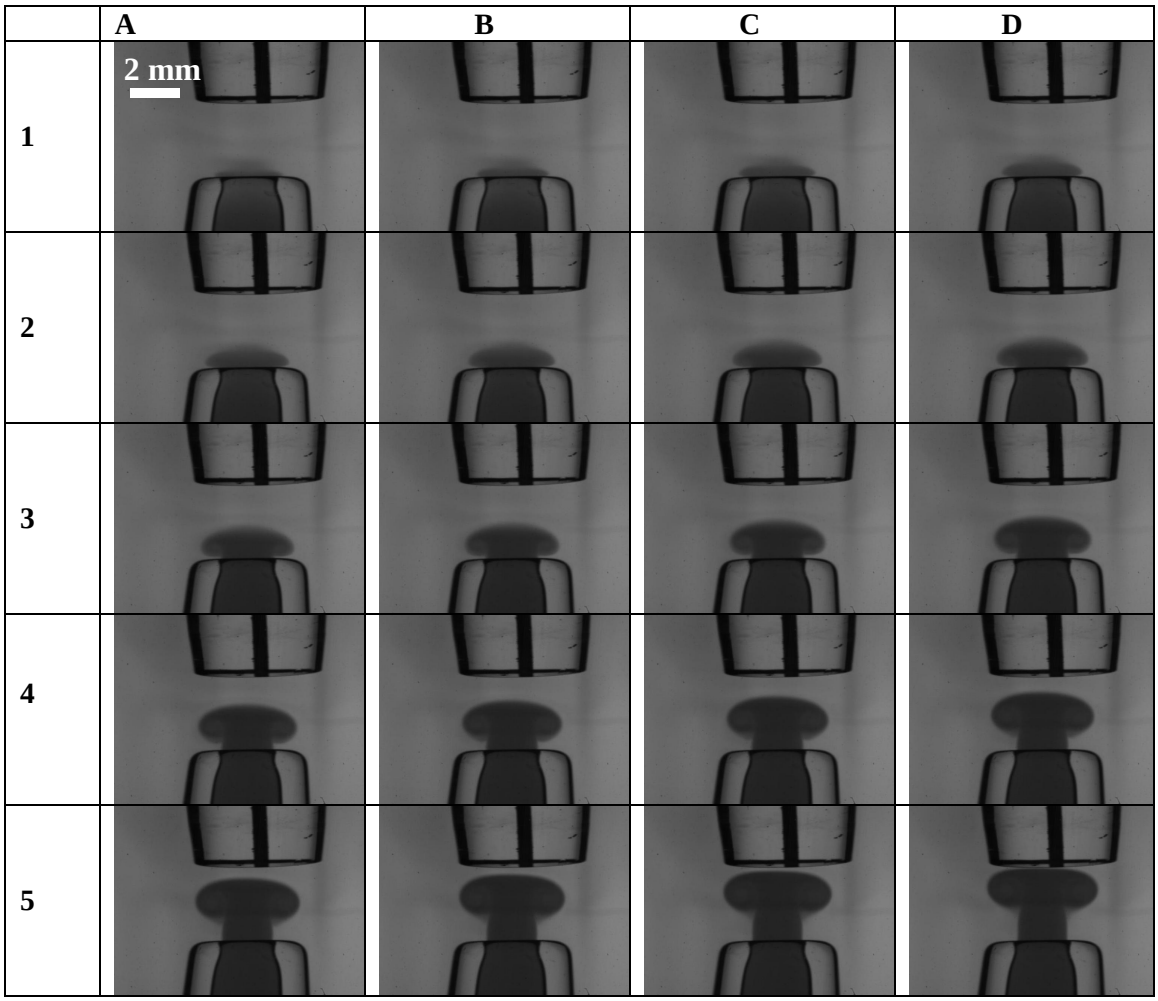

Figure 4.16. Continues overleaf.

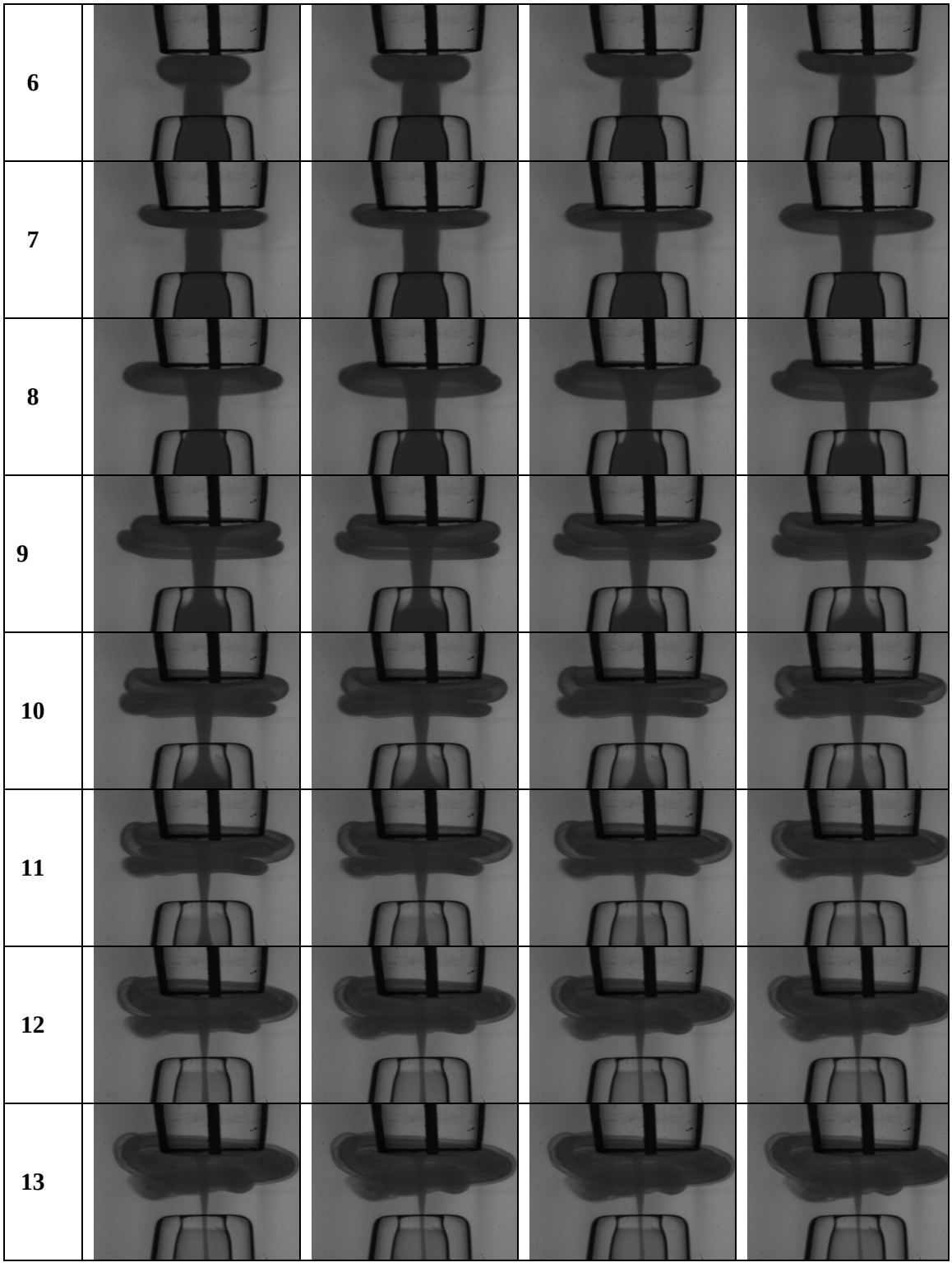

Figure 4.16. Video sequences showing the vortex rising during the jet oscillation. In all cases the capture rate was 500 f.p.s. The interframe time is 2 ms and the first frame is at t = 0 ms. The frames read left to right (A to D) top to bottom (1-13). The jet was oscillating at 16 Hz. The membrane cell was employed in the experiments and the zero to peak displacement amplitude of the membrane was 0.178 ± 0.001 mm. The electrode was positioned 3 mm above the jet exit.

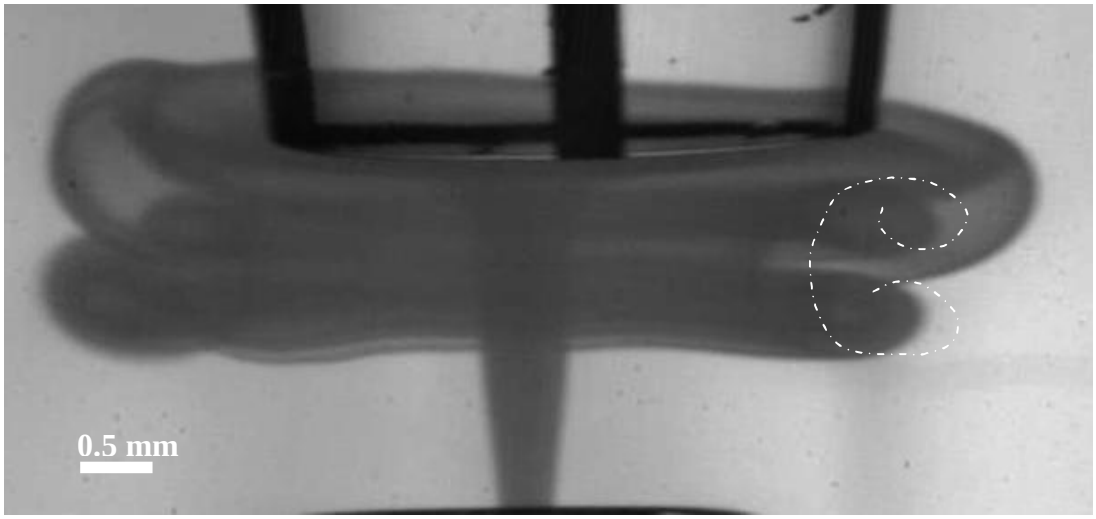

Figure 4.17. The image of the vortex rings approaching the electrode surface. The frame is taken from the video sequences presented in figure 4.16 and was labelled as C10. The jet was oscillated at 16 Hz and the zero to peak displacement amplitude of the membrane was 0.178 ± 0.001 mm. The white annotation is indicating the first and second vortices.

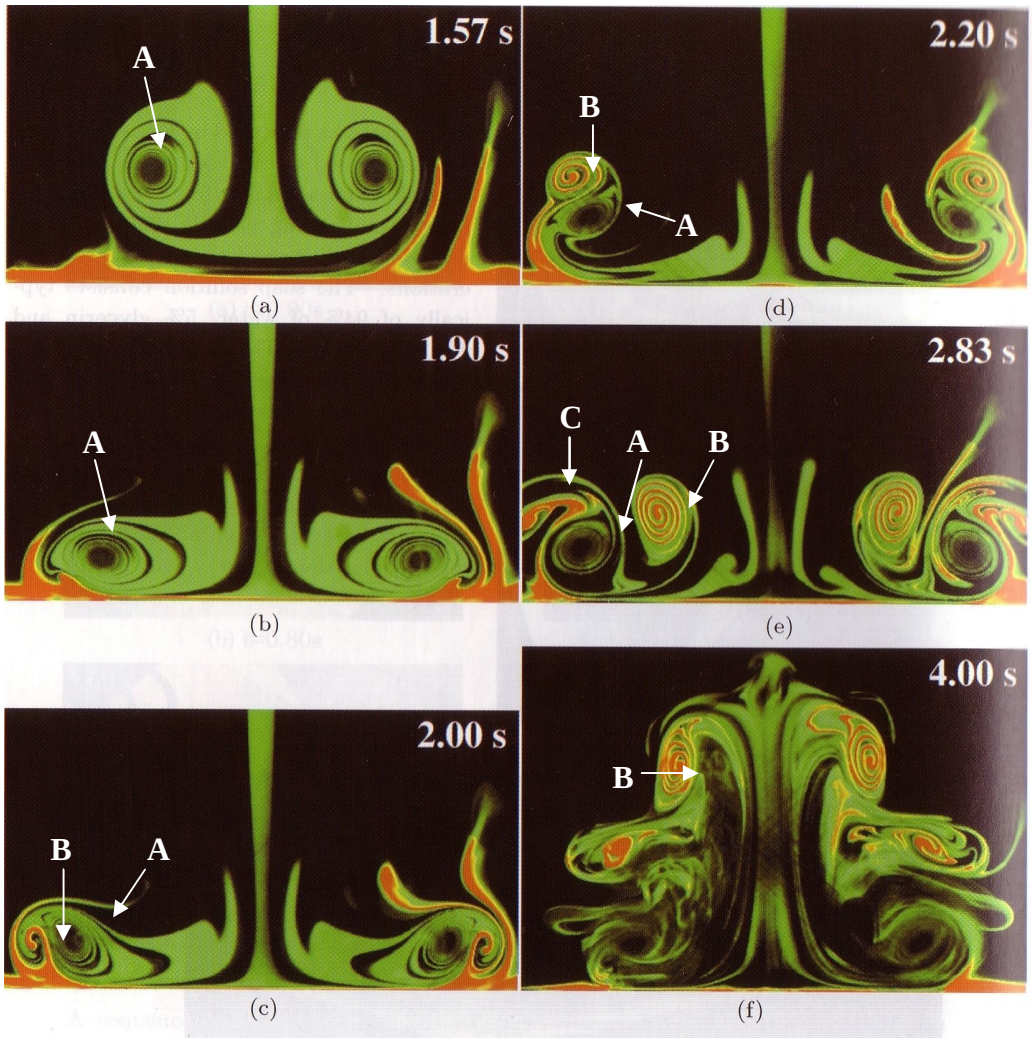

Figure 4.18. Photos showing the vortex rings approaching the wall. The flow visualization images shown here were obtained using two colours dye. (Taken from reference (*180*)).

This behaviour of the vortex ring near the solid walls is widely described in the literature (*180, 197, 203, 204*). These studies showed that if a vortex ring approaches the wall at 90°, several vortex rings, depending on the strength of the primary vortex can be induced at the wall sequentially. The first induced vortex, or secondary vortex, tries to push the primary vortex away from the wall. During this time the influence of the secondary vortex on the primary one diminishes, and the primary vortex approaches the wall again. If it is still strong enough it induces another secondary vortex, and so on (*204*). An example of a behaviour of the vortex approaching the wall is shown in Figure 4.18 (*180*). The images show that as the primary vortex (labelled as A) interacts with a solid wall a secondary vortices (labelled as B) (figure 4.18c) are produced. Figure 4.18 d and e illustrates formation of a tertiary vortex (labelled as C) as result of contact of primary and secondary vortices. Later in time the secondary (labelled B) one moves quickly away from the wall (figure 4.18f), pushed by other vortices.

The investigations carried out in this project and the previous results reported in the literature suggest that the presence of the electrode would increase the vorticity of the flow (*197, 203, 204*). Therefore it is expected that the size of the electrode surround will be important in these experiments. The electrochemical investigations (see Chapter 3) verify this assumption.

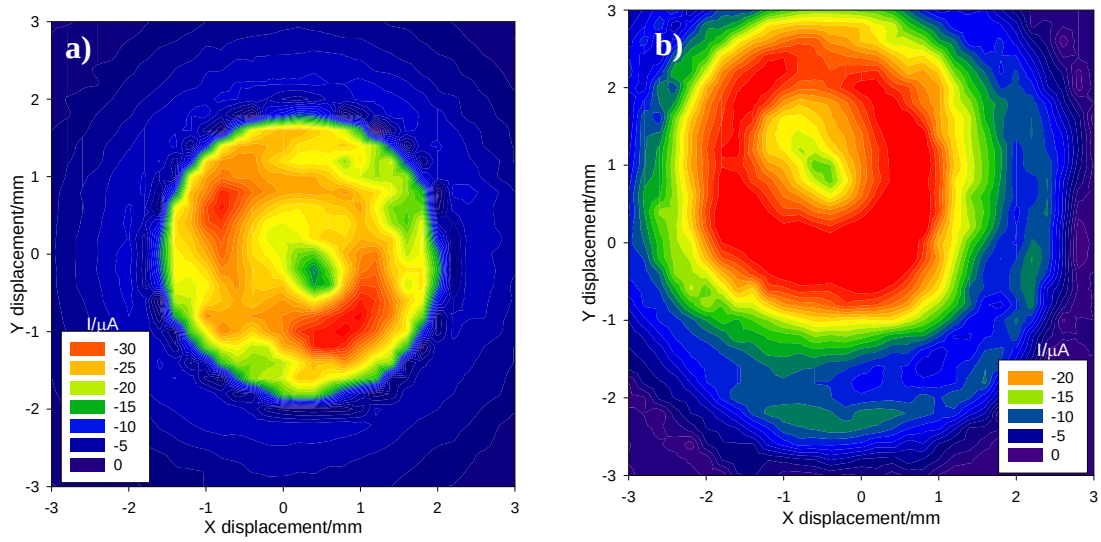

Figure 4.19. Contour plots of the HMV current recorded at the 25 µm diameter Pt electrodes with the glass surrounding of **a)** 2mm and **b)** 5.5 mm as a function of electrode position in the XY plane at a distance Z = 1 mm from the funnel mouth. The solution used was a 0.1 mol dm^{-3} $Sr(NO_3)_2$ electrolyte containing 5 mmol dm^{-3} $[Fe(CN)_6]^{3-}$. For more details on the investigations please see figures 3.6 and 3.7.

Figure 4.19 shows the contour plots of the HMV current as a function of the position with respect to the jet exit recorded at the 25 μm diameter Pt electrodes. The results show dramatic change when the surround of the electrode was changed from 2 mm (figure 4.19a) to 5.5 mm diameter (figure 4.19b). As the support diameter is increased the region of the increased current spreads further from electrode. It is also noticeable that the maximum current ring is significantly wider and better defined for large diameter sheath electrode. Figure 4.20 shows the current profile as a function of position of the electrode with a constant X value of -0.6 mm.

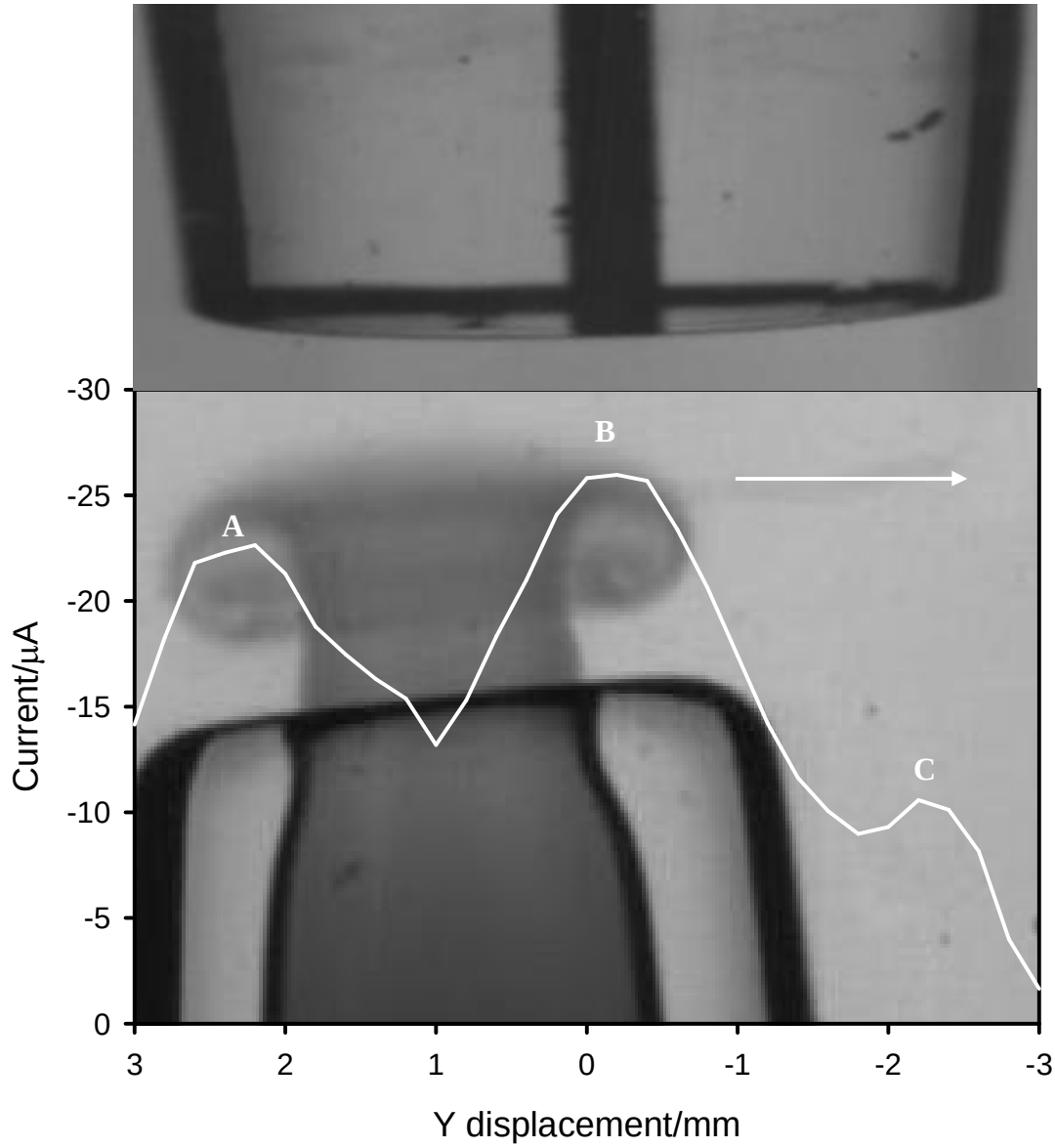

Figure 4.20. Plot showing the current recorded at the 500 μm diameter Pt electrode (5.5 mm diameter glass surrounding) as a function of the displacement in Y direction (the X = -0.6 mm). The electrode was positioned 1 mm above the mouth of the funnel. The figure also includes the images of the electrode and the jet exit. The images are in the scale with the electrochemical measurements.

In order to clarify the results, images of the vortex and electrode were added to the graph. Note the image is to scale with respect to the plot. The position of the vortex rings coincides with the maximum current recorded at the electrode (labelled as A and B, figure 4.20). In the case when the electrode (5.5 mm diameter) was positioned close to the edge of the jet (as it shown in figure 4.20) an impact of the vortex ring with the electrode surface was expected. Hence the influence of this flow on the electrochemical response was expected to be the most effective in this region. As the electrode moved away from this position in the direction shown with an arrow on figure 4.20 then a decrease in current is observed. In this case the electrode support is in contact with only one vortex ring. It is interesting to note that as the electrode was moved ~2 mm away from the jet centre an unexpected increase in current was observed (figure 4.20, peak C). In this position the edge of the electrode surround reaches the edge of the vortex ring. Previous studies of vortices reported in the literature (*203*) described a similar effect. It was shown (see figure 4.21) that as the primary vortex hits the edge of a plate a secondary vortex ring of opposite rotation has formed (*197*). This followed by the disintegration of both vortex rings as shown in figure 4.21 c and d.

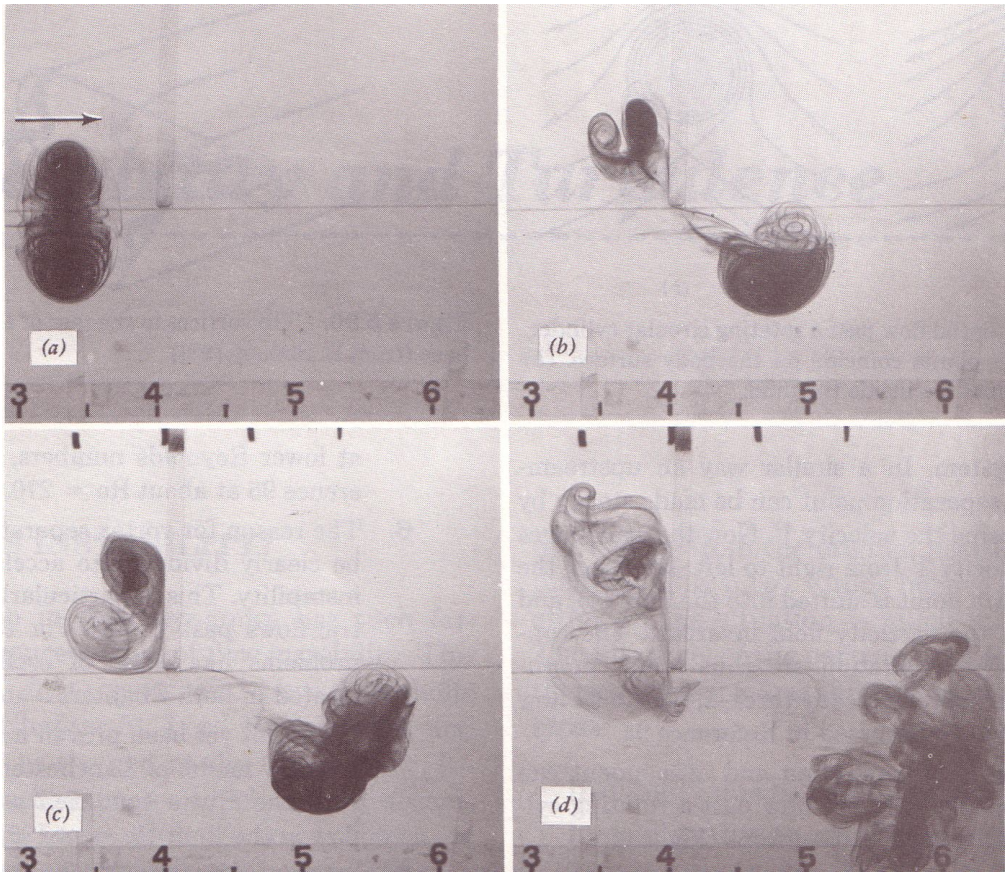

Figure 4.21. A vortex ring approaches the lower edge of a vertical plate left to right. The sequence of pictures shows the formation of a secondary vortex ring and the disintegration of both vortex rings (*197*).

It is proposed here that this edge effect could be the reason for the current increase (halo effect) shown in figure 4.20, C.

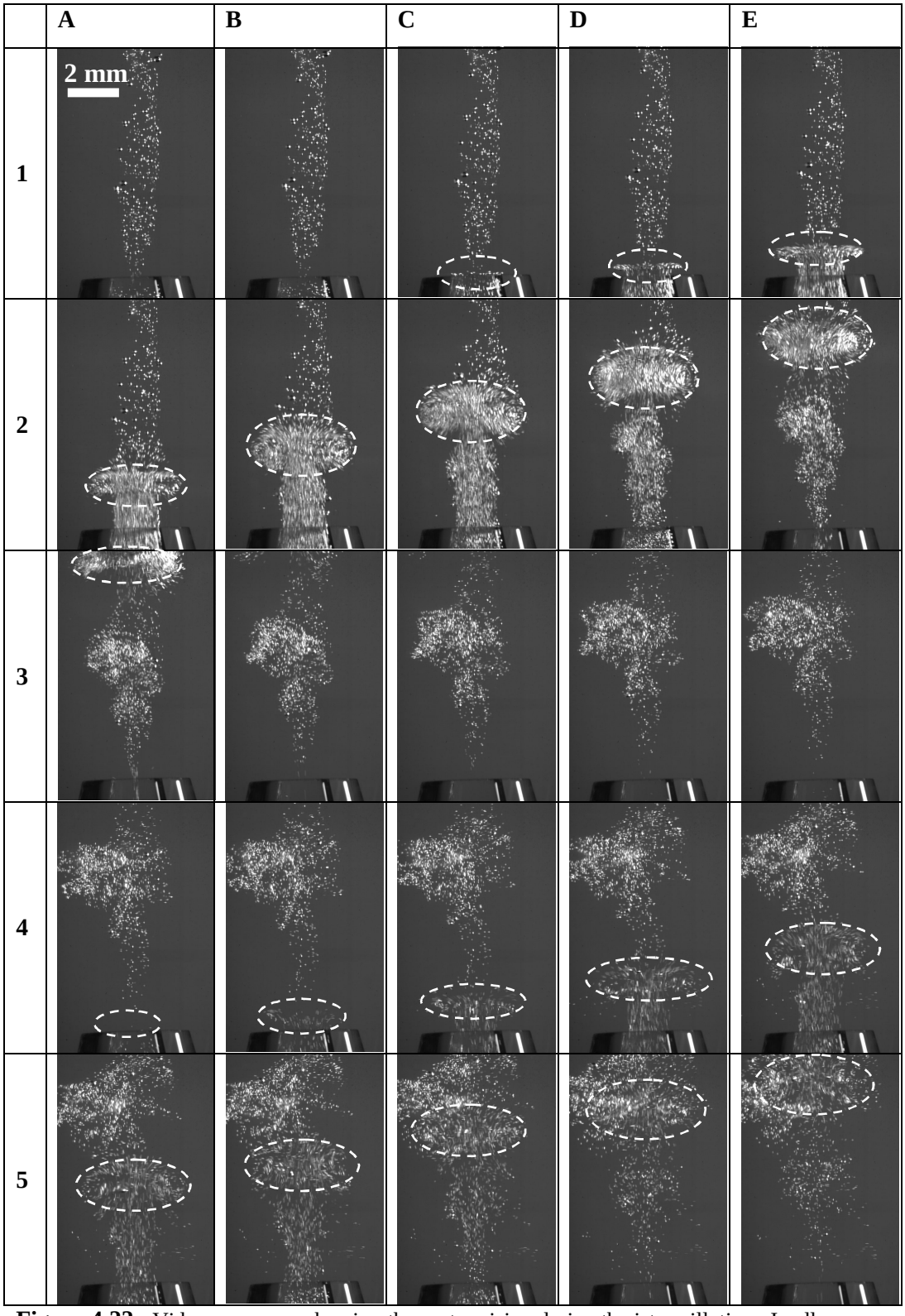

Figure 4.22. Video sequences showing the vortex rising during the jet oscillation. In all cases the capture rate was 2000 f.p.s. The interframe time is 5 ms and the first frame is at t = 0 ms. The frames read left to right (A to F) top to bottom (1-7). The jet was oscillating at 16 Hz.

In order to investigate the reproducibility of the jet system, hydrogen bubble tracer experiments were performed. Figure 4.22 shows the results of these studies. The white annotations on the images are added to illustrate the path of the vortex travelling through the cell. In addition a second cycle of the vortex could be clearly observed in images of figure 4.22 (images A4-E5). This suggests that vortex formation is reproducible between pulses of the jet. The time difference between the two jet pulses measured from these high-speed imaging experiments was 62.5 ms consistent with the 16 Hz oscillating frequency applied to the piston.

In next section the performance of the oscillating jet system will be further tested.

4.3 Modulation of the Jet at High Frequencies

It would be desirable to create an HMV technique what would allow higher frequency modulations to be generated. This is due to a variety of different reasons (e.g. discrimination against the flicker noise, employment of high sweep rates etc.). Therefore it was important to investigate the performance of the oscillating jet set-up at higher frequency modulation conditions. Visualisation of the flow under a variety of different frequencies was achieved with the help of electrochemically generated hydrogen bubbles. Figure 4.23 illustrates the result of this study. In this case the frequency of modulation of the piston was 50 Hz.

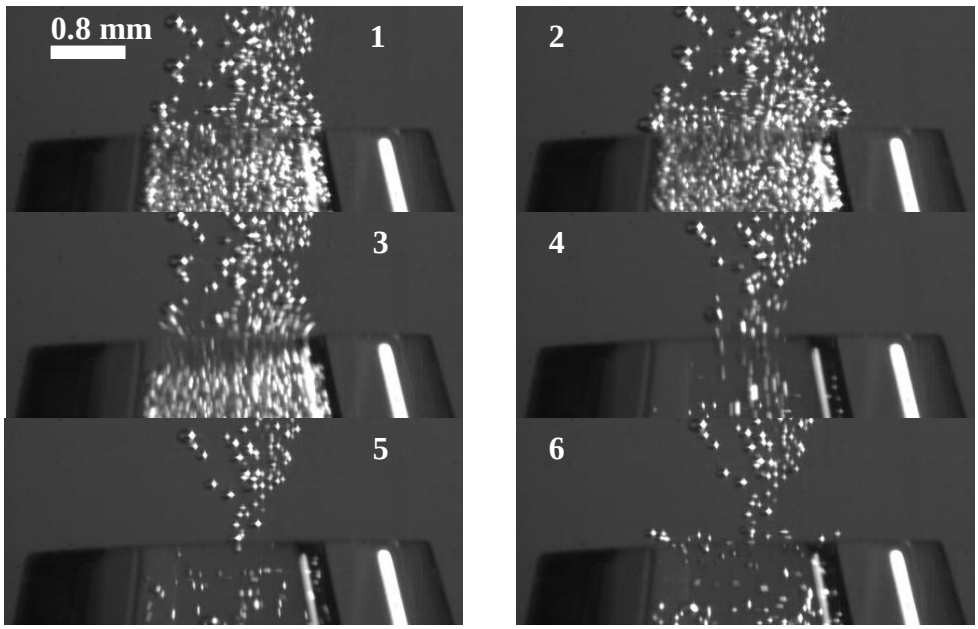

Figure 4.23. Video images showing the flow motion at the exit of the jet as the piston was modulated at 50 Hz. The hydrogen bubbles were used to visualize the flow. The interframe time is 5 ms and the first frame is at t = 0 ms. In all cases the capture rate was 2000 f.p.s.

Figure 4.23 shows that the motion of the liquid at the exit of the jet was insignificant. Vortex formation, which characterised the 16 Hz modulations, was not observed. The possible reason for the behaviour is the inability of the system to accelerate the high volume of the liquid inside the funnel. This may be explained by a simple force argument. For example, in order to move the ~0.150 kg of liquid (the approximate mass of the liquid inside the funnel) with the velocity of 0.86 m s^{-1} and at frequency 16 Hz the force which the shaker should apply to complete the task should be ~0.44 N. For the same conditions but at faster oscillating frequencies (50 Hz) the applied force will increase up to ~4.30 N. The maximum operating force for the shaker is 8.9 N. Therefore the limitations of the equipment won't allow the high frequency modulations. This is clearly one of the disadvantages of the developed technique. However the employment of the more powerful vibrating system could improve the performance of the set-up in the high frequency conditions.

4.4 Summary and Conclusion

In this chapter a visual investigation of the flow produced by the oscillating jet system using a high-speed camera was reported. The performance of the two different jet systems, specifically a membrane and a piston system, were tested. It was demonstrated that the non-ideal motion of the membrane results in disagreement between the measured and predicted displacement of the liquid. The piston cell, in turn, showed excellent performance. The experimental data showed a good agreement between the predicted and calculated values. However, both designs (membrane and piston) produced significant periodic flow rates. Hence both sets of apparatus could be employed in HMV analysis. The investigation of the flow at the exit of the jet revealed its vortex behaviour. These results were compared to the previous studies for oscillating jet systems reported in the literature. The similarities between the systems were clearly seen. The combination of the high-speed camera and electrochemical experiments showed that the vortex rings play a significant role in spatial distribution of the mass transport enhancement observed. The decrease of the current as the electrode moves away from the jet in the XZ direction was explained. In addition a loss in vortex velocity as it travels through the liquid was observed. This in turn was attributed to the entrainment of the fluid from the surroundings resulting in the increase of the size of the rings. The video recordings of the flow with the electrode positioned

above the jet exit showed that the presence of the electrode resulted in the formation of the secondary vortices. Therefore, it was suggested that the size and shape of the electrode surround would be an important factor in the investigations. Further characterisation of the HMV system showed that the fluid motion between the pulses is reproducible. However, the employment of the set-up at high frequencies was unsuccessful.

In the next chapter an application of the HMV technique will be presented. In particular, reduction of molecular oxygen will be studied.

Chapter 5

HMV Study of Oxygen Electroreduction at Nanostructured Pt Electrodes

Chapter three introduced the initial investigation of an oscillating jet as a novel hydrodynamic modulation technique. It was demonstrated how the sensitivity of this system could be improved by increasing the mass transfer to the electrode associated with forced convection of the liquid, produced by the oscillating jet.

In this chapter the electrochemical reduction of molecular oxygen is studied using the oscillating hydrodynamic jet and a variety of different modified electrodes. In particular the signal from this experimental arrangement is analysed using a 'lock-in' approach. The results of this methodology and the corresponding electrochemistry of the electrodes employed are now presented.

5.1 Surface Electrochemistry of Polycrystalline Platinum

The surface electrochemistry of platinum is explored extensively in chapter 1. However, a brief overview is given here to aid the reader. The electrochemistry of Pt in aqueous solution has a number of characteristic features. These include: adsorbed hydrogen H_{ads} and oxygen OH_{ads} layers which are formed and removed electrochemically. A typical cyclic voltammogram showing these processes on polycrystalline Pt in dilute aqueous H_2SO_4 medium is presented in figure 5.1. Figure 5.1, region A shows two pairs of peaks corresponding to UPD adsorption, and desorption of H at two different Pt sites. The two types (strong H_s and weak H_w) adsorbed hydrogen are designated to indicate the relative strengths of adsorption. The anodic current at potentials between +0.15 and +0.75 V *vs.* MMS (region C) corresponds to OH_{ads} and oxide formation on the platinum surface.

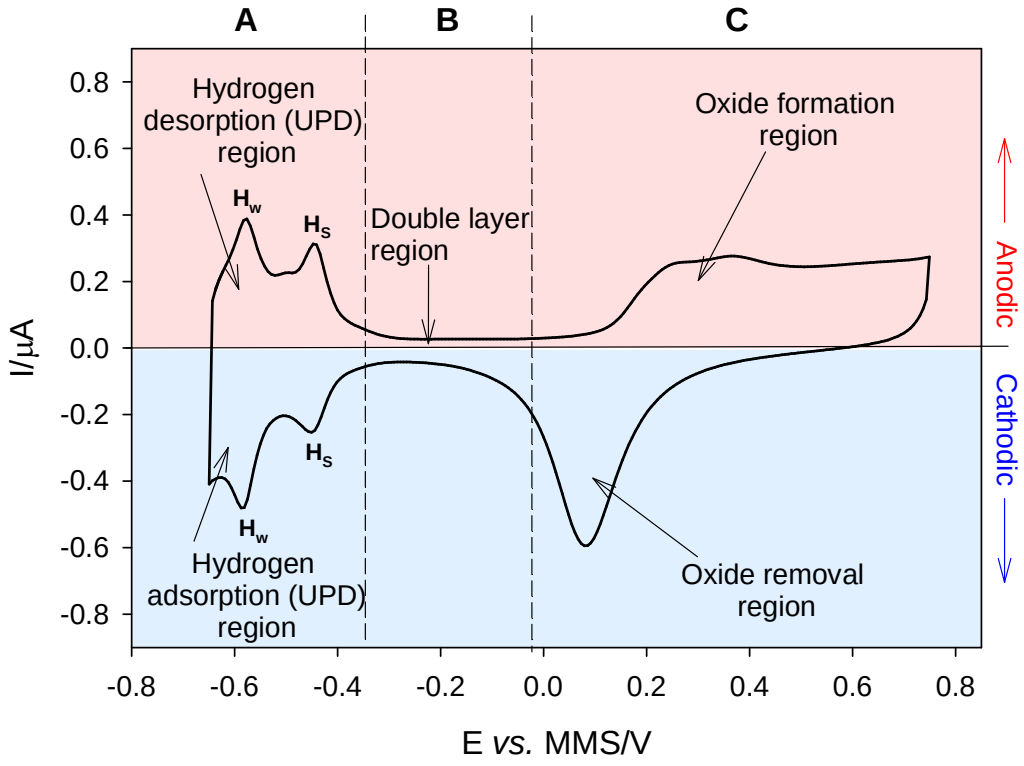

Figure 5.1. Cyclic voltammogram recorded at 500 µm diameter polished Pt electrode in anaerobic 1 mol dm^{-3} sulphuric acid solution. The sweep was performed at 50 mV s^{-1}. The temperature of solution was 18 – 22 °C.

When the potential is reversed, the oxide layer is reduced and a single peak at potential +0.08 V *vs.* MMS, as result of this process, is recorded. In region B between -0.3 and +0.1 V, only a very small current passes, no faradaic electrode reaction is taking place, and the so called "double layer charging" region is observed.

It has been found that the shape of the voltammogram will strongly depend on the type of electrolyte used (*119, 125-127, 205-208*). For example, linear potential sweep voltammograms of polycrystalline platinum electrodes in sulphuric, phosphoric and perchloric acids are presented in figure 5.2. In general, the voltammogram in phosphoric acid is very similar to the one obtained in sulphuric acid. However, the H_{UPD} peaks in phosphoric acid occur at slightly lower potentials (20 mV) compared to the sulphuric acid. The voltammogram in perchloric acid shows significantly different response: the hydrogen region is much broader and extends to more positive potentials, while the oxide region begins at less positive potentials than in sulphuric or phosphoric acid. These differences are attributed to the adsorption of the electrolytes' anions on the platinum surface. The basis for this conclusion was first shown when Clavilier

(*119*) reported the comparative study of the electrochemical hydrogen adsorption/desorption on Pt (111) electrode in sulphuric and perchloric acid solutions. The author showed that the H_{UPD} shifts to the more negative potential and the oxide formation was extensively inhibited in sulphuric acid solution when compared to the perchloric acid response.

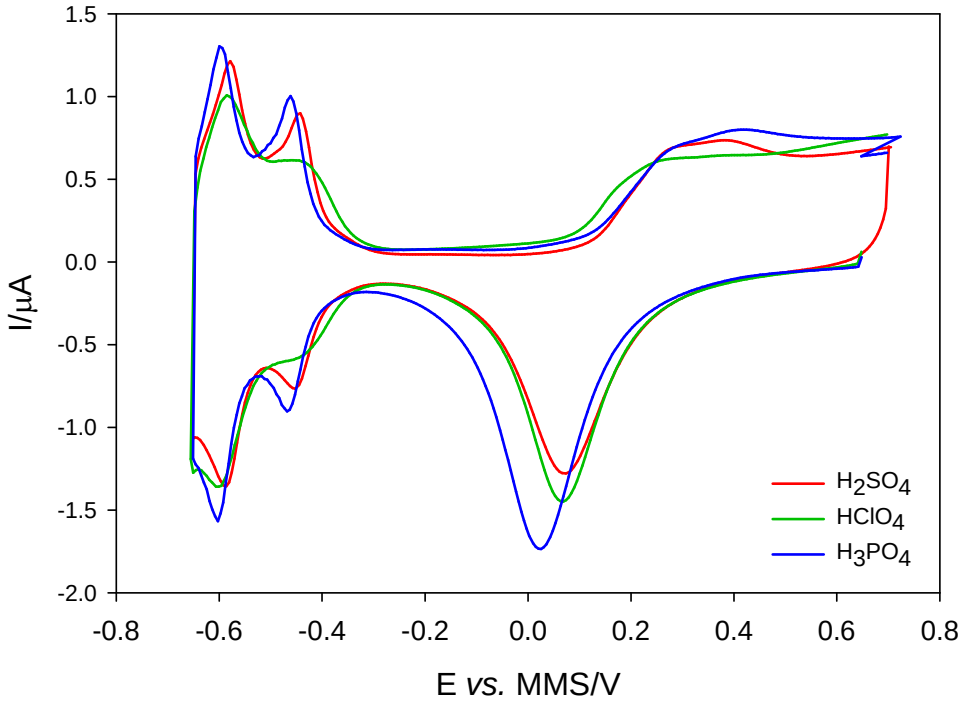

Figure 5.2. Cyclic voltammograms of polished platinum (500 μm diameter) in different media[2]: 1 mol dm^{-3} H_2SO_4 (—), 2 mol dm^{-3} H_3PO_4 (—) and 1 mol dm^{-3} $HClO_4$ (—) at sweep rate of 200 mV s^{-1}. The pH of these solutions was 0. The temperature of solution was 18 – 22 °C.

Figure 5.2 and the literature (*119*, *127*, *206*, *207*) show that the anion adsorption strength decreases in the order:

$$ClO_4^- < HSO_4^- < H_2PO^-$$

Hence a shift of the hydrogen UPD peaks towards more negative potential would be expected through this series (see figure 5.2).

In addition to these acid systems extensive investigation of other ions, and their effect on the voltammetry of Pt in acid, can be found. For example, the effect of Cl^- (widely

[2] Note: the solution concentrations are approximate. The pH of each solution was adjusted to zero by titrating the appropriate concentrated acid into the dilute acid media.

used in electrochemical experiments) has a significant effect. The influence of Cl^- ions on surface hydride and oxide formation on platinum electrode are presented in figures 5.3 and 5.4 respectively.

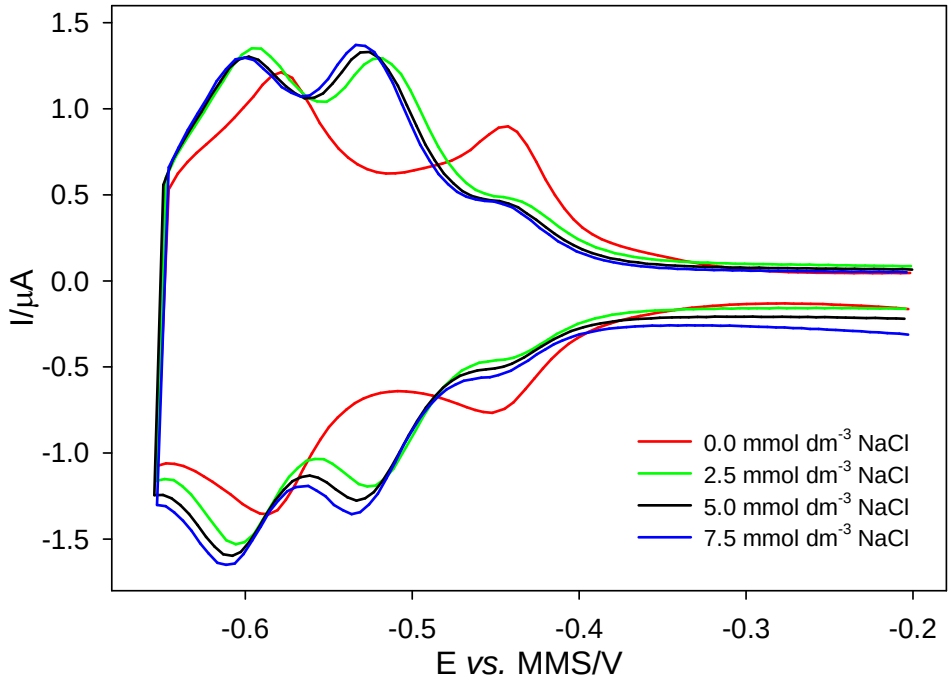

Figure 5.3. Voltammograms of polished 500 μm platinum electrode showing the hydrogen adsorption/desorption process in 1 mol dm^{-3} sulphuric acid solution containing different amount of Cl^- ions: — 0.0, — 2.5, — 5.0 and — 7.5 mmol dm^{-3} of NaCl. Sweep rate 200 mV s^{-1}. The temperature of solution was 18 – 22 °C.

The strong adsorption of Cl^- ions compared to SO_4^{2-} or HSO_4^- ions results in the shifting of the hydrogen adsorption/desorption peaks towards more negative potential. In this case the strongly adsorbed hydrogen is clearly more affected by the Cl^- ion adsorption and a potential shift by 100 mV was recorded over this concentration range compared to the 40 mV for weakly adsorbed hydrogen peak.

Interestingly, Cl^- ion adsorption also influences the oxygen adsorption/desorption process (see figure 5.4). It is to be noted that the presence of the Cl^- deposition of the oxygen species at Pt in sulphuric acid takes place at potentials significantly positive from those observed in pure sulphuric acid.

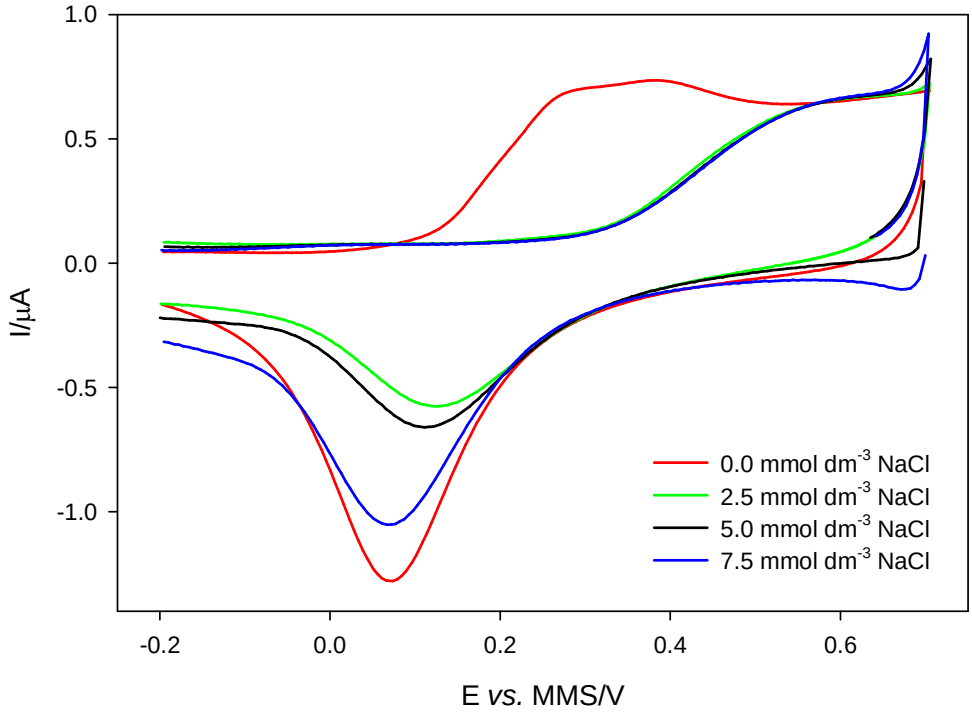

Figure 5.4. Voltammograms of polished 500 μm platinum electrode showing the oxygen adsorption/desorption process in 1 mol dm^{-3} sulphuric acid solution containing different amount of Cl^- ions: — 0.0, — 2.5, — 5.0 and — 7.5 mmol dm^{-3} of NaCl. Sweep rate 50 mV s^{-1}. The temperature of solution was 18 – 22 °C.

The examples above suggest that the nature of the surface processes, and hence the electrochemical response, strongly depends on the adsorbed species on the electrode surface. In turn it was previously reported (*123, 126, 127, 208*) that the type of anions adsorbing on the surface will strongly depend on the potential of the electrode, the electrode material and pH of solution. The detailed information on the investigations is presented in Chapter 1. However, it is not only anion adsorption that affects the experimental signal in this Pt system. The presence of the electroactive species in the solution (e.g., molecular oxygen) will also influence the results obtained. This is the subject of the next section.

5.2 Oxygen Reduction on Polycrystalline Platinum Electrodes

It should be noted that the previous cyclic voltammograms were recorded under anaerobic conditions. However, the electroreduction of molecular oxygen is well known and is indeed of immense technological importance.

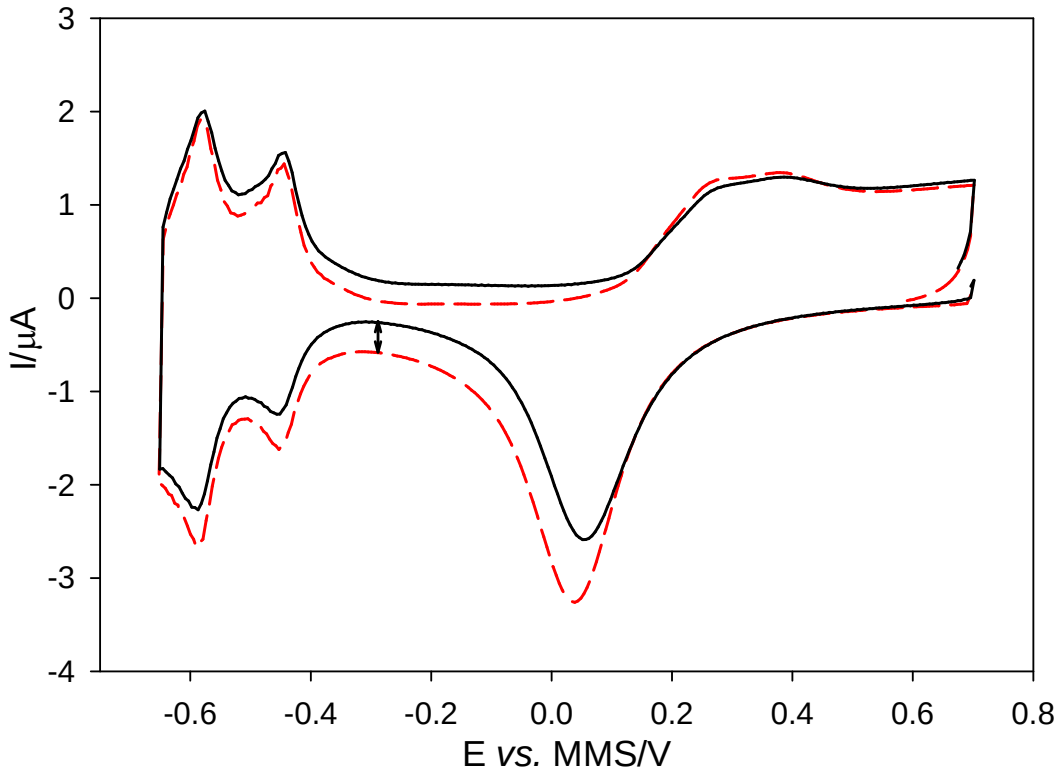

Figure 5.5. Cyclic voltammograms recorded at 500 μm diameter polished Pt electrode in anaerobic (——) and aerobic (– – –) 1 mol dm^{-3} sulphuric acid solution. The sweep was performed at 200 mV s^{-1}. The temperature of solution was 18 – 22 °C.

Hence figure 5.5 shows how the presence of oxygen affects the voltammetry of Pt in H_2SO_4. In this case in addition to these well defined and documented surface processes on polycrystalline platinum, the voltammetry in acid includes a signal from the electroreduction of molecular oxygen. This cathodic offset is depicted as a double headed arrow in figure 5.5. Note, in this case the mass transfer to the electrode surface is attributed to the diffusion only.

However, the inclusion of hydrodynamic stimuli, which results in increased mass transfer due to forced convection, is presented in figure 5.6.

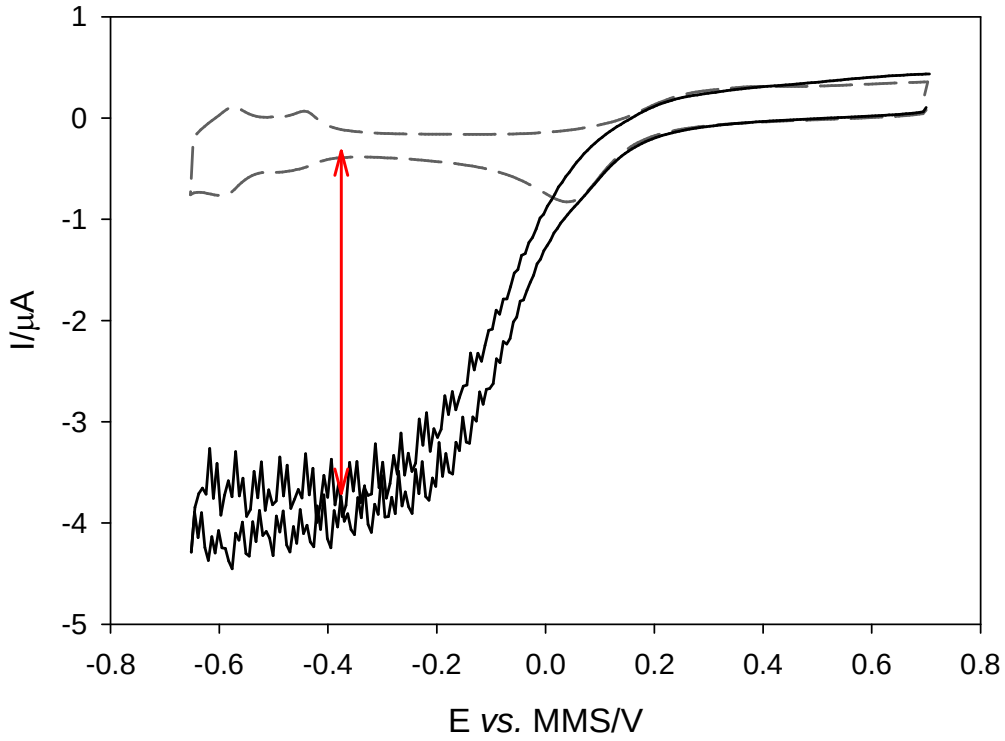

Figure 5.6. Plot showing the cyclic voltammograms recorded at 500 μm diameter polished Pt electrode in aerobic 1 mol dm^{-3} sulphuric acid solution with (——) and without (— —) jet running. The sweep was performed at 50 mV s^{-1}. The oscillating jet was modulated at a frequency of 16 Hz and with piston displacement amplitude (zero to peak) of 0.010 ± 0.001 mm. The temperature of solution was 18 – 22 °C.

Here an oscillating jet (see figure 2.1) was employed. (Note the membrane used in previous experiments (see Chapter 3) was replaced with metal piston to improve performance of the set up.) The vibration of the piston resulted in the large fluid flow at the jet outlet (see chapter 4). In this case an electrode (Pt polished, 500 μm diameter) was positioned 1 mm above the jet's exit. Under these conditions the forced convection produced by the jet's action caused a large enhancement in the mass transport controlled signal recorded at the electrode (see figure 5.6, double headed arrow). Clearly the electroreduction of molecular oxygen occurs below ~ +0.2 V *vs.* MMS. Since surface processes described above are not mass transport controlled, their current will not change with the jet oscillation. Hence, the study of this system is ideally suited to an HMV approach particularly if high surface area electrodes (such as nanostructured) are employed. This HMV approach will be documented in the next section.

5.3 Oxygen Reduction at Nanostructured Platinum Electrodes

The high electrocatalytic activity of nanostructured Pt electrodes has attracted the attention of many researchers (*169-172*). However, it must be recognised that as well as creating electrodes which have highly active catalytic surface, double layer and other surface phenomena are also amplified. These surface components can cause considerable difficulty in the interpretation of results from an experiment investigating a solution phase species. Birkin *et al.* (*172*) reported that when studying ORR on Pt mesoporous modified electrodes in order to suppress the large background signals associated with the rich surface electrochemistry of platinum, it was necessary to cycle the electrodes at very low sweep rates (2 mV s^{-1}). Even though the voltammetry of the mesostructured microelectrode was performed at such sweep rates, distortion in voltammetry was still observed. While it is possible, under some circumstances, to follow the electrochemistry of the target molecules, it is desirable to enable the dynamic range of the experiment to be increased (i.e. the time scale reduced). This must be achieved as well as allowing faradaic electrochemistry of solution species to be studied at potentials where surface electrochemistry could otherwise distort the response. These requirements are satisfied by the employment of an HMV approach.

Employing an oscillating jet as a hydrodynamic modulation method, should therefore make it possible to analyse oxygen reduction on nanostructured materials despite the high background signal characteristic of these electrodes. In order to monitor the electrochemical signal obtained from the pulsating jet apparatus, bespoke software was used to capture the data and extract the amplitude of the HMV signal as a function of electrode potential. This allows the isolation of the faradaic signal from the background processes. The principle of the "lock-in" technique was described in chapter 3. Briefly the first step of this process was to identify the phase angle between the appropriate signals. For this purpose the electrode potential was held at -0.65 V *vs.* MMS. This corresponds to the mass transfer limited region for molecular oxygen reduction (see figure 5.6 for example). The reference and electrochemical signals gathered under these conditions are analysed to find the appropriate phase angle. Results of this analysis are then used to give the maximum (in the case of molecular oxygen reduction, most negative) HMV amplitude. The voltammetry is then recorded and the HMV data extracted. Figure 5.8 shows the voltammograms of molecular oxygen reduction on a 500 μm diameter nanostructured platinum electrode with a

roughness factor (RF) of 42.4 (see chapter 2 for roughness factor calculations) using this approach. The plot includes both averaged (I_{av}, —) and HMV (I_{HMV}, —) signals.

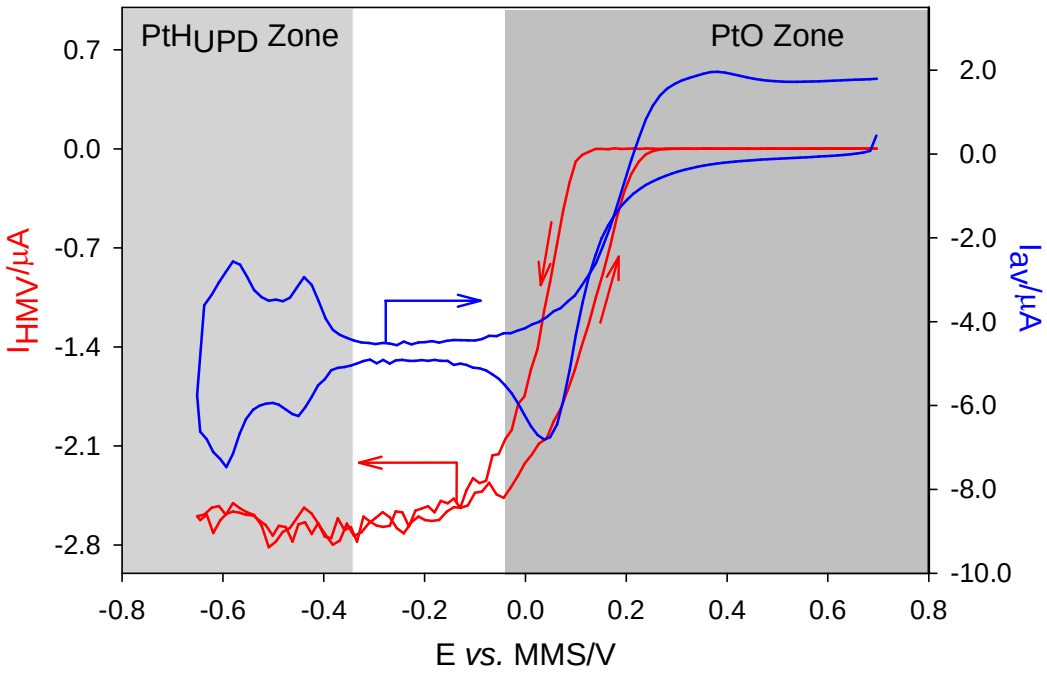

Figure 5.8. Plot showing the HMV signal (I_{HMV}, —) and average current signal (I_{av}, —) as a function of electrode potential recorded at 500 µm diameter nanostructured Pt electrode (RF = 42.4) in aerobic 1 mol dm^{-3} sulphuric acid solution. The sweep was performed at 20 mV s^{-1}. The oscillating jet was modulated at a frequency of 16 Hz and with piston displacement amplitude (zero to peak) of 0.021 ± 0.001 mm. The temperature of solution was 18-22°C.

Note that in this experiment the electrode potential started at +0.7 V *vs.* MMS and was scanned negatively. No I_{HMV} signal was recorded in the region between +0.1 V and +0.7 V *vs.* MMS. This region corresponds to the Pt oxide zone (see figure 5.1) and no redox reactions take place in the region. Therefore the signal recorded within the potential range won't be affected by the convective flow of the liquid. However, from +0.1 V *vs.* MMS oxygen reduction starts and the cathodic increase in current was obtained. The mass transfer limited signal was observed between -0.2 and -0.6 V *vs.* MMS. Scanning the potential forward from this point results in a hysteresis in the molecular oxygen signal. The reason for this behaviour is attributed to the fact that oxide formation and oxide removal processes take place at different potentials. Figure 5.8 also includes the time averaged signal. The interference of the surface processes at the electrode surface clearly makes it more difficult to analyse the oxygen reduction as the potentials for all the processes overlap. This is not the case for the HMV data.

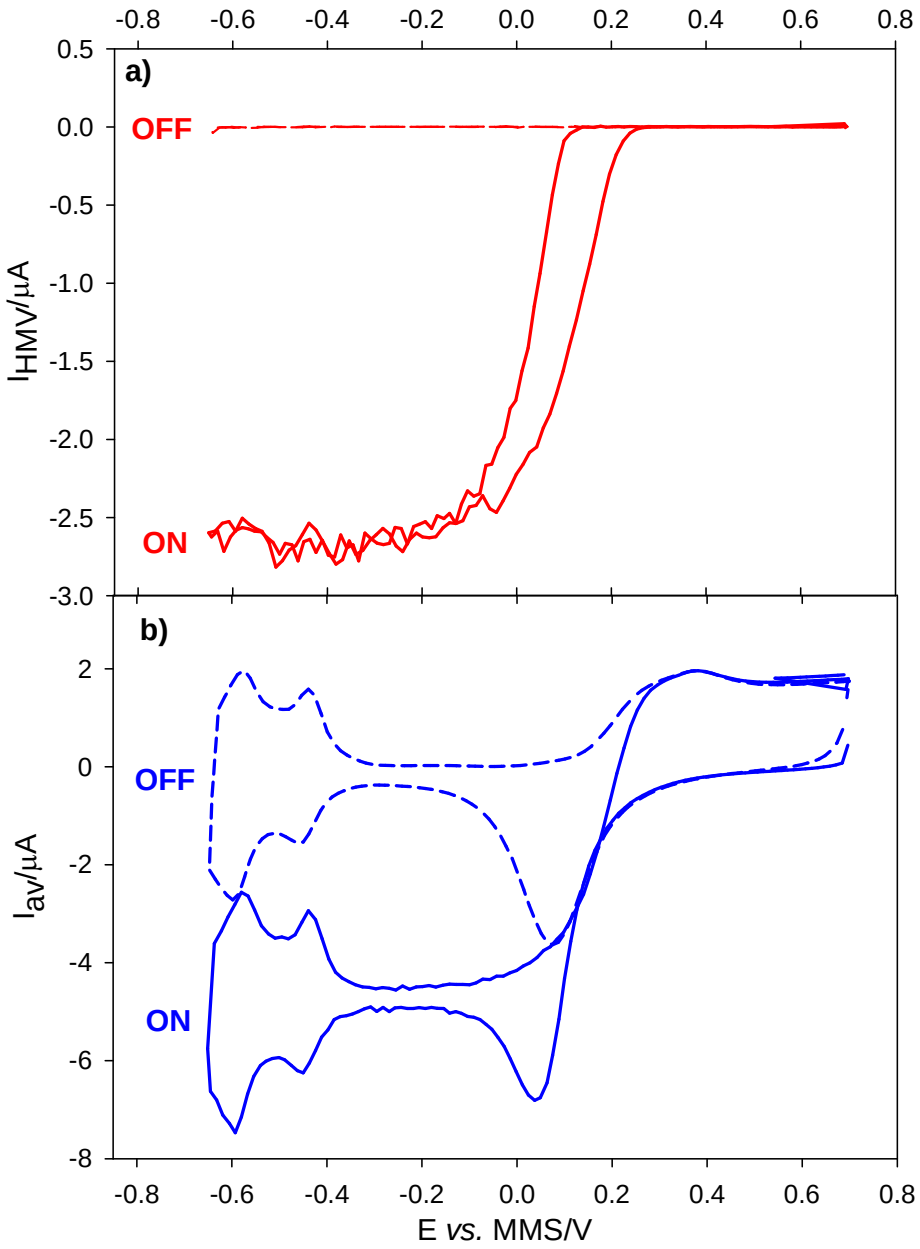

Figure 5.9. Plot showing **a)** the HMV signal with (—) and without (— —) the jet running and **b)** the time-averaged signal with (—) and without (— —) the jet running as a function of electrode potential recorded at 500 µm diameter nanostructured Pt electrode (RF = 42.4) in 1 mol dm^{-3} sulphuric acid solution. The sweep rate was at 20 mV s^{-1}. The jet was modulated at a frequency of 16 Hz with piston zero to peak displacement amplitude of 0.021 ± 0.001 mm. The temperature of solution was 18-22°C.

Figure 5.9a shows that when the oscillating jet was terminated (dashed line), no apparent HMV signal can be observed over the entire potential region. This indicates that the detected signal is the HMV signal and not a parasitic background processes and highlights the clarity of this approach to this problem. This could be compared to the time-averaged signal (see figure 5.9b). In this case, the termination of the jet results in the decrease of mass transfer of molecular oxygen when the surface processes signal

stay unaffected. The electrochemical "interference" from faradaic and non-faradaic signals is clearly avoided.

In order to verify that the signal obtained is molecular oxygen reduction, the concentration of dissolved oxygen was increased to saturation by sparging with oxygen gas. Figure 5.10 shows that after saturating the solution with oxygen, the electrochemical signal (Figure 5.10, ▬ ▬) significantly increased corresponding to the increase of concentration of dissolved oxygen.

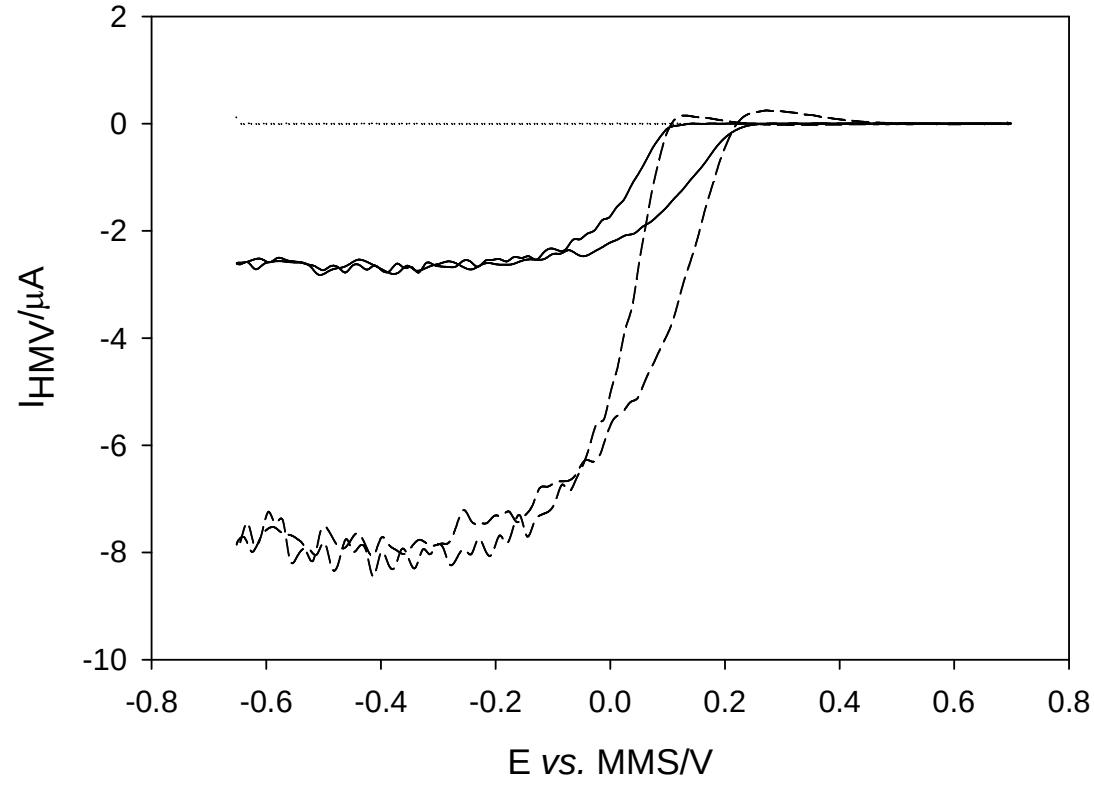

Figure 5.10. The plot showing electrochemical signal recorded at a nanostructured Pt electrode (RF = 42.4, 500 μm diameter) in a 1 mol dm^{-3} sulphuric acid solution using lock-in program at a sweep rate of 20 mV s^{-1}. The solid line (▬▬) showing the hydrodynamic modulation voltammetry before adding oxygen and the medium- dotted line (— —) represents the voltammogram recorded after adding oxygen into solution. The frequency of oscillation was 16 Hz with piston displacement amplitude of 0.021 ± 0.001 mm. The dotted line (**. . . .**) showing an electrochemical signal obtained after adding oxygen and after switching off the oscillating jet. The temperature of solution was 18-22°C.

However, according to the Henry's law (*209*) under the current experimental conditions the concentration of molecular oxygen should increase by a factor of ~4.6. This is significantly bigger than the result of ~3.5 obtained experimentally (*209, 210*). The difference could be attributed to the construction of the cell or incomplete saturation of the solution with molecular oxygen. Note that the dotted line on the graph shows the

electrochemical signal obtained after adding oxygen and after switching off the oscillating jet. The electrochemical signal completely disappears indicating the HMV nature of the recorded signal. The advantages of the employed HMV technique can be clearly seen, the background signal was completely removed and only the mass transport controlled signal was recorded. In order to explore the HMV approach to this problem further oxygen reduction on nanostructured platinum electrodes was studied for a variety of electrode roughness factors. The values chosen are significantly higher than the ~42.4 used here. In the next section the results obtained using the HMV technique for the increased surface area electrodes will be presented.

5.4 Influence of Roughness Factor of Pt Electrodes on Electrochemical Response

Figure 5.11 shows the data obtained for a nanostructured platinum electrode with a roughness factor of 280.8. The HMV response of this electrode to molecular oxygen reduction was found to be broadly similar to the results presented in figure 5.8. However, when scanning below -0.35 V *vs.* MMS an anomalous effect was observed. It was noted that as the electrode enters the hydride region the HMV signal drops by *ca.* 70 % of its maximum value. The hysteresis in molecular oxygen signal was also affected (see figure 5.11 I_{HMV} reverse scan, — —). Interestingly the averaged current signal (I_{av}, —) doesn't show the current drop off observed for HMV data. The current time response of the electrode is illustrated in the inserts in figure 5.11. These show how the amplitude of signal varies at different potentials over the range of interest. There is no AC signal observed at the potential +0.4 V *vs.* MMS (figure 5.11 A) because of absence of any redox processes in the potential region. As the electrode potential progresses negatively, the electrochemical reduction of molecular oxygen is initiated. The amplitude of this signal reaches a maximum and the periodic nature is clearly seen (figure 5.11 B). This occurs at the potential of -0.3 V *vs.* MMS and corresponds to the molecular oxygen reduction at the electrode surface. However, the HMV signal almost disappears as the electrode potential enters the -0.3 V to -0.6 V *vs.* MMS region. This can be seen in figure 5.11 C.

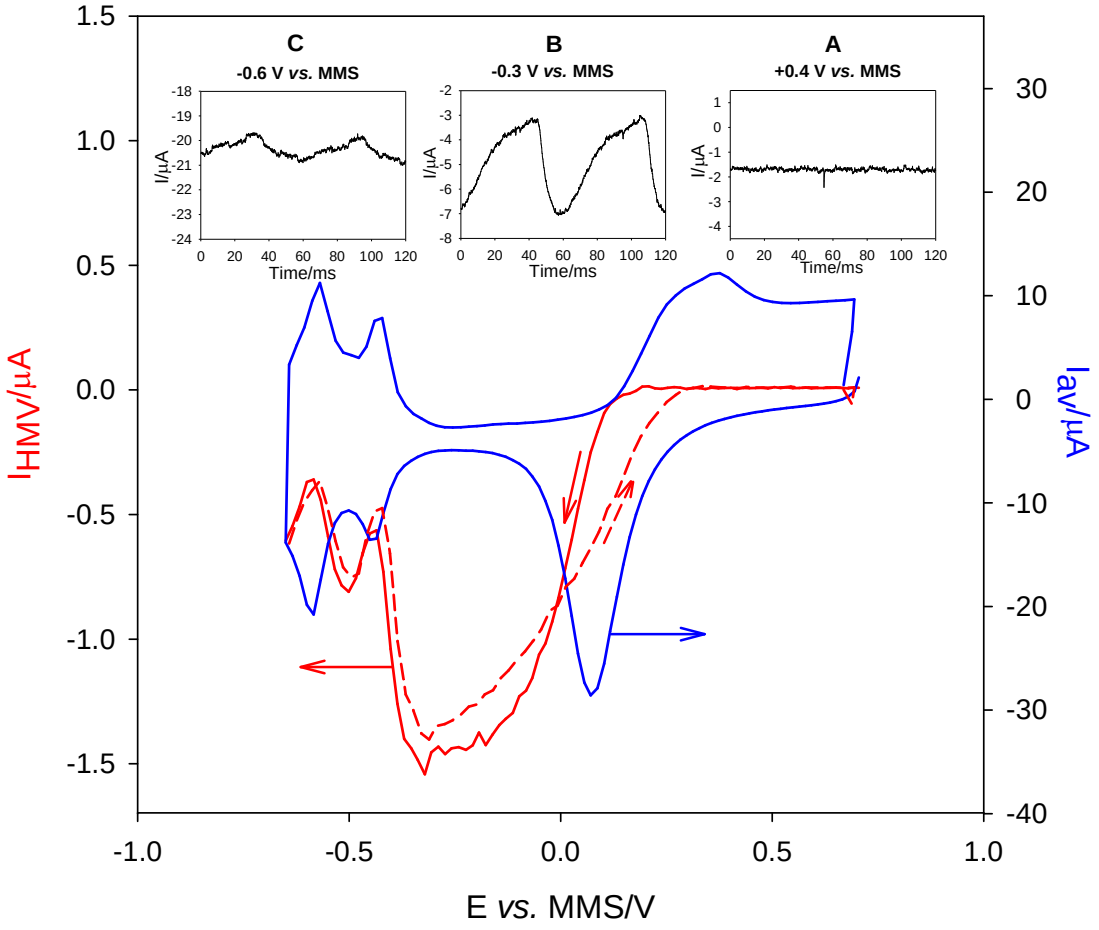

Figure 5.11. Plot showing the HMV signal (forward scan I_{HMV}, ▬; reverse scan I_{HMV} ▬ ▬) and average current signal (I_{av}, ▬) as a function of electrode potential recorded at a 500 μm diameter nanostructured Pt electrode (RF = 280.8) in 1 mol dm^{-3} sulphuric acid solution. The sweep was performed at 20 mV s^{-1}. The jet was modulated at a frequency of 16 Hz and with piston zero to peak displacement amplitude of 0.011 ± 0.001 mm. The inserts in figure show current as a function of time under different potential conditions. The temperature of solution was 18-22°C.

In order to investigate the effect of RF values on the HMV response, a series of Pt electrodes with the same geometric area but different RF values were fabricated (see chapter 2 for details). To take into account differences in electrode position etc. it is convenient to plot the HMV data as normalised to the maximum current response. Figure 5.12 shows such a plot of normalized current (i/i^{c}_{max}) (the HMV current recorded at the electrode divided by the maximum cathodic HMV current) as a function of electrode potential for different roughness factor electrodes. It can be clearly seen that the drop in signal becomes more significant as the roughness factor of the electrode increases. It is interesting to note that the shape of drop follows the shape of the hydrogen adsorption region. This is illustrated as H_w and H_s.

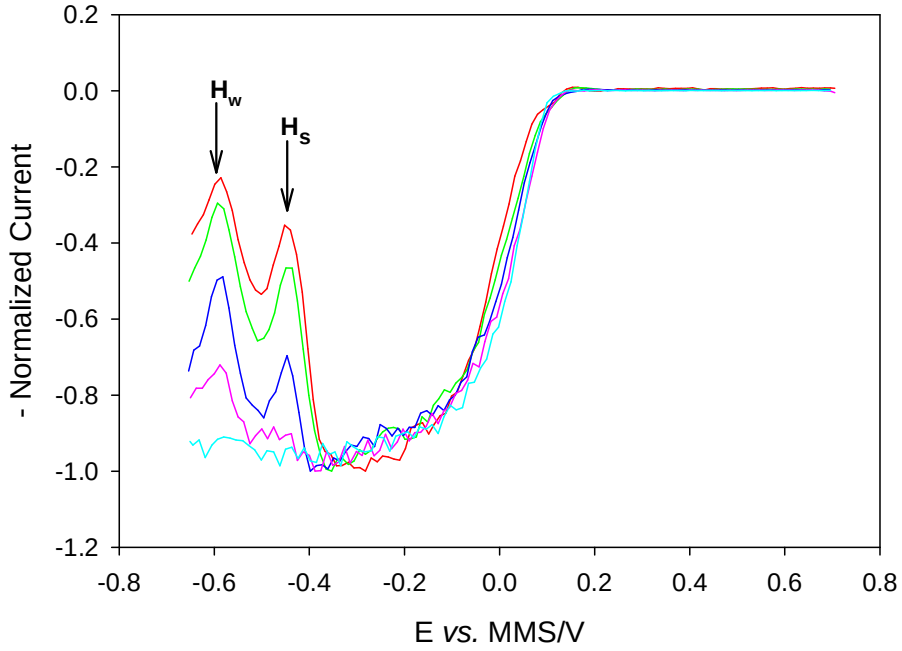

Figure 5.12. Graph of normalised current versus potential recorded at variety of different roughness factor platinum (diameter of 500 µm) electrodes: RF = 42.4 (—); 50.1 (—); 107.9 (—); 213.8 (—); 280.8 (—). The solution used was a 1 mol dm^{-3} sulphuric acid. The sweep was performed at 20 mV s^{-1}. The jet was modulated at frequency of 16 Hz and with piston zero to peak displacement amplitude of 0.011 ± 0.001 mm. The temperature of solution was 18-22°C.

The potentials at which these current fluctuations occur are equivalent to the two peaks formation potentials. This observation will be discussed in Chapter 7.

In order to elucidate the cause of these observations a series of different experiments were performed. These will now be discussed.

5.5 Phase Angle Analysis as Function of Potential in the ORR Analysis

It was observed previously (and described in chapter 3) that the lock-in signal depends on the phase angle between the experimental current and the reference signal. Therefore it was important to investigate whether the decrease in signal described above was caused by a phase change during the experiments. For this purpose bespoke software was developed (Appendix A.2). This software allows analysis of the phase angle for each data point collected. This could then be used to correct the HMV signal. An HMV signal recorded at nanostructured platinum electrode (RF = 280.8) (see figure 5.11) was analysed using the "phase corrected lock-in" software. The result of this

analysis is illustrated in figure 5.13. In the region between +0.7 V and +0.1 V *vs.* MMS, no mass transport controlled signal could be observed (figure 5.13, section A). This explains the apparent 'noise' in the phase angle calculated within this potential range. This was followed by a stable reproducible region between +0.1 V and -0.3 V *vs.* MMS (figure 5.13, section B) where the oxygen reduction takes place. Interestingly there is a slight change in the phase angle in the region above -0.3 V *vs.* MMS (figure 5.13, section C).

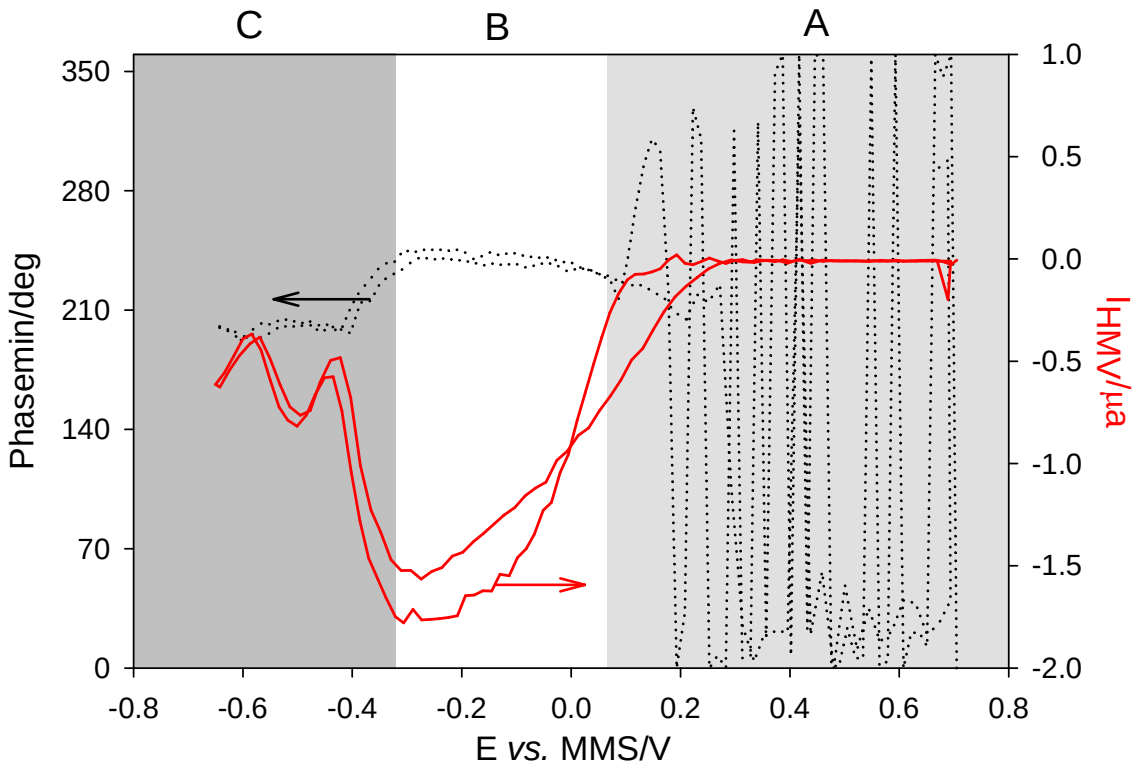

Figure 5.13. Plot showing phase angle (▪▪▪) and phase corrected I_{HMV} (—) as a function of electrode potential calculated for lock-in signal (see figure 5.11) recorded at 500 µm diameter nanostructured platinum electrode in 1 mol dm^{-3} sulphuric acid solution. The sweep was performed at 20 mV s^{-1}. The jet was modulated at frequency of 16 Hz and with piston displacement amplitude of 0.011 ± 0.001 mm.

However, the variation in the phase angle over the complete sweep is relatively small (~ 35°). Figure 5.14 illustrates this as the result of subtracting the original HMV signal from the dynamic phase corrected lock-in signal. Clearly figure 5.14 shows that the phase corrected signal has little or no effect on the H region. Indeed only the +0.1 to -0.3 V region is affected. However, it should be noted that -0.65 V *vs.* MMS is the potential at which the original phase angle was determined.

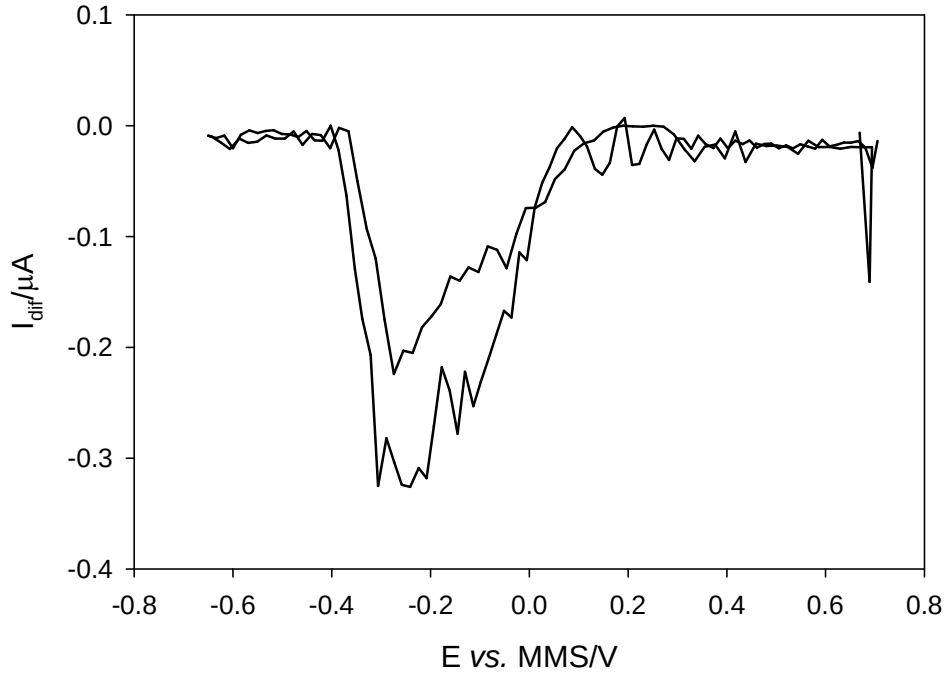

Figure 5.14. Plot showing I_{dif} ($I_{original}$ - $I_{phase\ corrected}$) as a function of potential recorded at 500 μm diameter nanostructured platinum electrode (RF = 280.8) in 1 mol dm^{-3} sulphuric acid solution. The sweep was performed at 20 mV s^{-1}. The jet was modulated at frequency of 16 Hz and with piston displacement amplitude 0.011 ± 0.001 mm.

The data analysis shown and presented in figures 5.13 and 5.14 suggests that the decrease in signal in the hydrogen adsorption/desorption region was not caused by a phase change. Another possible effect is a pH change near the electrode surface. These are known to occur at Pt surface particularly if high sweep rates are employed (*211-215*). This effect was subsequently investigated, and the results will now be discussed.

5.6 pH Effect on Electrochemical Response

The pH changes in the vicinity of a platinum electrode surface have been studied extensively. Pletcher and Sotiropoulos (*214*) studied the influence of mass transport on the voltammetric response of Pt and proposed a proton concentration change close to a Pt surface. Franaszczuk and Sobkowski (*215*) found that the higher the roughness factor of the Pt electrodes the more the shape of the voltammograms in unbuffered solution differ from the shape of "regular" voltammetric curves for acid solution. These authors proposed that differences were due to a local pH change during voltammetry. Yang and Denuault (*211-213*) used scanning electrochemical microscopy (SECM) to probe the pH changes near the electrode surface while cycling

the potential of the substrate. The results showed that a transient pH decrease as high as 2.3 pH units exists during hydrogen desorption while a pH increase occurs during hydrogen adsorption. All these studies suggest that pH swings at Pt are possible. However, it is unclear whether they occur at nanostructured Pt under the conditions employed.

There are at least three points of interest when considering the voltammetric behaviour of Pt surfaces as a function of pH. First, how does the sweep rate (and hence current density) affect the local pH? Second, how does mass transfer to/from the electrode instigate pH effects? Finally, how does the buffering capacity influence the changes driven by the electrochemical reductions? In order to answer these questions a series of experiments were performed within the HMV test rig. The findings of these experiments are now detailed.

In these studies a different concentration phosphate buffer (at pH 7.0) were used in an attempt to keep the pH of the solution close to the electrode the same during voltammetry. Nernstian equilibrium suggests that the potential for hydrogen adsorption/desorption and oxide formation/reduction peaks should shift 420 mV negatively when the solution pH is changed from 0 to 7. Table 5.1 shows peak potentials determined from voltammetric experiments recorded at a nanostructured Pt electrode (500 μm diameter, RF = 280.8) in ~2 mol dm^{-3} phosphoric acid (pH 0.0). While the expected peak potentials at pH 7.0 are presented in Table 5.2.

pH	**E_p/V *vs.* MMS**			
	H adsorption (s, w)	**H desorption (w, s)**	**Oxide formation**	**Oxide Reduction**
0	-0.45, -0.60	-0.60, -0.45	+0.40	+0.05

Table 5.1. Peak potentials for surface processes on nanostructured Pt at pH 0.0 (~2 mol dm^{-3} H_3PO_4)

pH	**E_p/V *vs.* MMS**			
	H adsorption	**H desorption**	**Oxide formation**	**Oxide Reduction**
7	-0.87, -1.02	-1.02, -0.87	-0.02	-0.37

Table 5.2. Expected peak potentials for surface processes on nanostructured Pt at pH 7.0 for the H_3PO_4

Considering the effect of sweep rate and mass transfer phenomena first, figures 5.15 and 5.16 (black line) show cyclic voltammograms recorded at a nanostructured platinum electrode in 0.1 mol dm^{-3} phosphate buffer (pH 7), with and without jet running, at a potential scan rate of 20 mV s^{-1} and 5 mV s^{-1} respectively. The peak potentials determined from the experimental data are also reported in Table 5.3.

Consider the voltammetry recorded at 20 mV s^{-1} first (see figure 5.15). The cathodic peak at -0.35 V *vs.* MMS (labelled O) corresponds to oxide removal peak at pH 7 and is in agreement with theoretical data presented in Table 5.2. However, there is a second peak (labelled O') which appears at a potential of -0.70 V *vs.* MMS particularly for the voltammetry in the absence of forced convection. It can clearly be seen that the hydrogen adsorption and desorption peaks are now well separated. The hydride formation is taking place at potential below -0.90 V *vs.* MMS. The formation of the first peak only could be seen as the rest of the peaks are outside the experimentally chosen potential limits.

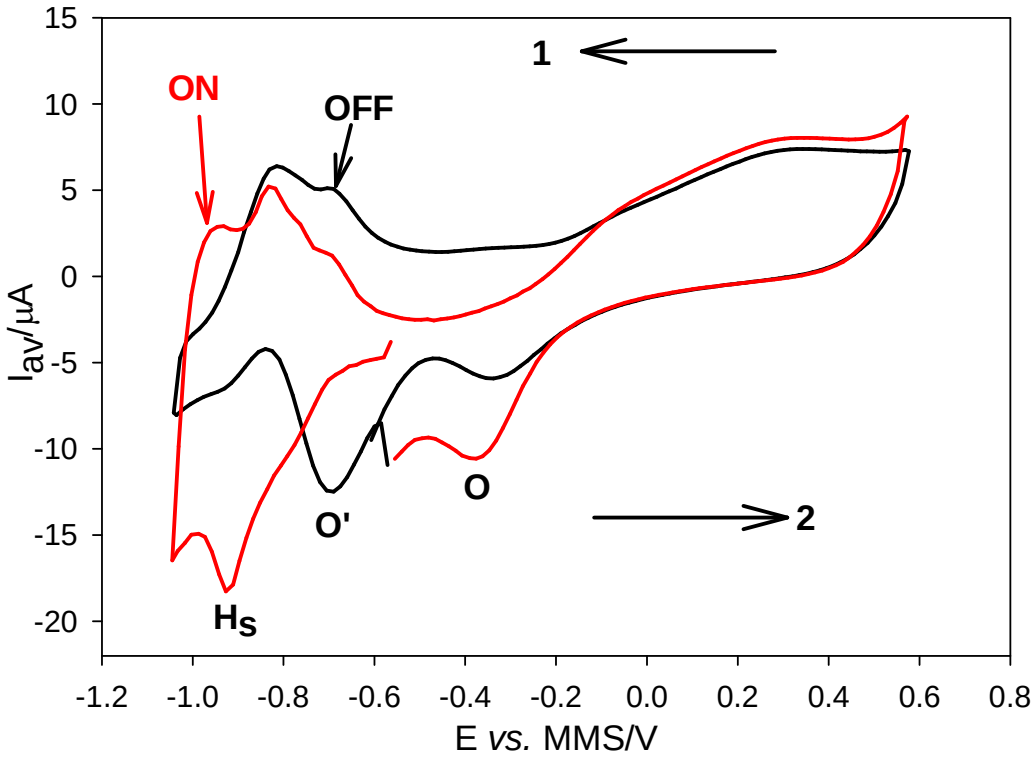

Figure 5.15. Cyclic voltammograms recorded at a nanostructured Pt electrode (RF = 280.8, 500 μm diameter) with (I_{av}, —) and without (I_{av}, —) jet running at sweep rates of 20 mV s^{-1}. The solution used was 0.1 mol dm^{-3} phosphate buffer at pH 7. The jet was modulated at 16 Hz and with piston displacement amplitude 0.010 ± 0.001 mm. Arrow 1 indicates the forward scan and 2- backwards scan. The temperature of solution was 20 – 25 °C.

Experimental conditions	E_p/V *vs.* MMS			
	H adsorption (H_s, H_w)	**H desorption (H_w, H_s)**	**Oxide formation**	**Oxide Reduction (O', O)**
0.1 M buffer, 20 mV s^{-1}, jet OFF	-0.94, ?[3]	-0.82, -0.70	+0.35	-0.35, -0.70
0.1 M buffer, 5 mV s^{-1}, jet OFF	-0.78, -0.90	-0.84, -0.71	+0.2	-0.33, -0.62
0.1 M buffer, 20 mV s^{-1}, jet ON	-0.80, -0.92	-0.84, -0.68	+0.32	-0.38
0.1 M buffer, 5 mV s^{-1}, jet ON	-0.76, -0.89	-0.85, -0.72	+0.2	-0.37

Table 5.3. Peak potentials for surface processes on nanostructured Pt in 0.1 mol dm^{-3} buffer at different experimental conditions

The expected potentials for hydride desorption peaks are around -1.00 V and -0.85 V *vs.* MMS. However, the experimental data presented in Table 5.3 shows that the peaks appear at higher -0.70 V and -0.82 V *vs.* MMS potentials. All these observations indicate a pH shift near the electrode surface during the voltammetric experiments. It suggests that as the electrochemical reactions involving H^+ proceed the buffer capacitance becomes exhausted and the local pH of the solution changes. This can be interpreted as a local pH changes in the mesoporous structure leading to relatively large pH swings. It is possible to estimate the pH swing resulting from the PtO stripping process. If we consider the -0.35 to -0.70 V change and the following electrochemical reaction

$$PtO + 2H^+ + 2e^- \rightarrow Pt + H_2O$$

one would expect the pH at the electrode to increase by ~6 pH units during the stripping process under the conditions employed. Considering these observations one is hardly surprised that the hydride region is similarly affected. Clearly the PtH_s adsorption potential would be estimated at -0.81 V a value close to that observed in the voltammetry (see figure 5.15 and table 5.3, H_s). The Pt H_w would occur outside the

[3] The formation of the second peak takes place at potentials outside the experimental potential region.

voltammetric window. These pH swings (to pH 13) are extreme (note a high roughness factor was deployed here) but can be mitigated by mass transfer enhancement.

Figure 5.15 (—) shows that in the presence of the forced convection the voltammetric response changes dramatically. In particular the oxide stripping and hydride regions become more defined (and indeed more reminiscent of "typical" polycrystalline Pt electrochemistry). This is understandable as the convective flow of the liquid will continuously refresh the solution close to the electrode surface. With increasing of mass-transport the protons and hydroxide ions will leave the surface more rapidly and there will be a smaller pH change within the layer adjacent to the surface.

It is possible to demonstrate that the voltammetric induced pH swings are also sweep rate dependant (as expected). Keeping all other conditions the same, the voltammogram changes greatly (figure 5.16) when the scan rate is decreased to 5 mV s^{-1}. At low scan rates pH changes are minimised by buffer/H^+ transport towards or away from the electrode before the start of the next surface reaction and there will be a smaller pH change within the layer adjacent to the surface.

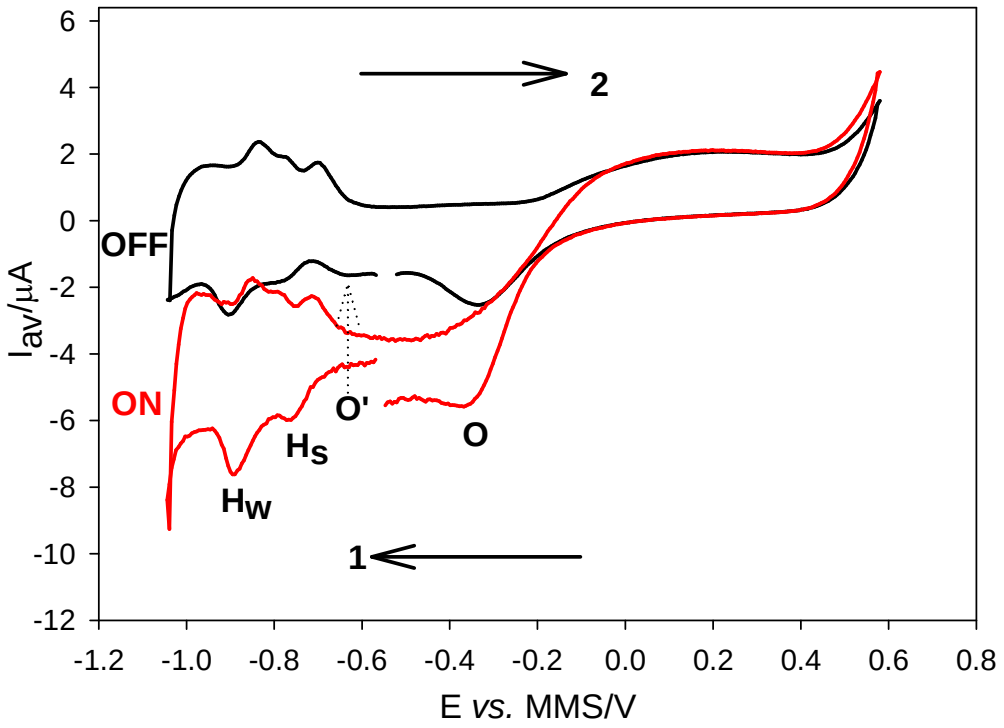

Figure 5.16. Cyclic voltammograms recorded at a nanostructured Pt electrode (RF = 280.8, 500 µm diameter) with (I_{av}, —) and without (I_{av}, —) jet running at sweep rates of 5 mV s^{-1}. The solution used was 0.1 mol dm^{-3} phosphate buffer at pH 7. The jet was modulated at 16 Hz and with piston displacement amplitude 0.010 ± 0.001 mm. Arrow 1 indicates the forward scan and 2- backwards scan. The temperature of solution was 20 – 25 °C.

In stagnant solution and at sweep rate of 5 mV s^{-1} the O' peak at -0.7 V *vs.* MMS significantly decreases. In addition, the sharpness of the hydrogen adsorption-desorption peaks increases compared to those recorded at 20 mV s^{-1}. However, the peak separation (for adsorption/desorption) is of the order of 70 mV (Table 5.3) suggesting that the pH effect has not been completely removed. The voltammetry was improved when the jet was modulated and the peak separation decreased to 40 mV.

The observations listed are limited to the time averaged signal. However, it is interesting to note the effect of local pH in the HMV analysis mode. Figure 5.17 shows the HMV signal as a function of electrode potential recorded using the lock-in approach. The red line (—) corresponds to the current recorded at potential sweep rate of 20 mV s^{-1} and black (—) 5 mV s^{-1}.

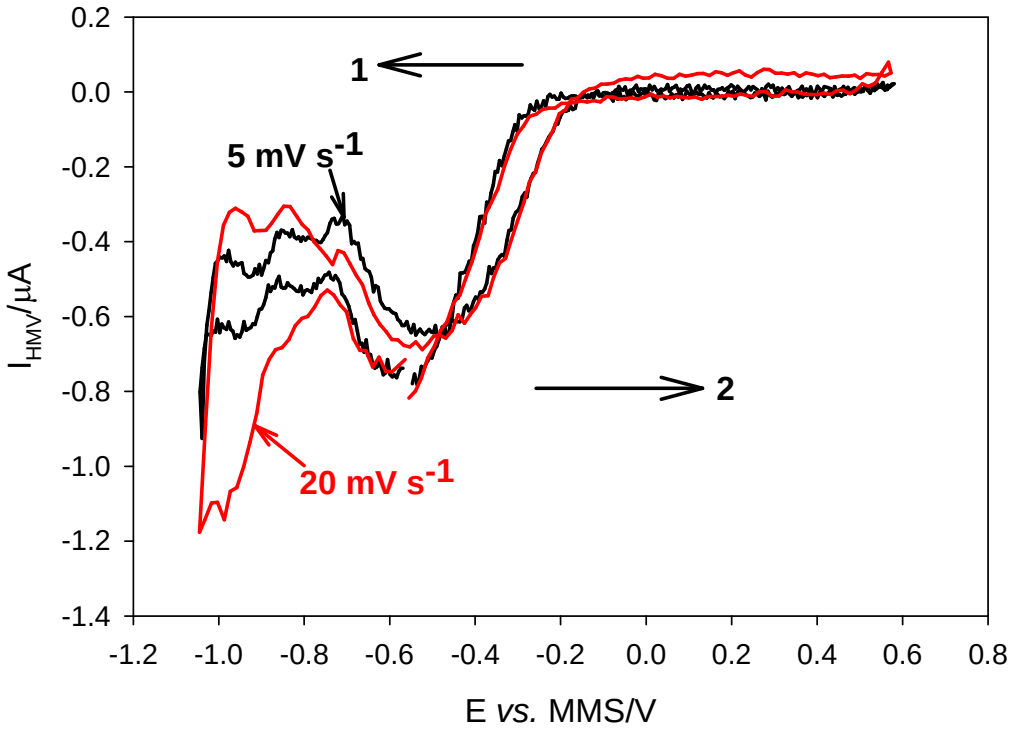

Figure 5.17. Graph represents the hydrodynamic modulation voltammetry recorded using lock-in approach nanostructured at a Pt electrode (RF = 280.8, 500 μm diameter) with sweep rates of 20 mV s^{-1} (I_{HMV}, —) and 5 mV s^{-1} (I_{HMV}, —). The solution used was 0.1 mol dm^{-3} phosphate buffer at pH 7. The jet was modulated at 16 Hz and with piston displacement amplitude 0.010 ± 0.001 mm. Arrow 1 indicates the forward scan and 2- backwards scan. The temperature of solution was 20 – 25 °C.

The higher scan rate voltammogram shows much bigger distortion in both oxide and hydride region compared to the lower scan rate voltammogram. The current drop at potential below -0.6 V *vs.* MMS is still observed at both sweep rates. However, the

distortion in the HMV signal in the potential region between -0.7 V and -1.05 V *vs.* MMS is more significant at 20 mV s^{-1}.

The aim of this experiment was to see if the drop off in current in the hydride region recorded at high roughness factor nanostructured platinum electrodes was caused by the change of the pH in vicinity of the electrode surface. Several conclusions could be made as a result of these investigations. First, the buffer capacitance was not high enough (particularly in the absence of flow) to keep the pH unchangeable near the electrode surface. Second, the pH change clearly affects the electrochemical response in the hydride and oxide regions. Third, the employment of low scan rates and increased mass transport will decrease the pH effect. However, the HMV signal still generally shows a decrease in current in the hydride region, particularly where pH effects are minimised.

In further experiments, in attempts to completely remove/minimise the pH distortion effect, the concentration of phosphate buffer was increased from 0.1 mol dm^{-3} to 1 mol dm^{-3}. However, while moving between electrolyte solutions, it should be noted that this change will also induce corresponding alteration in the solution properties. In particular the viscosity of the solution will change. This parameter is important as the Stokes-Einstein relationship (eq. 5.1) implies that the diffusion coefficient (*D*) will be affected (*209*).

$$D = \frac{kT}{6\pi a \eta} \tag{5.1}$$

Here η represents the solution viscosity and a the hydrodynamic radius. A falling sphere viscometer was used to analyse this parameter. The result of this analysis showed that the viscosities of the 0.1 mol dm^{-3} and 1 mol dm^{-3} solutions are 0.925 cP and 1.663 cP respectively. Assuming that the hydrodynamic radius is not significantly affected one would expect a considerable change in the diffusion coefficient of a species in solution. Figure 5.18 shows voltammograms of ferricyanide reduction in different concentrations of buffer electrolyte. These voltammograms illustrate that the limiting current for the redox couple strongly depends on the concentration of the phosphate buffer as expected. In the 1 mol dm^{-3} phosphate buffer solution the current value is almost half than observed in 0.1 mol dm^{-3} solution. Interestingly the plateau is less defined for the 0.1 mol dm^{-3} electrolyte. However, Pletcher *et al.* have reported that the kinetics of this particular redox system are heavily dependant on the ionic strength of the solution (*189*). Nevertheless these observations indicate that the oxygen

mass transport will be affected by the change in the solution composition. This fact should be taken into account when using the high concentration buffer solutions.

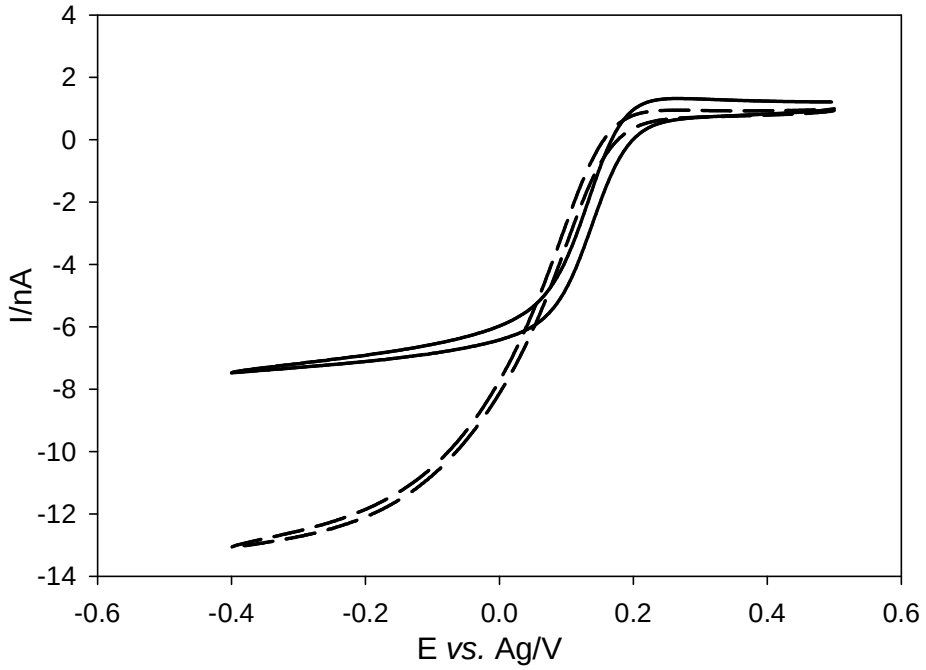

Figure 5.18. Cyclic voltammograms recorded at an Au disc electrode (diameter 25 μm) in an anaerobic 0.1 mol dm^{-3} (— —) and 1 mol dm^{-3} (——) phosphate buffer (pH 7) containing 5 mmol dm^{-3} $[Fe(CN)_6]^{3-}$ at sweep rate of 20 mV s^{-1}. The temperature of solution was 20 – 25 °C.

Figure 5.19 illustrates the cyclic voltammograms recorded at the nanostructured Pt electrode in the 1 mol dm^{-3} buffer solution at different sweep rates and mass transfer regime. The summary of the experiments is also presented in the Table 5.4. A clear improvement in the electrochemical response compared to the results obtained in the 0.1 mol dm^{-3} concentration buffer can be seen. For example at 20 mV s^{-1} and in the stagnant solution (figure 5.19a, —) the cyclic voltammogram of the nanostructured Pt electrode is well defined. In this case hydrogen adsorption/desorption peaks are sharp, occur approximately at the same potential and can be clearly identified. In addition the oxide formation region is more pronounced and arises at more negative potentials. Lastly the beginning of the oxygen evolution process can be observed at +0.6 v *vs.* MMS. The results obtained at 5 mV s^{-1} (see figure 5.19b, —) were similar indicating that the voltammetry was largely sweep rate independent. In the previous experiments, in a lower capacity electrolyte, mass transfer enhancement (due to forced convection

induced by the operation of the pulsating jet) improved (or reduced) the local pH distortion as a result of the electrode processes.

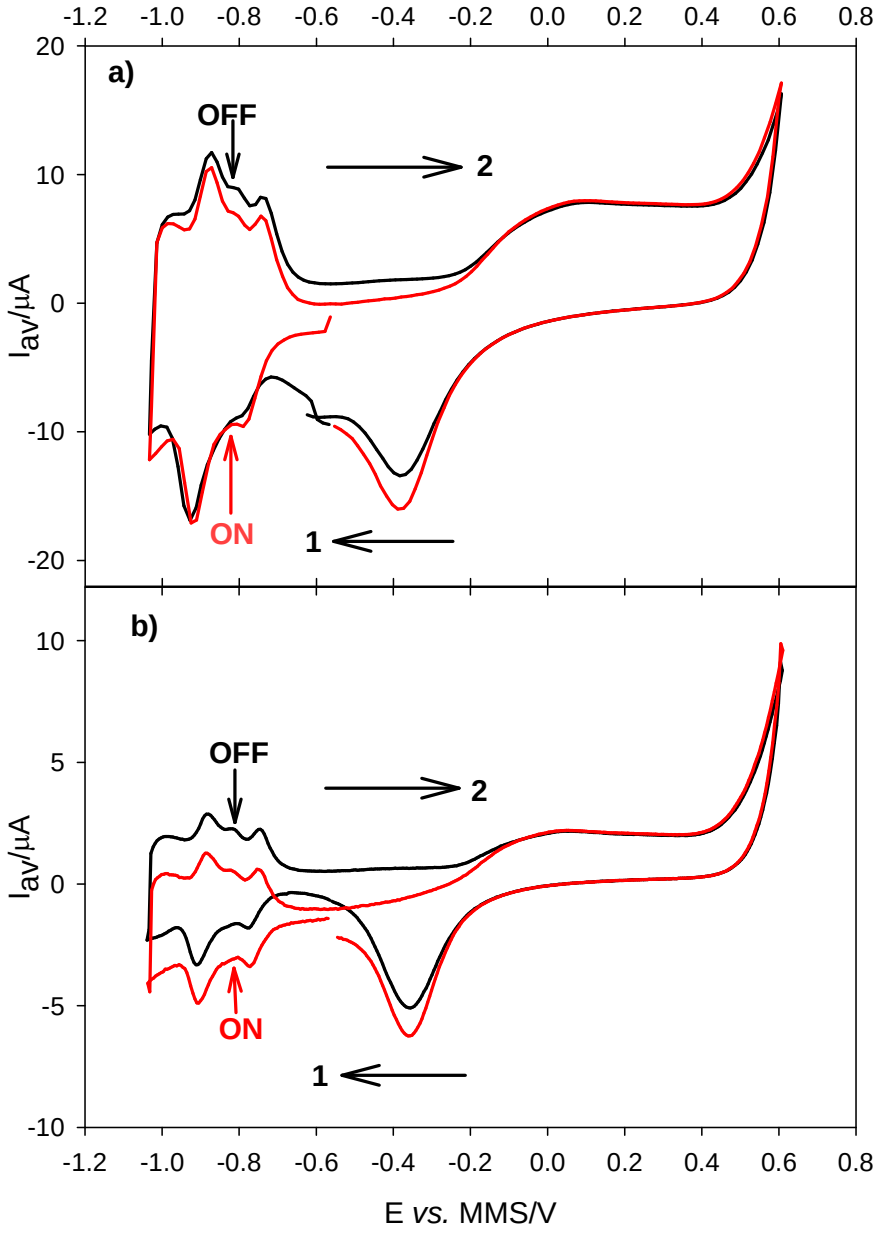

Figure 5.19. Cyclic voltammograms recorded at a nanostructured Pt electrode (RF = 280.8, 500 μm diameter) with (I_{av}, —) and without (I_{av}, —) jet running at sweep rates of **a)** 20 mV s^{-1} and **b)** 5 mV s^{-1}. The solution used was 1 mol dm^{-3} phosphate buffer at pH 7. The jet was modulated at 16 Hz and with piston displacement amplitude 0.010 ± 0.001 mm. Arrow 1 indicates the forward scan and 2- backwards scan. The temperature of solution was 20 – 25 °C.

In the 1 mol dm^{-3} phosphate buffer solutions, when the jet was modulated (see figure 5.19, —), there were no significant changes observed for the surface processes and only an increase in the mass transfer dependent current as a result of the oxygen reduction

process was observed. This is expected as mass transfer enhancement would minimise pH changes as a result of the electrode reactions.

Experimental conditions	**E_p/V *vs.* MMS**			
	H adsorption	**H desorption**	**Oxide formation**	**Oxide Reduction**
1 M buffer, 20 mV s^{-1}, jet OFF	-0.80, -0.92	-0.88, -0.75	+0.01	-0.37
1 M buffer, 5 mV s^{-1}, jet OFF	-0.77, -0.90	-0.88, -0.75	-0.04	-0.36
1 M buffer, 20 mV s^{-1}, jet ON	-0.79, -0.92	-0.88, -0.75	+0.01	-0.37
1 M buffer, 5 mV s^{-1}, jet ON	-0.77, -0.90	-0.88, -0.75	-0.04	-0.36

Table 5.4. Peak potentials for surface processes on nanostructured Pt in 1 mol dm^{-3} buffer at different experimental conditions

Hence as the stagnant experiments demonstrated little perturbations of the voltammetry, it is expected that mass transfer effects should be minimal.

Figure 5.20 illustrates the HMV signal for 0.5 mm diameter nanostructured platinum (RF=280.8) electrode in 1 mol dm^{-3} phosphate buffer at two different scan rates. The voltammogram at 20 mV s^{-1} is clearly more distorted in the hydride region compared to the 5 mV s^{-1} case. This suggests that there is still a slight pH contribution to the electrochemical signal at higher scan rate. However, both plots show similar characteristics: an increase in current below -0.2 V *vs.* MMS as result of molecular oxygen reduction followed by signal drop off below -0.6 V *vs.* MMS. While there are differences in the HMV response it appears that if pH effects are eliminated, a drop off in the signal is still observed. This is supported by direct comparison to the data shown in 1 mol dm^{-3} sulphuric acid (see figure 5.11). In this case the time averaged data shows little if any discrepancy in the PtH adsorption/desorption peaks. This indicates that local pH changes are not significant under these conditions either. However, a signal drop off in the potential range below -0.6 V *vs.* MMS was still observed.

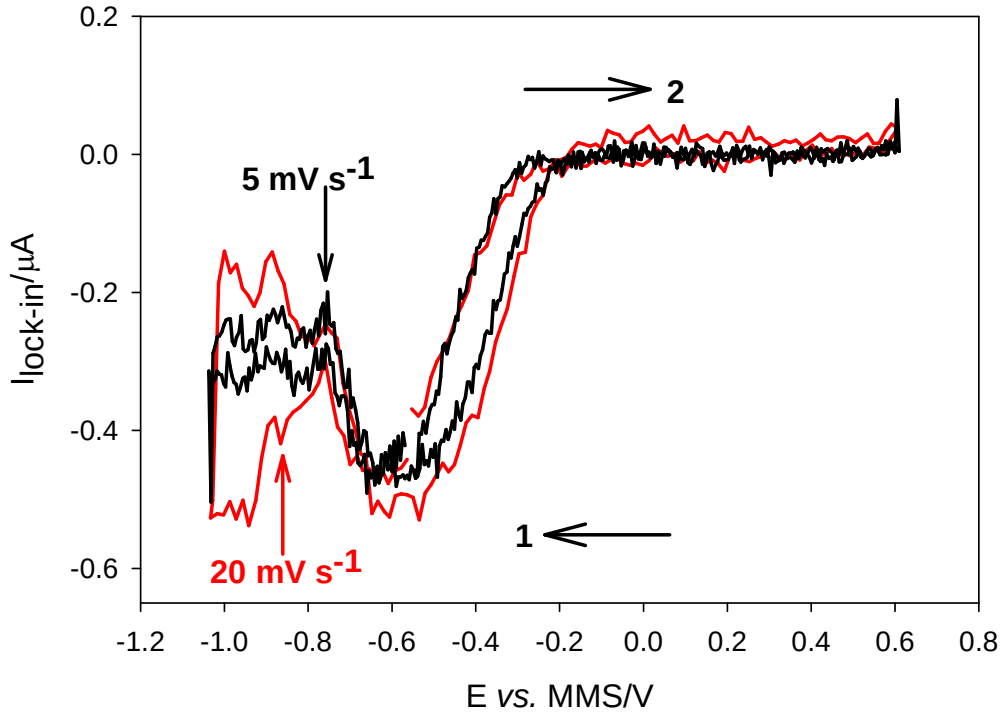

Figure 5.20 Graph represents the hydrodynamic modulation voltammetry recorded using lock-in approach nanostructured Pt electrode (RF = 280.8, 500 µm diameter) at a sweep rates of 20 mV s^{-1} (I_{HMV}, —) and 5 mV s^{-1}(I_{HMV}, —). The solution used was 1 mol dm^{-3} phosphate buffer at pH 7. The jet was modulated at 16 Hz and with piston displacement amplitude 0.010 ± 0.001 mm. Arrow 1 indicates the forward scan and 2- backwards scan. The temperature of solution was 20 – 25 °C.

Clearly these results and observations point to other effects responsible for the current alterations.

5.7 Surface Chemistry Investigations. (Observation Section)

It was observed that the experimental results reported in Table 5.4 are different to those suggested by the theoretical predictions (Table 5.2). Note that results obtained in the 1 mol dm^{-3} phosphate buffer at scan rate of 5 mV s^{-1} without jet running were used for these discussions. The experiments show that although the oxide reduction peak appears at a potential close to the calculated value, the hydrogen adsorption/desorption processes take place at slightly lower potentials than those expected. Note that as the pH of a solution changed from 0 to 7, the potentials of the peaks should shift negatively by ~420 mV according to Nernstian predictions. However, the current results show that a shift in potential of the order of 410 mV was observed for the oxide formation and reduction processes whereas the positions of hydrogen adsorption and desorption

shifted negatively by only ~320 mV. This observation suggests that the hydride region does not follow the 59 mV/pH unit rule. This is illustrated in figure 5.21.

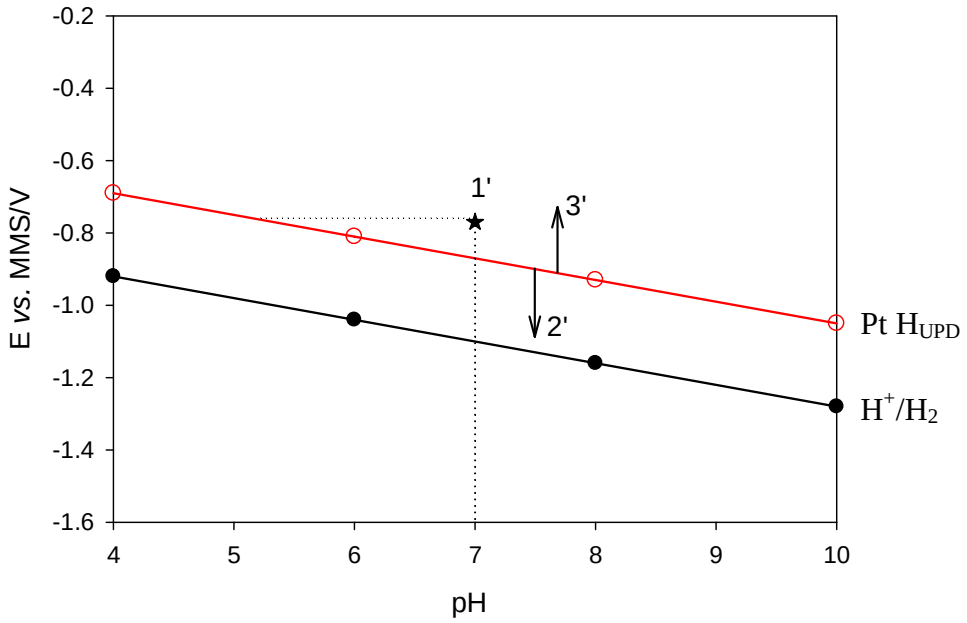

Figure 5.21. Potential dependence of the pH for: ▬ ●, calculated H^+/H_2 and ▬○ calculated Pt-H_{UPD} (strongly adsorbed peak). The experimental data at pH 7 in phosphate buffer solution is also included (1'). The arrows show the direction of the potential changes in case of ion co-adsorption (2') and pH surface change (3').

A similar effect can be found in the communication by Yang and Denuault (*212*). However, the unusual potential was not further commented on. It was previously shown in section 4.1 how anion adsorption can affect the experimental results. Clearly these observations are of interest particularly if local pH changes are to be inferred from peak potential data. Hence we shall discuss the findings of our investigations here and put them in context to the available literature on this topic.

The effect of ion adsorption has been investigated by many authors (*119, 123, 125-127, 208*) and was previously demonstrated in the current work (see section 1.4 and 5.1). (Consider the phosphate buffer solutions employed in figure 5.19.) According to the previous literature reports (*125, 126*) the phosphate solutions at pH 7 contain HPO_4^{2-} and $H_2PO_4^-$ ions in the concentration ratio of 1:2 (see more details in Table 1.1 of Chapter 1). It was also shown that (see figure 1.16a in chapter 1) there is no change in ion adsorption in the potential range between +0.4 and +0.8 V *vs.* RHE. Indeed it was demonstrated previously (see figure 5.2) that an increase in the strength of ion adsorption moves peaks to more negative potentials. These effects are illustrated in

figure 5.21 with arrow 2'. These observations do not explain the unusual peak potentials observed and reported in this work. However, other authors, who have investigated ion effects at surfaces, have suggested local or surface pH to be a relevant parameter. For example interesting observations were made by Kunimatsu *et al.* (*123*), when studying (bi)sulphate ions adsorption. They noticed that the ratio of intensity of the adsorbed sulphate band to the adsorbed bisulphate band does not correlate directly with the activity ratio of the two ions in solution.

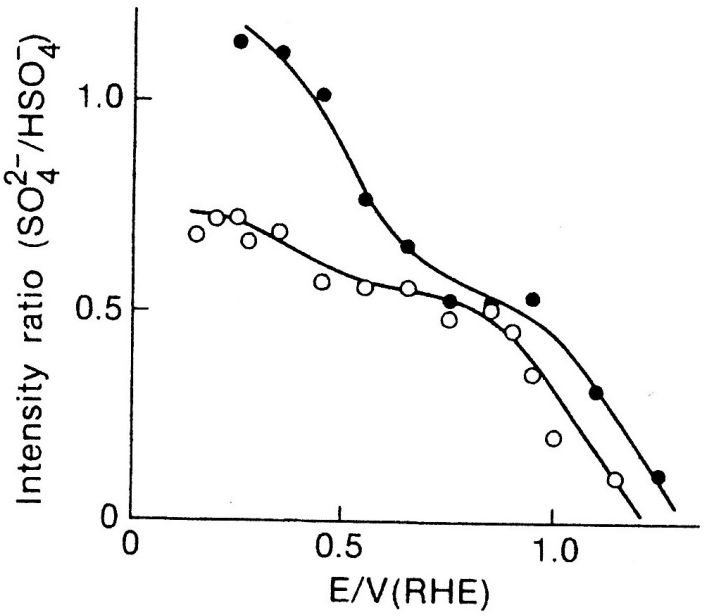

Figure 5.22. Potential dependence of the intensity ratio, SO_4^{2-}/HSO_4^-, of the asymmetric S-O stretching bands of sulphate and bisulphate ions adsorbed on Pt in 0.05 (•) and 0.5 (○) mol dm^{-3} sulphuric acid. Taken from reference (*123*).

The authors suggested that one of the factors that could affect the intensity ratio of the surface species is the H^+ concentration, $[H^+]$, in the double layer. Since the pzc of Pt lies close to 0.16 V *vs.* RHE (*216, 217*), local $[H^+]$ can be expected to decrease at more positive potentials. This should increase the sulphate concentration in the double layer, resulting in increased sulphate adsorption. However, the experimental results showed exactly the opposite of this (see figure 5.22). In addition the difference in the H^+ concentration between the 0.5 and 0.05 mol dm^{-3} H_2SO_4 solutions is approximately a factor of ten. Yet the intensity ratio of the surface species is of the same order of magnitude for the two solutions in the hydrogen UPD and double-layer regions. Kunimatsu *et al.* (*123*) proposed that one possible explanation is that, the equilibrium between the solution species and surface species is not the dominant factor. Instead the

equilibrium between the species on the surface is of more importance. This concept is represented pictorially in figure 5.23.

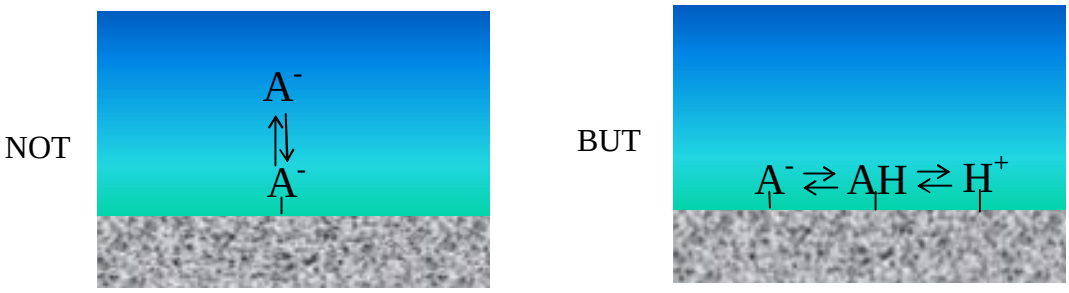

Figure 5.23. Schematic representation of surface-anion equilibrium

Under these conditions (for $A^- = SO_4^{2-}$) we can write,

$$(HSO_4^-)_{ad} = (H^+)_{ad} + (SO_4^{2-})_{ad}$$

and hence a surface equilibrium constant K_{ad} exists such that

$$\frac{K_{ad}}{[H^+]_{ad}} = \frac{[SO_4^{2-}]_{ad}}{[HSO_4^-]_{ad}}$$

If it was assumed that the amount of H^+ adsorbed may be small but of the same order as K_{ad}, then if adsorbed H^+ has some saturation limit, then the $[SO_4^{2-}]/[HSO_4^-]$ is expected to be constant and independent of the solution concentration. Kunimatsu *et al.* (*123*), proposed that the adsorbed H^+ concentration is strongly related to the electrode potential, as figure 5.22 suggests; this is equivalent to a potential dependent surface pH. These observations suggest that the pH near the electrode surface below the PZC is lower than the one expected for the bulk. Such a local pH change in the vicinity of the electrode compared to the solution pH could explain the positive potential shift of the H_{UPD} peaks (see figure 5.21, → 3'). While these observations are of interest they do not explain the observed behaviour of molecular oxygen reduction at nanostructure Pt electrodes. Hence further investigation is necessary. One key parameter known to affect oxygen reduction is the actual mechanism of electroreduction. In order to probe this mechanism, many authors have investigated the amount of hydrogen peroxide produced as a function of electrode potential. This was also investigated here and will be the subject of the next section.

5.8 Detection of the Hydrogen Peroxide at the Rotating Ring Disk Electrode

It was shown in figure 1.22 that molecular oxygen reduction may be considered as two parallel reaction pathways with H_2O_2 formation as an intermediate species. Hence the production of H_2O_2 decreases the molecular oxygen reduction signal. It is known that for the reduction of O_2 in highly purified acid solutions, no H_2O_2 is formed until a potential as negative as 0.1 V *vs.* NHE (*162*) is applied. This represents the hydride region for polycrystalline Pt. For less well purified solutions, some H_2O_2 is seen at less negative potentials and reaches a maximum near the pzc (where an adsorbed impurity might be expected to maximize its surface concentration (*101*) at the electrode. Clearly these observations suggest that the anomalous current drop off (figure 5.11) could be caused by the production of hydrogen peroxide. In the following section we assess H_2O_2 production at nanostructured Pt using a RRDE in an attempt to clarify the issue.

Damjanovic *et al.* were the first to introduce a way of using the rotating ring disk electrode (RRDE) to distinguish between H_2O_2 as an intermediate in the four-electron reduction of O_2 to water and H_2O_2 as a product of the reaction (*161*). The RRDE measurement process is shown in figure 5.24.

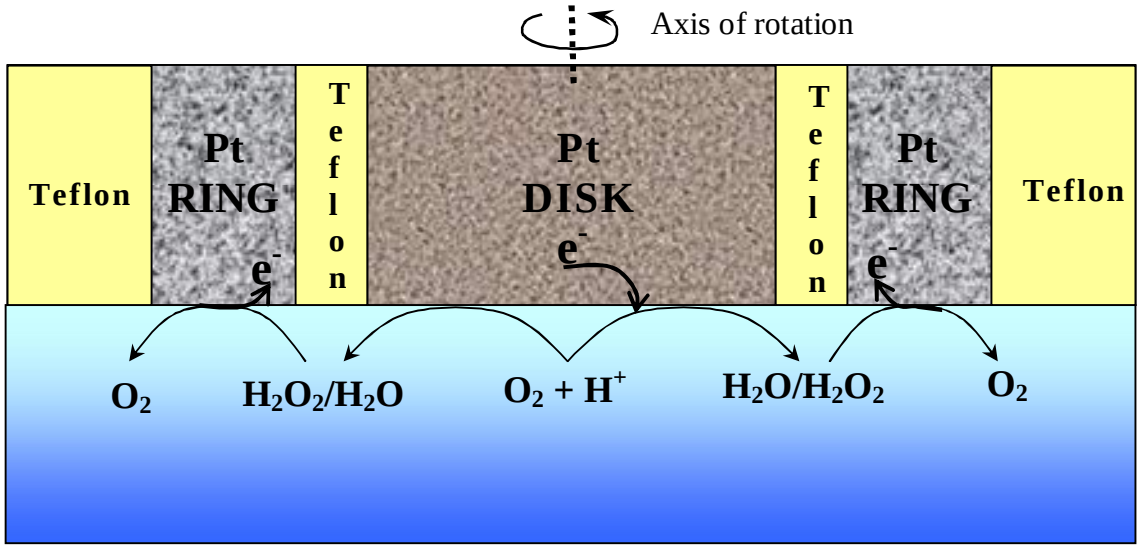

Figure 5.24 Schematic showing a cross section of a RRDE and associated generation and collection reactions.

In this system molecular oxygen will be reduced at the disk's surface which is swept through an appropriate potential range. Depending on the exact mechanism, the amount of hydrogen peroxide will differ. However, the "down stream" Pt ring (which

has been nanostructured to ensure good H_2O_2 detection characteristics (*218*) (see experimental section for further details) and was held at a potential to detect any resulting H_2O_2 production. Hence enable evaluation of the apparent number of electron used.

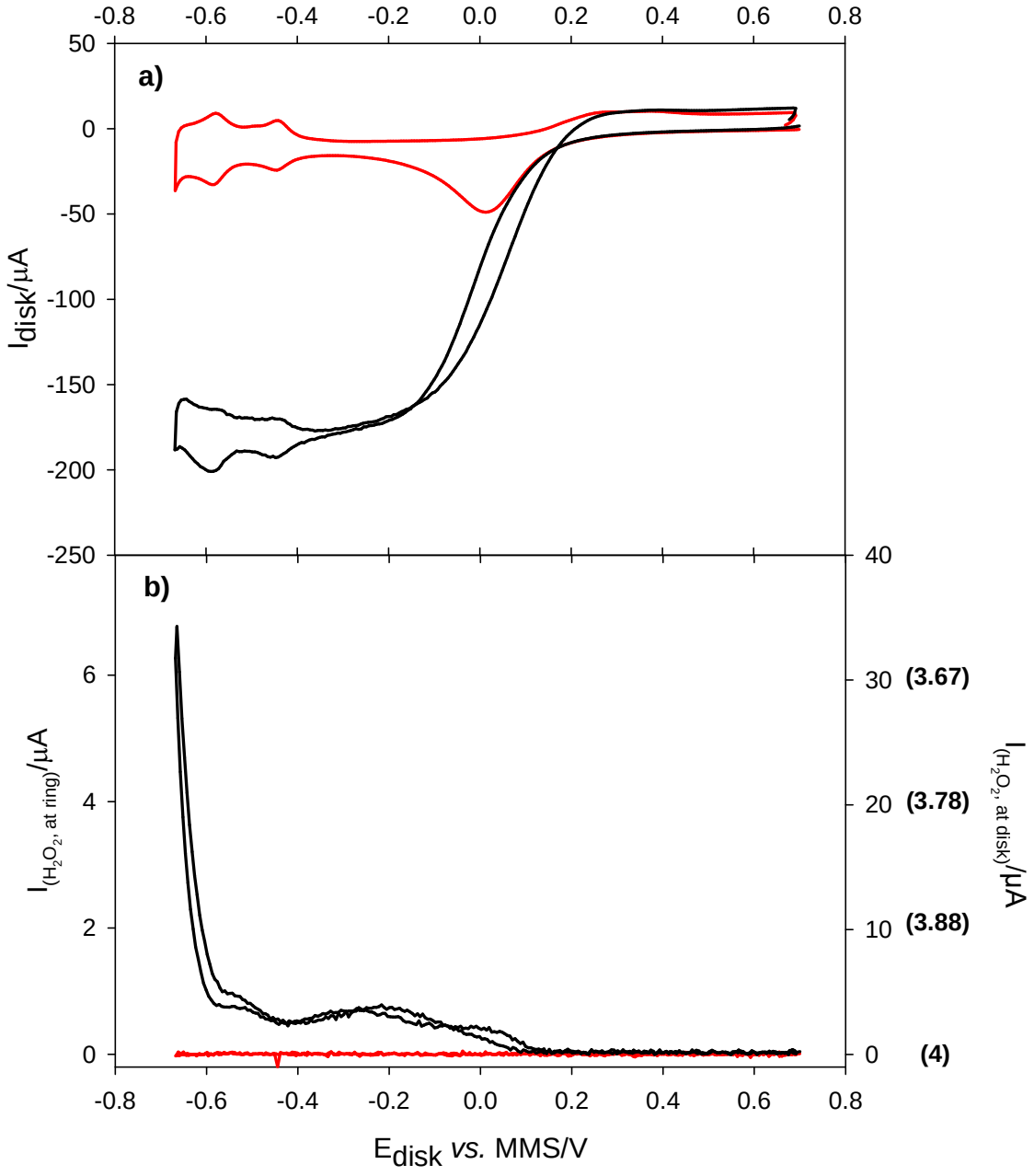

Figure 5.25. a) Cyclic voltammograms recorded at a polished Pt disk in 1 mol dm^{-3} aerobic H_2SO_4; rotation speed (—) 0 rpm and (—) 2500 rpm, potential scan rate was 50 mV s^{-1}. **b)** Current- potential curves recorded at nanostructured Pt ring; the ring's potential was held at + 0.4 V *vs.* MMS. Left Y-axis corresponds to the signal recorded at the ring, right Y-axis is the calculated current for H_2O_2 recorded at the disk. The values in the brackets represent the estimated number of electrons n_{app} during oxygen reduction on the Pt disk calculated using the eq. 5.3 and 5.4. The temperature of solution was 18 – 22 °C.

Figure 5.25a shows oxygen reduction reaction (ORR) recorded at a polished platinum disk using this regime. The ring was held at +0.4 V *vs.* MMS corresponding to the mass transfer limited potential for H_2O_2 oxidation (Figure 5.25b) (*218*). Figure 5.25a shows the voltammetry obtained at the polished polycrystalline Pt disk in the absence (red line) and presence (black line) of electrode rotation. In the absence of rotation the voltammetry shows classic surface electrochemistry (see figure 5.1). However, O_2 electrochemistry is still present but masked by the relatively high surface dependant signals. In the presence of rotation a clear voltammetric wave for O_2 electroreduction was observed between 0.2 V and -0.65 V *vs.* MMS. Figure 5.25b shows the corresponding ring current in the absence (red line) and presence (black line) of electrode rotation. In the absence of rotation no ring signal was observed (as expected). However, in the presence of rotation H_2O_2 is detected from 0.1 V to -0.6 V *vs.* MMS. Note that the majority of the H_2O_2 signal appears when the Pt surface is covered with PtH_{UPD}. Figure 5.25b also shows the average number of electrons as a function of the disk potential. In order to calculate these figures the following protocol was adopted.

The total current recorded at the disk electrode could be expressed as the sum of two (I_{2e}-) and four-electron currents (eq. 5.2):

$$I_D = n_{app} F A k_m c_{ox} = \underbrace{\theta(2FAk_m c_{ox})}_{\mathbf{I_{2e^-}}} + \underbrace{(1-\theta)(4FAk_m c_{ox})}_{\mathbf{I_{4e^-}}}. \quad (5.2)$$

Here n_{app} is defined as the average number of electrons exchanged during the ORR one molecular oxygen. Thus,

$$n_{app} = 2\theta + 4(1-\theta), \quad (5.3)$$

where θ is the fraction of molecular oxygen converted to H_2O_2. This is given by:

$$\theta = \frac{I_{2e^-}}{I_d} = \frac{I_R}{N I_D}. \quad (5.4)$$

Note that only part of the intermediate H_2O_2 can be captured by the ring electrode and oxidized to O_2. Therefore, N (the collection efficiency) has to be included. The $[Fe(CN)_6]^{4-}/[Fe(CN)_6^{3-}]$ redox couple was employed to determine N (see experimental section). The collection efficiency calculated using the method was found to be 0.214 ± 0.001 (*10*).

Figure 5.25 shows that the n_{app} decreases and the H_2O_2 proportion increases when the disk potential changes to more negative (below + 0.1 V *vs.* MMS). However, the maximum amount of H_2O_2 produced was found to be below +0.6 V *vs.* MMS (corresponding to PtH_{UPD} formation).

In order to verify that the signal obtained (Figure 5.25b) is hydrogen peroxide oxidation produced at the disk; the concentration of H_2O_2 in solution was varied from 0.0 to 1.5 mmol dm^{-3}. The results of this experiment are presented in Figure 5.26.

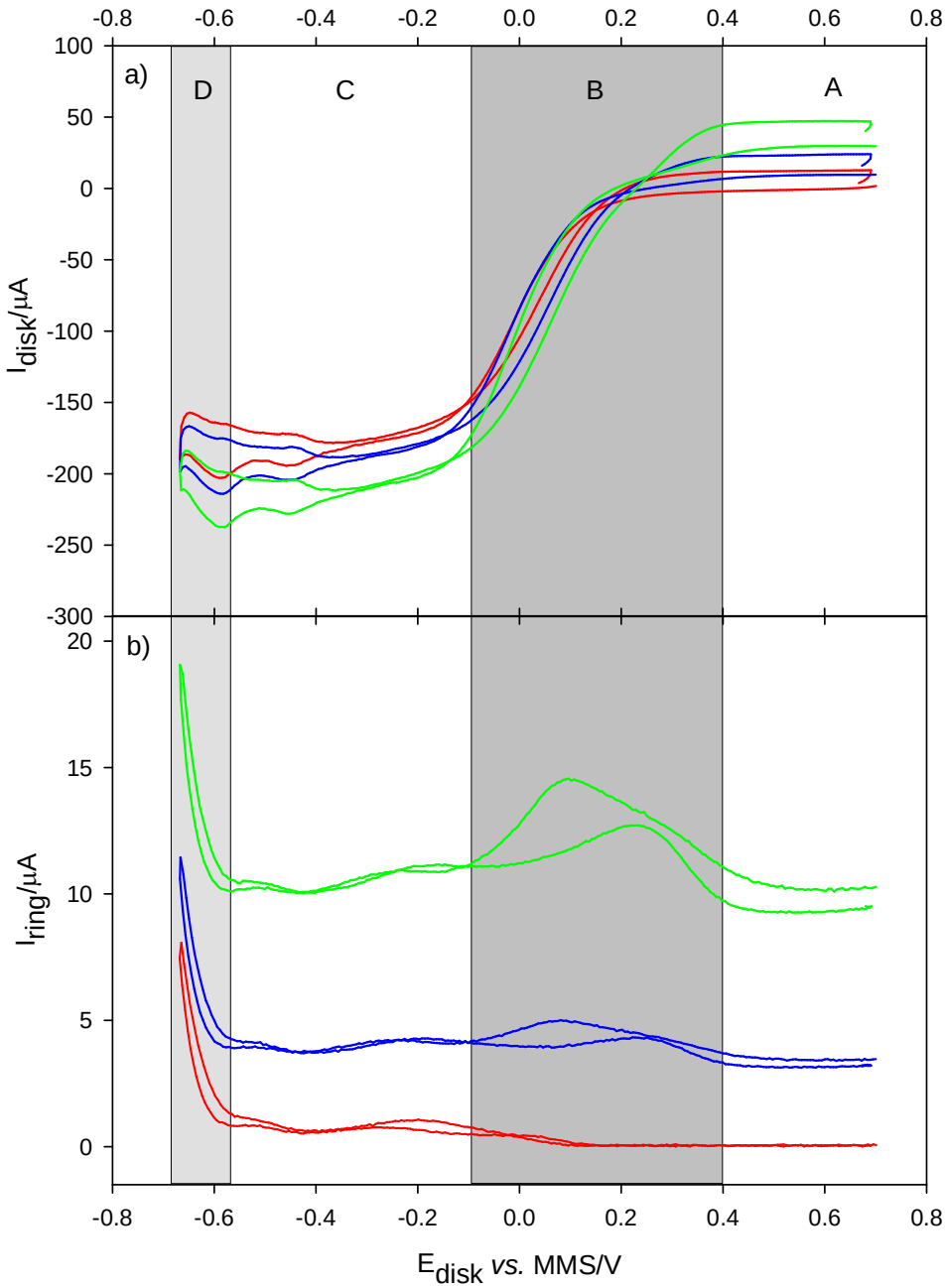

Figure 5.26. Current-potential curves recorded at a) polished Pt disk and b) nanostructured Pt ring in 1 mol dm^{-3} aerobic H_2SO_4. The ring's potential was + 0.4 V *vs.* MMS. The rotation speed was 2500 rpm, potential scan rates 50 mV s^{-1}. The concentration of H_2O_2 in solution was (—) 0 mmol dm^{-3}; (—) 0.5 mmol dm^{-3}; (—) 1.5 mmol dm^{-3}. The temperature of solution was 18 – 22 °C.

In order to clarify the results obtained figure 5.26 has been divided into 4 regions in order to depict the different processes occurring at the disk (note figure 5.26b denoted the ring current but as will be shown subsequently, in this experiment this is a combination of solution species and disk electrochemistry). Consider figure 5.26b region 'A'. Here the disk is at an oxidising potential with respect to bulk hydrogen peroxide. Hence addition of hydrogen peroxide (through appropriate titration) increases the signal at the ring but is shielded by electrochemical oxidation at the disk. This is confirmed by the results shown in figure 5.26a which indicate an anodic current over this potential range. However, as the potential of the disk moves more negative, oxidation of hydrogen peroxide slows. Under these conditions the shielding effect of the disk on the ring is diminished and a greater oxidation current at the ring is observed (see figure 5.26b section 'B'). As the potential of the disk moves further negative still (see figure 5.26b region 'C') electrochemical reduction of hydrogen peroxide and oxygen are observed at the disk. However, shielding of the disk from bulk hydrogen peroxide appears to be dominant as the anodic current at the ring in this region decreases. Finally figure 5.26b region 'D' shows that oxygen reduction at the disk deviates from a 4 electron process and hence a greater anodic signal is observed at the ring in this region. Figure 5.26b also shows that in the absence of added hydrogen peroxide, detectable hydrogen peroxide is seen in the potential region negative of +0.1V *vs.* MMS and is significant below -0.55 V *vs.* MMS. These experiments show that the anodic signal detected by the ring is likely to be associated with hydrogen peroxide as both shielding and generation collection experiments are supportive. The experimental results obtained agree with the observations reported in literature (*162*).

The fractional hydrogen peroxide yield $\chi_{H_2O_2}$ in the ORR, which describes the fraction of H_2O_2 formed relative to the total amount of O_2 consumed, was calculated as (*219*):

$$\chi_{H_2O_2} = (2I_{col} / N)/(I_{gen} + I_{col} / N). \quad (5.8)$$

According to the equation 5.8 the maximum fraction of hydrogen peroxide[4] produced at the polished disk electrode is in the order of 38 % at a potential of -0.67 V *vs.* MMS (note, 100% corresponds to $n_{app} = 2$ and 0% is to $n_{app} = 4$).

[4] Note: at these potentials the contribution to the ring current by molecular hydrogen production at the disk will become important. However, in these calculations this has been assumed to be insignificant. Further experiments are required to quantify this contribution.

The same series of experiments were repeated for a nanostructured RRDE (Figure 5.27 and 5.28). The voltammetry of the disk electrode (see figure 5.27a) showed enhanced signals for PtH_{UPD} + PtO_x formation as expected. In addition in the presence of electrode rotation (—) clear oxygen signal was observed. Interestingly hydrogen peroxide production is only marked below -0.55V. In addition a small "pulse" of H_2O_2 production is seen at +0.1 V *vs.* MMS. This presumably corresponds to low surface sites availability as PtO is initially stripped from the electrode.

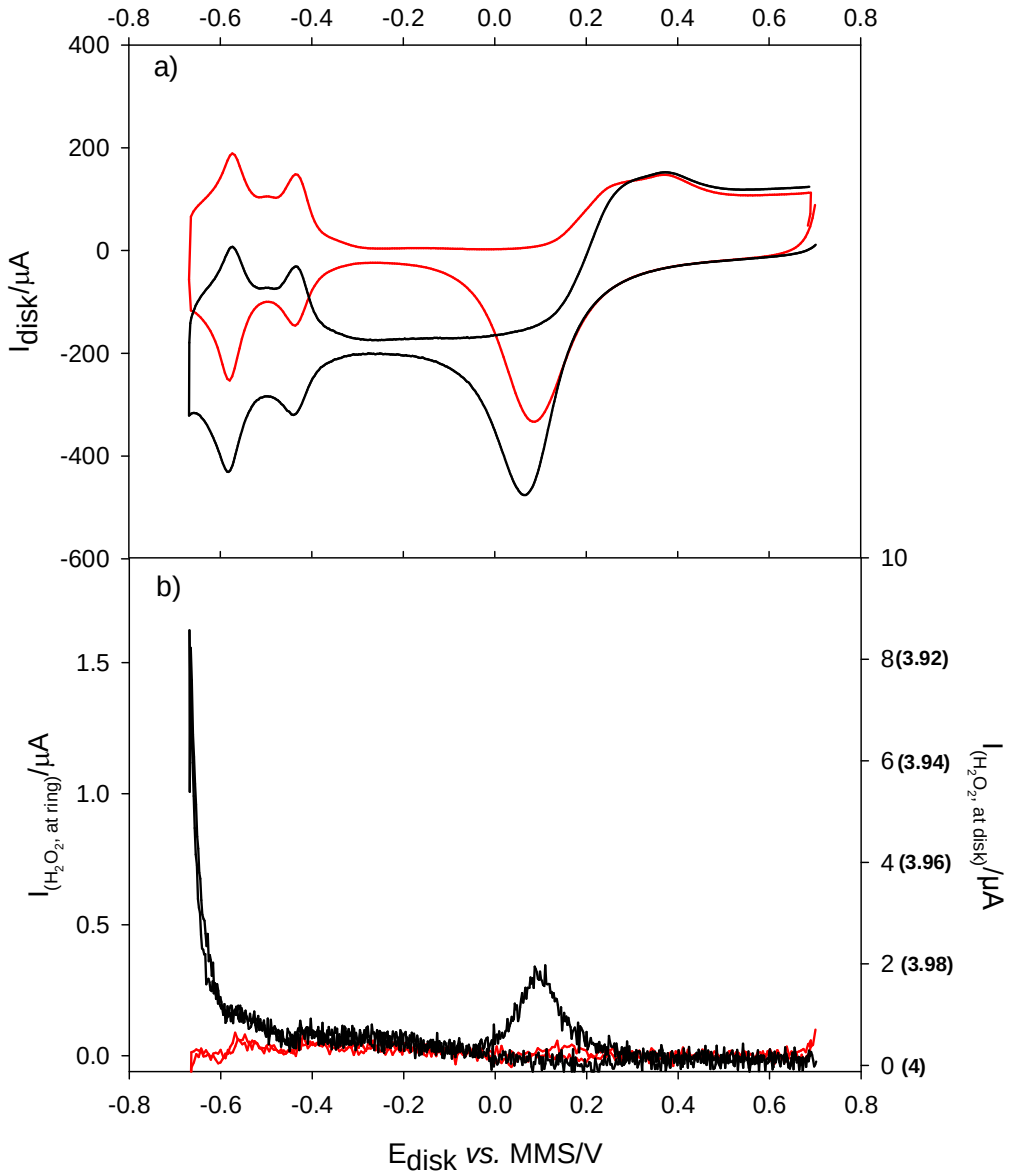

Figure 5.27. a) Cyclic voltammograms recorded at a nanostructured Pt disk in 1 mol dm^{-3} aerobic H_2SO_4 solution; rotation speed (—) 0 rpm and (—) 2500 rpm, potential scan rate was 20 mV s^{-1}. **b)** Current- potential curves recorded at nanostructured Pt ring; the ring's potential was held at + 0.4 V *vs.* MMS. Left Y-axis corresponds to the signal recorded at the ring, right Y-axis is the calculated current recorded at the disk. The values in the brackets represent the estimated number of electrons during oxygen reduction on the Pt disk. The temperature of solution was 18 – 22 °C.

However, over the entire potential region the amount of hydrogen peroxide produced is less than on the corresponding polished Pt surface. This is indicated by the higher apparent number of electrons shown in the brackets in figure 5.27b.

Turning to the titration experiments, figure 5.28 shows the effect of the addition of hydrogen peroxide to the bulk solution. It should be noted that the general features of shielding and generation collection are the same for the nanostructure as the polished Pt disk.

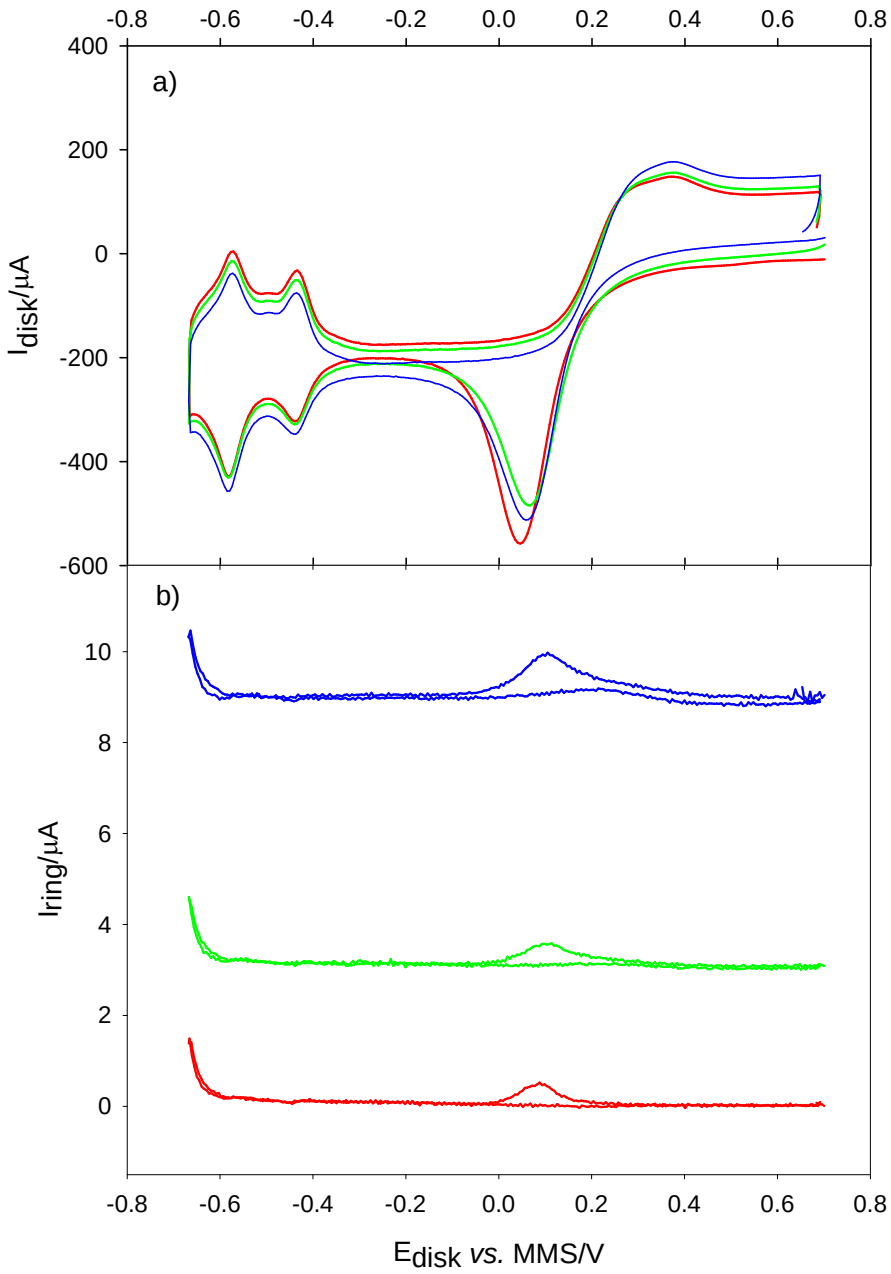

Figure 5.28. Current-potential curves recorded at a) nanostructured Pt disk and b) nanostructured Pt ring in 1 mol dm^{-3} aerobic H_2SO_4. The ring's potential was + 0.4 V *vs.* MMS. The rotation speed was 2500 rpm, potential scan rates 20 mV s^{-1}. The concentration of H_2O_2 in solution was (—) 0.0 mmol dm^{-3}; (—) 0.5 mmol dm^{-3}; (—) 1.5 mmol dm^{-3}. The temperature of solution was 18 – 22 °C.

Nevertheless there are some subtle differences. For example all the currents detected at the ring appear reduced. This indicates that the shielding efficiency of the disk is improved for both hydrogen peroxide oxidation and reduction.

The maximum fraction of H_2O_2 formed relative to the total amount of O_2 consumed is ~8.3 % for nanostructured disk electrode at potential below -0.6 V *vs.* MMS what is 4.5 times less than in case of polished electrode. This would seem supported by the increased efficiency of hydrogen peroxide electrochemistry reported for nanostructures (*218*).

The results reported here (for Pt polished and nanostructured RRDE) indicate that the drop in HMV signal amplitude are unlikely to be solely attributed to a change in the oxygen electrochemistry at the Pt surface investigated. Clearly both surfaces consume O_2 in a $4e^-$ mechanism predominantly. Hence, other contributing factors must be investigated. This is the subject of the following section.

5.9 Summary and Conclusion

The experimental investigations and results presented in this chapter suggest that a number of conclusions can be drawn from the data. First, the 'drop off' of the HMV signal cannot be explained by a change in the local pH of the solution (this was shown by the experiments in the phosphate buffer solutions and in the sulphuric acid experiments). Second, in addition the RRDE experiments also indicate that although interesting differences between the polished and nanostructured electrodes can be seen, the apparent number of electrons is close to 4 in both cases over the entire potential range explored. Third, the phase of the HMV signal with respect to the reference signal was investigated over the potential range employed. Although small changes in the phase were observed. These were shown not to be responsible for the drop off in the HMV signal observed.

However, a number of other observations are noteworthy. For example, increasing the roughness factor (from 42 to 280) increased the damping effect in the potential region of interest. In addition the shape of the current drop off clearly repeats the shape of the H_{UPD} peaks. This suggests that the current decrease could be related to the properties (in particular, high capacitance) of the nanostructured platinum electrodes. This will be discussed in detail in chapter 7. In the next chapter we turn to a different and popular method for the generation of HMV data specifically a vibrating wire electrode.

However, we use a FFT approach to the data analysis and explore the parameters effecting the response of the redox system employed (for example, O_2, $Fe(CN)_6^{3-/4-}$ and $IrCl_6^{2-}$).

Chapter 6

Study of Oxygen Electroreduction at Vibrated "Tight-rope" Pt Electrode Using a FFT Approach

In chapters three and four the oscillating jet system was described and used as a method for the generation of hydrodynamic modulation. It was demonstrated that the pulsation of the jet results in the periodic increase of mass transport of species to an electrode surface. The 'lock-in' approach was applied to the technique so the signal of interest could be isolated from the background signal. In particular this approach was employed in studies of the electrochemical reduction of molecular oxygen on nanostructured platinum electrodes. However, while the method showed clear success in distinguishing the mass transport dependent signal from the background noise there were limitations. These are associated with properties of the nanostructured materials (see Chapter 4 for details).

In this chapter the vibration of a "tight-rope" will be employed as a type of hydrodynamic modulation in order to produce high frequency oscillations. In addition Fast Fourier Transform (FFT) analysis will be employed in these studies in order to extract the relevant signal.

6.1 Fourier Transform Methods in Hydrodynamic Modulation Voltammetry

The electrochemical system this project addresses is hydrodynamic modulation voltammetry. The advantages of the technique have been widely discussed in the previous chapters where the single-frequency HMV measurements were employed. However, it is also common in HMV studies to require signal measurements at many frequencies (*e.g.* square wave rotation modulation studies (*32*)). This has been done in

the past by either mechanically modulated flow at discrete frequencies or by scanning the frequencies (*33, 35, 220-223*). As an alternative to these approaches, a FFT method could be applied in the HMV analysis to investigate the frequency response characteristics of the mass-transfer limited current (*31, 32*).

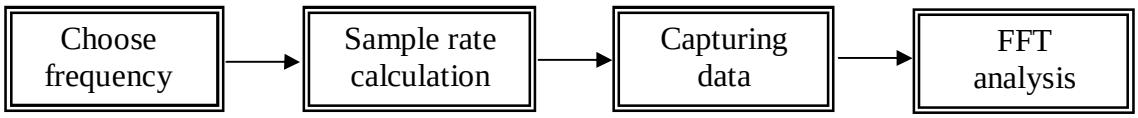

Figure 6.1. Schematic representation of the FFT method procedure.

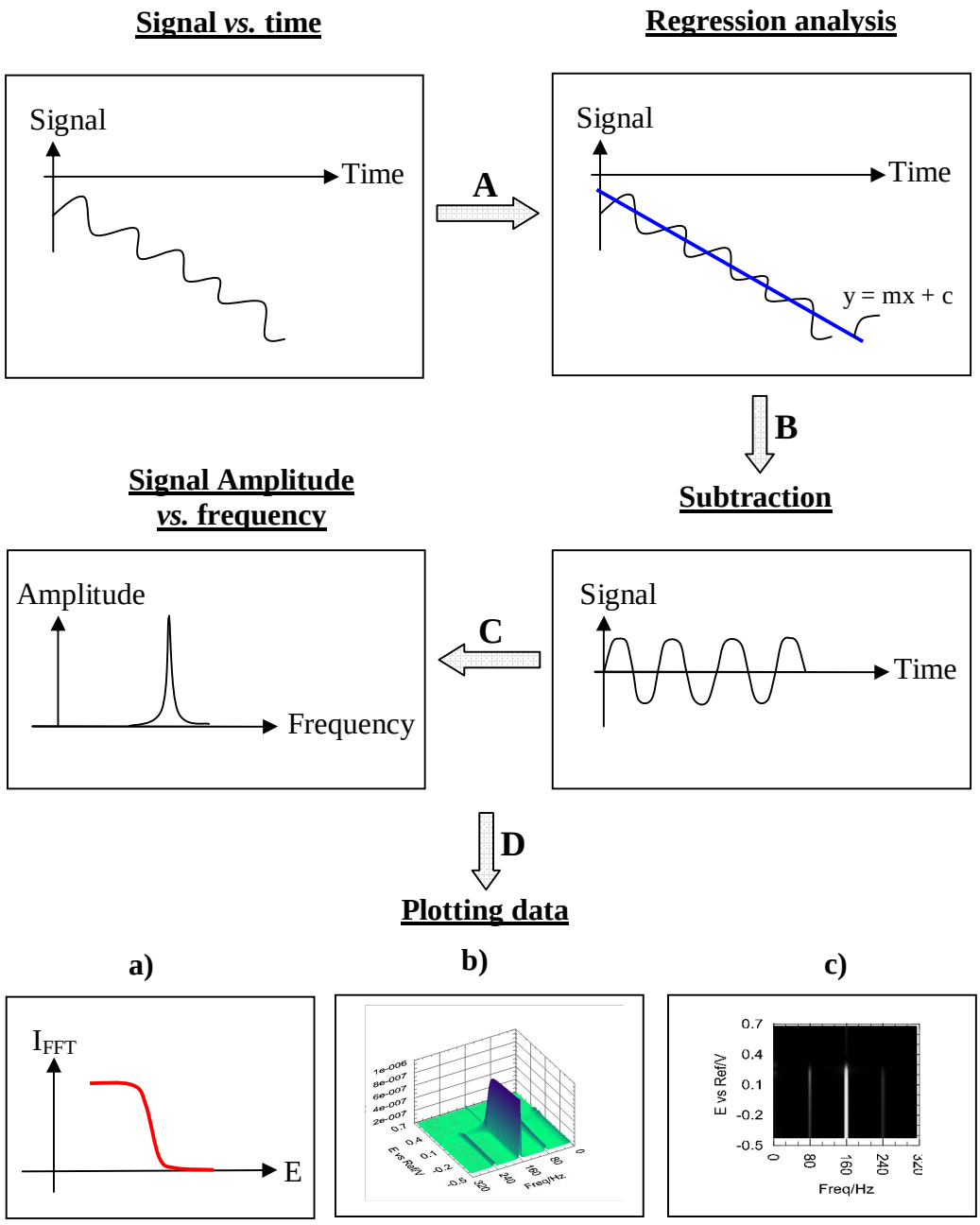

Figure 6.2. Schematic representation of the FFT data processing. The steps in the data analysis are described in the text.

In this chapter a FFT method is employed to analyse the frequency response of the experimental data. The signal acquisition and processing were performed using bespoke software (Appendix A.3). Figure 6.1 shows the order in which events took place.

This approach will be applied to an oscillating electrode. However, it could in general be applied to any periodic signal from an electrode. Consider the case where any system is driven at a particular frequency. The signal generated from the electrode motion will be analysed by a FFT approach. Here it is important to realise that this was a discrete, and not a continuous analysis routine (*e.g.* a sample of 2^n was always considered and produced a specific set of 2^{n-1} points). Hence the need to target a particular frequency to get a "part" at the exact chosen frequency. More details of this analysis routine (and examples of this processing requirement are shown in Appendix A.3). This targeting procedure relied on an appropriate sample rate to be chosen. To calculate the sample rate for a particular modulation frequency a "Sampler" program (Appendix A.3.1) was employed. This was followed by the capturing of data (Appendix A.3.2) and finally the FFT analysis (Appendix A.3.3-A.3.4). In order to remove the noise and DC component from the initial (signal-time) data linear regression analysis followed by subtraction of the original data were carried out. The amplitude of the signal was then measured and plotted as a function of potential. The analysing software also allowed data plotting in a 2D or 3D format. In this case the signal as a function of potential and frequency can be displayed if required.

The experimental results recorded and analysed using the software will be discussed in this chapter. This work also involved the use of a novel vibrating wire, "tight-rope", electrode. Its properties and deployment are described in the following sections.

6.2 Concepts of the "Tight-rope" Electrode

The majority of HMV techniques developed employ low frequency modulation due to a variety of different reasons. In the case of the HMRDE, it was found that the concentration profile adjusted slowly to a sudden change in the rotation speed compared to the rapid readjustment of the fluid velocity (*28*). Further investigations also showed that the modulation frequency must be small compared to the centre rotation speed to ensure that the modulated component of the current at the fundamental frequency is a significant fraction of the total signal (*30, 35, 224*). HMV

techniques employing stopped or pulsed-flow through solid electrodes unable to use high modulation frequency, due to the slow response time of this approach. Similarly, the modulation frequency of the stopped-rotation voltammetry is limited by the inertia and response time of the motor-electrode assembly (*8*). Higher modulation frequency would be desirable for trace analysis due to the discrimination against flicker noise available at higher frequencies, the simpler signal processing and the ability to employ faster potential scan rates. Schuette and McCreery significantly increased the modulation frequency (80-160 Hz) by employing a vibrating microcylinder electrode (*53*). They examined the current produced at twice the fundamental vibration frequency. Under the conditions employed, excellent modulation efficiency was observed.

In the work presented here the vibration of a wire electrode will be investigated. However, the set up differs from that previously reported in the literature where a microcylinder electrode was held vertically and vibrated perpendicularly. A schematic of the electrodes used here is shown in figure 6.3 and a full description of the experimental set up is reported in Chapter 2. The vertical vibration of the rod (illustrated as a double headed arrow 1' on figure 6.3) will lead to the modulation of the "tight-rope" electrode (figure 6.3, double headed arrow 2') stretched across the rod's channel within the electrolyte solution. If the motion of the wire and fluid is ideal, the current recorded at the electrode will be at twice the fundamental frequency of mechanical oscillation, as previously reported and described by Schuette and McCreery (*53*).

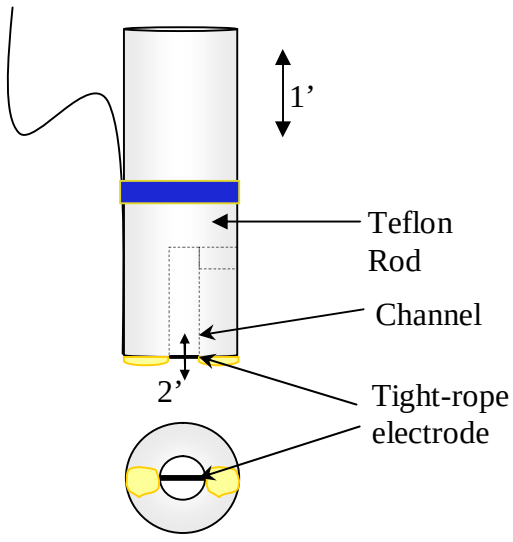

Figure 6.3. Schematic of the "tight-rope" electrode used.

The results obtained from the employment of this "tight-rope" electrode and Fast Fourier Transform-Hydrodynamic Modulation Voltammetry (FFT-HMV) analysis will now be presented.

6.3 FFT-HMV at the "Tight-rope" Pt Electrode when Studying the Reduction/Oxidation of $[Fe(CN)6]^{3-/4-}$

The cyclic voltammograms of the reduction at a stationary and modulated "tight-rope" electrode are presented in Figure 6.4. The cyclic voltammetry (—) at the stationary electrode shows the conventional response for the $[Fe(CN)_6]^{3-/4-}$ redox couple. At an electrode potential of +0.5 V *vs.* Ag the oxidation of $[Fe(CN)_6]^{4-}$ occurred. As a result of this electrochemical reaction an anodic current was observed at the 50 µm Pt "tight-rope" electrode. The reduction of $[Fe(CN)_6]^{3-}$ at potentials below +0.1 V *vs.* Ag results in a cathodic current being observed. The vibration of the electrode (see figure 6.4, — —) caused an increase in current for both oxidised and reduced species.

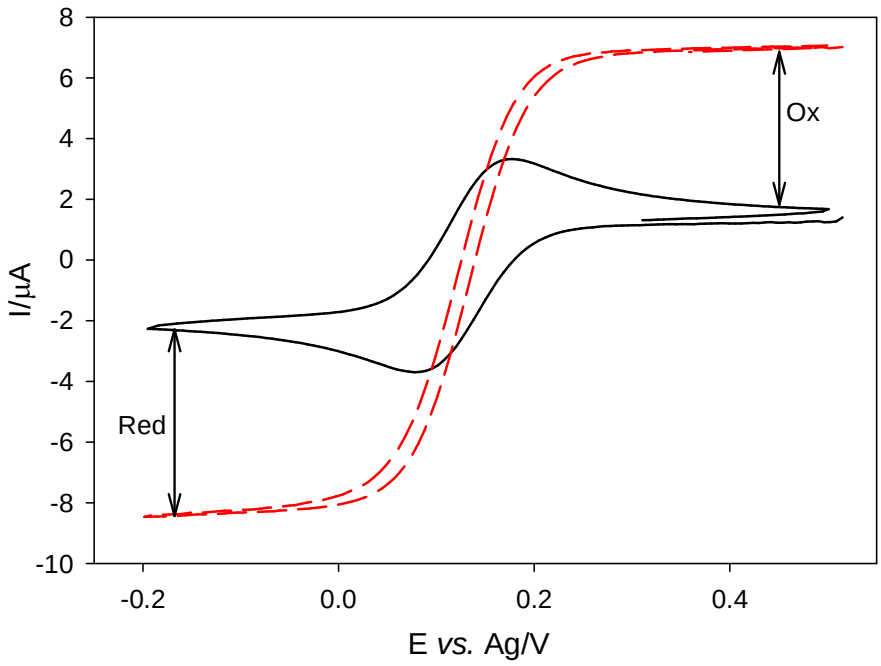

Figure 6.4. Cyclic voltammograms obtained at a stationary (—) and vibrated (— —) 50 µm diameter "tight-rope" Pt electrode in a solution containing 5 mmol dm^{-3} $Fe(CN)_6^{3-}$, 5 mmol dm^{-3} $Fe(CN)_6^{4-}$ and 0.1 mol dm^{-3} $Sr(NO_3)_2$. The modulation frequency was 80 Hz and with displacement amplitude (zero to peak) was 0.194 ± 0.001 mm. The sweep was performed at 200 mV s^{-1}. The measurements were made at room temperature 20-25 °C.

This is illustrated as double-headed arrows on figure 6.4. This figure shows that the electrochemistry is well defined, due to the extended steady state regions above +0.2 V and below 0.0 V *vs.* Ag.

The voltammogram for the $[Fe(CN)_6]^{3-/4-}$ redox system is shown in figure 6.5a as the electrode was modulated.

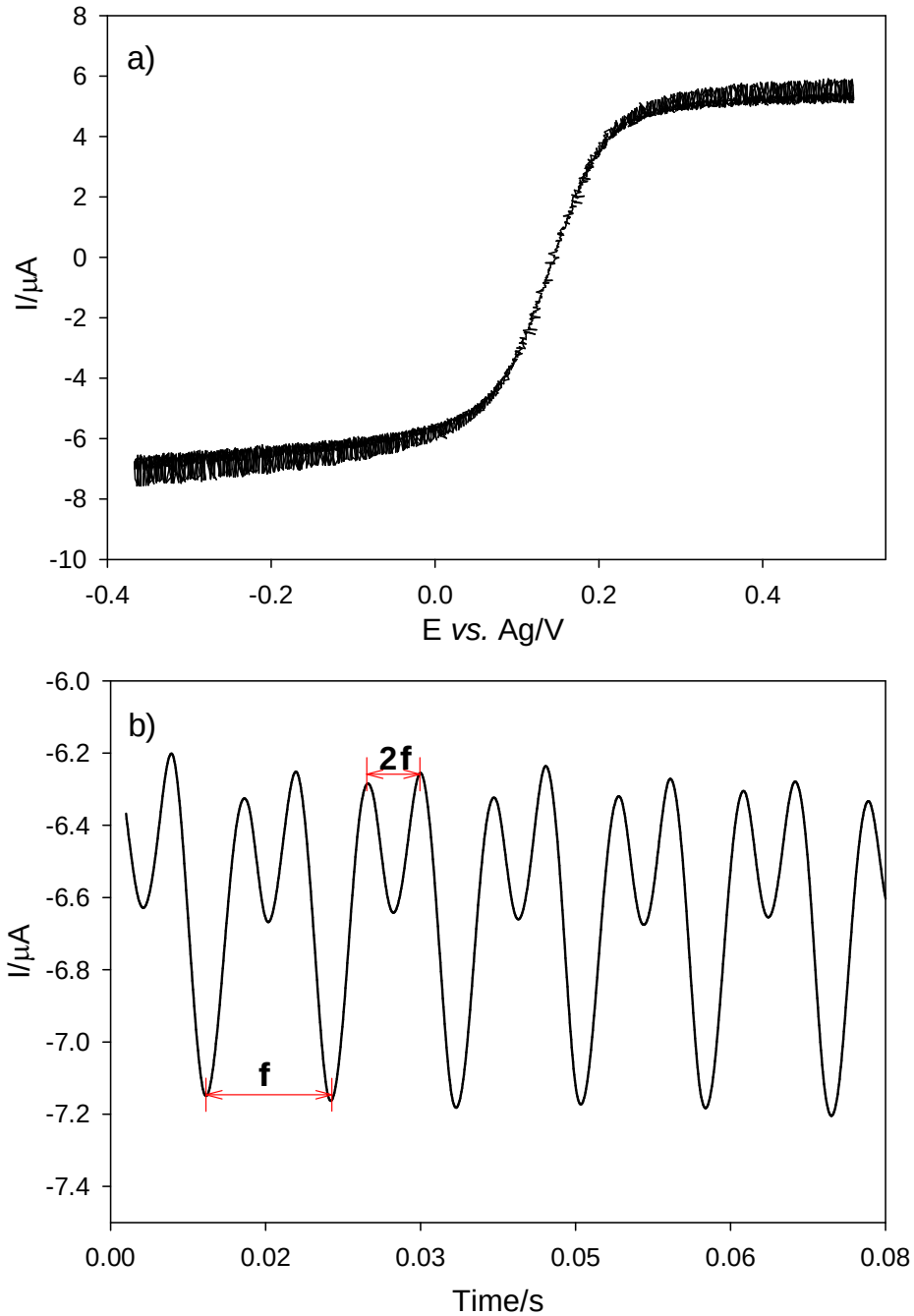

Figure 6.5. Plots showing **a)** the cyclic voltammogram recorded at the vibrated 50 µm diameter "tight-rope" Pt electrode at a sweep rate of 200 mV s^{-1} and **b)** the time current response of the electrode at the potential of -0.2 V *vs.* Ag. The solution used contained 5 mmol dm^{-3} $Fe(CN)_6^{3-}$, 5 mmol dm^{-3} $Fe(CN)_6^{4-}$ and 0.1 mol dm^{-3} $Sr(NO_3)_2$. The electrode was modulated at a frequency of 80 Hz and with displacement amplitude (zero to peak) of 0.194 ± 0.001 mm. The sample rate was 645 Hz. The measurements were made at room temperature, 20-25 °C.

The voltammetry here changes from the stagnant case (see figure 6.4) to a pseudo steady state scenario. However, the data clearly shows a "noise-like" signal on top of the sigmoidal response. The nature of this signal is shown in figure 6.5b. The aim of this section is to extract the modulating components of the signal. It was shown in a previous chapter how this could be done by using a lock-in technique. Another way of completing this task would be to use an FFT approach in the data processing (see section 6.3). However, before moving to the analysis section it would be useful to look at the current in the mass transport controlled region. Figure 6.5b shows the current time response recorded at the "tight-rope" for the $Fe(CN)_6^{3-}$ reduction at the potential of -0.2V *vs.* Ag. The modulation frequency of the electrode was 80 Hz. Considering the observations reported by McCreery *et al.* the recorded current should appear at twice the fundamental modulation frequency (80Hz) here 160 Hz. However, the current response shows the presence of both fundamental, f, and twice of the fundamental, $2f$, components. This suggests non-ideal behaviour of the flow within this system.

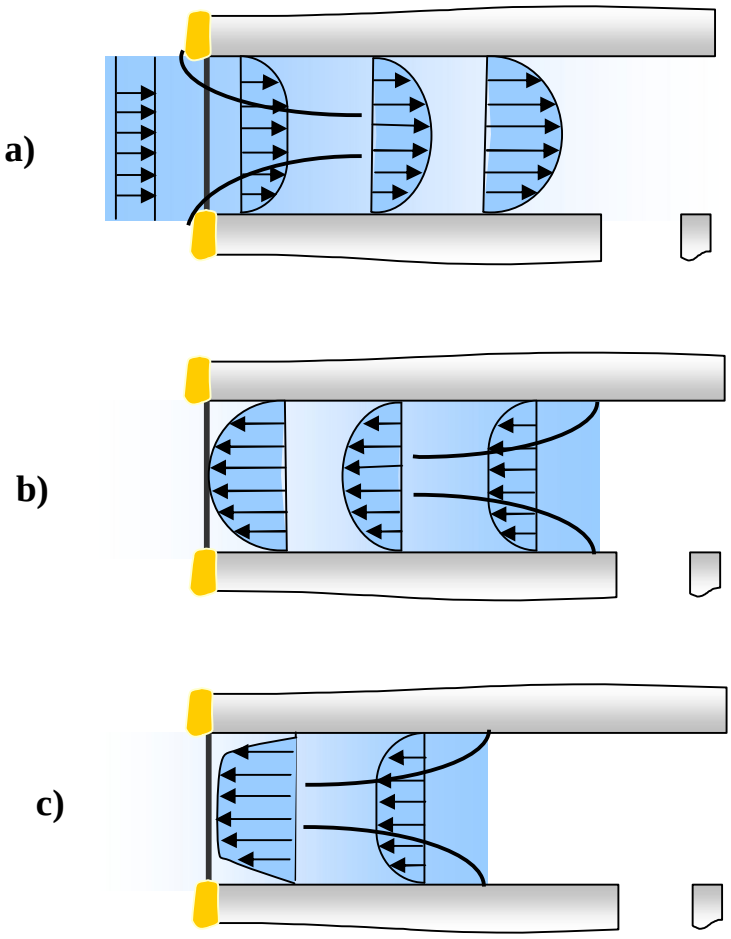

Figure 6.6. Schematic representation of the flow **a)** entering, **b)** exiting the tube (laminar parabolic flow) and **c)** exiting the tube (turbulent flow). (Redrawn from Reference (*225*)).

The non-ideal nature of the current could be explained in terms of development of the flow inside the tube. This is represented schematically in figure 6.6. Clearly the flow regime entering the tube will be significantly different to that leaving the tube. Fluid entering the tube creates flow patterns that remain inviscid (see figure 6.6a). As the flow propagates down the channel the friction near the wall of the tube will result in different flow velocities distribution within the tube. Under conditions of steady state laminar flow, the velocity profile may be described by a parabola (see figure 6.6b) (*225-228*). In order to achieve the laminar flow two parameters should be satisfied. First, the Reynolds number, *Re*, should be below a critical value (*229*) of $Re_{crit} \sim 2000$ (see eq. 1.3 for *Re* value calculation). Second, the length of the tube, *L*, should be sufficient for laminar flow to become fully developed (*226, 227*). The length could be given by:

$$L = 0.06d\,\mathrm{Re} \qquad \text{eq. 6.1}$$

where *d* is the diameter of the tube (*226*). If the experimental conditions do not satisfy the parameters then the flow carries a turbulent character (see figure 6.6c). A flow velocity, υ, of 9.75×10^{-2} m s^{-1} and the radius of the tube of 2 mm were used to obtain the *Re* value. In the case presented here $Re \sim 195$ which is consistent with laminar flow requirements. However, for the *Re* value and radius of the tube, the length, *L*, required for developing of laminar flow is equal 39 mm what is significantly less than the experimentally employed. This therefore suggests that the flow in the tube is more likely to have "turbulent" character. Hence the experimental current response will differ from the predicted. Nevertheless this device proved to be extremely successful in producing regular and controllable signals.

The application of an FFT approach to the data captured from the ferricyanide redox system is presented in figure 6.7. At potential above +0.15 V *vs.* Ag the increase in current is detected for both total current (—) and the FFT (— —) signal. This increase is attributed to ferrocyanide oxidation at the electrode surface. Alternatively as the potential of the electrode progresses below +0.15 V *vs.* Ag, another increase in current was recorded due to the ferricyanide reduction process in this potential region. These results are expected for the current analysing system.

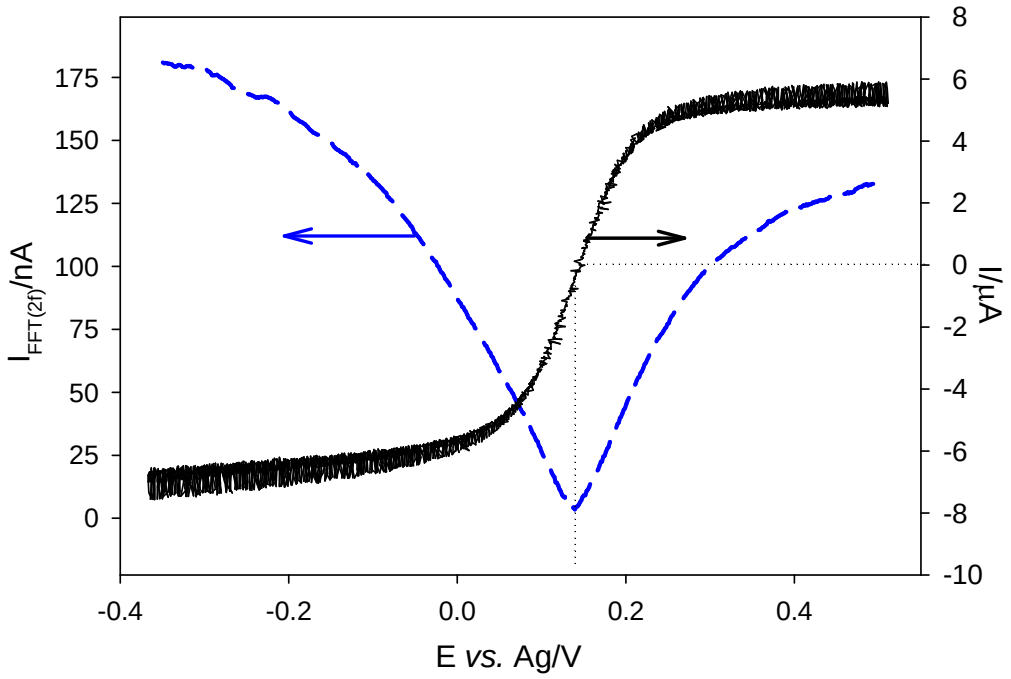

Figure 6.7. Plot showing the current response (—) recorded at a vibrated 50 μm diameter "tight-rope" Pt electrode in an anaerobic solution containing 5 mmol dm^{-3} $Fe(CN)_6^{3-}$, 5 mmol dm^{-3} $Fe(CN)_6^{4-}$ and 0.1 mol dm^{-3} $Sr(NO_3)_2$. The dashed line (– – –) denotes the AC component of the current at twice of fundamental frequency recovered using the FFT approach. The electrode was modulated at a frequency of 80 Hz and with a displacement amplitude (zero to peak) of 0.194 ± 0.001 mm. The sweep was performed at 200 mV s^{-1} and the sample rate was 645 Hz. The measurements were made at room temperature, 20-25 °C.

Figure 6.8 shows a contour map of the current monitored at the vibrated "tight-rope" electrode as a function of potential and frequency using the FFT software. The graph shows strong signals at 80 and 160 Hz and a slightly weaker signal at the 240 Hz. From the predictions made by McCreery *et al. (53)* and the non-idealities of the flow in/out of the electrode housing, detection of signals at 80 and 160 Hz is expected in this system considering a mechanical oscillation of the device at 80 Hz. In addition to these main signals, background "noise" was also observed which mimics the shape of figure 6.7. However the reason for this is unclear at this time.

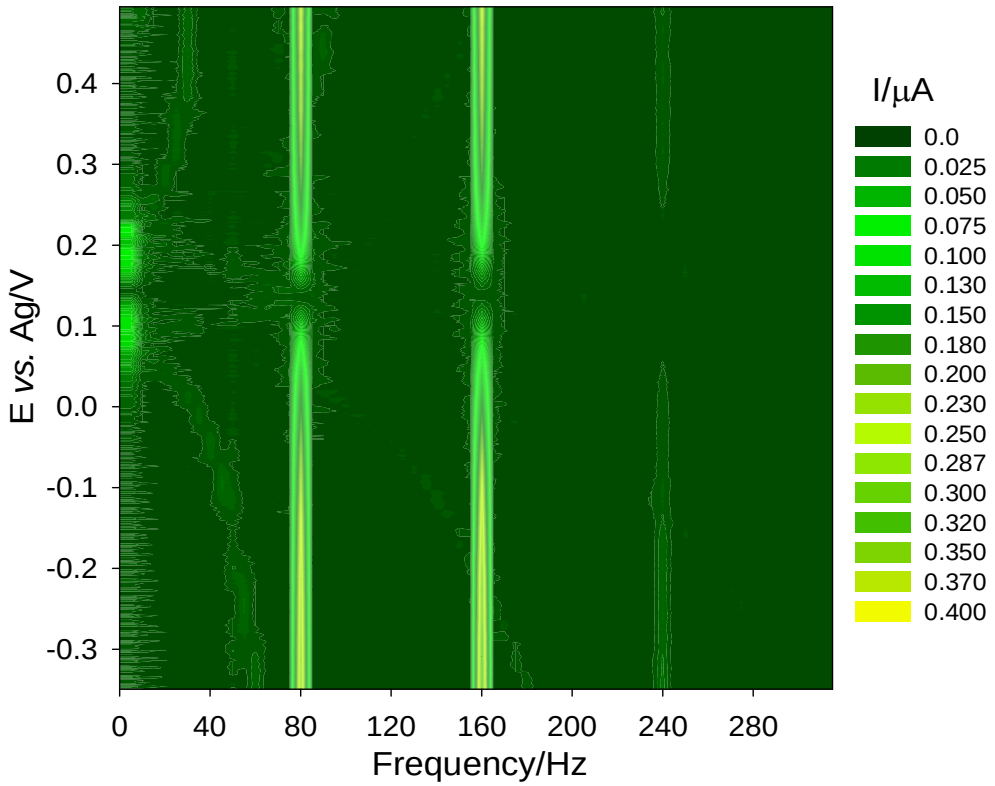

Figure 6.8. Contour maps showing the current response as a function of potential and frequency recorded at a 50 μm diameter "tight-rope" Pt electrode in an anaerobic solution containing 5 mmol dm^{-3} $Fe(CN)_6^{3-}$, 5 mmol dm^{-3} $Fe(CN)_6^{4-}$ and 0.1 mol dm^{-3} $Sr(NO_3)_2$. The electrodes modulation frequency was 80 Hz and the displacement amplitude (zero to peak) was 0.194 ± 0.001 mm. The measurements were made at room temperature, 20-25 °C.

The next redox system investigated using the FFT technique was the reduction of molecular oxygen. The results of these studies will be now detailed.

6.4 Oxygen Reduction at a Vibrated "Tight-rope" Pt Electrode

A 50 μm "tight-rope" Pt electrode was employed in these investigations. The results are presented in figure 6.9. The red line (—) on the graph shows the time-averaged current recorded at the stationary electrode in an aerobic sulfuric acid solution. The plot also includes the total current (figure 6.9a, —) for the system when the electrode was modulated. Clearly the vibration of the electrode resulted in an increase in the current below 0.0 V *vs.* MMS. This is attributed to an enhancement of the mass transfer of molecular oxygen to the electrode surface. At this stage the experimental data shown

combines both mass-transport and non-mass transport dependent components of the current.

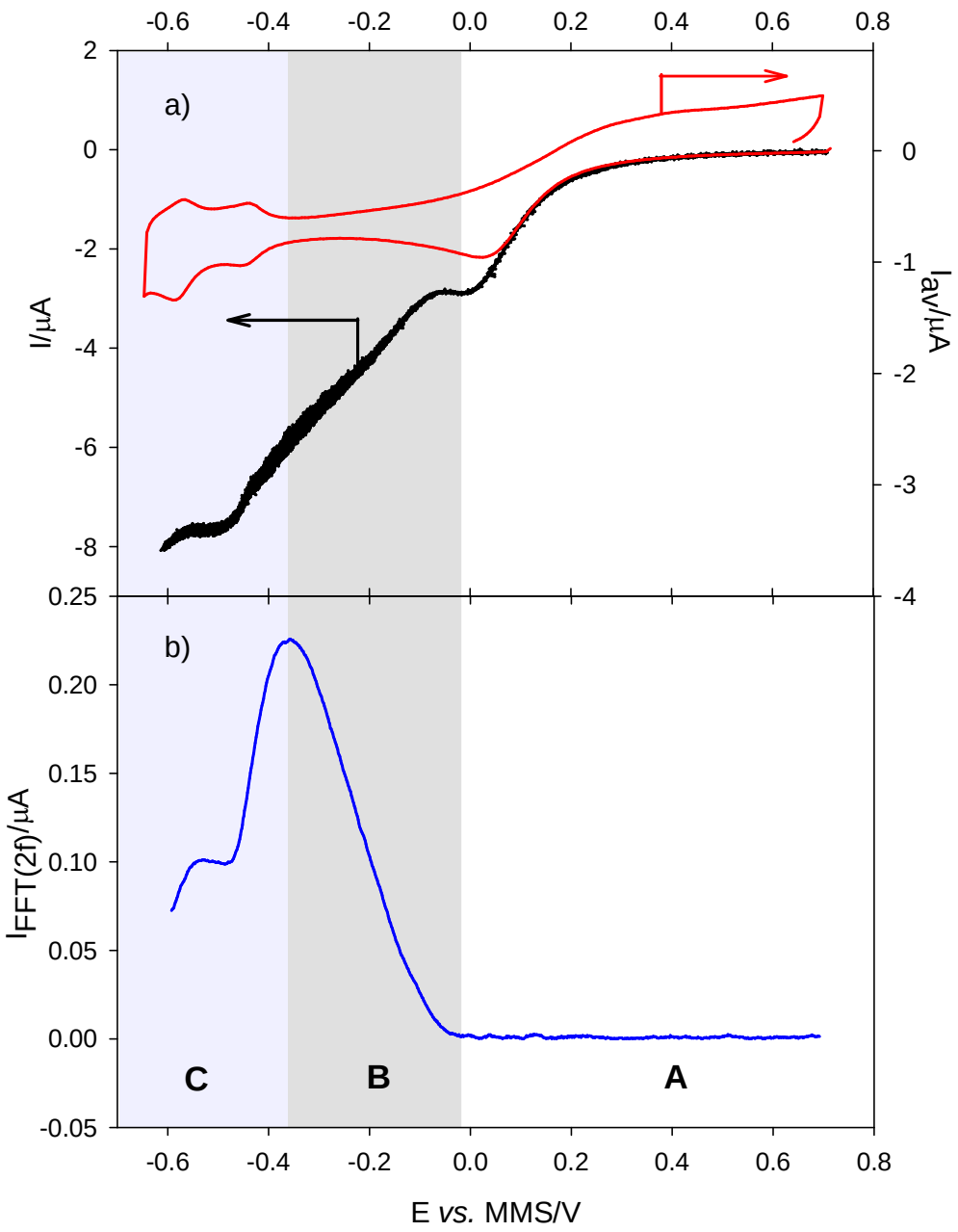

Figure 6.9. **a)** Plot showing the total current response I (—) as a function of potential recorded at the vibrated electrode. Graph also includes the time averaged signal (I_{av}, —) obtained from the stationary electrode. **b)** Plot showing the AC component of the total current at twice the fundamental frequency recovered using the FFT approach. For all plots the electrode used was a 50 μm diameter "tight-rope" Pt electrode. The solution employed was a 1 mol dm^{-3} sulfuric acid. The electrode was modulated at a frequency of 80 Hz and with a displacement amplitude (zero to peak) of 0.194 ± 0.001 mm. The sweep was performed at 200 mV s^{-1} and the sample rate was 645 Hz. The measurements were performed at room temperature, 20-25 °C.

In order to discriminate between the two signals the FFT approach to data processing was applied. Under these conditions it was found that as the electrode was cycled from

the positive (+0.7 V *vs.* MMS) to the negative potential limit (-0.65 V *vs.* MMS) the magnitude of the harmonic signal (2 *f*) was the most significant. Hence this is plotted as a function of electrode potential in figure 6.9b. Figure 6.9b shows that there is no 2 *f* signal recorded at potentials between +0.7 and 0.0 V *vs.* MMS (section A) suggesting the absence of a mass-transport dependent signal in this region. This is expected as electrochemical reduction of molecular oxygen does not occur in this potential region. Below 0.0 V *vs.* MMS variations in current were observed. In section B of figure 6.9b, an expected increase in current was recorded as a result of molecular oxygen reduction at the electrode. At potentials below -0.35 V *vs.* MMS as shown in section C in figure 6.9b, an unexpected effect was observed. Here a drop off in current was recorded as the Pt electrode entered the hydride region. The raw data for the experiment (figure 6.9a, ▬) also shows a change in thickness of the line in this potential region in agreement with the FFT (2 *f*) component plotted in figure 6.9b. The origin of this effect will be discussed later.

The 3D plot for the oxygen reduction process is shown in figure 6.10.

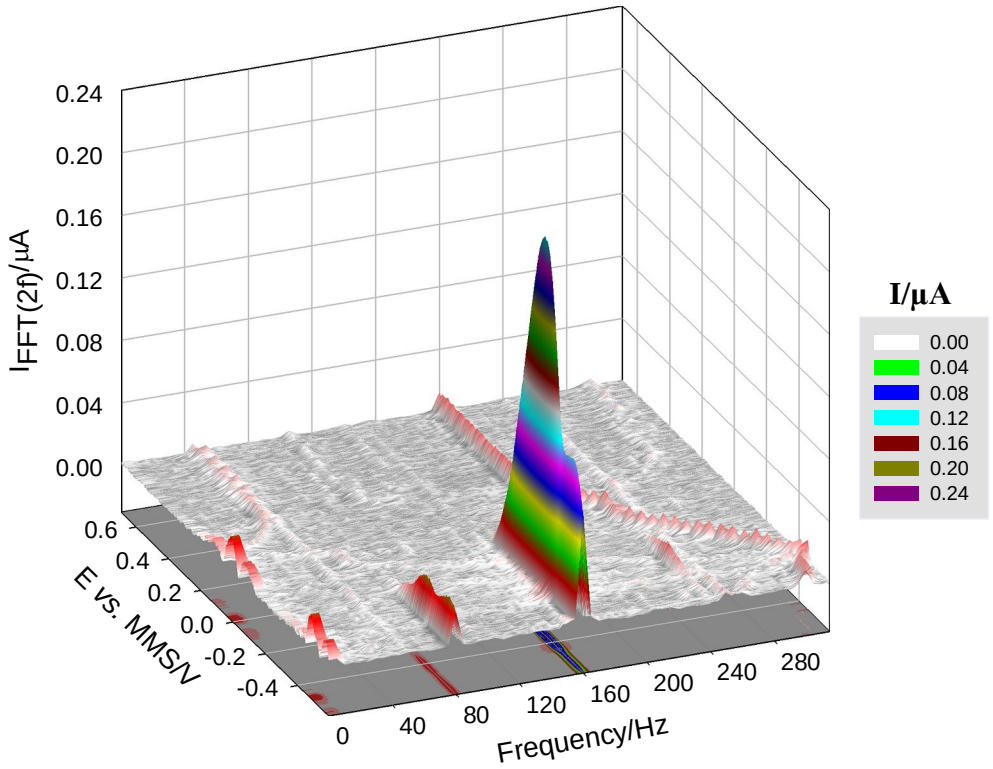

Figure 6.10. 3D plot showing current profile for molecular oxygen reduction as a function of potential and frequency recorded at a 50 µm diameter "tight-rope" Pt electrode. The solution employed was a 1 mol dm^{-3} sulfuric acid. The electrode was modulated at a frequency of 80 Hz and with a displacement amplitude (zero to peak) of 0.194 ± 0.001 mm. The sweep was performed at 200 mV s^{-1} and the sample rate was 645 Hz. The measurements were performed at room temperature, 20-25 °C.

This gives general information on current profile with respect to frequency as the electrode potential was changed from one value to another. The results indicate that the main changes in current occur at frequencies of 80 and 160 Hz. However, the harmonic signal dominates. Again the current decrease at potentials below -0.35 V *vs.* MMS can be clearly seen. Note a similar drop off in current was observed when studying oxygen reduction on high roughness factor nanostructured platinum electrodes using a lock-in approach. This was discussed in chapter 5. Clear similarities in current potential behaviour when using both lock-in at nanostructured electrodes and FFT analysis of a vibrating microwire necessitate comparative analysis of the results.

Figure 6.11 includes current profiles obtained using lock-in (—) and FFT (—) methods.

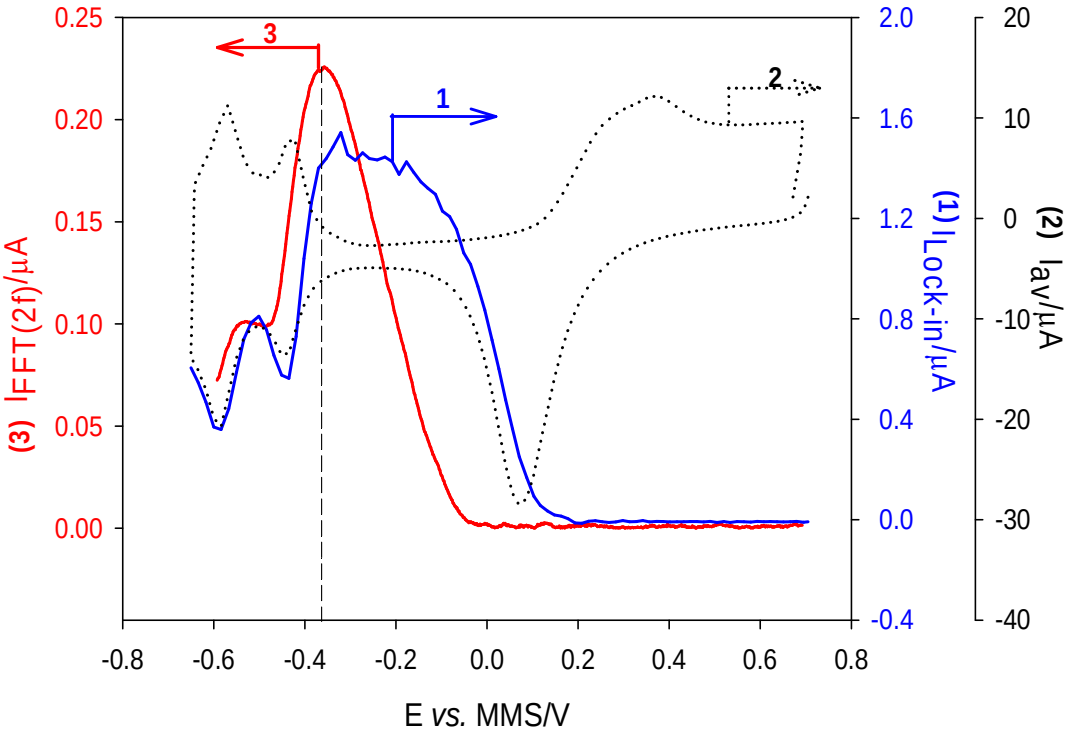

Figure 6.11. Plot showing the data analysed using the FFT approach ($I_{FFT(2f)}$, —) compared to the data obtained using the lock-in technique ($I_{Lock-in}$, —) for molecular oxygen electroreduction in 1 mol dm^{-3} sulfuric acid solution. The $I_{FFT(2f)}$ was recorded at a vibrated "tight-rope" Pt electrode (80 Hz, 50 μm diameter) with a scan rate of 200 mV s^{-1}. The $I_{Lock-in}$ was monitored at the nanostructured Pt electrode (500 μm diameter, RF = 280.8) positioned above a pulsating jet (modulation frequency 16 Hz) at a sweep rate of 20 mV s^{-1}. The dotted line represents the cyclic voltammogram for the nanostructured Pt electrode at a sweep rate of 20 mV s^{-1}.

It should be noted that the difference in potential at which reduction of molecular oxygen proceeds is due to the different type of electrodes employed in the experiments. In particular the lock-in signal was obtained at a nanostructured Pt disk electrode (500

µm diameter, RF = 280.8) whilst the FFT analysis was carried out at a polished "tight-rope" electrode (50 µm diameter). The increased surface area of the nanostructured electrodes has beneficial kinetic effects. This results in the reduction of molecular oxygen at a significantly more positive potential compared to the polished electrode surface (*172*). However, the plot also shows that the current drop occurs at the same potential for both electrodes, -0.35 V *vs.* MMS. This is the potential at which hydrogen adsorption starts taking place at the electrode (see figure 6.11,⋯⋯). Note that in both experiments the current profiles repeat the shape of the H_{UPD} peaks. It was previously proposed (see section 5.9) that the current drop off was associated with the high capacitance of the electrodes used. However, the electrodes employed in the microwire experiments are non-modified electrodes. This implies that because of the relatively small surface area of the electrodes, the capacitance is low. Clearly there should be another reason for the observed "damping" effect to occur at a Pt "tight-rope" electrode. At this stage it is unclear if the effect described above is due to oxygen electrochemistry or other unknown factors. In order to clarify the situation an electrochemical system which does not depend on surface sites of the electrodes was studied. Sodium hexachloroiridate (IV) hexahydrate is a good candidate for this type of experiments as the compound is known to have fast electron transfer kinetics (*230*). The results of the investigations are now presented.

6.5 Control Experiments Replacing Oxygen Reduction System with $[IrCl6]^{2-/3-}$ Electrochemistry

Initially, the cell was filled with aerobic 0.1 mol dm^{-3} sulfuric acid solution. As the electrode was modulated the electrochemical signal was measured and the results were analysed using the FFT approach. In this case the current recorded at the electrode corresponds to the molecular oxygen reduction signal. The current profile is shown as a blue line (— —) in figure 6.12b. As previously shown (section 5.4) an increase in current below 0 V *vs.* MMS followed by a sudden drop off at -0.35 V *vs.* MMS was observed. The graph also includes the electrode response after molecular oxygen was removed from the solution (see figure 6.12b, red line). Absence of any electrochemical activity over the entire potential range indicates the success of this procedure. Hence any signal recorded at the electrode after adding $[IrCl_6]^{2-}$ to this solution will not be

influenced by oxygen electrochemistry. The results of these experiments are shown in figure 6.12b (—). The raw data for the system is also presented in figure 6.12a.

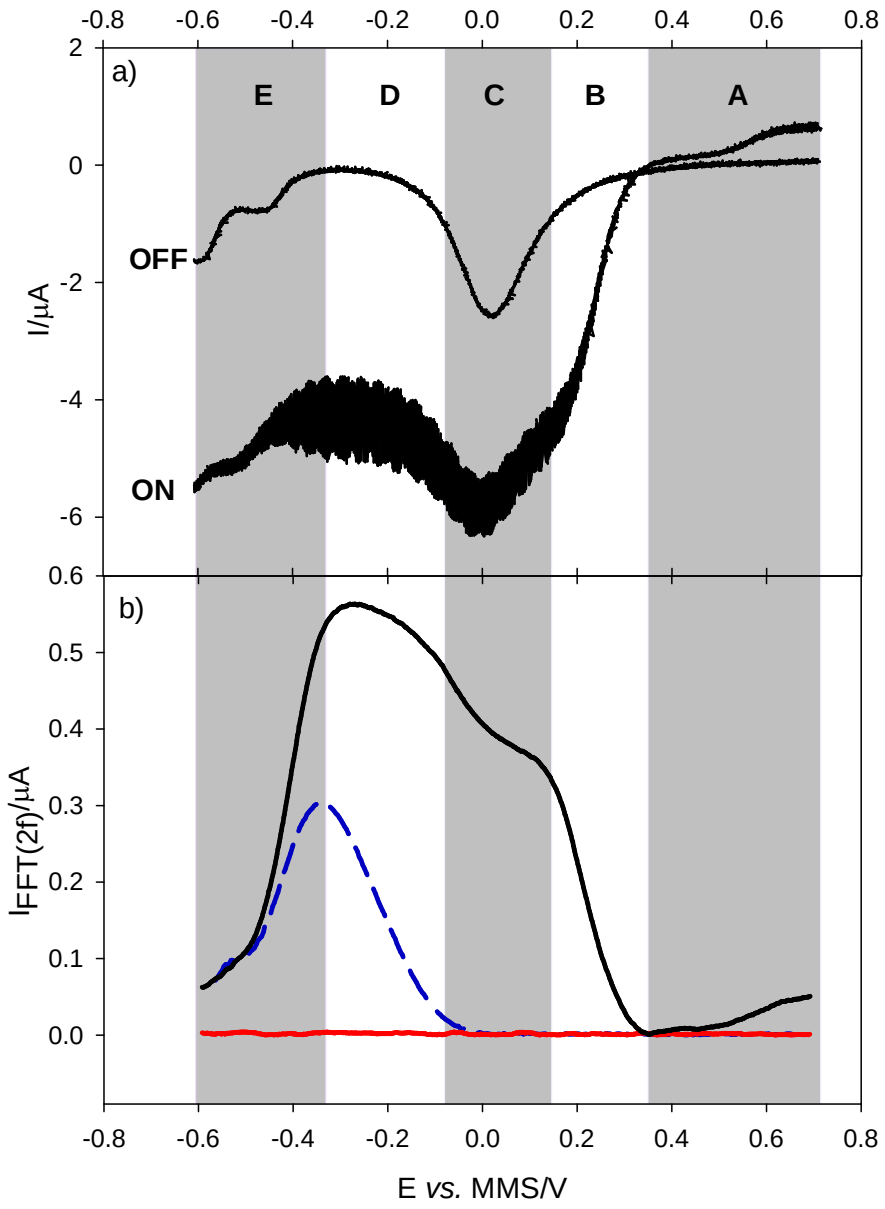

Figure 6.12. Plot **a)** showing the current response (—) recorded at a vibrated 50 μm diameter "tight-rope" Pt electrode in an anaerobic solution containing 1 mmol dm^{-3} $[IrCl_6]^{2-}$ in 0.1 mol dm^{-3} H_2SO_4. The dashed blue line (– – –) on the plot **b)** illustrates the current for molecular oxygen reduction at twice the fundamental frequency of mechanical oscillation in the 0.1 mol dm^{-3} H_2SO_4 recovered using the FFT approach. The red line (—) represents the FFT signal obtained in the anaerobic sulphuric acid solution. The black line (—) corresponds to the signal recorded in the anaerobic 1 mmol dm^{-3} $[IrCl_6]^{2-}$ solution. The electrode was modulated at a frequency of 80 Hz and with a displacement amplitude (zero to peak) of 0.194 ± 0.001 mm. The sweep was performed at 200 mV s^{-1} and the sample rate was 645 Hz. The measurements were performed at room temperature, 20-25 °C.

In these experiments the potential of electrode started at +0.7 V *vs.* MMS and was scanned negatively. Section A corresponds to a region for the redox system where no

signal is expected. Hence the zero current is expected within the potential range. However, at high positive potentials a current deviation from zero was observed. This was attributed to the presence of the impurities in the solution. A significant increase in current was recorded as the electrode potential progressed below +0.35 V *vs.* MMS. This corresponds to the beginning of the $[IrCl_6]^{2-}$ reduction process (Section B). As the electrode enters the oxide formation zone, Section C on figure 6.12, the current showed sign of a deflection from ideal sigmoidal response. The signal recovers as the electrode moves to the double layer region (Section D) and a current maximum was recorded at a potential of -0.3 V *vs.* MMS. In the region E, where the hydrogen adsorption takes place, significant "drop off" in current was observed. Note that the raw data also showed a decrease in "thickness" of the signal in the H_{UPD} region.

Two conclusions could be made based on the results of the experiments. First, the anomalous effect doesn't depend on the redox species as both molecular oxygen and $[IrCl_6]^{2-}$ reduction showed similar current deviation in the hydride adsorption region. Second, the faraday current deviations are clearly related to the surface processes proceeding on the electrode surface.

In order to understand the damping effect observed below -0.5 V *vs.* MMS, the influence of different experimental settings on the signal was investigated. First, the current as a function of the modulation frequency was studied. In order to remove any mechanical variations in the current the FFT data was plotted normalised to the maximum current response at a potential of -0.3 V *vs.* MMS. Figure 6.13b shows the results of the experiments. Clearly the mechanical modulation frequency affects the electrochemical response. In particular, the current distortion in the oxide region (arrow A, figure 6.13b) reduces as the modulation frequency decreases. In addition the signal's "drop off" in the H_{UPD} region (see figure 6.13a) was found to be smaller when the current perturbations caused by the electrode vibration are at a lower frequency (arrow B, figure 6.13b). This suggests that the signal and damping effect is frequency dependent.

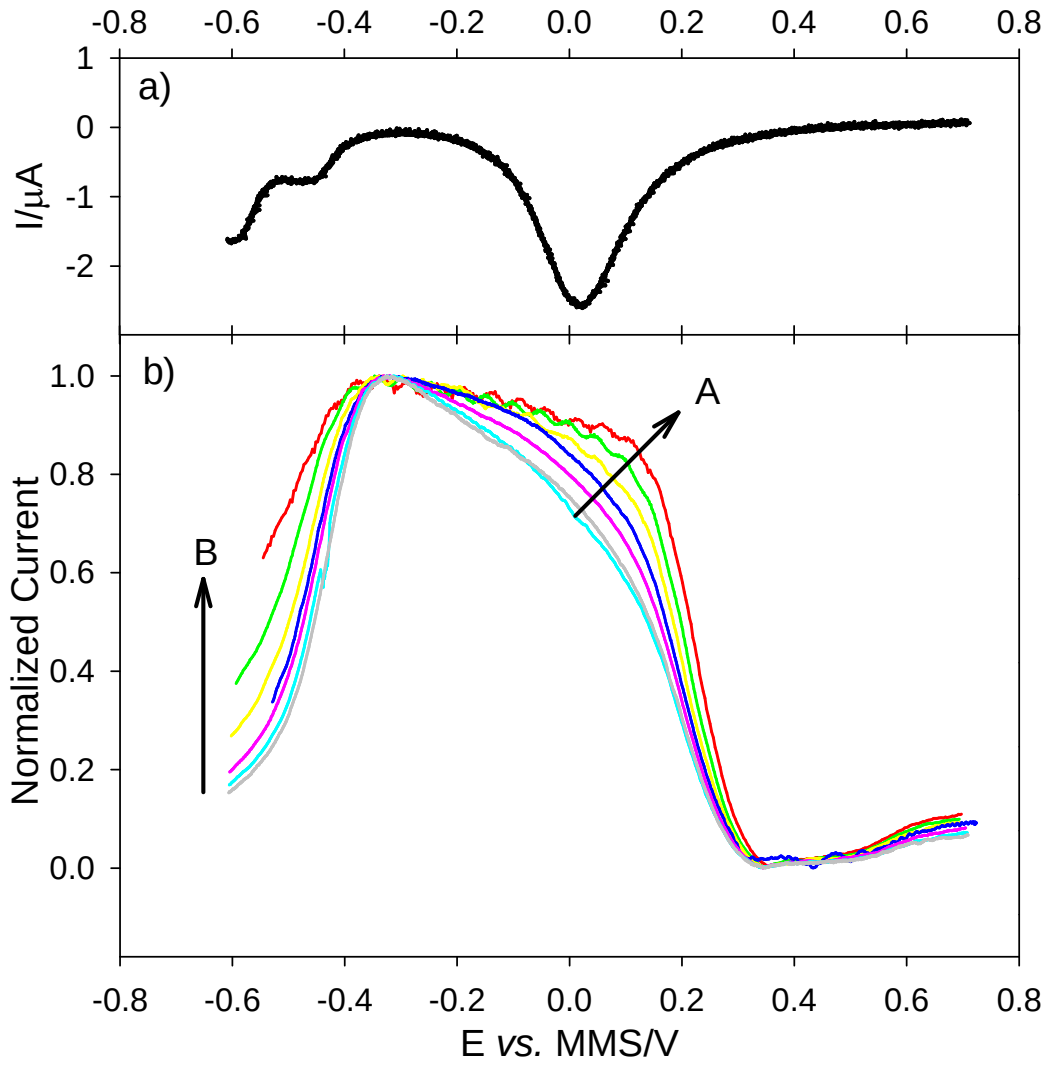

Figure 6.13. **a)** Plot showing time averaged current as a function of potential recorded at a stationary 50 μm diameter "tight-rope" Pt electrode. **b)** Plot showing normalized current (I/I_{max}) as a function of potential recorded at a vibrated 50 μm diameter "tight-rope" Pt electrode modulated at: 10 Hz (—), 20 Hz (—), 30 Hz (—), 40 Hz (—), 50 Hz (—), 60 Hz (—) and 70 Hz (—). The sweep was performed at 200 mV s^{-1}. The displacement amplitude of the electrode was 0.194 ± 0.001 mm. The presented data is for a component at twice the fundamental frequency of the mechanical oscillation. The solution used contained 1mmol dm^{-3} $[IrCl_6]^{2-}$ in 1 mol dm^{-3} H_2SO_4. The arrows show the direction of the modulation frequency decrease.

In the next step, the frequency of the modulation was kept constant (80 Hz) and the displacement amplitude was varied. Figure 6.14 shows that as the amplitude of electrode modulation was increased the signal magnitude at $2f$ also increased. This is expected as an increase in the amplitude of modulation results in an increase of the mass transfer of the electroactive species to the electrode surface as the electrode velocity is related to the displacement amplitude.

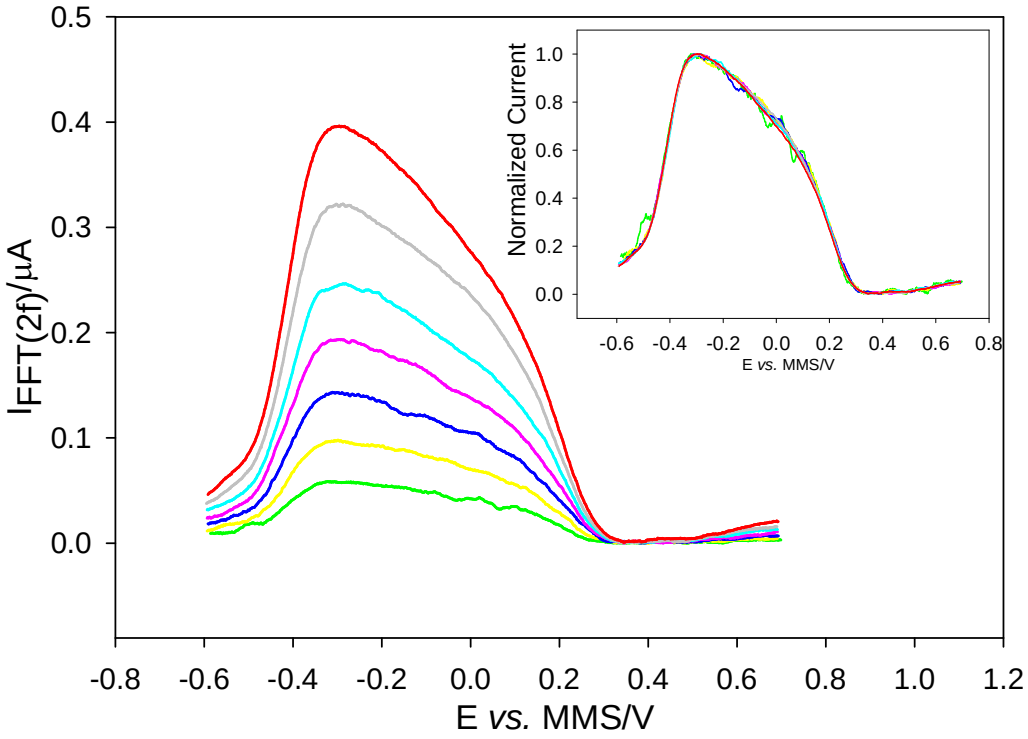

Figure 6.14. Plot showing current as a function of potential recorded at a vibrated 50 µm diameter "tight-rope" Pt electrode modulated at 80 Hz with a displacement amplitude of: 0.04 mm (—), 0.06 mm (—), 0.08 mm (—), 0.1 mm (—), 0.12 mm (—) and 0.14 mm (—). The presented data is at twice the fundamental frequency obtained using the FFT software. The sweep was performed at 200 mV s^{-1} and the sample rate was 645 Hz. The solution used contained 1mmol dm^{-3} $[IrCl_6]^{2-}$ in 1 mol dm^{-3} H_2SO_4. The measurements were performed at room temperature, 20-25 °C.

This can be interpreted mathematically as:

$$\dot{x} = A2\pi f \cos 2\pi ft \tag{6.1}$$

where $\dot{x}$ is the electrode velocity, A – the zero to peak displacement amplitude and f – the modulation frequency. Hence an increase of A results in an increase of $\dot{x}$. At the same time the shape of the voltammograms is not affected (see insert of figure 6.14) by the change in mechanical modulation amplitude.

In further experiments the influence of the sweep rate on the experimental results was investigated. It was interesting to note (figure 6.15) that at higher sweep rates the current potential response undergoes much higher distortion compared to those at the low sweep rate. In detail, the distortion in the oxide region is greater for 500 mV s^{-1} than for 50 mV s^{-1}. The maximum current at -0.3 V *vs.* MMS also showed a decrease as the sweep rate increased. Hence the time scale of the experiment is particularly important in determining the magnitude of the oscillating current signal.

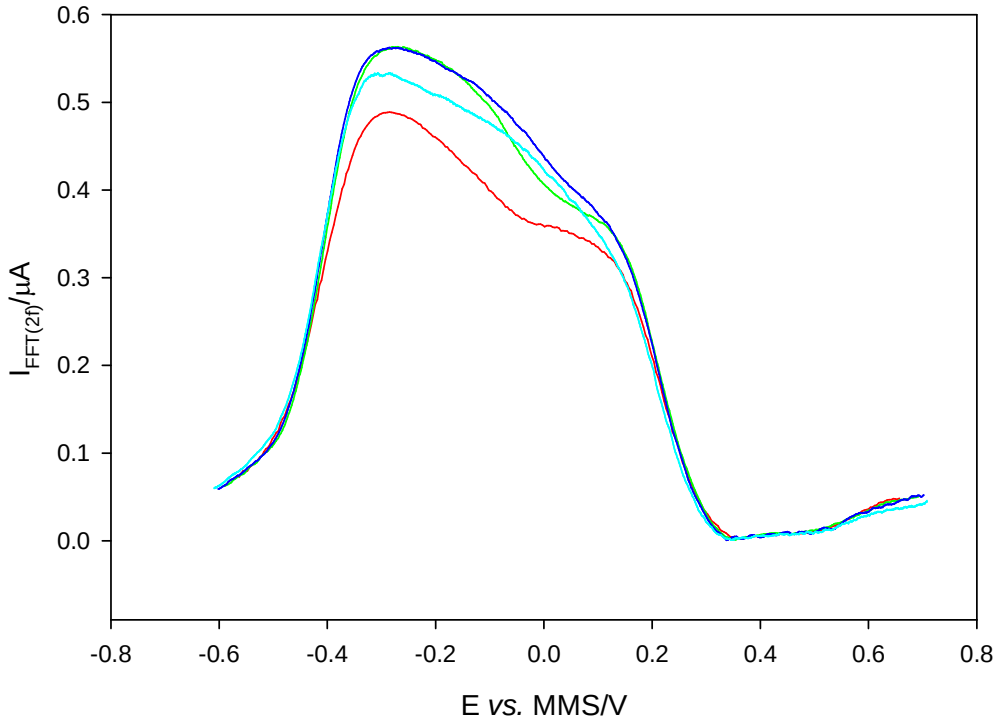

Figure 6.15. Plot showing current as a function of potential recorded at a vibrated 50 μm diameter "tight-rope" Pt electrode modulated at 80 Hz with a displacement amplitude of 0.194 ± 0.001 mm. The sweep was performed at 500 mV s^{-1} (—), 200 mV s^{-1} (—), 100 mV s^{-1} (—) and 50 mV s^{-1} (—). The presented data is at twice the fundamental frequency obtained using the FFT software. The sample rate was 645 Hz. The solution used contained 1mmol dm^{-3} $[IrCl_6]^{2-}$ in 1 mol dm^{-3} H_2SO_4. The measurements were performed at room temperature, 20-25 °C.

Overall, it has been shown that the distortions observed depend on the modulation amplitude, frequency and sweep rates employed. However, it is still unclear what caused this effect to appear. At the same time it was noticed that there is a clear relationship between the electrode's surface processes and the current distortions. The origin of these effects will now be discussed further.

6.6 Comparison of $[IrCl_6]^{2-}$ Electrochemistry on Pt and Au Electrodes when Using the FFT Approach

In order to highlight the role of capacitive effects platinum was replaced with a gold electrode. This is because of a number useful characteristics (*231, 232*). First, the double-layer region observed in cyclic voltammograms recorded for gold in aqueous media extends from approximately -0.6 to 0.7 V *vs.* MMS (figure 6.16). Second, molecular hydrogen does not chemisorb on bulk gold because of the high activation energy for this reaction (*231*). Hence, the $[IrCl_6]^{2-}$ reduction reaction will fall in the

double layer region and should not be affected by any surface process (and the corresponding capacitive effect).

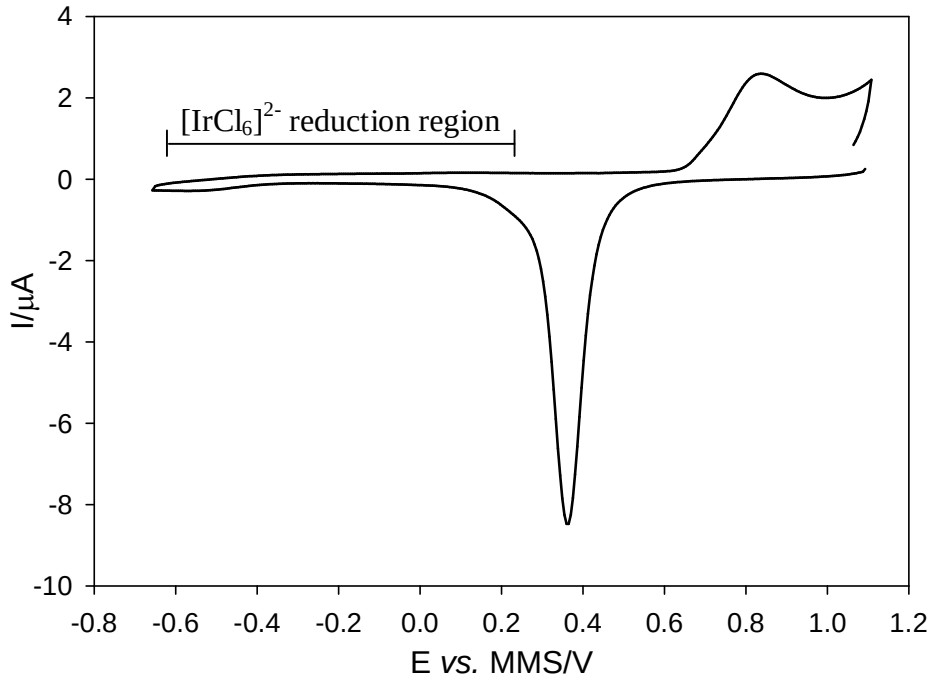

Figure 6.16. Cyclic voltammetry recorded at stationary "tight-rope" Au electrode (50 μm diameter) in anaerobic 1 mol dm^{-3} sulfuric acid solution. The sweep rate employed was 200 mV s^{-1}. The measurements were performed at room temperature, 20-25 °C.

The electrochemistry of $[IrCl_6]^{2-}$ was investigated for both gold and platinum electrodes under the same experimental conditions. The FFT analysis of the data obtained from these experiments is presented in figure 6.17. It was observed that the current distortions recorded at the Pt electrode (figure 6.17a) were removed when a Au electrode was employed (figure 6.17b). A classic sigmoidal voltammogram was obtained at the Au electrode (see figure 6.17b). A steady state region could be clearly seen below -0.1 V *vs.* MMS. Note that the geometric area of the two electrodes slightly differs (see Chapter 2 for more details). The ratio was found to be 4:5 for Pt:Au. However, the data in figure 6.17 shows that current recorded at the Au electrode is four times bigger than the Pt case. This indicates that the current within the whole potential region below +0.2 V *vs.* MMS for platinum electrode is significantly attenuated. The Pt results show that the biggest distortions are observed at potentials where hydrogen adsorption takes place at the platinum surface.

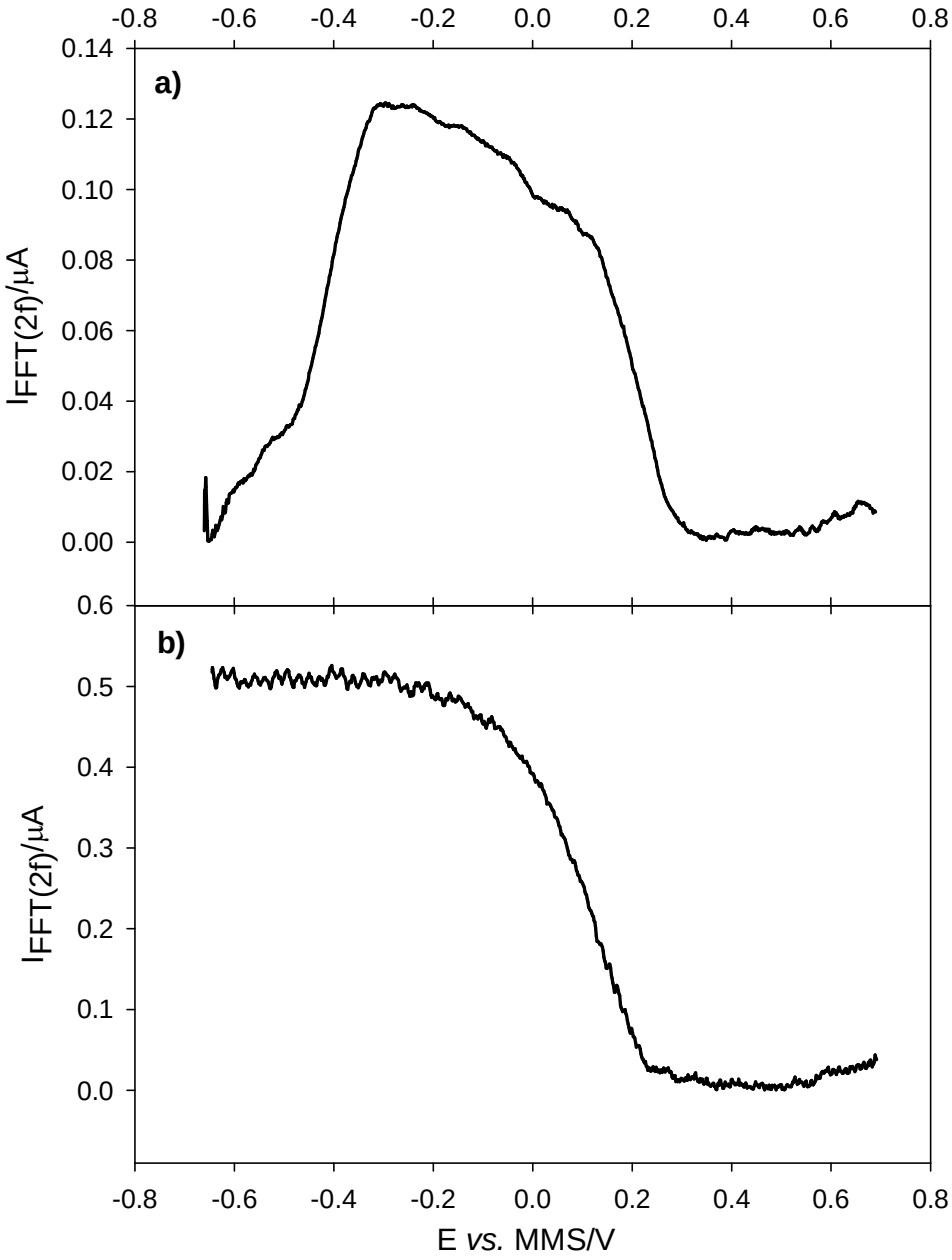

Figure 6.17. Graphs illustrating the current response at twice the fundamental frequency at **a)** 50 μm diameter Pt and **b)** 50 μm diameter Au "tight-rope" electrodes obtained using the FFT approach. Both electrodes were modulated at 80 Hz (sample rate 645 Hz) and the displacement amplitude was 0.159 ± 0.001 mm. The scan rate used was 200 mV s^{-1}. The solution used contained 1 mmol dm^{-3} $[IrCl_6]^{2-}$ in 1 mol dm^{-3} H_2SO_4. The measurements were performed at room temperature, 20-25 °C.

The absence of any anomalous current changes for a gold electrode confirms that the current distortions are clearly related to the surface properties of the electrodes used. The capacitance (see later discussion in chapter 7) of the electrode is less likely to be the reason for the current changes because of the relatively low surface area electrode used (~0.47 mm^2). However, a clear question remains; could the uncompensated

resistance, R_U, of the cell play a role in the measurements? The next section examines this effect.

6.7 Cell Design Investigations

The cell design can play a crucial role in the electrochemical response. It is important in designing a cell that the experimental data would be determined by the properties of the reaction at the working electrode (*225*). In this section we look at two different designs of cells and try to identify the changes these rearrangements bring. In particular, the electrochemical response of two and three electrodes systems will be compared.

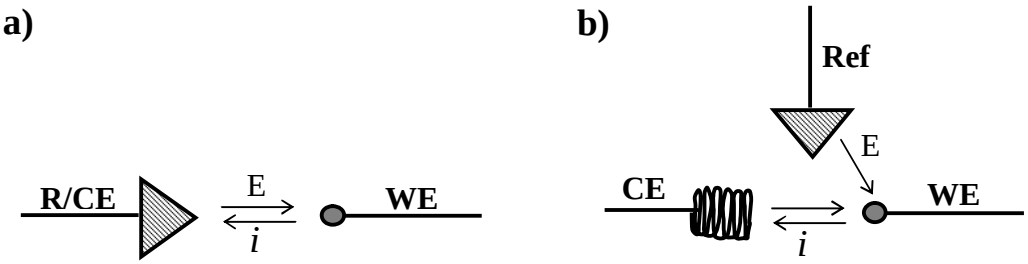

Figure 6.18. Schematic representation of **a)** 2- and **b)** 3- electrode electrochemical cells design.

In a two-electrode cell (figure 6.18a) the current flows between the working (WE) and the reference/counter (R/CE) electrodes. Here, the role of the reference electrode is to be able to maintain constant potential even when current passes through its surface. But flowing current should be sufficiently small to avoid the polarisation of the reference electrode. The uncompensated resistance of the cell depends on both the working and reference electrodes. In the case of the three electrode system (figure 6.18b) the current flows between the working and the counter electrode, and the role of reference electrode is to provide a fixed potential. In this arrangement the uncompensated resistance of the working electrode dominates over the small resistance of the counter electrode. In all previous experiments because of the relatively small current passed, a two-electrode system was used. In order to find out if changing of the R_U value of the cell had an effect upon the electrochemical response, the signal for two- and three- electrode cells were compared. Figure 6.19 shows the dramatic change in the shape of the voltammogram when the design of the cell was changed from a two to three electrode system.

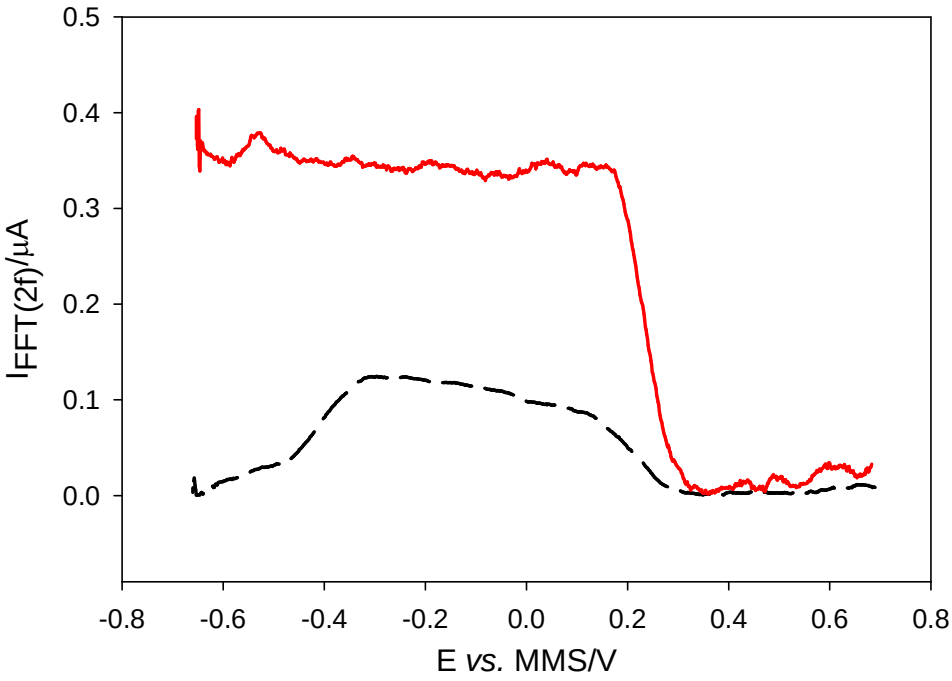

Figure 6.19. FFT analysis for $(IrCl_6)^{2-}$ reduction at a 50 µm diameter Pt "tight-rope" electrode in a 2- (— —) and a 3- (—) electrode cells respectively. The frequency of the electrode vibration was 80 Hz (sample frequency was 645 Hz) and the displacement amplitude was 0.159 ± 0.001 mm. The sweep rate used was 200 mV s^{-1}. The presented signal is at frequency of 160 Hz. The solution employed was anaerobic 0.6 mmol dm^{-3} $[IrCl_6]^{2-}$ in 1 mol dm^{-3} sulfuric acid. The experiments were performed at room temperature, 20-25 °C.

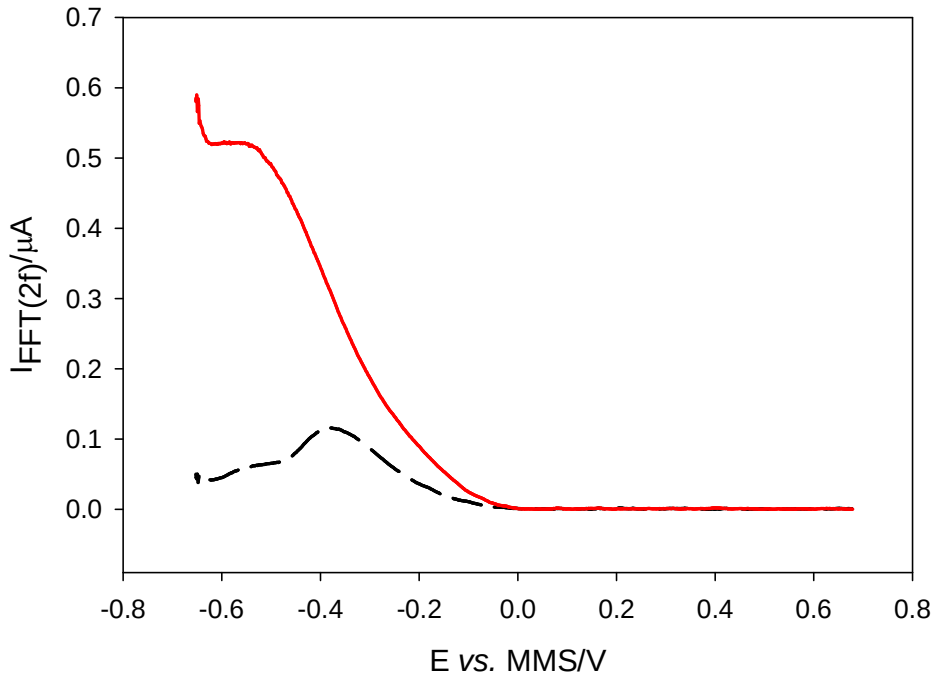

Figure 6.20. FFT analysis for molecular oxygen reduction at a 50 µm diameter Pt "tight-rope" electrode in a 2- (— —) and a 3- (—) electrode. The frequency of the electrode vibration was 80 Hz (sample frequency was 645 Hz) and the displacement amplitude was 0.194 ± 0.001 mm. The sweep rate used was 200 mV s^{-1}. The presented signal is at twice the fundamental frequency. The solution employed was 1 mol dm^{-3} sulphuric acid. The experiments were performed at room temperature of 20-25 °C.

The damping observed for the two electrode system (— —) disappears with the change to the three electrode set up (—). A sigmoidal-shape voltammogram was obtained. In addition an increase in current was recorded below +0.3 V *vs.* MMS followed by a clear steady state region (from +0.2 to -0.6 V *vs.* MMS). A similar effect was observed when molecular oxygen reduction (see figure 6.20) was investigated. These results suggest that the damping effect observed was related to the uncompensated resistance of the cell. This is however unusual as the current is relatively small and *i*R should be negligible (*10*). Another source of the uncompensated resistance, which can be important in these measurements, is the reference electrode's resistance. This consideration was checked by replacing the MMS electrode with a Ag wire reference electrode. Again a two-electrode cell was employed in this experiment. The results are illustrated in figure 6.21. In this case no damping effect was observed, the classic sigmoidal-shape voltammogram was obtained with this type of arrangement. This implies that the Ag REF/Counter has a significant effect, compared to MMS on the signal and avoids the "damping" effect.

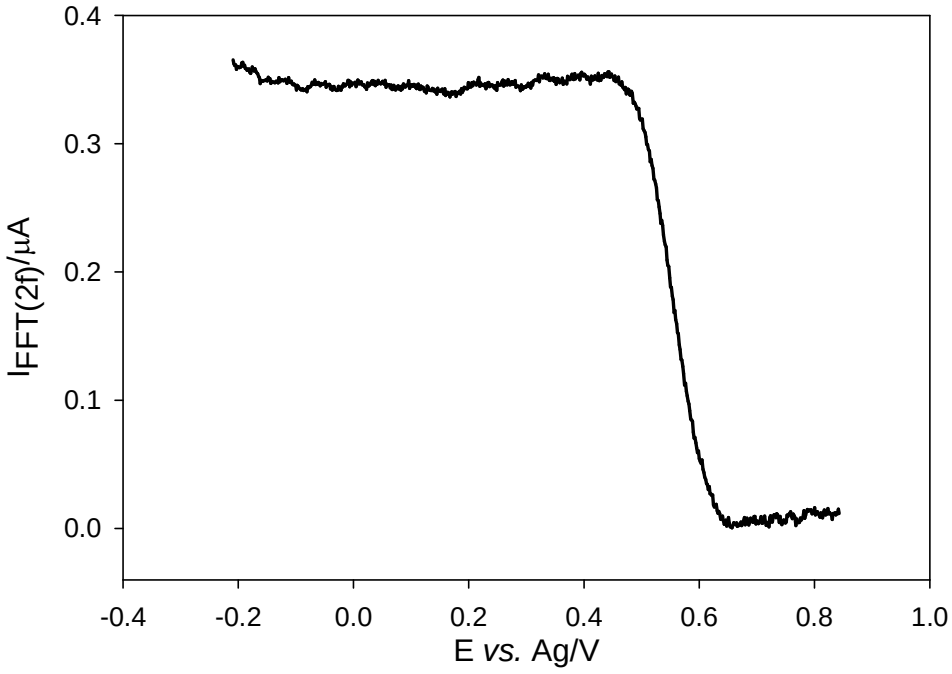

Figure 6.21. FFT analysis for $(IrCl_6)^{2-}$ reduction at a 50 μm diameter Pt "tight-rope" electrode in a 2- electrode cell. The reference electrode used was a Ag-wire. The frequency of the electrode vibration was 80 Hz with a sample frequency of 645 Hz and the displacement amplitude was 0.159 ± 0.001 mm. The sweep rate used was 200 mV s^{-1}. The presented signal is at twice of the fundamental frequency. The solution employed was anaerobic 0.6 mmol dm^{-3} $[IrCl_6]^{2-}$ in 1 mol dm^{-3} sulfuric acid. The experiments were performed at room temperature, 20-25 °C.

In addition, the R_U values for both reference electrodes were determined. This was done by applying a high frequency AC voltage (20 kHz, 20 mV (p-p) amplitude) to a reference electrode and measuring the corresponding AC current. Here we assume that all capacitance effects are avoided under these conditions. Applying Ohm's law enables the calculation of the uncompensated resistance of the cell. These measurements showed that R_U for the Ag reference electrode cell was 88.5 Ω while for the MMS electrode a value of 2.63 kΩ was determined. Note in both cases the solution used was 1 mol dm^{-3} sulfuric acid. The significant difference in the uncompensated resistances values for Ag and MMS electrodes may explain the dissimilar response of the two systems. This was further checked by experiments. Figure 6.22 shows that if a 2.7 kΩ resistor was added to the three-electrode cell (in series with the WE) the response recorded for molecular oxygen reduction became damped at potentials below -0.35 V *vs.* MMS.

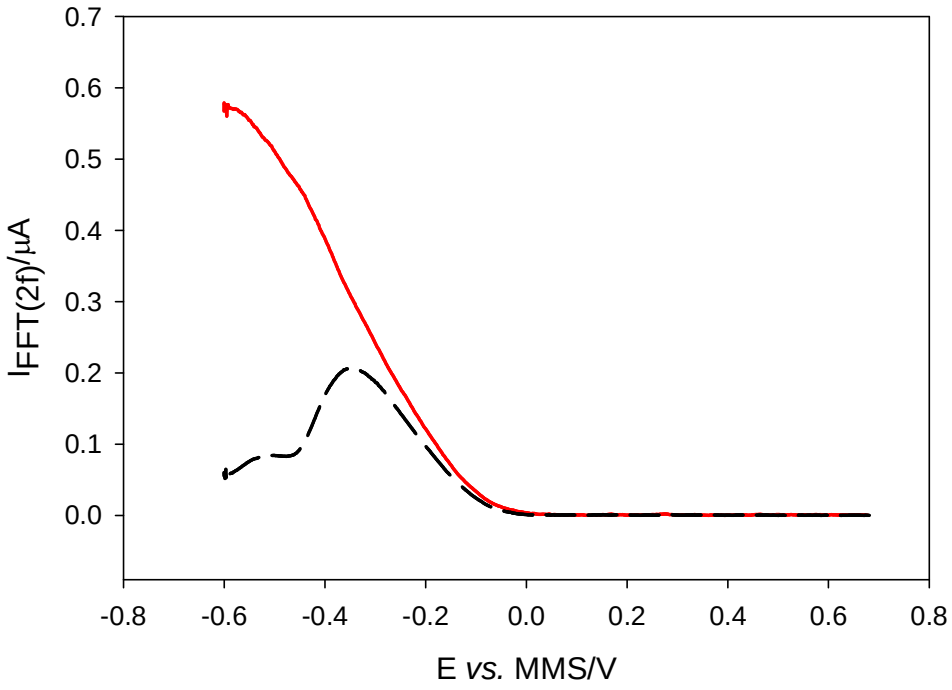

Figure 6.22. FFT analysis for molecular oxygen reduction at a 50 μm diameter Pt "tight-rope" electrode in a three-electrode cell with (— —) and without (—) 2.7 kΩ resistor added. The frequency of the electrode vibration was 80 Hz (sample frequency was 645 Hz) and the displacement amplitude was 0.194 ± 0.001 mm. The sweep rate used was 200 mV s^{-1}. The presented signal is at twice the fundamental mechanical modulation frequency. The solution employed was 1 mol dm^{-3} sulfuric acid. The experiments were performed at room temperature, 20-25 °C.

These investigations clearly show the effect of the uncompensated resistance on the electrochemical response. These also demonstrate the importance of cell design for the measurements.

It should be also noted that all HMV measurements on the nanostructured Pt electrodes (see chapter 5) were performed using the 3-electrode systems and the uncompensated resistance here should be at a minimum.

6.8 Summary and Conclusion

This chapter introduced a novel hydrodynamic electrode, the vibrated wire, "tight-rope" electrode. High frequency oscillations (>80 Hz) were produced using the electrodes. In order to analyse the frequency response of the experimental data a FFT method was employed. First, the technique was applied when studying the reduction/oxidation of $[Fe(CN)]_6^{3-}$ species. The strong signals at 80 Hz and 160 Hz were detected as expected in this system considering a mechanical modulation of the electrode at 80 Hz. Second, the FFT-HMV at "tight-rope" electrode was employed to investigate the reduction of molecular oxygen. The role of the FFT approach was to eliminate a background (surface processes, double layer charging *etc.*) signal from mass transport dependent component signal. Increase in current was recorded in the potential region between 0.00 and -0.35 V *vs.* MMS as the result of molecular oxygen reduction at the microwire electrode. However, at potentials below -0.35 V *vs.* MMS (H_{UPD} region) a drop off in current was observed. The current potential behaviour was similar to the one obtained at the high roughness factor nanostructured electrodes described in chapter 5. The effect was investigated further when the oxygen reduction system was replaced with $[IrCl_6]^{2-/3-}$ electrochemistry. A deflection in current was observed in Pt-oxide region followed by a current drop off in the Pt-hydride region when the reduction of the $[IrCl_6]^{2-}$ was studied using the FFT-HMV. The distortion effect was shown to be frequency and sweep rate dependent. The relationship of the effect and surface processes was further investigated when the Pt electrode was replaced with Au. The reduction of $[IrCl_6]^{2-}$ at the gold electrode falls in the double layer region. Therefore it was expected that the electrochemistry of $[IrCl_6]^{2-}$ would not be affected by surface process. The absence of any anomalous current changes for a gold electrode confirmed the relation of the distortions to the surface properties of the electrodes employed. In further experiments a role of uncompensated resistance was investigated. In this case

the electrochemical response for two- and three- electrode cells were recorded. It was observed that the damping effect disappears on changing from a two- to three-electrode setup. Therefore it was concluded that the uncompensated resistance was the reason for the damping effect observed when the reduction of both molecular oxygen and $[IrCl_6]^{2-}$ was studied. It was found that the source of the uncompensated resistance is the reference electrode's resistance. The conclusion was made when the MMS reference electrode was replaced with Ag-wire as a reference/counter electrode. This simple rearrangement removed current distortions from the experimental signal with MMS as reference electrode. In addition, the R_U values for both reference electrodes were determined. These were 88.5 Ω for Ag reference electrode cell and 2.63 kΩ for MMS reference electrode cell. Further when a 2.7 kΩ resistor (in series with the WE) was added to the three-electrode cell the response recorded for molecular oxygen reduction became damped. This again suggested that the damping effect is due to the uncompensated resistance of the cell.

Chapter 7

Understanding the Temporal Behaviour of a Pulsed Mass Transfer System

7.1 Overview

The results presented in this thesis in relation to the pulsed response of an electrochemical cell have several clear characteristics. First, the response of a nanostructured electrode to a pulsed mass transfer regime (specifically the flow created from a hydrodynamic jet) shows "damping" as the electrode enters the high pseudo capacitive region of the voltammetry. Figure 7.1 illustrates this effect in relation to the capacitance of the electrode (determined by analysis of cyclic voltammetry see figure 7.1 a). This shows the correlation between the capacitance of the electrode and the "damping effect" observed in the hydride region. Chapter 5 showed that the damping effect increased as the roughness factor of the electrode was raised.

Second, the resistance of the cell has a significant effect on the response of an electrode when a vibrating wire microelectrode (the so called "tight rope" electrode, see chapter 6) is employed at relatively high oscillation frequencies (here up to 150 Hz). Both of these observations are indicative of the cell design and electrical characteristics thereof, playing a role in the performance of the electrode. This is surprising as one may not expect either R_u or C_{dl} to play a role in the mass transfer response of the electrode. However, as will be shown here, this appears not to be the case and consideration of these effects must be employed for electrodes with either high capacitance values or cells with high uncompensated resistance. In order to explain these experimental observations we will employ a simple equivalent circuit to describe the function of the modulated hydrodynamic voltammetry in question and use appropriate parameters to duplicate those within the electrochemical systems employed.

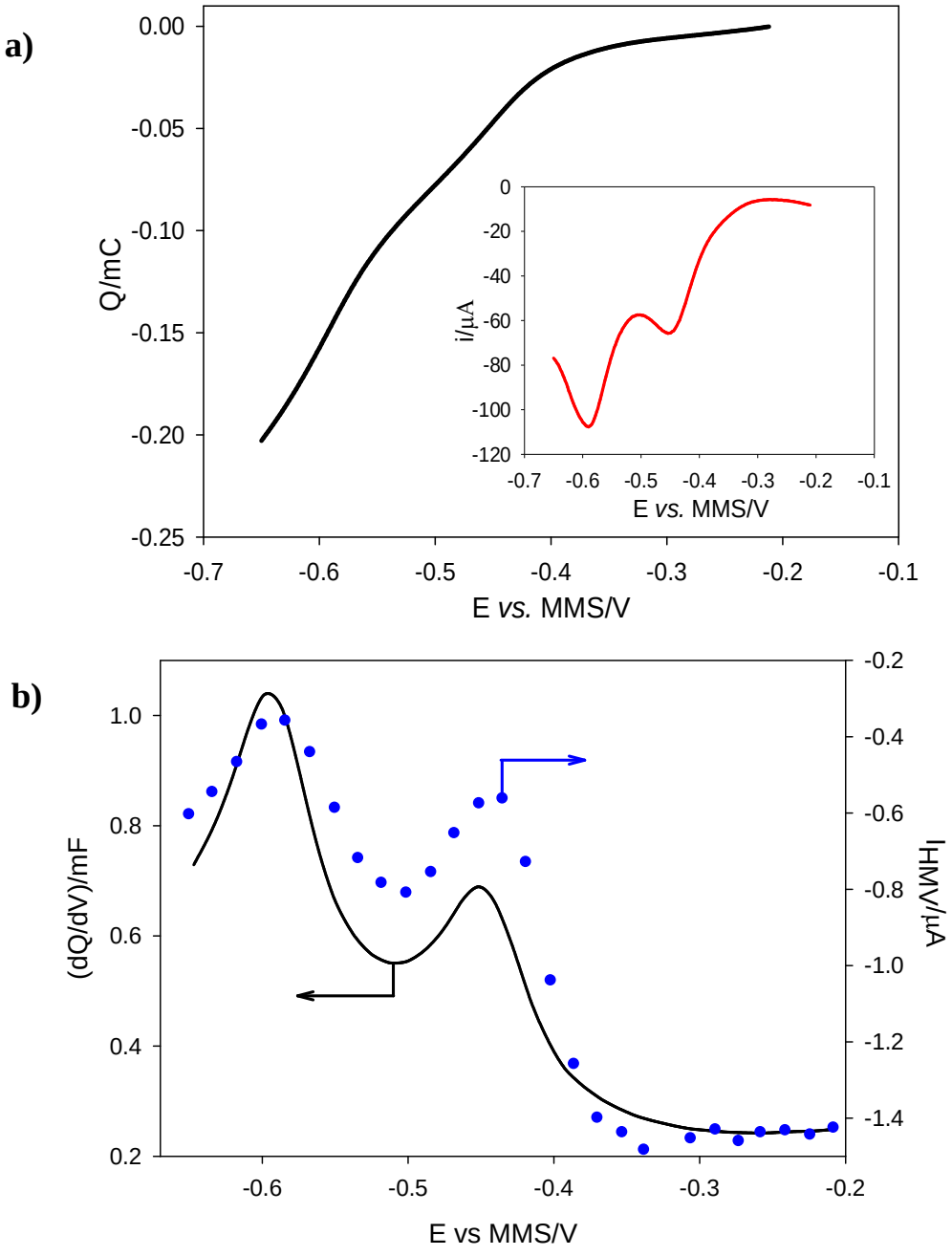

Figure 7.1. a) Plots showing the time averaged current I (—) and charge Q (—) as a function of the applied potential for the H_{UPD} region on a nanostructured platinum (500 μm diameter, RF = 280.8) electrode in contact with a 1 mol dm^{-3} sulphuric acid solution. The sweep rate was 100 mV s^{-1}. b) Plot showing the Capacitance (dQ/dV, —) and HMV current (I_{HMV}, •) profiles as a function of the applied potential for the hydrogen adsorption process at a platinum electrode (500 μm diameter, RF = 280.8) surface in 1 mol dm^{-3} sulphuric acid solution. The HMV sweep was performed at 20 mVs^{-1}. The jet was modulated at a frequency of 16 Hz with a piston displacement amplitude of 0.011 ± 0.001 mm.

Figure 7.2 shows a schematic of an electrochemical cell as an equivalent circuit (*10*).

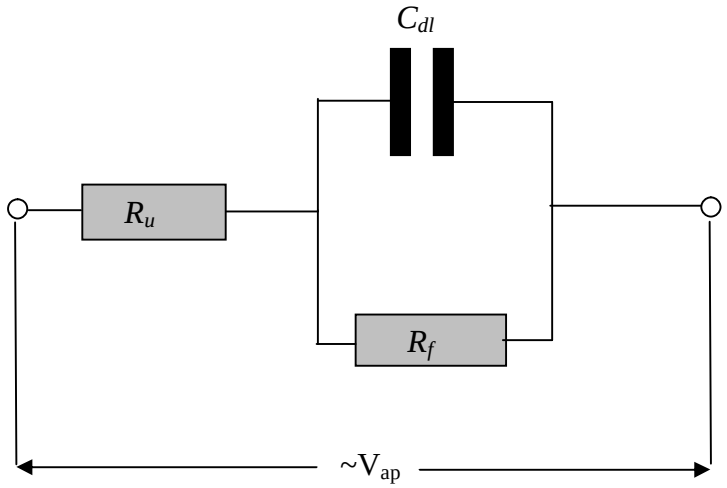

Figure 7.2. Schematic representation of an equivalent circuit for an electrochemical cell. Here ~V_{ap} is the cell voltage, R_u the uncompensated resistance, R_f the faradaic resistance and C_{dl} the double layer capacitance.

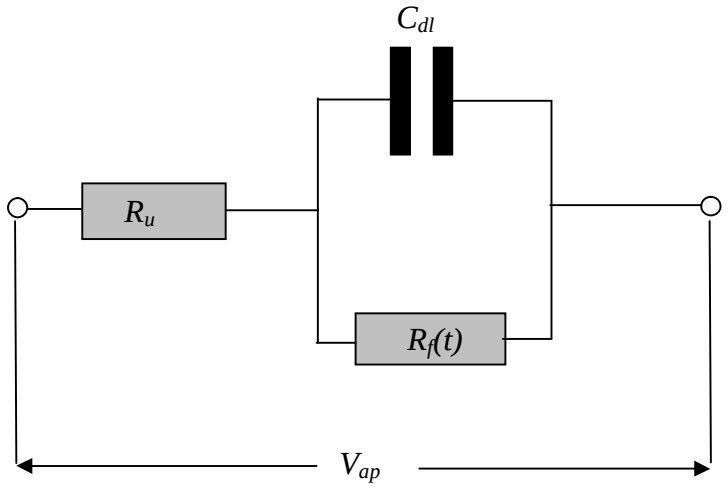

Figure 7.3. Schematic representation of an equivalent circuit for an electrochemical cell operating in an HMV experiment. Here V_{ap} is the applied cell voltage, R_f the time dependant faradaic resistance. All other components are described in figure 7.2.

In normal impendence experiments, the cell voltage is modulated (~V_{ac}) and the frequency characteristics of the circuit components are measured (*233*). However, in the HMV experiments the cell voltage is kept constant (for example at the mass transfer limited potential) and the value of the faradaic resistance changes as a function of time (in line with the operation of the pulsating jet or the oscillation of the tight rope assembly). Hence figure 7.3 is a more representative schematic of the equivalent cell.

Under the conditions operating in the HMV cell, R_f varies allowing current to modulate between 3 and 7 μA (see chapter 5, figure 5.11). A set of experiments, designed to

investigate this type of system, were performed. These are presented in the next section.

7.2 Test Circuits

The current generated by the HMV action will not be sinusoidal in nature (see high-speed imaging, chapter 4 and the current time traces in chapter 3). Instead a square wave function (where the mass transfer modulation from the jet manifest itself as an 'on and off' transient) is more appropriate. In order to explore the behaviour of such a system, a set of simple test circuits were constructed and tested. Figure 7.4 shows a schematic of the test cell employed and the variables explored in the experiments.

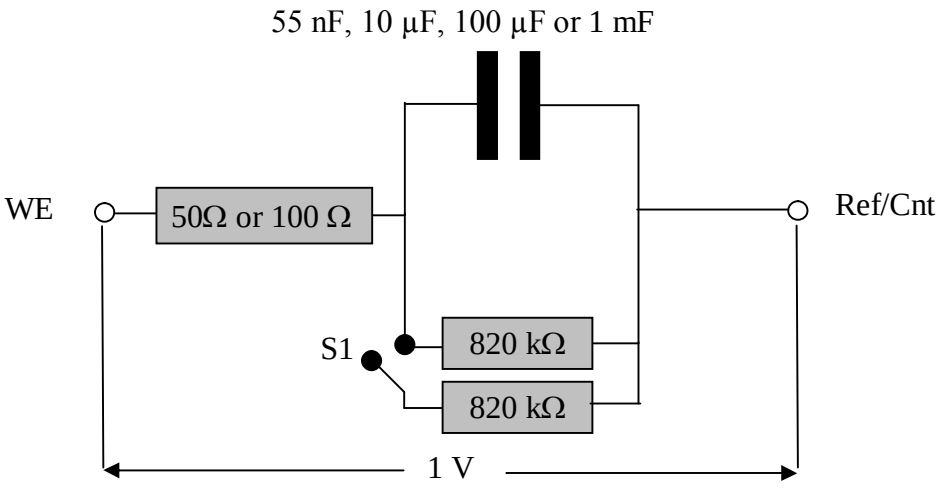

Figure 7.4. Schematic representation of a test equivalent circuit for an electrochemical cell operating in an HMV experiment. Here the applied cell voltage was kept constant at 1 V, the time dependant faradaic resistance was switched (using switch S1) between 820 kΩ and 410 kΩ. A variety of double layer capacitances and uncompensated resistances were employed. The cell current was measured as a function of time in response to a faradaic resistance step using a potentiostat and recorded on an oscilloscope.

Figure 7.5 and 7.6 show the response of two test circuits to a step in the faradaic component of the circuit. In both cases the current measured by the potentiostat has a time component dependant on the size of the double layer capacitance employed.

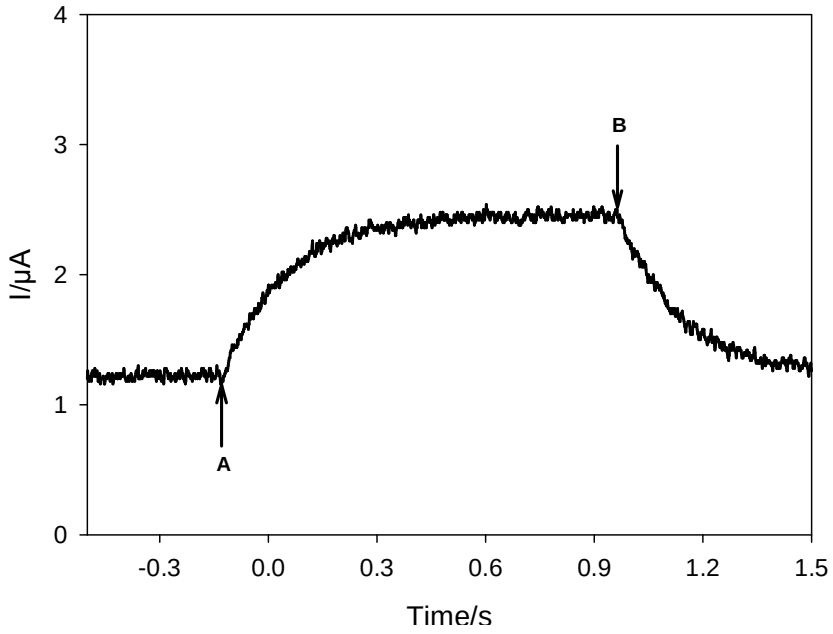

Figure 7.5. Plot showing the current time response of a test circuit to a faradaic current step. Here C_{dl} = 1 mF and R_u = 100 Ω. The faradaic component of the circuit was switched from 820 to 410 kΩ and back again at point 'A' and 'B' respectively.

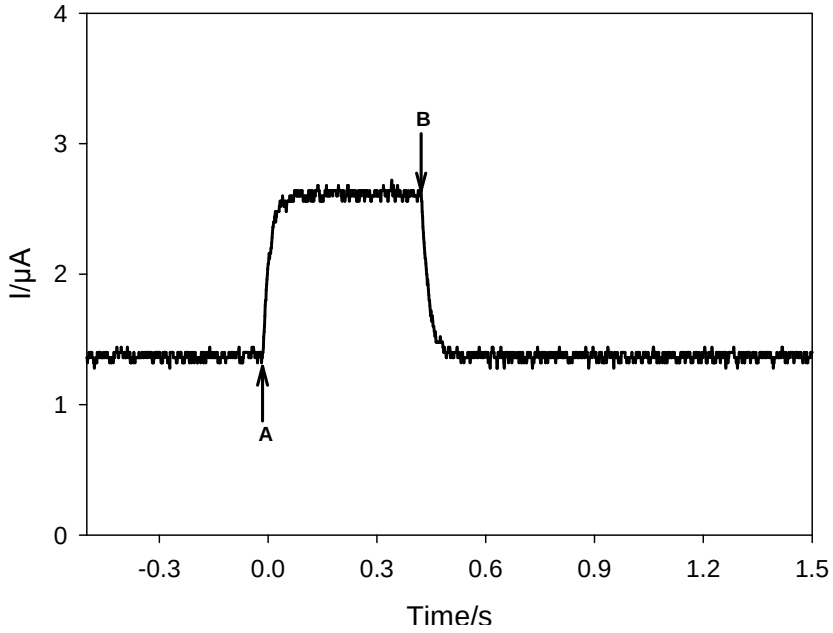

Figure 7.6. Plot showing the current time response of a test circuit to a faradaic current step. Here C_{dl} = 100 µF and R_u = 100 Ω. The faradaic component of the circuit was switched from 820 to 410 kΩ and back again at point 'A' and 'B' respectively.

Figure 7.7 and 7.8 show the effect of decreasing the double layer capacitance still further. Note in figure 7.8 the value of C_{dl} was chosen to match that of a polished 0.5 mm diameter Pt electrode (e.g. 55 nF assuming a capacitance value of 30 µF cm^{-2}). Under these conditions the response of the test circuit closely matches the circuit in the absence of a double layer capacitance (**—**, figure 7.8).

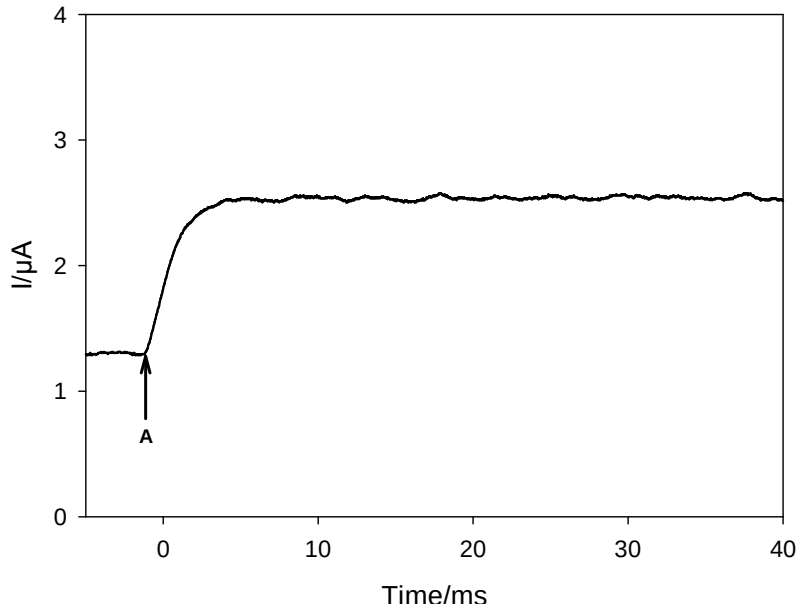

Figure 7.7. Plot showing the current time response of a test circuit to a faradaic current step. Here C_{dl} = 10 µF and R_u = 100 Ω. The faradaic component of the circuit was switched from 820 to 410 kΩ at point 'A'.

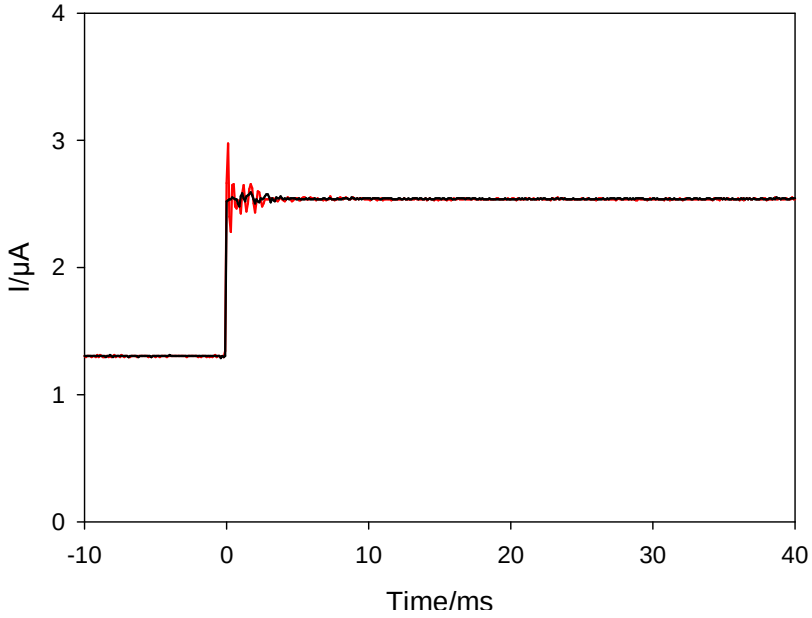

Figure 7.8. Plot showing the current time response of a test circuit to a faradaic current step. Here C_{dl} = 55 nF (—) or 0 nF (—) and R_u = 100 Ω. The faradaic component of the circuit was switched from 820 to 410 kΩ at point time = 0 s.

Clearly the experiments reported in this thesis suggest that far from being a passive component the double layer of an electrode can be an active element in a faradaic reaction.

Further interesting observations can be made if the transients obtained from these test circuits are fitted to an exponential response expected for a classic *RC* circuit. Note the

reason for this choice is based on the observation that the transients appear like an '*RC*' type signal. Figure 7.9 shows one result of such an analysis.

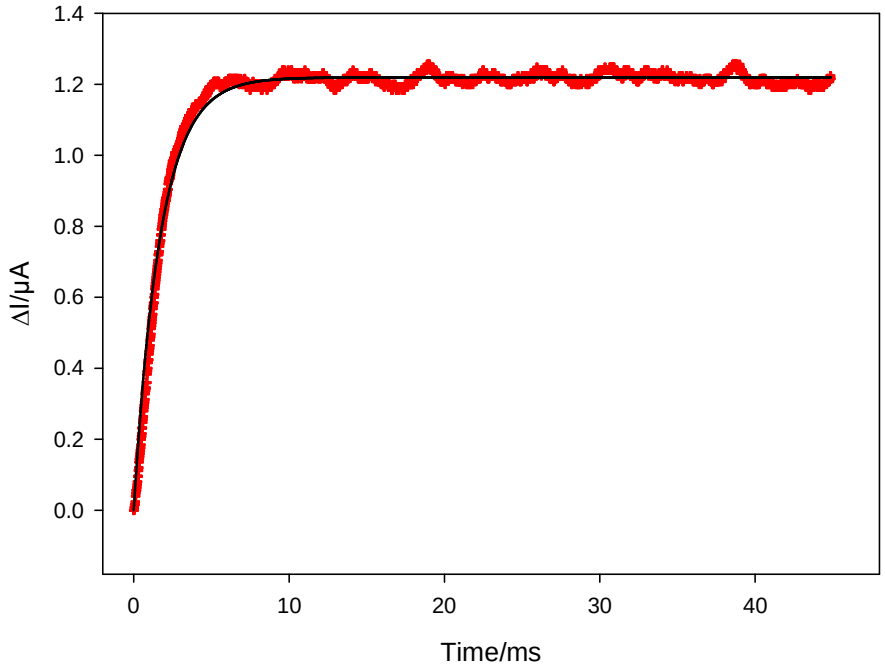

Figure 7.9. Plot showing the response of a test circuit to a faradaic current step. Here C_{dl} = 10 μF and R_u = 100 Ω. (—) represents the curve fit to an exponential response while (●) represents the experimental data. In this case the change in current (ΔI) relative to the step time is plotted and fitted.

While the fit is reasonable some deviation from the perfect response is seen at short times. Nevertheless this procedure was repeated for a number of different test circuits. Table 7.1 shows a collection of results from this analysis.

R_u/Ω	C_{dl}/μF	$(1/R_uC_{dl})$ fit/s^{-1}	$(1/R_uC_{dl})$/s^{-1}
50	100	72.0	200
100	10	586	1000
	100	51.0	100
	1000	5.5	10

Table 7.1. Table showing the fit parameters obtained from the data analysis. Note the last column represents the $(1/R_uC_{dl})$ value considering the value of R_u and C_{dl} only employed in the test circuit.

This analysis shows that the response time of the circuit scales linearly with the capacitance value employed. In addition the value of the uncompensated resistance has an effect on the measured response. However, the values obtained do not match the classic R_uC_{dl} values (see last column table 7.1).

7.3 The Currents Flowing

The previous section sets the scene for an interesting discussion. The question must be asked, where does the current come from that must ultimately be flowing through the faradaic resistors (as we assume that mass transfer limiting conditions are always invoked)? One possibility is that the current flows from the capacitive element of the circuit. Hence, as the switch is closed (or the pulse of liquid hits the electrode in the HMV experiment) charge flows from the double layer capacitor into the faradaic reaction. This suggests that the path for current flow is easiest from this route at short times. Indeed the connections between the capacitance of the double layer and the faradaic component of the circuit are thought to have a small resistance. This causes the double layer to discharge slightly before electrons are pumped in from the external supply through the higher resistance path (the R_u). Clearly the bigger the capacitance (as shown in the test experiments and the HMV experiments at high surface area electrodes) the longer this process appears to continue. In turn it seems that it takes a longer time for the external circuit to respond to the step function resistance change. As far as the electrochemistry of, for example, molecular oxygen is concerned, we presume it is still under mass transfer control (note the time averaged signal shows no deviation in the H_{UPD} region). Hence the initial electrons are supplied from the double layer rather than the outer circuit (the potentiostat). In order to maintain electro-neutrality ions escape from the double layer. In time however, the electron source is the potentiostat. This argument implies that the larger the capacitance the longer this process should take and the smaller the uncompensated resistance the faster the external circuit should be involved. This is observed from both the experiments (see chapters 5 and 6) and the test circuits. The capacitance can be thought of here as a fast response electron source.

This argument has some interesting permutations. For example, what consequences are there for general HMV systems? We are already in a position to investigate the limitations of this technique. Clearly, the capacitive damping effects, observed here, imply that large electrodes with high surface roughness will not be able to respond to even modest dynamic changes in mass transfer. However, if the electrode geometric area were to be reduced, then the HMV response should be restored. Figure 7.10 shows such an experiment. Here a high surface area nanostructured electrode has been

fabricated with an impressive roughness factor of 941. However, this was a 50 µm diameter Pt microelectrode.

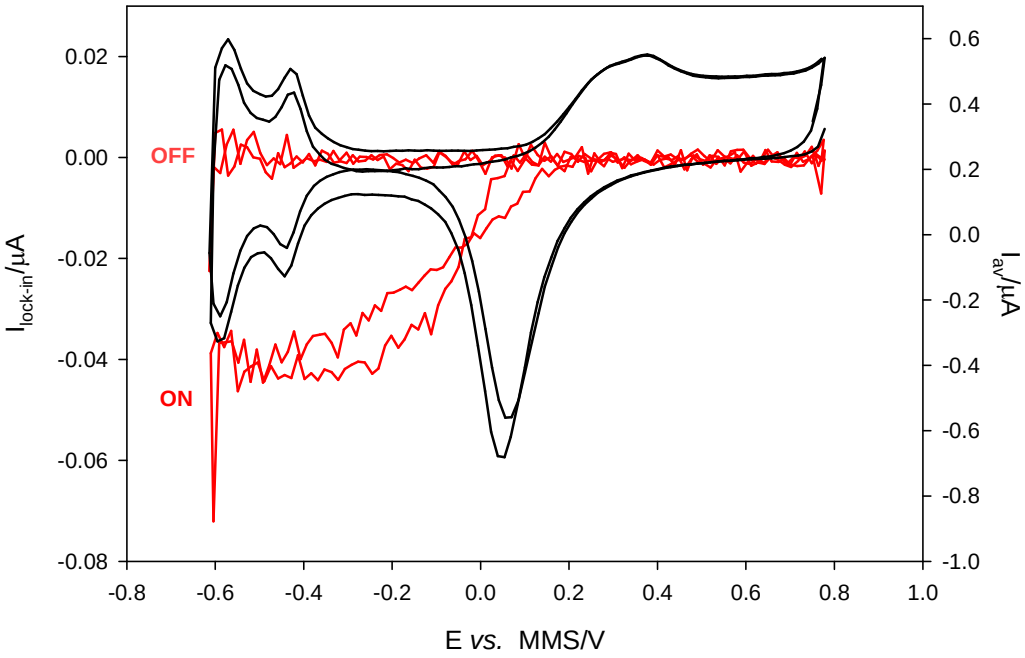

Figure 7.10. Plot showing the HMV signal (I_{HMV}, —) and average current signal (I_{av}, —) as a function of electrode potential recorded at 50 µm diameter nanostructured Pt microelectrode (RF = 941) in 1 mol dm^{-3} sulphuric acid solution. The plot shows the results from the jet on and the jet off. The sweep was performed at 20 mVs^{-1}. The jet was modulated at a frequency of 16 Hz and with a piston displacement amplitude of 0.014 ± 0.001 mm. The temperature of solution was 18-22°C.

The HMV analysis clearly shows no damping effect in the hydride region. This is expected as even though the roughness factor is greater by a factor of two compared to any 500 µm diameter electrode system described in chapter 5, the geometric surface area (and hence capacitance) is a factor of 100 smaller. Hence, under these conditions the capacitance is ~ 50 times less than that for the 500 µm diameter Pt nanostructured electrodes described in chapter 5. This improves the response time of this electrode and avoids the dramatic capacitive damping observed in chapter 5 (see figure 5.11).

7.4 Previous HMV Experiments

The experiments and conclusions drawn from the above discussion apply to HMV experiments but where would these effects be observed? Clearly the results reported here imply that high surface area electrodes are limited to low mass transfer modulation frequencies in HMV applications. However, it is important to put these conclusions in

context to the available literature. Table 7.2 lists some of the available literature and estimates of '*RC*' constants in comparison to the frequency regime employed.

HMV type	**Experimental**	**Estimated (1/*RC*)**	**Frequency range/s^{-1}**	**Expected Capacitive damping**
HMRDE (12)	0.316 cm^2	3516 – 35.16 Hz	3	No
Porous electrode (25)	5.9 cm^2 RVC disk	188 – 1.88 Hz	Step change	Possible as '*RC*' like response reported.
CF-MJE (72)	25 μm diameter disk	226 MHz – 2.26 MHz	0.67	No
FT HMRDE (31)	RDE 2.8 mm diameter	180 Hz – 18 kHz	0.02-12.6	No
Vibrating microwire (53)	800 μm diameter wire x 3 mm	14 kHz – 139 Hz	160	Possible for larger electrodes employed or higher uncompensated resistance. Could contribute to 'hydrodynamic efficiency' effects.
Vibrating micro and planar band (56)	10 μm x 2 mm 1 mm^2	55 kHz – 5.3 MHz 111 kHz – 1.1 kHz	2 - 50	No, although large planar electrode was quoted as not showing a modulated response. In addition the cell configuration was quoted as either 2 or 3 electrode.

Table 7.2. Estimated response times of a variety of HMV techniques. Note in many cases R_u values are not known (through either use of 2 or 3 electrode systems or unusual electrode geometries). Hence we will give a range of 10 – 1000 Ω for R_u within the calculations. Assuming a typical C_{dl} value of 90 μF cm^{-2} in all cases (a roughness factor of 3 for normal electrodes).

Table 7.2 indicates that for most systems reported in the literature, the experimental conditions (frequency range, area of electrodes and uncompensated resistance etc.) do not allow for this 'damping effect' to be observed. However, some exceptions may be noted. For example the microwire experiments where higher frequencies and larger electrodes have been combined do give some evidence for this possible effect.

7.5 Summary and Conclusions

The results and observations drawn from the experiments reported here and elsewhere in this thesis indicate that the design of the experimental set-up, the electrodes employed and the frequency range employed are key to successful HMV experiments. Interestingly, the 'damping effect' has been linked to both the capacitance (including pseudo capacitance) and uncompensated resistance of the systems employed. While there seems to be clear experimental evidence for this effect, further theoretical and complimentary experiments are required to elucidate the exact mechanistic details of this system.

Chapter 8

Conclusion

This thesis has investigated a mechanically driven pulsating jet as a new type of HMV technique. This system consisted of an inverted funnel with a membrane/piston attached to the bottom of the funnel. The modulation of the membrane/piston, caused by the vibration of a mini-shaker attached to the centre of the membrane, resulted in fluid flow (~ 1 m s^{-1}) at the funnel outlet. Positioning of the electrode at the exit of the jet significantly increased the current recorded at the electrode. The mass transfer rates (time averaged) of ~ 0.015 cm s^{-1} were achieved by the HMV set-up. The periodical character of the modulated current allowed a lock-in approach to be employed in investigations of a redox system. This was demonstrated for the $[Fe(CN)_6]^{3-/4-}$ redox system. Here lock-in to the modulated hydrodynamic signal was achieved through the deployment of bespoke software. The apparatus and analysing procedure produced a simple and efficient way to obtain the desired signal. The clear advantage of the technique over a conventional (time averaged) analysis was demonstrated when scanning across the jet in the XY and XZ plane. In particular, the HMV and phase angle mapping measurements were characterised by significantly improved spatial resolution of the jet orifice compared to the direct measurement of time averaged current for the same modulated system. Interesting observations were made from the scanning experiments. First, a ring like HMV signal was recorded around the funnel mouth. Second, the edge effect extended vertically into the solution. Third, the spatial extent of the signals detected in the XY and XZ planes showed clear dependence on diameters of the electrode and its glass support. These observations were clarified when the high-speed camera was used. The investigations of the flow at the exit of the jet revealed its vortex behaviour. The combination of high-speed camera and electrochemical experiments showed that the vortex rings play a significant role in spatial distribution of mass transport enhancement observed.

Interaction of the vortex rings with the electrode positioned above the jet resulted in formation of the secondary vortices. Therefore, it was proposed that the size and shape of the electrode support is an important factor in these investigations. The optimum modulation frequency employed in these studies was 16 Hz. The employment of the set-up at higher frequency was unsuccessful because of the limitations of the equipment. The application of this HMV technique to traces analysis experiments demonstrated excellent background noise to signal resolution and low (45×10^{-9} mol dm^{-3}) detection limits.

The HMV method was also applied to study reduction of molecular oxygen at nanostructured H_I-*Pt* electrodes. These electrodes are known to have high catalytic activity. However, the analysis of the solution phase species (*e.g.* oxygen) at the modified electrodes is often complicated by the background processes taking place at the surface of the electrode. In this thesis the elimination of the background currents from the faradaic signal has been undertaken using the lock-in approach. It was first employed when studied the reduction of molecular oxygen at 0.5 mm diameter nanostructured Pt electrode with roughness factor of ~42.4. Here the background signal was completely removed and only the mass transport controlled signal was recorded. Further investigations were carried out using a variety of roughness factors electrodes. A conventional response for the oxygen reduction was recorded at the high roughness electrodes (> 50) in the potential range between +0.5 and -0.3 V *vs.* MMS. However, an unexpected behaviour was monitored when the electrode entered the hydride region (< 0.3 V). A significant current drop was recorded at the nanostructured electrodes. It was also observed that the anomalous effect was only characteristic for the HMV signal and the time averaged current stayed unchangeable. The current drop was more significant as the roughness factor of the electrode increased. It was demonstrated that the decrease in signal was not caused by an error in the data analysis associated with a phase change. The possibility of the pH change during the experiment was also considered. However, the investigations showed that even when pH effects are eliminated (high buffer concentrations, low scan rates) a drop off in the signal still was observed. Another key parameter known to affect oxygen reduction is the actual mechanism of electroreduction, specifically the production of hydrogen peroxide as an intermediate species. Therefore further investigations were focused on the role of hydrogen peroxide in the anomalous effect observed. The RRDE-s with nanostructured and polished disks

were employed to study this problem. Note in both cases ring electrodes were nanostructured. According to these investigations the maximum fraction of H_2O_2 formed relative to the total amount of O_2 consumed is ~8.3 % for nanostructured disk electrode at potential below -0.6 V *vs.* MMS. This is 4.5 times less than that observed for the polished electrode. This suggested that the relatively small amount of hydrogen peroxide produced at the nanostructured RRDE are unlikely to be solely attributed to a change in the oxygen electrochemistry at the Pt electrodes investigated. It also was interesting to note that the shape of the drop followed the shape of the hydrogen adsorption region. It was proposed that a possible reason for the current "drop off" in the hydride region is the high capacitance of the electrodes used.

Similar "drop off" in current was observed when studying oxygen reduction at a 50 μm diameter "tight-rope" Pt electrodes. In this case higher frequency modulations (up to 160 Hz) of the electrode were employed. In order to eliminate the background processes from the mass transport controlled signal, FFT data processing was performed. The capacitive effect, suggested in the case of the nanostructured Pt electrodes, cannot be the case for the current decrease for the microwire electrodes. Clearly the low capacitance of the electrodes suggests that there should be another contribution to the observed "damping" effect at a Pt "tight-rope" electrode. The effect was investigated further by replacing the molecular oxygen reduction with the $[IrCl_6]^{2-/3-}$ redox system. Several observations were made as a result of these studies. First, the signal deviations were observed for the $[IrCl_6]^{2-}$. This suggested that the effect described does not depend on the redox species. Second, the damping effect becomes more dramatic as the frequency of modulation or sweep rates increase. Third, deflection in current was observed in Pt-oxide region followed by a current drop off in Pt-hydride region when the reduction of the $[IrCl_6]^{2-}$ was studied using the FFT-HMV. A clear relationship between the electrode surface processes and the current distortions lead to the further investigations where the Pt electrode was replaced with Au. Here no anomalous current changes were observed. This confirmed that the current distortions are still related to the surface properties of the electrodes used. As the capacitance of the Au microelectrode is relatively low it was suggested that the uncompensated resistance can be responsible for the effect observed. This was tested when the two-electrode cell was changed to the three-electrode assembly. These investigations showed that the "damping" effect characterising the two-electrode set-up disappears with the change to the three-electrode system. It was found that the source of the

uncompensated resistance is the resistance of the reference electrode. This conclusion was made when the MMS reference electrode was changed to the Ag-wire reference/counter electrode. The current drop characterised for the MMS reference electrode cell was completely removed when Ag wire electrode was used as a reference electrode. In addition, the R_U values for both reference electrodes were determined. These were 88.5 Ω for Ag reference electrode cell and 2.63 kΩ for MMS reference electrode cell. In further experiments when a 2.7 kΩ resistor (in series with the WE) was added to the three-electrode cell the response recorded for molecular oxygen reduction became damped. The clear role of the uncompensated resistance on the HMV signal was demonstrated.

Finally, a test circuit showed that the capacitance and uncompensated resistance of the cell are important factors in the HMV response. These will affect the experimental HMV signal when the capacity (or R_U value) is high. Therefore the employment of high surface area electrodes in the HMV investigations will be complicated by these factors. However, reducing the geometric area, by the employment of a microelectrode, can avoid this effect and extends the HMV technique to the study of very high (here > 900) roughness factors.

Appendix A

Visual Basic Programs

All the software described as "in-house" in this thesis was written using Microsoft Visual Basic Version 6. The programs were written with collaboration with Dr Peter Birkin.

A.1 Lock-in program

This software was written to extract the relevant data from the obtained signal taking into account the phase between the reference and analysing signal.

A.1.1 Phase adjuster

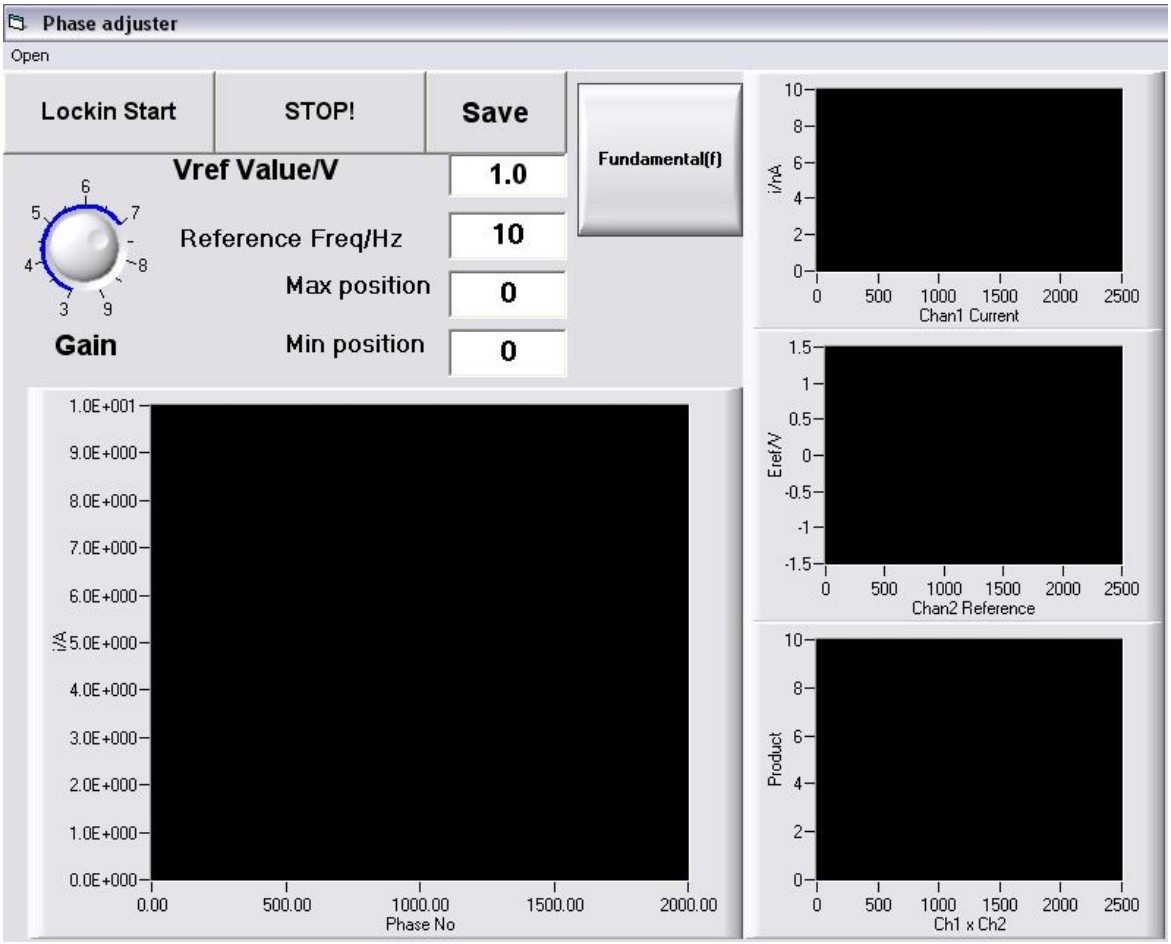

Figure A.1. Screenshot of the user interface for "Phase adjuster"

Visual Basic Code

```
Const FirstPoint& = 0 ' set first element in buffer to transfer to
array
Dim ADData%(NumPoints&)' dimension an array to hold the input values
Dim chan1(5001)
Dim chan2(5001)
Dim FC(5001)
Dim wey
Dim gainEC
Dim average(10000)
Dim E(10000)
Dim ns As Single
Dim nsa As Single
Dim nc As Single
Dim EngUnits(NumPoints&)
Dim MemHandle&        ' define a variable to contain the handle for
Private Sub Command1_Click()
CWGraph4.ChartLength = 5000
chan1(5001) = Null
chan2(5001) = Null
FC(5001) = Null
E(10000) = Null
average(10000) = Null
Max = 0
Min = 0
wey = 1
CWGraph4.ClearData
BoardNum% = 1
For eav = 1 To 100
Ulstat% = cbAIn(BoardNum%, 0, Gain, DataValue%)
If Ulstat% = 30 Then MsgBox "Change the Gain argument to one supported
by this board.", 0, "Unsupported Gain"
If Ulstat% <> 0 Then Stop
Ulstat% = cbToEngUnits(BoardNum%, Gain, DataValue%, eng)
If Ulstat% <> 0 Then Stop
sume = sume + eng
Next eav
E(0) = -(sume / 100)
gainEC = 1 * 10 ^ (CWKnob1.Value)
nc = 0
Form2.CWGraph4.ClearData
CBCount& = 10000          ' total number of data points to collect
CBRate& = 10000           ' sampling rate (samples per second)
Options = CONVERTDATA     ' return data as 12-bit values
Gain = BIP10VOLTS         ' set the gain
LowChan% = 1
HighChan% = 2
BoardNum% = 1
If MemHandle& = 0 Then Stop ' check that a handle to a memory buffer
exists
Ulstat% = cbAInScan(BoardNum%, LowChan%, HighChan%, CBCount&, CBRate&,
Gain, MemHandle&, Options)
If Ulstat% = 30 Then MsgBox "Change the Gain argument to one supported
by this board.", 0, "Unsupported Gain"
```

```
If Ulstat% <> 0 And Ulstat% <> 91 Then Stop
' Transfer the data from the memory buffer set up by Windows to an
array for use by Visual Basic
Ulstat% = cbWinBufToArray(MemHandle&, ADData%(0), FirstPoint&,
CBCount&)
If Ulstat% <> 0 Then Stop
CWGraph1.ClearData
CWGraph2.ClearData
CWGraph3.ClearData
sumsig = 0
n = 0
For X = 0 To 9998 Step 2
Ulstat% = cbToEngUnits(BoardNum%, Gain, ADData(X), EngUnits(X))
If Ulstat% <> 0 Then Stop
chan1(n) = EngUnits(X)
sumsig = sumsig + chan1(n)
n = n + 1
Next X
sumsig = sumsig / 5000
sumref = 0
n = 0
For X = 1 To 9999 Step 2 ' reference data
Ulstat% = cbToEngUnits(BoardNum%, Gain, ADData(X), EngUnits(X))
If Ulstat% <> 0 Then Stop
chan2(n) = EngUnits(X)
sumref = sumref + chan2(n)
n = n + 1
Next X
sumref = sumref / 5000
'let time progress
factor = 1
If CWButton1 = True Then factor = 0.5
For n = 1 To 2500
Form2.CWGraph1.ChartY ((chan1(factor * n) / gainEC) / 0.000000001)
Next n
Sum = 0
fo = Text2               ' reference frequency
phasemax = 10000 / (fo) ' maximum shift of 360 deg
For Phase = 0 To phasemax Step 1
nc = nc + 1
Sum = 0
For n = 1 To (5000 - Phase)
FC(n) = (chan1(factor * n) - sumsig) * (chan2(n + Phase) - sumref)
Sum = Sum + FC(n)
Next n
Eo = Text1           ' this is the reference voltage
average(nc) = (2 * (Sum / (5000 - Phase)) / (gainEC * Eo))
Form2.CWGraph4.ChartXvsY Phase, average(nc)
CWGraph2.ClearData
CWGraph3.ClearData
For n = 1 To 2500 Step 10
Form2.CWGraph2.ChartXvsY n, (chan2(n + Phase))
Form2.CWGraph3.ChartXvsY n, (FC(n))
Next n
If average(nc) > Max Then
Max = average(nc)
Textmax = Phase
End If
If average(nc) < Min Then
Min = average(nc)
Textmin = Phase
```

```
End If
Start = Timer
Do
eh = DoEvents()
If wey = 0 Then GoTo Terminate
Loop Until Timer - Start > 0
Next Phase
eh = DoEvents()
Terminate:
End Sub
```

```
Private Sub Command2_Click()
wey = 0
End Sub
```

```
Private Sub Command3_Click()
Form1.filebox.CancelError = True
On Error GoTo ErrHandle
Form1.filebox.Flags = &H2&
Form1.filebox.FileName = "*.dat"
Form1.filebox.InitDir = "C:\katie\"
Form1.filebox.Action = 2
Form1.Caption = Form1.filebox.FileName
Open Form1.filebox.FileName For Output As #2
ns = 0
Do
ns = ns + 1
Print #2, Format(ns, "0"); ","; Format(average(ns), "0.000E-000")
Loop Until ns = nc
For nsa = 1 To 5000
Print #2, Format(((chan1(nsa)) / gainEC), "0.000E-000"); ",";
Format(chan2(nsa), "0.000")
Next nsa
Close #2
ErrHandle:     Exit Sub
End Sub
```

```
' memory allocated by Windows through cbWinBufAlloc%()
Private Sub Form_Load()
Dim Ulstat%   ' declare revision level of Universal Library
Ulstat% = cbDeclareRevision(CURRENTREVNUM)
Ulstat% = cbErrHandling(PRINTALL, DONTSTOP)
If Ulstat% <> 0 Then Stop
MemHandle& = cbWinBufAlloc(NumPoints&)' set aside memory to hold data
If MemHandle& = 0 Then Stop
End Sub
```

```
Private Sub Open_Click()
Dim datax(10000)
Dim datay(10000)
Dim No
Dim E$
Dim i$
Dim nop
'configure commondialog box for open
Form2.filebox.CancelError = True
'On Error GoTo ErrHandle
Form2.filebox.FileName = "*.dat"
Form2.filebox.InitDir = "C:\doug\data"
Form2.filebox.Action = 1
Form2.Caption = Form2.filebox.FileName
```

```
Open Form2.filebox.FileName For Input As #4
Form2.CWGraph1.ClearData
Form2.CWGraph2.ClearData
'load data to variables
No = -1
Do
No = No + 1
Input #4, E$
datax(No) = Val(E$)
Input #4, i$
datay(No) = Val(i$)
Loop Until datax(No) < 0.9
Input #4, E$ ' aviod first line
Form2.CWGraph1.ChartLength = 5000
Form2.CWGraph2.ChartLength = 5000
Form2.CWGraph4.ChartLength = 5000
For nd = 1 To 4998
Input #4, E$
Form2.CWGraph2.ChartY Val(E$) 'plots the sample i
Input #4, i$
Form2.CWGraph1.ChartY Val(i$)
Next nd
Close #4
Form2.CWGraph4.ClearData
For nop = 0 To No - 1
Form2.CWGraph4.ChartY datay(nop)
Next
End Sub
```

A.1.2 Lock-in XY Program

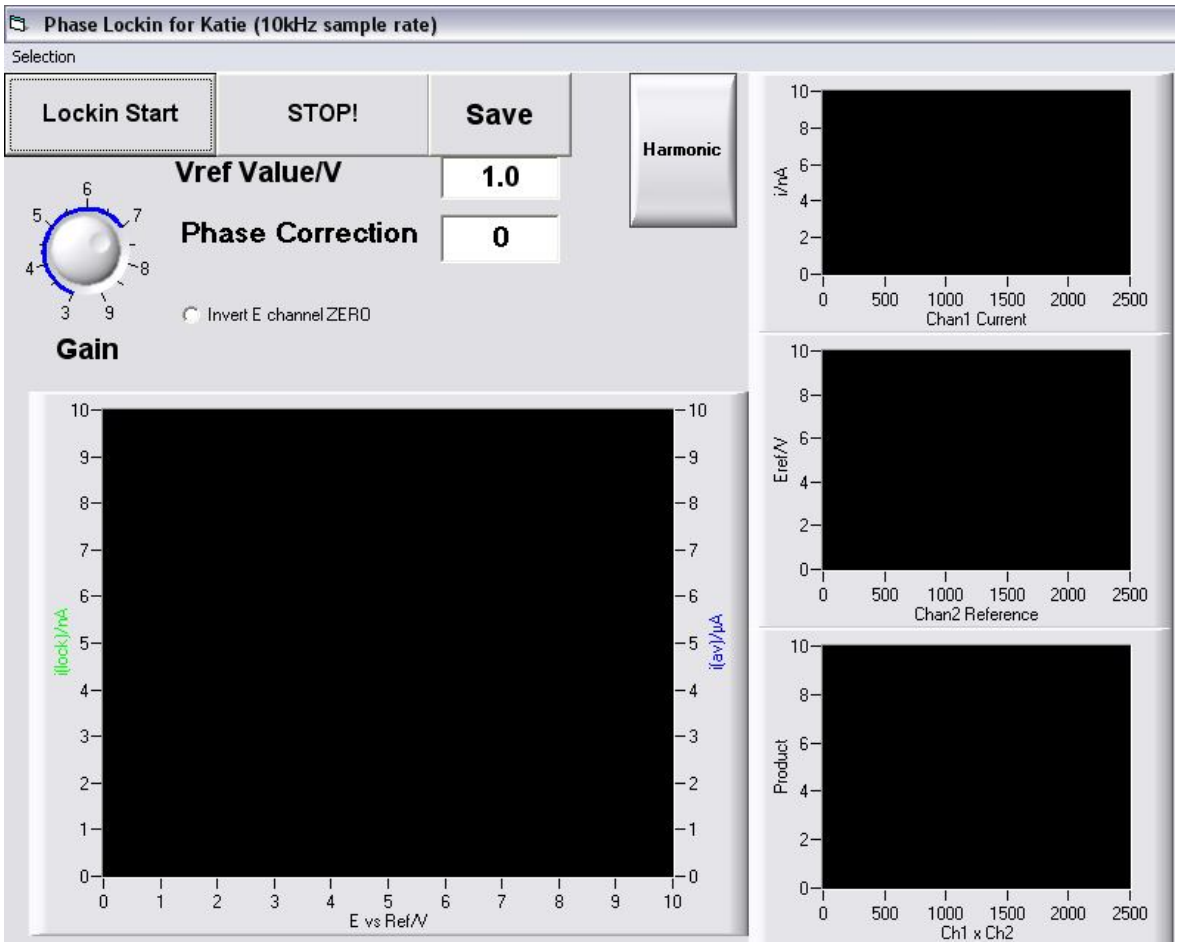

Figure A.2. Screenshot of the user interface for "Phase adjuster"

Visual Basic Code

```
Const NumPoints& = 10000 ' Number of data points to collect
Const FirstPoint& = 0'set first element in buffer to transfer to array
Dim ADData%(NumPoints&)' dimension an array to hold the input values
Dim chan1(5001)
Dim chan2(5001)
Dim FC(5001)
Dim wey
Dim average(10000)
Dim E(10000)
Dim iav(10000)
Dim datagraph(3) As Single
Dim ns As Single
Dim nc As Single
Dim EngUnits(NumPoints&)
Dim MemHandle&   ' define a variable to contain the handle for

Private Sub AS_Click()
average_slow.Show
End Sub
```

```
Private Sub autosave_Click()
```

```
file_save.Show
End Sub
```

```
Private Sub Command1_Click()
CWGraph4.ChartLength = 5000
chan1(5001) = Null
chan2(5001) = Null
FC(5001) = Null
E(10000) = Null
average(10000) = Null
BoardNum% = 1
wey = 1
CWGraph4.ClearData
For eav = 1 To 100
Ulstat% = cbAIn(BoardNum%, 0, Gain, DataValue%)
If Ulstat% = 30 Then MsgBox "Change the Gain argument to one supported
by this board.", 0, "Unsupported Gain"
If Ulstat% <> 0 Then Stop
Ulstat% = cbToEngUnits(BoardNum%, Gain, DataValue%, eng)
If Ulstat% <> 0 Then Stop
sume = sume + eng
Next eav
E(0) = -(sume / 100)
gainEC = 1 * 10 ^ (CWKnob1.Value)
nc = 0
Do
nc = nc + 1
CBCount& = 10000    ' total number of data points to collect
CBRate& = 10000     ' sampling rate (samples per second)
Options = CONVERTDATA   ' return data as 12-bit values
Gain = BIP10VOLTS         ' set the gain
LowChan% = 1
HighChan% = 2
BoardNum% = 1
If MemHandle& = 0 Then Stop  'check that a handle to a memory buffer
exists
Ulstat% = cbAInScan(BoardNum%, LowChan%, HighChan%, CBCount&, CBRate&,
Gain, MemHandle&, Options)
If Ulstat% = 30 Then MsgBox "Change the Gain argument to one supported
by this board.", 0, "Unsupported Gain"
If Ulstat% <> 0 And Ulstat% <> 91 Then Stop
' Transfer the data from the memory buffer set up by Windows to an
array for use by Visual Basic
Ulstat% = cbWinBufToArray(MemHandle&, ADData%(0), FirstPoint&,
CBCount&)
If Ulstat% <> 0 Then Stop
CWGraph1.ClearData
CWGraph2.ClearData
CWGraph3.ClearData
sumsig = 0
n = 0
For X = 0 To 9998 Step 2
Ulstat% = cbToEngUnits(BoardNum%, Gain, ADData(X), EngUnits(X))
If Ulstat% <> 0 Then Stop
chan1(n) = EngUnits(X)
sumsig = sumsig + chan1(n)
n = n + 1
Next X
sumsig = sumsig / 5000
iav(nc) = sumsig / gainEC
sumref = 0
```

```
n = 0
For X = 1 To 9999 Step 2        ' reference data
Ulstat% = cbToEngUnits(BoardNum%, Gain, ADData(X), EngUnits(X))
If Ulstat% <> 0 Then Stop
chan2(n) = EngUnits(X)
sumref = sumref + chan2(n)
n = n + 1
Next X
sumref = sumref / 5000
'get the electrode potential through channel 0
Do
sume = 0
For eav = 1 To 100
Ulstat% = cbAIn(BoardNum%, 0, Gain, DataValue%)
If Ulstat% = 30 Then MsgBox "Change the Gain argument to one supported
by this board.", 0, "Unsupported Gain"
If Ulstat% <> 0 Then Stop
Ulstat% = cbToEngUnits(BoardNum%, Gain, DataValue%, eng)
If Ulstat% <> 0 Then Stop
sume = sume + eng
Next eav
E(nc) = -(sume / 100)
Loop Until Abs(E(nc) - E(nc - 1)) > 0.005
If Option1.Value = True Then
E(nc) = -E(nc)
Else
End If
factor = 1
If CWButton1 = True Then factor = 0.5
Sum = 0
phasec = Text3
For n = 1 To 5000 - phasec
FC(n) = (chan1(factor * n) - sumsig) * (chan2(n + phasec) - sumref)
Sum = Sum + FC(n)
Next n
Eo = Text1 ' this is the reference voltage
average(nc) = (2 * (Sum / (5000 - phasec)) / (gainEC * Eo))
For n = 1 To 2500 Step 10
CWGraph1.ChartXvsY n, (chan1(factor * n) / gainEC) / 0.000000001
CWGraph2.ChartXvsY n, (chan2(n))
CWGraph3.ChartXvsY n, (FC(n))
Next n
datagraph(0) = E(nc)
datagraph(1) = average(nc) / 0.000000001
datagraph(2) = iav(nc) / 0.000001
CWGraph4.ChartXY datagraph, bPlotPerRow = True
eh = DoEvents()
Loop Until wey = 0
End Sub
```

```
Private Sub Command2_Click()
wey = 0
End Sub
```

```
Private Sub Command3_Click()
Form1.filebox.CancelError = True
On Error GoTo ErrHandle
Form1.filebox.Flags = &H2&
Form1.filebox.FileName = "*.dat"
Form1.filebox.InitDir = "C:\katie\"
Form1.filebox.Action = 2
```

```
Form1.Caption = Form1.filebox.FileName
Open Form1.filebox.FileName For Output As #2
ns = 0
Do
ns = ns + 1
Print #2, Format(E(ns), "0.000"); ","; Format(average(ns), "0.000E-
000"); ","; Format(iav(ns), "0.000E-000")
Loop Until ns = nc
Close #2
ErrHandle:     Exit Sub
End Sub
```

```
' memory allocated by Windows through cbWinBufAlloc%()
Private Sub Form_Load()
Dim Ulstat%   ' declare revision level of Universal Library
Ulstat% = cbDeclareRevision(CURRENTREVNUM)
Ulstat% = cbErrHandling(PRINTALL, DONTSTOP)
If Ulstat% <> 0 Then Stop
MemHandle& = cbWinBufAlloc(NumPoints&)' set aside memory to hold data
If MemHandle& = 0 Then Stop
End Sub
```

```
Private Sub Open_Click()
Dim datax(10000)
Dim datay1(10000)
Dim datay2(10000)
Dim No
Dim E$
Dim i$
Dim nop
'configure commondialog box for open
Form1.filebox.CancelError = True
'On Error GoTo ErrHandle
Form1.filebox.FileName = "*.dat"
Form1.filebox.InitDir = "C:\doug\data"
Form1.filebox.Action = 1
Form1.Caption = Form1.filebox.FileName
Open Form1.filebox.FileName For Input As #4
'load data to variables
No = -1
Do
No = No + 1
Input #4, E$
datax(No) = Val(E$)
Input #4, i$
datay1(No) = Val(i$)
Input #4, i$
datay2(No) = Val(i$)
Loop Until EOF(4)
Close #4
Form1.CWGraph4.ClearData
For nop = 0 To No
datagraph(0) = datax(nop)
datagraph(1) = datay1(nop) / 0.000000001
datagraph(2) = datay2(nop) / 0.000001
Form1.CWGraph4.ChartXY datagraph, bPlotPerRow = True
Next
End Sub
```

```
Private Sub PD_Click()
Form2.Show
```

```
End Sub

Private Sub TD_Click()
Time.Show
End Sub
```

A.2 Phase Correction Program

The program calculates the phase between the analysing and reference signals for each data point. The lock-in data is then corrected according to the calculations.

Figure A.3. Screenshot of the user interface for the "Phase Correction Program"

Visual Basic Code

```
Dim i(5000)
Dim E(5000)
Dim Ecv(5000)
Dim it$
Dim wey
Dim datax(5000)
Dim phasmax(1000)
Dim phasmin(1000)
Dim datagraph(3) As Single
Dim datagraph2(3) As Single
Dim Fc(5000)
Dim iav(5000)
Dim average(5000)
Dim averagead(5000)
Dim averageadmax(5000)
Dim ref$
Private Sub Command1_Click()
Dim E(5000)
X = 0
```

```
wey = 1
CWGraph5.ClearData
CWGraph1.ClearData
For N = 1 To Text4
Min = 0
Max = 0
Text7 = N
FileName = Text3.Text + Str(N) + ".dat"
Open FileName For Input As #2
Do
Input #2, ref$
Input #2, it$
E(X) = Val(ref$) 'assign to array
i(X) = Val(it$) 'assign to array
X = X + 1
Loop Until EOF(2)
Close #2
X = 0
'now data loaded we analyse
'first take an average
sumsig = 0
For w = 0 To 4999
sumsig = sumsig + i(w)
Next w
sumsig = sumsig / 5000
iav(N - 1) = sumsig
sumref = 0
For w = 0 To 4999 ' reference data
sumref = sumref + E(w)
Next w
sumref = sumref / 5000
Sum = 0
fo = Text1 ' reference frequency
phasemax = 10000 / (fo) ' maximum shift of 360 deg
nc = 0
For phase = 0 To phasemax Step 1
nc = nc + 1
Sum = 0
For Na = 1 To (5000 - phase)
Fc(Na) = (i(Na) - sumsig) * (E(Na + phase) - sumref)
Sum = Sum + Fc(Na)
Next Na
Eo = Text2 ' this is the reference voltage
average(N - 1) = (2 * (Sum / (5000 - phase)) / (Eo))
If average(N - 1) > Max Then
Max = average(N - 1)
Text5 = phase
phasmax(N - 1) = phase
End If
If average(N - 1) < Min Then
Min = average(N - 1)
Text6 = phase
phasmin(N - 1) = phase
End If
'now recalculate the data with the correct phase at all times
Sum = 0
For Na = 1 To (5000 - phasmin(N - 1))
Fc(Na) = (i(Na) - sumsig) * (E(Na + phasmin(N - 1)) - sumref)
Sum = Sum + Fc(Na)
Next Na
Eo = Text2 ' this is the reference voltage
```

```
averagead(N - 1) = (2 * (Sum / (5000 - phasmin(N - 1))) / (Eo))
Sum = 0
For Na = 1 To (5000 - phasmax(N - 1))
Fc(Na) = (i(Na) - sumsig) * (E(Na + phasmax(N - 1)) - sumref)
Sum = Sum + Fc(Na)
Next Na
Eo = Text2 ' this is the reference voltage
averageadmax(N - 1) = (2 * (Sum / (5000 - phasmax(N - 1))) / (Eo))
eh = DoEvents()
If wey = 0 Then GoTo terminate
Next phase
phasmax(N - 1) = ((phasmax(N - 1)) / phasemax) * 360
phasmin(N - 1) = ((phasmin(N - 1)) / phasemax) * 360
datagraph(0) = Ecv(N - 1)
datagraph(1) = phasmax(N - 1)
datagraph(2) = phasmin(N - 1)
CWGraph5.ChartXY datagraph, bPlotPerRow = True
datagraph2(0) = Ecv(N - 1)
datagraph2(1) = iav(N - 1)
datagraph2(2) = averagead(N - 1)
CWGraph1.ChartXY datagraph2, bPlotPerRow = True
Next N
terminate:
End Sub
```

```
Private Sub Command2_Click()
wey = 0

End Sub
```

```
Private Sub Open_Click()
Dim datay1(10000)
Dim datay2(10000)
Dim No
Dim Ep$
Dim i$
Dim nop
Dim datagraph3(3) As Single
'configure commondialog box for open
form1.filebox.CancelError = True
'On Error GoTo ErrHandle
form1.filebox.FileName = "*.dat"
form1.filebox.InitDir = "C:\data"
form1.filebox.Action = 1
form1.Caption = form1.filebox.FileName
Open form1.filebox.FileName For Input As #4
'load data to variables
No = -1
Do
No = No + 1
Input #4, Ep$
Ecv(No) = Val(Ep$)
Input #4, i$
datay1(No) = Val(i$)
Input #4, i$
datay2(No) = Val(i$)
Loop Until EOF(4)
Close #4
form1.CWGraph4.ClearData
CWGraph4.ChartLength = 1000
For nop = 0 To No
```

```
datagraph3(0) = Ecv(nop)
datagraph3(1) = datay1(nop) '/ 0.000000001
datagraph3(2) = datay2(nop) '/ 0.000001
form1.CWGraph4.ChartXY datagraph3, bPlotPerRow = True
Next

End Sub
```

```
Private Sub Save_Click()
'configure commondialog box for open
form1.filebox.CancelError = True
'On Error GoTo ErrHandle
form1.filebox.FileName = "*.dat"
form1.filebox.InitDir = "C:\data"
form1.filebox.Action = 2
form1.Caption = form1.filebox.FileName
Open form1.filebox.FileName For Output As #4
'load data to variables
Print #4, "E/V, iav/A, ihmV old/A, Phasemax/deg, Phasemin/deg, ihmv
min/A, ihmv max/V"
For ns = 0 To Text4
Print #4, Format(Ecv(ns), "0.000"); ","; Format(iav(ns), "0.000E-
000"); ","; Format(average(ns), "0.000E-000"); ",";
Format(phasmax(ns), "000.0"); ","; Format(phasmin(ns), "000.0"); ",";
Format(averagead(ns), "0.000E-000"); ","; Format(averageadmax(ns),
"0.000E-000")
Next ns
Close #4
End Sub
```

A.3 FFT program

This software was written to process data using the FFT analysis.

A.3.1 Sampler

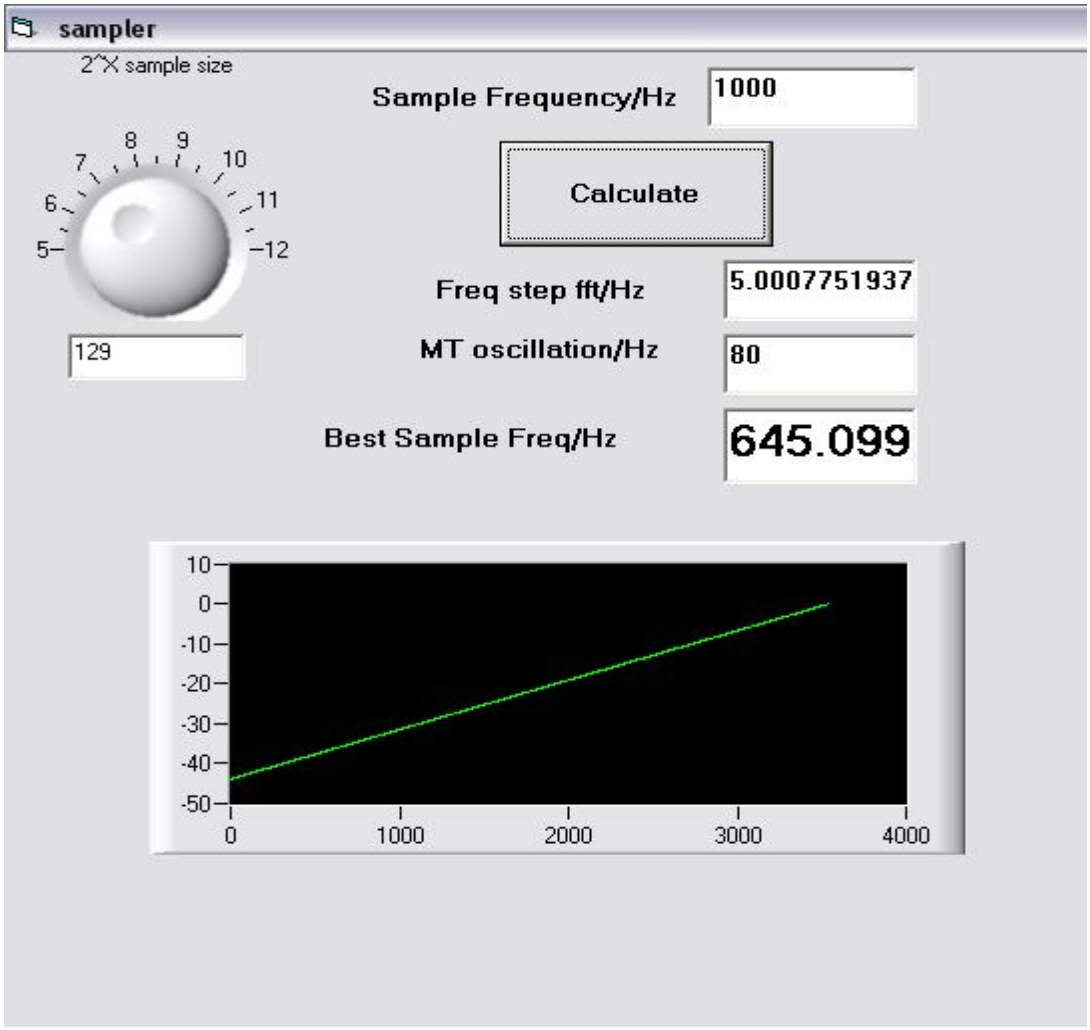

Figure A.3. Screenshot of the user interface for the Sampler

Visual Basic Code

```
Private Sub Command1_Click()
n = (2 ^ CWKnob1.Value) + 1
Text1 = n                    ' actual data sample
sample = Text2
pick = ((n - 1) / 8) ' position of peak in set to 1/4 way through
bsample = (sample / n) * pick
lo = 0
CWGraph1.ChartLength = 10000
Do
errata = Text4 - bsample
If errata < 0 Then
sample = sample - 0.1
Else
sample = sample + 0.1
End If
lo = lo + 1
```

```
CWGraph1.ChartXvsY lo, errata
bsample = (sample / n) * pick
Loop Until Abs(errata) < 0.01
Text3 = sample / n
Text5 = sample
End Sub
```

A.3.2 Data Acquisition

Figure A.4. Screenshot of the user interface for the "Time detector".

Visual Basic Code

```
Const FirstPoint& = 0' set first element in buffer to transfer to
      array
Dim ADData%(NumPoints&)' dimension an array to hold the input values
Dim chan1(100000)
Dim chan2(100000)
Dim timew
Dim wey
Dim DataValue%
Dim eng
Dim eng1
Dim samplelength
Dim datagraph(3) As Single
Dim ns As Single
Dim nc As Single
Dim EngUnits(NumPoints&)
Dim MemHandle&  ' define a variable to contain the handle for
Private Sub AS_Click()
average_slow.Show
End Sub
```

```
Private Sub Command1_Click()
If Text3 < 0 Then
```

```
timew = (Text1 + Abs(Text3)) / Text4
Else
timew = Abs((Text1 - Abs(Text3)) / Text4)
End If
Text5 = timew
BoardNum% = 1
Ulstat% = cbAIn(BoardNum%, 0, Gain, DataValue%)
If Ulstat% = 30 Then MsgBox "Change the Gain argument to one supported
      by this board.", 0, "Unsupported Gain"
If Ulstat% <> 0 Then Stop
Ulstat% = cbToEngUnits(BoardNum%, Gain, DataValue%, eng)
If Ulstat% <> 0 Then Stop
Do   ' trigger for start
Ulstat% = cbAIn(BoardNum%, 0, Gain, DataValue%)
If Ulstat% = 30 Then MsgBox "Change the Gain argument to one supported
      by this board.", 0, "Unsupported Gain"
If Ulstat% <> 0 Then Stop
Ulstat% = cbToEngUnits(BoardNum%, Gain, DataValue%, eng1)
If Ulstat% <> 0 Then Stop
Loop Until Abs(eng - eng1 > 0.01)
chan1(10000) = Null
chan2(10000) = Null
BoardNum% = 1
wey = 1
CWGraph3.ClearData
CWGraph3.ChartLength = 10000
gainEC = 1 * 10 ^ (CWKnob1.Value)
ss = CWNumEdit1.Value
samplelength = ss * timew * 2
CBCount& = ss * timew * 2' total number of data points to collect
CBRate& = ss                    ' sampling rate (samples per second)
Options = CONVERTDATA            ' return data as 12-bit values
Gain = BIP10VOLTS                ' set the gain
LowChan% = 0
HighChan% = 1
If MemHandle& = 0 Then Stop 'check that a handle to a memory buffer
      exists
Ulstat% = cbAInScan(BoardNum%, LowChan%, HighChan%, CBCount&, CBRate&,
      Gain, MemHandle&, Options)
If Ulstat% = 30 Then MsgBox "Change the Gain argument to one supported
      by this board.", 0, "Unsupported Gain"
If Ulstat% <> 0 And Ulstat% <> 91 Then Stop
' Transfer the data from the memory buffer set up by Windows to an
      array for use by Visual Basic
Ulstat% = cbWinBufToArray(MemHandle&, ADData%(0), FirstPoint&,
      CBCount&)
If Ulstat% <> 0 Then Stop
CWGraph1.ClearData
CWGraph2.ClearData
sumsig = 0
n = 0
For X = 0 To samplelength - 2 Step 2    ' extract E vs time
Ulstat% = cbToEngUnits(BoardNum%, Gain, ADData(X), EngUnits(X))
If Ulstat% <> 0 Then Stop
chan1(n) = EngUnits(X)
n = n + 1
Next X
n = 0
For X = 1 To samplelength - 1 Step 2    ' extract i vs time
Ulstat% = cbToEngUnits(BoardNum%, Gain, ADData(X), EngUnits(X))
If Ulstat% <> 0 Then Stop
```

```
chan2(n) = -EngUnits(X) / gainEC
n = n + 1
Next X
For n = 0 To (samplelength / 2) - 1 Step 1
CWGraph1.ChartXvsY n, (chan2(n))          'i
CWGraph2.ChartXvsY n, (chan1(n))          'E
CWGraph3.ChartXvsY chan1(n), chan2(n)
Next n
Text2 = samplelength
eh = DoEvents()
 'Loop Until wey = 0
End Sub
```

```
Private Sub Command2_Click()
wey = 0
End Sub
Private Sub Command3_Click()
Time.filebox.CancelError = True
On Error GoTo ErrHandle
Time.filebox.Flags = &H2&
Time.filebox.FileName = "*.dat"
Time.filebox.InitDir = "C:\katie\"
Time.filebox.Action = 2
Time.Caption = Time.filebox.FileName
Open Time.filebox.FileName For Output As #2
ns = 0
Do
ns = ns + 1
Print #2, Format(chan1(ns), "0.000"); ","; Format(chan2(ns), "0.000E-
      000")
Loop Until ns = Int((samplelength / 2) - 2)
Close #2
ErrHandle:     Exit Sub
End Sub
```

```
Private Sub CWKnob2_PointerValueChanged(ByVal Pointer As Long, Value
      As Variant)
Text2 = CWKnob2.Value
End Sub
```

```
' memory allocated by Windows through cbWinBufAlloc%()
Private Sub Form_Load()
Dim Ulstat%   ' declare revision level of Universal Library
Ulstat% = cbDeclareRevision(CURRENTREVNUM)
Ulstat% = cbErrHandling(PRINTALL, DONTSTOP)
If Ulstat% <> 0 Then Stop
MemHandle& = cbWinBufAlloc(NumPoints&)' set aside memory to hold data
If MemHandle& = 0 Then Stop
End Sub
```

```
Private Sub op_Click()
Dim datax(10000)
Dim datay1(10000)
Dim datay2(10000)
Dim No
Dim E$
Dim i$
Dim nop
'configure commondialog box for open
Time.filebox.CancelError = True
```

```
'On Error GoTo ErrHandle
Time.filebox.FileName = "*.dat"
Time.filebox.InitDir = "C:\doug\data"
Time.filebox.Action = 1
Time.Caption = Time.filebox.FileName
Open Time.filebox.FileName For Input As #4
'load data to variables
No = -1
Do
No = No + 1
Input #4, E$
datax(No) = Val(E$)
Input #4, i$
datay1(No) = Val(i$)
Input #4, i$
datay2(No) = Val(i$)
Loop Until EOF(4)
Close #4
End Sub
```

```
Private Sub PD_Click()
Form2.Show
End Sub
```

A.3.3 FFT analysis

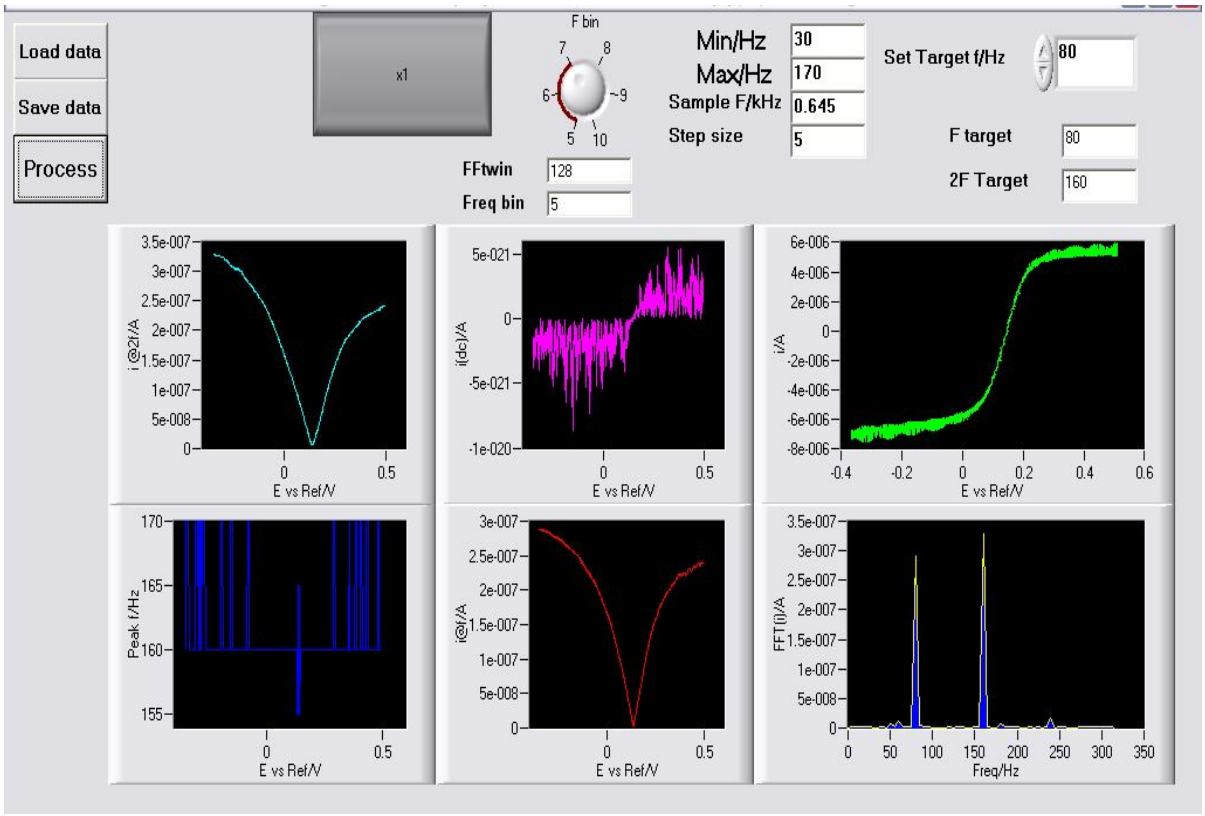

Figure A.5. Screenshot of the user interface for the "FFT Analysis".

Visual Basic Code

```
Dim sumffti(20000)
Dim avEe(20000)
Dim peak(20000)
Dim peak2f(20000)
Dim dc(20000)
Dim peakval(20000)
Dim intfre(20000)
Dim df As Variant
Dim y As Variant
Dim datagraph(3) As Single
Dim pwrspecouta As Variant
Dim numfft As Single
Dim t(2000000)
Dim E(2000000)
Dim i(2000000)
Dim n
Dim fftwin As Integer
Dim tin$
Dim ein$
Dim iin$

Private Sub Command1_Click()
CommonDialog1.Flags = &H2&
CommonDialog1.FileName = "*.dat"
CommonDialog1.InitDir = "C:\1 11 2007\"
CommonDialog1.Action = 1
```

```
Caption = CommonDialog1.FileName
Open CommonDialog1.FileName For Input As #2
n = 0
Do
Input #2, ein$
Input #2, iin$
E(n) = Val(ein$)
i(n) = Val(iin$)
n = n + 1
Loop Until EOF(2)
Close #2
End Sub
```

```
Private Sub Command2_Click()
CommonDialog1.Flags = &H2&
CommonDialog1.FileName = "*.dat"
CommonDialog1.InitDir = "C:\1 11 2007\"
CommonDialog1.Action = 2
Open CommonDialog1.FileName For Output As #2
Print #2, "avEe/V , dc/A , peakval/A , peak/Hz , peak2f/A"
For xs = 1 To numfft
Print #2, avEe(xs); ","; dc(xs); ","; peakval(xs); ","; peak(xs); ",";
      peak2f(xs)
Next xs
Close #2
End Sub
```

```
Private Sub Command3_Click()
CWGraph1.ClearData
CWGraph2.ClearData
CWGraph3.ClearData
CWGraph4.ClearData
CWGraph5.ClearData
CWGraph6.ClearData
CWGraph1.ChartLength = 100000
CWGraph2.ChartLength = 512
CWGraph3.ChartLength = 200000
CWGraph4.ChartLength = 200000
CWGraph5.ChartLength = 200000
CWGraph6.ChartLength = 200000
fftwin = 2 ^ (CWKnob2.Value)
Text5 = fftwin
ReDim Data(fftwin) As Variant    'array chunk to process
ReDim fftdata(fftwin)            'As Variant
ReDim fft(fftwin)
Step = Text4
numfft = Int(n / Step) - (Int(fftwin / Step) + 1)
samplefreq = Text3 * 1000
dttime = 1 / samplefreq
If n > 100000 Then
mu = 10
Else
mu = 1
End If
If CWButton1.Value = False Then
factor = -1
Else
factor = 1
End If
For w = 0 To n - 1 Step (2 * mu)
CWGraph1.ChartXvsY E(w), factor * (i(w)) 'plots the sample i
```

```
Next w
df = 1 / (fftwin * dttime)
rm = ((2) ^ 0.5)
For lo = 0 To numfft
ave = 0
sumi = 0
ReDim xr(fftwin) As Variant
Dim z As Variant
For r = 0 To fftwin Step 1
xr(r) = r
ave = ave + E(r + (lo * Step)) ' step forward by step size at a time
Data(r) = i(r + (lo * Step))
sumi = sumi + (factor * i(r + (lo * Step)))
Next r
avEe(lo) = ave / fftwin
sumi = sumi / fftwin ' average i
If sumi > 0 Then
dcfactor = 1
Else
dcfactor = -1
End If
CWStat1.LinFit xr, Data, z, slope, intercept, mse 'linear fit to data
      y = slope*xr+intercept
For r = 0 To fftwin Step 1
Data(r) = Data(r) - ((slope * xr(r)) + intercept) 'corrects for offset
Next r
CWGraph2.ClearData
CWDSP1.AutoPowerSpectrum Data, dttime, pwrspecouta, df
Text6 = df
pwrspecouta(0) = (Sqr(pwrspecouta(0)))
For se = 1 To (fftwin / 2) - 1
pwrspecouta(se) = rm * (Sqr(pwrspecouta(se)))
Next se
CWGraph2.PlotY pwrspecouta, 0, df
CWGraph3.ChartXvsY avEe(lo), (pwrspecouta(0)) * dcfactor
dc(lo) = (pwrspecouta(0)) * dcfactor
fmin = CInt(Text1 / df)
fmax = CInt(Text2 / df)
ftarget = (CInt(CWNumEdit1.Value / df)) ' gets frequency target
ftargettwo = (2 * CInt(CWNumEdit1.Value / df)) ' gets 2 * frequency
      target
Text7 = CInt(ftarget * df)
Text8 = CInt(ftargettwo * df)
peak(lo) = fmin * df
peakval(lo) = 0
intfre(lo) = 0
For sam = fmin To fmax Step 1
If pwrspecouta(sam) > pwrspecouta(sam - 1) Then
peak(lo) = sam * df
Else
End If
Next sam
peakval(lo) = pwrspecouta(ftarget)
CWGraph4.ChartXvsY avEe(lo), peakval(lo)
CWGraph5.ChartXvsY avEe(lo), peak(lo)
CWGraph6.ChartXvsY avEe(lo), pwrspecouta(ftargettwo)
peak2f(lo) = pwrspecouta(ftargettwo) ' gets harmonic and includes
Next lo
End Sub
```

A.3.4 3D and Contour Plots

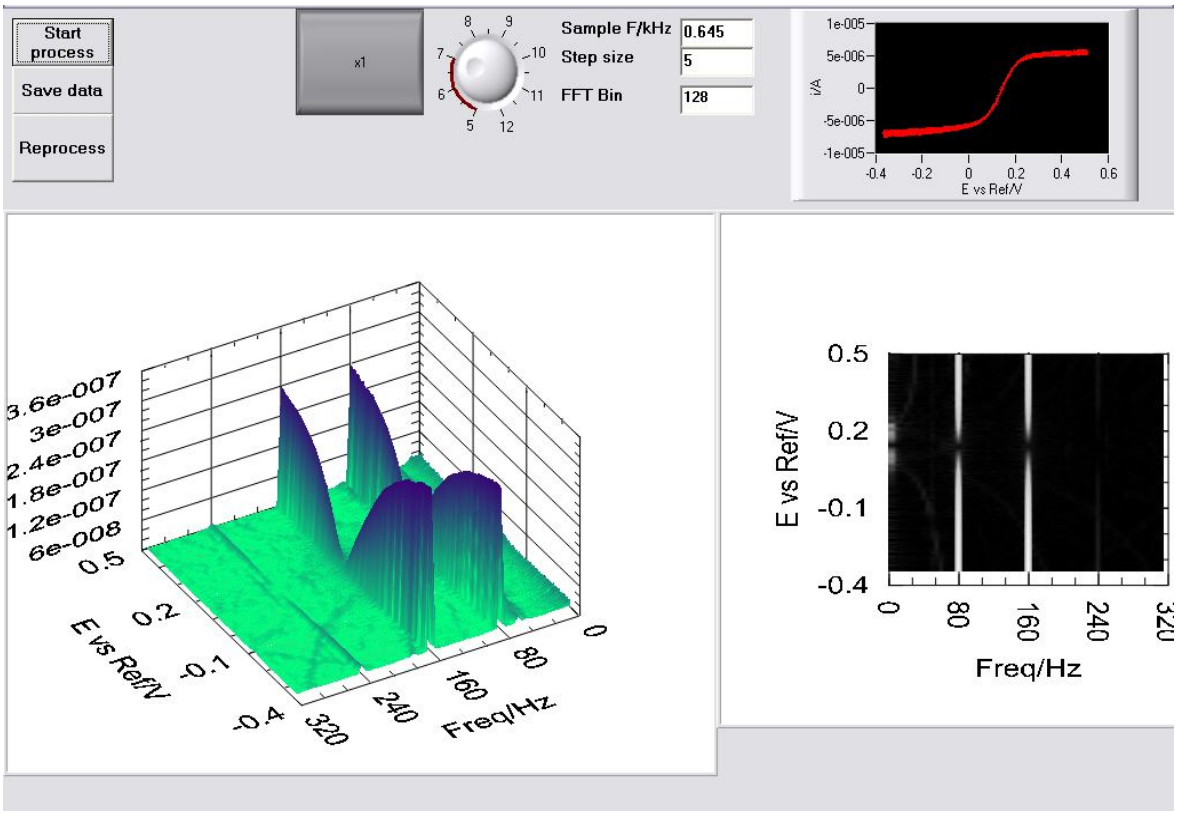

Figure A.6. Screenshot of the user interface for the "3D Plot".

Visual Basic Code

```
Dim sumffti(20000)
Dim avEe(20000)
Dim peak(20000)
Dim dc(20000)
Dim peakval(20000)
Dim intfre(20000)
Dim df As Variant
Dim y As Variant
Dim n
Dim fftdata(1024) 'As Variant
Dim pwrspecouta As Variant
Dim datap
Dim xp
Dim yp
Dim t(2000000)
Dim E(2000000)
Dim i(2000000)
Dim fft(1024)
Dim fftb As Integer
Dim numfft As Integer
Dim tin$
Dim ein$
Dim iin$

Private Sub Command1_Click()
CommonDialog1.Flags = &H2&
CommonDialog1.FileName = "*.dat"
```

```
CommonDialog1.InitDir = "C:\1 11 2007\"
CommonDialog1.Action = 1
Caption = CommonDialog1.FileName
Open CommonDialog1.FileName For Input As #2
CWGraph1.ClearData
CWGraph3D1.ClearData
CWGraph1.ChartLength = 100000
n = 0
Do
Input #2, ein$
Input #2, iin$
E(n) = Val(ein$)
i(n) = Val(iin$)
n = n + 1
Loop Until EOF(2)
Close #2
fftb = 2 ^ (CWKnob2.Value)
ReDim Data(fftb) As Variant 'array chunk to process
Text1 = fftb
Step = Text4
numfft = Int(n / Step) - (Int(fftb / Step) + 1)
ReDim datap(((fftb / 2) - 1), numfft)
ReDim xp((fftb / 2) - 1)
ReDim yp(numfft)
samplefreq = Text3 * 1000
dttime = 1 / samplefreq
Gain = 1 * 10 ^ (CWKnob1.Value)
If n > 100000 Then
mu = 10
Else
mu = 1
End If

If CWButton1.Value = False Then
factor = -1
Else
factor = 1
End If
For w = 0 To n - 1 Step (1 * mu)
CWGraph1.ChartXvsY E(w), factor * (i(w) / Gain) 'plots the sample i
Next w
df = 1 / (fftb * dttime)
rm = (Sqr(2))
ReDim xr(fftb) As Variant
Dim z As Variant
For lo = 0 To numfft
ave = 0
For r = 0 To fftb Step 1
xr(r) = r
ave = ave + E(r + (lo * Step)) ' step forward by 100 at a time
Data(r) = i(r + (lo * Step)) / Gain
Next r
CWStat1.LinFit xr, Data, z, slope, intercept, mse 'linear fit to data
      y = slope*xr+intercept
For r = 0 To fftb Step 1
Data(r) = Data(r) - ((slope * xr(r)) + intercept) 'corrects for offset
Next r
avEe(lo) = ave / fftb
CWDSP1.AutoPowerSpectrum Data, dttime, pwrspecouta, df
pwrspecouta(0) = rm * (Sqr(pwrspecouta(1))) 'avoid zero dc
datap(0, lo) = pwrspecouta(0)
```

```
For se = 1 To (fftb / 2) - 1
pwrspecouta(se) = rm * (Sqr(pwrspecouta(se)))
datap(se, lo) = pwrspecouta(se)
Next se
Next lo
For ip = 0 To (fftb / 2) - 1 'set frequency axis
xp(ip) = df * ip
Next ip
For ipp = 0 To numfft  'set potential axis
yp(ipp) = avEe(ipp)
Next ipp
' Plot surface
CWGraph3D1.Plot3DSurface xp, yp, datap
CWGraph3D2.Plot3DSurface xp, yp, datap
End Sub
```

```
Private Sub Command2_Click()
CommonDialog1.Flags = &H2&
CommonDialog1.DialogTitle = "Data Save"
CommonDialog1.FileName = "*.dat"
CommonDialog1.InitDir = "C:\1 11 2007\"
CommonDialog1.Action = 2
Open CommonDialog1.FileName For Output As #2
For xs = 0 To (fftb / 2) - 1
For xr = 0 To numfft - 1
Print #2, datap(xs, xr); ",";
Next xr
Print #2, datap(xs, numfft)
Next xs
Close #2
CommonDialog1.Flags = &H2&
CommonDialog1.DialogTitle = "XY Save"
CommonDialog1.FileName = "*.xyd"
CommonDialog1.InitDir = "C:\1 11 2007\"
CommonDialog1.Action = 2
Open CommonDialog1.FileName For Output As #1
For xs = 0 To (fftb / 2) - 1
Print #1, xp(xs)
Next xs
For xs = 0 To numfft
Print #1, Format$(yp(xs), "#.####")
Next xs
Close #1
End Sub
```

```
Private Sub Command3_Click()
CWGraph1.ClearData
CWGraph3D1.ClearData
CWGraph3D2.ClearData
fftb = 2 ^ (CWKnob2.Value)
ReDim Data(fftb) As Variant 'array chunk to process
Text1 = fftb
Step = Text4
numfft = Int(n / Step) - (Int(fftb / Step) + 1)
ReDim datap(((fftb / 2) - 1), numfft)
ReDim xp((fftb / 2) - 1)
ReDim yp(numfft)
samplefreq = Text3 * 1000
dttime = 1 / samplefreq
```

```
Gain = 1 * 10 ^ (CWKnob1.Value)
If n > 100000 Then
mu = 10
Else
mu = 1
End If
If CWButton1.Value = False Then
factor = -1
Else
factor = 1
End If
For w = 0 To n - 1 Step (1 * mu)
CWGraph1.ChartXvsY E(w), factor * (i(w) / Gain) 'plots the sample i
Next w
df = 1 / (fftb * dttime)
rm = (Sqr(2))
ReDim xr(fftb) As Variant
Dim z As Variant
For lo = 0 To numfft
ave = 0
For r = 0 To fftb Step 1
xr(r) = r
ave = ave + E(r + (lo * Step)) ' step forward by 100 at a time
Data(r) = i(r + (lo * Step)) / Gain
Next r
CWStat1.LinFit xr, Data, z, slope, intercept, mse 'linear fit to data
      y = slope*xr+intercept
For r = 0 To fftb Step 1
Data(r) = Data(r) - ((slope * xr(r)) + intercept) 'corrects for offset
Next r
avEe(lo) = ave / fftb
CWDSP1.AutoPowerSpectrum Data, dttime, pwrspecouta, df
pwrspecouta(0) = rm * (Sqr(pwrspecouta(1))) 'avoid zero dc
datap(0, lo) = pwrspecouta(0)
For se = 1 To (fftb / 2) - 1
pwrspecouta(se) = rm * (Sqr(pwrspecouta(se)))
datap(se, lo) = pwrspecouta(se)
Next se
Next lo
For ip = 0 To (fftb / 2) - 1 'set frequency axis
xp(ip) = df * ip
Next ip
For ipp = 0 To numfft  'set potential axis
yp(ipp) = avEe(ipp)
Next ipp
' Plot surface
CWGraph3D1.Plot3DSurface xp, yp, datap
CWGraph3D2.Plot3DSurface xp, yp, datap
End Sub
```

Appendix B

Calculating the Force Required to Accelerate the Cone of Liquid

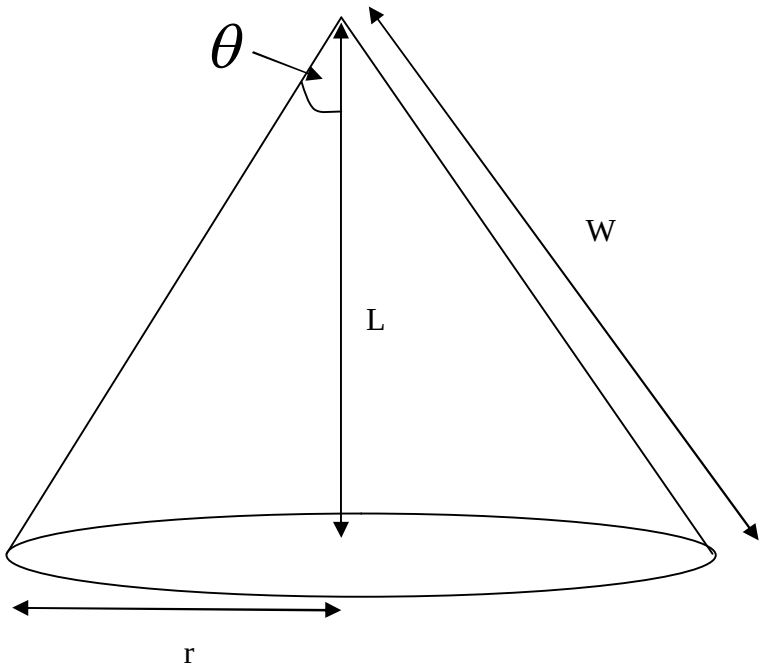

Figure B.1. Schematic of a cone used for a force calculation.

According to the experimental settings:

W = 0.061033 m

θ = 0.610726 rad

Radius of piston, $r_p = 3.50 \times 10^{-2}$ m

Height of the cone from centre, $L = 5.00 \times 10^{-2}$ m

$dp = 2.00 \times 10^{-4}$ m

Density, $\rho = 1000$ kg cm^{-3}

Modulation frequency, f = 100 Hz

The total force is calculated as the sum of a series of disks of constant mass.

W	**dz**	**dl**	**dF**
$W_i = \frac{L - dz_i}{\cos\theta}$	$dz_i = dz_{i-1} + dl_i$ *where* $dz_0 = dp$	$dl_i = \frac{r_p^2 dp}{(W_i \sin\theta)^2}$	$dF_i = \pi r_p^2 \rho\, dp\, (dl_i (2\pi f)^2)$
$W_{i+1} = \frac{L - dz_{i+1}}{\cos\theta}$	$dz_{i+1} = dz_i + dl_{i+1}$	$dl_{i+1} = \frac{r_p^2 dp}{(W_{i+1} \sin\theta)^2}$	$dF_{i+1} = \pi r_p^2 \rho\, dp\, (dl_{i+1} (2\pi f)^2)$
$W_n = \frac{L - dz_n}{\cos\theta}$	$dz_n = dz_{n-1} + dl_n$	$dl_n = \frac{r_p^2 dp}{(W_n \sin\theta)^2}$	$dF_n = \pi r_p^2 \rho\, dp\, (dl_n (2\pi f)^2)$

Force applied = $dF_i + dF_{i+1} + \ldots + dF_n$

Table B1. Matrix used to calculate the Force required accelerating the cone of liquid

Therefore for experimental settings presented here the force required to accelerate the liquid inside the funnel is **17.3 N** for a 100 Hz oscillation.

Appendix C

Table for calculating of collection efficiency at RRDE

Values of N_o for common radius ratios

r_3 / r_2	r_2 / r_1								
	1.02	1.03	1.04	1.05	1.06	1.07	1.08	1.09	1.10
1.02	.1013	.0976	.0947	.0922	.0902	.0884	.0869	.0855	.0843
1.03	.1293	.1250	.1215	.1186	.1162	.1140	.1121	.1104	.1089
1.04	.1529	.1483	.1444	.1412	.1385	.1360	.1339	.1320	.1302
1.05	.1737	.1687	.1647	.1612	.1582	.1556	.1533	.1512	.1493
1.06	.1923	.1872	.1829	.1793	.1761	.1733	.1708	.1686	.1665
1.07	.2092	.2039	.1996	.1958	.1925	.1896	.1869	.1846	.1824
1.08	.2247	.2194	.2149	.2110	.2076	.2046	.2019	.1994	.1972
1.09	.2392	.2338	.2292	.2252	.2217	.2186	.2158	.2133	.2110
1.10	.2526	.2472	.2426	.2385	.2350	.2318	.2289	.2263	.2240
1.12	.2272	.2717	.2670	.2629	.2593	.2560	.2530	.2503	.2479
1.14	.2992	.2938	.2890	.2849	.2812	.2778	.2748	.2720	.2695
1.16	.3192	.3138	.3090	.3048	.3011	.2977	.2947	.2919	.2893
1.18	.3375	.3321	.3274	.3232	.3194	.3161	.3130	.3101	.3075
1.20	.3544	.3490	.3443	.3402	.3364	.3330	.3299	.3271	.3245
1.22	.3701	.3648	.3601	.3560	.3523	.3489	.3458	.3429	.3403
1.24	.3848	.3795	.3749	.3708	.3671	.3637	.3606	.3577	.3551
1.26	.3985	.3933	.3887	.3847	.3810	.3776	.3745	.3717	.3691
1.28	.4115	.4063	.4018	.3977	.3941	.3907	.3877	.3849	.3822
1.30	.4237	.4186	.4141	.4101	.4065	.4032	.4001	.3973	.3947
1.32	.4353	.4302	.4258	.4218	.4183	.4150	.4119	.4092	.4066
1.34	.4463	.4413	.4369	.4330	.4294	.4262	.4232	.4204	.4178
1.36	.4567	.4518	.4475	.4436	.4401	.4369	.4339	.4311	.4286
1.38	.4667	.4619	.4576	.4538	.4503	.4471	.4441	.4414	.4389

The shaded area is the theoretical collection efficiency for the RRDE used in the present work. This numbers can be calculated from Albery and Hitchman (*234*).

References

1. T. M. H. Lee, *Sensors* **8**, 5535 (Sep, 2008).
2. F. Valentini, G. Palleschi, *Analytical Letters* **41**, 479 (2008).
3. Y. Wang, H. Xu, J. M. Zhang, G. Li, *Sensors* **8**, 2043 (Apr, 2008).
4. N. Serrano, J. M. Diaz-Cruz, C. Arino, M. Esteban, *Electroanalysis* **19**, 2039 (Oct, 2007).
5. B. Fleet, H. Gunasingham, *Talanta* **39**, 1449 (Nov, 1992).
6. K. Xu, D. T. Pierce, A. Li, J. X. Zhao, *Synthesis and Reactivity in Inorganic Metal-Organic and Nano-Metal Chemistry* **38**, 394 (2008).
7. L. Taberna, S. Mitra, P. Poizot, P. Simon, J. M. Tarascon, *Nature Materials* **5**, 567 (Jul, 2006).
8. J. Wang, *Talanta* **28**, 369 (1981).
9. J. V. Macpherson, *Electroanalysis* **12**, 1001 (Sep, 2000).
10. A. J. Bard, L. R. Faulkner, *Electrochemical Methods. Fundamentals and Applications.* (John Wiley & Sons, Inc., ed. 2nd, 2001).
11. D. Pletcher, *A First Course in Electrode Processes* (The Electrochemical Consultancy, 1991).
12. B. Miller, Bruckens.S, *Analytical Chemistry* **46**, 2026 (1974).
13. B. Miller, J. M. Rosamilia, *Abstracts of Papers of the American Chemical Society* **186**, 44 (1983).
14. D. E. Williams *et al.*, *J. Electroanal.Chem.* **432**, 159 (1997).
15. K. W. Pratt, D. C. Johnson, *Electrochim. Acta* **27**, 1013 (1982).
16. K. W. Pratt, D. C. Johnson, *Anal. Chim. Acta* **148**, 87 (1983).
17. S. A. Schuette, R. L. McCreery, *Anal. Chem.* **58**, 1778 (1986).
18. S. A. Schuette, R. L. McCreery, *Anal. Chem.* **59**, 2692 (1987).
19. W. Blaedel, J. Wang, *Anal. Chem.* **51**, 799 (1979).
20. W. J. Blaedel, D. G. Iverson, *Anal. Chem.* **49**, 1563 (1977).
21. W. J. Blaedel, S. L. Boyer, *Anal. Chem.* **43**, 1538 (1971).
22. W. J. Blaedel, Z. Yim, *Anal. Chem.* **52**, 564 (1980).
23. J. Wang, *Analytical Chemistry* **53**, 1528 (1981).
24. W. J. Blaedel, R. C. Engstrom, *Analytical Chemistry* **50**, 476 (1978).
25. W. J. Blaedel, J. Wang, *Analytical Chemistry* **52**, 1697 (1980).
26. W. J. Blaedel, J. Wang, *Analytica Chimica Acta* **116**, 315 (1980).
27. B. Miller, Bruckens.S, Bellavan.Mi, *Analytical Chemistry* **44**, 1983 (1972).
28. K. Tokuda, S. Bruckenstein, B. Miller, *Journal of the Electrochemical Society* **122**, 1316 (1975).
29. B. Miller, Bruckens.S, *Journal of the Electrochemical Society* **121**, 1558 (1974).
30. K. Tokuda, S. Bruckenstein, *Journal of the Electrochemical Society* **126**, 431 (1979).
31. D. T. Schwartz, P. Stroeve, B. G. Higgins, *Journal of the Electrochemical Society* **136**, 1755 (Jun, 1989).
32. D. T. Schwartz, *Journal of the Electrochemical Society* **140**, 452 (Feb, 1993).
33. J. M. Rosamilia, B. Miller, *Analytical Chemistry* **55**, 1142 (1983).

34. C. Deslouis, B. Tribollet, in *Advances in Electrochemical Science and Engineering* C. Tobias, H. Gerischer, Eds. (VCH Weinhein, New York, 1991), vol. 2, pp. 205.
35. C. Deslouis, C. Gabrielli, P. S. Fanchine, B. Tribollet, *Journal of the Electrochemical Society* **129**, 107 (1982).
36. C. Deslouis, B. Tribollet, *Journal of Electroanalytical Chemistry* **185**, 171 (1985).
37. C. Deslouis, B. Tribollet, *Electrochimica Acta* **35**, 1637 (1990).
38. C. Deslouis, B. Tribollet, *Journal of Electroanalytical Chemistry* **572**, 389 (Nov, 2004).
39. S. Vandeputte, A. Hubin, J. Vereecken, *Electrochimica Acta* **42**, 3429 (1997).
40. C. Deslouis, N. Tabti, B. Tribollet, *Journal of Applied Electrochemistry* **27**, 109 (Jan, 1997).
41. S. Vandeputte, B. Tribollet, A. Hubin, J. Vereecken, *Electrochimica Acta* **39**, 2729 (1994).
42. C. Deslouis, G. Maurin, N. Pebere, B. Tribollet, *Electrochimica Acta* **34**, 1229 (1989).
43. E. Lhostis, C. Deslouis, B. Tribollet, D. Festy, *Electrochimica Acta* **41**, 1393 (1996).
44. B. Basle, C. Deslouis, D. Festy, T. El Moustafid, B. Tribollet, *Proceedings of the Symposium on Fundamental Aspects of Electrochemical Deposition and Dissolution Including Modeling* **97**, 387 (1998).
45. A. C. West, R. D. Grimm, D. Landolt, C. Deslouis, B. Tribollet, *Journal of Electroanalytical Chemistry* **330**, 693 (1992).
46. O. E. Barcia, O. R. Mattos, N. Pebere, B. Tribollet, *Journal of the Electrochemical Society* **140**, 2825 (1993).
47. E. D. Harris, A. J. Lindsey, *Nature* **162**, 413 (1948).
48. E. D. Harris, A. J. Lindsey, *Analyst* **76**, 647 (1951).
49. E. D. Harris, A. J. Lindsey, *Analyst* **76**, 650 (1951).
50. Facsko, *Revue. roum. Chim.* **11**, 191 (1966).
51. K. W. Pratt, D. C. Johnson, *Electrochimica Acta* **27**, 1013 (1982).
52. K. W. Pratt, D. C. Johnson, *Analytica Chimica Acta* **148**, 87 (1983).
53. S. A. Schuette, R. L. McCreery, *Analytical Chemistry* **58**, 1778 (Jul, 1986).
54. A. J. Lindsey, *J. Phys. Chem.* **56**, 439 (1952).
55. S. A. Schuette, R. L. McCreery, *Analytical Chemistry* **59**, 2692 (Nov, 1987).
56. D. E. Williams *et al.*, *Journal of Electroanalytical Chemistry* **432**, 159 (Jul, 1997).
57. W. J. Blaedel, S. L. Boyer, *Analytical Chemistry* **43**, 1538 (1971).
58. W. J. Blaedel, J. Wang, *Analytical Chemistry* **51**, 799 (1979).
59. W. J. Blaedel, D. G. Iverson, *Analytical Chemistry* **49**, 1563 (1977).
60. W. J. Blaedel, Z. Yim, *Analytical Chemistry* **52**, 564 (1980).
61. W. J. Blaedel, J. Wang, *Analytical Chemistry* **53**, 78 (1981).
62. R. G. Compton, A. C. Fisher, R. G. Wellington, *J. Phys. Chem.* **97**, 10410 (1993).
63. P. R. Unwin, R. G. Compton, in *Comprehensive Chemical Kinetics* R. G. Compton, A. Hamnett, Eds. (Elsevier, Amsterdam, 1989), vol. 29, pp. 173-209.
64. J. V. Macpherson, N. Simjee, P. R. Unwin, *Electrochimica Acta* **47**, 29 (Sep, 2001).
65. J. V. Macpherson, P. R. Unwin, *Analytical Chemistry* **71**, 2939 (Jul, 1999).

66. J. V. Macpherson, P. R. Unwin, *Analytical Chemistry* **70**, 2914 (Jul, 1998).
67. J. V. Macpherson, C. E. Jones, P. R. Unwin, *Journal of Physical Chemistry B* **102**, 9891 (Dec, 1998).
68. J. V. Macpherson, S. Marcar, P. R. Unwin, *Analytical Chemistry* **66**, 2175 (Jul, 1994).
69. J. V. Macpherson, M. A. Beeston, P. R. Unwin, *Journal of the Chemical Society-Faraday Transactions* **91**, 899 (Mar, 1995).
70. J. V. Macpherson, P. R. Unwin, *Analytical Chemistry* **71**, 4642 (Oct, 1999).
71. E. Bitziou, N. C. Rudd, M. A. Edwards, P. R. Unwin, *Analytical Chemistry* **78**, 1435 (Mar, 2006).
72. N. Simjee, P. R. Unwin, J. V. Macpherson, *Electroanalysis* **15**, 1445 (Oct, 2003).
73. A. J. Bard, *Analytical Chemistry* **35**, 1125 (1963).
74. H. D. Dewald, B. A. Peterson, *Analytical Chemistry* **62**, 779 (Apr, 1990).
75. E. L. Cooper, L. A. Coury, *J. Electrochem. Soc.* **145**, 1994 (1988).
76. P. R. Birkin, S. SilvaMartinez, *Journal of Electroanalytical Chemistry* **416**, 127 (Nov, 1996).
77. R. G. Compton *et al.*, *Electrochimica Acta* **42**, 2919 (1997).
78. K. S. Kim, N. Winograd, R. E. Davis, *J. Am. chem. Soc.* **93**, 6296 (1971).
79. J. S. Hammond, N. Winograd, *J. Electroanal. Chem.* **78**, 55 (1977).
80. Angerste.H, B. E. Conway, W. B. A. Sharp, *Journal of Electroanalytical Chemistry* **43**, 9 (1973).
81. A. I. Slygin, A. N. Frumkin, *C. R. Acad. Sci. URSS* **2**, 173 (1934).
82. R. Parsons, in *Comprehensive Chemical Kinetics* R. G. Compton, Ed. (Elsevier, Amsterdam, 1989), vol. 29, pp. 105-147, and references therein.
83. B. V. Tilak, B. E. Conway, Angerste.H, *Journal of Electroanalytical Chemistry* **48**, 1 (1973).
84. D. H. Everett, W. I. Whitten, *Trans. Faraday Soc.* **48**, 749 (1952).
85. D. H. Everett, F. W. Smith, *Trans. Faraday Soc.* **50**, 187 (1954).
86. A. K. Reddy, M. A. Genshaw, J. O. Bockris, *J. Chem. Phys.* **48**, 671 (1969).
87. F. P. Bowden, *Proc. R. Soc. London Ser.A* **125**, 1929 (1929).
88. J. A. V. Butler, G. Armstrong, *Proc. R. Soc. London Ser. A* **137**, 504 (1929).
89. A. Damjanovic, A. Dey, J. O. Bockris, *J. Electrochem. Soc.* **133**, 739 (1966).
90. K. J. Vetter, J. W. Schultze, *Journal of Electroanalytical Chemistry* **34**, 141 (1972).
91. A. K. Reddy, M. A. Genshaw, J. O. Bockris, *J. Electroanal. Chem.* **8**, 406 (1964).
92. A. K. Reddy, M. A. Genshaw, J. O. Bockris, *J. Chem. Phys.* **48**, 671 (1968).
93. L. B. Harris, A. Damjanovic, *Journal of the Electrochemical Society* **122**, 593 (1975).
94. A. Damjanovic, A. T. Ward, B. Ulrick, M. Ojea, *Journal of the Electrochemical Society* **122**, 471 (1975).
95. A. Damjanovic, in *Modern Aspects of Electrochemistry* B. E. Conway, J. O. Bockris, Eds. (Plenum Press, New York, 1965), vol. 5.
96. B. E. Conway, B. Barnett, H. Angersteinkozlowska, B. V. Tilak, *Journal of Chemical Physics* **93**, 8361 (1990).
97. G. Jerkiewicz, G. Vatankhah, J. Lessard, M. P. Soriaga, Y. S. Park, *Electrochimica Acta* **49**, 1451 (2004).
98. B. E. Conway, *Progr. Surf. Sci.* **49**, 331 (1995).

99. M. R. Tarasevish, A. Sadkowski, E. Yeager, in *Comprehensive Treatise of Electrochemistry* B. E. Conway, J. O. Bockris, E. Yeager, S. U. M. Khan, R. E. White, Eds. (Plenum Press, New York, 1983), vol. 7, pp. 301.
100. M. Alsabet, M. Grden, G. Jerkiewicz, *Journal of Electroanalytical Chemistry* **589**, 120 (2006).
101. J. O. M. Bokris, S. U. M. Khan, *Surface Electrochemistry. A molecular Level Approach* (Plenum Press, New York-London, 1993), pp. 1014.
102. B. E. Conway, in *Interfacial Electrochemistry. Theory, Experiment, and Applications* A. Wieckowski, Ed. (Marcel Dekker, Inc, New York, 1999) pp. 131.
103. B. E. Conway, E. Gileadi, *Trans. Faraday Soc.* **58**, 2493 (1962).
104. B. E. Conway, J. Klinger, H. A. Kozlowska, *J. Electroanal. Chem.* **75**, 45 (1977).
105. A. Eucken, B. Weblus, *Z. Elektrochem.* **55**, 144 (1951).
106. F. G. Will, C. A. Knorr, *Z. Elektrochem.* **64**, 258 (1960).
107. J. M. Feliu, J. M. Orts, R. Gomez, A. Aldaz, J. Clavilier, *Journal of Electroanalytical Chemistry* **372**, 265 (1994).
108. F. G. Will, *J. Electrochem. Soc.* **112**, 451 (1965).
109. A. T. Hubbard, J. L. Stickney, S. D. Rosaco, M. P. Soriaga, S. Song, *J. Electroanal. Chem.* **150**, 165 (1983).
110. J. Clavilier, A. Rodes, K. Elachi, M. A. Zamakhchari, *Journal De Chimie Physique Et De Physico-Chimie Biologique* **88**, 1291 (Jul-Aug, 1991).
111. J. Clavilier, in *Interfacial Electrochemistry. Theory, Experiment, and Applications* A. Wieckowski, Ed. (Marcel Dekker, New York, 1999).
112. A. T. Hubbard, R. W. Ishikawa, J. Katekaru, *J. Electroanal. Chem.* **86**, 271 (1978).
113. R. Parsons, in *Comprehensive Chemical Kinetics* R. G. Compton, A. Hamnett, Eds. (Elsevier, Amsterdam, 1989), vol. 29, pp. 105-127.
114. M. W. Breiter, B. Kennel, *Z. Elektrochem.* **64**, 1180 (1960).
115. M. W. Breiter, *Electrochimica Acta* **8**, 925 (1963).
116. V. S. Bagotzky, Y. B. Vassiliev, I. I. Pyshnograeva, *Electrochimica Acta* **16**, 2141 (1971).
117. P. Stonehart, *Electrochimica Acta* **15**, 1853 (1970).
118. A. Capon, R. Parsons, *J. Electroanal. Chem.* **39**, 275 (1972).
119. J. Clavilier, *Journal of Electroanalytical Chemistry* **107**, 211 (1980).
120. N. Garcia-Araez, V. Climent, P. Rodriguez, J. M. Feliu, paper presented at the 58th Annual Meeting of the International-Society-of-Electrochemisty, Banff, CANADA, Sep 10-14 2007.
121. A. I. Slygin, A. N. Frumkin, *Acta Physicochim. URSS* **3**, 791 (1935).
122. A. N. Frumkin, A. I. Slygin, *Acta Physicochim. URSS* **6**, 819 (1936).
123. K. Kunimatsu, M. G. Samant, H. Seki, *Journal of Electroanalytical Chemistry* **258**, 163 (Jan, 1989).
124. V. B. Paulissen, C. Korzeniewski, *Journal of Electroanalytical Chemistry* **290**, 181 (1990).
125. M. Weber, F. C. Nart, I. R. deMoraes, T. Iwasita, *Journal of Physical Chemistry* **100**, 19933 (1996).
126. S. Ye, H. Kita, A. Aramata, *Journal of Electroanalytical Chemistry* **333**, 299 (1992).
127. S. Taguchi, A. Aramata, *Journal of Electroanalytical Chemistry* **457**, 73 (Oct, 1998).

128. J. Rouquerol *et al.*, *Pure & Appl. Chem.* **66**, 1739 (1994).
129. H. Taeghwan, S. M. Oh, L. Jinwoo, Y. Songhun, *Amorphous and Nanostructured Carbon. Symposium (Materials Research Society Symposium Proceedings Vol.593)*, 193 (2000).
130. G. S. Attard, J. M. Elliott, P. N. Bartlett, A. Whitehead, J. R. Owen, paper presented at the IUPAC 8th International Symposium on Macromolecule-Metal Complexes (MMC-8), Tokyo, Japan, Sep 05-09 1999.
131. H. T. Zhao, K. L. Nagy, J. S. Waples, G. F. Vance, *Environmental Science & Technology* **34**, 4822 (2000).
132. W. Z. Zhang, B. Glomski, T. R. Pauly, T. J. Pinnavaia, *Chemical Communications*, 1803 (1999).
133. G. D. Xuefeng, X. W. Weiping, Y. Qijie, *Chem. Comm.*, 709 (2001).
134. Z. Li *et al.*, *Rare Metal Mat. Eng.* **33**, 5 (2004).
135. A. Corma *et al.*, *New Journal of Chemistry* **32**, 1338 (Aug, 2008).
136. J. M. Thomas, W. J. Thomas, *Principles and practice of heterogenous catalysts* (VCH Publishers Inc., New York, 1997).
137. J. Caro, M. Noack, *Microporous and Mesoporous Materials* **115**, 215 (Nov, 2008).
138. G. L. Hollis, *Surfactants Europa* (Royal Society of Chemistry, ed. 3, 1995).
139. S. Chandarasekhar, *Liquid Crystals* (Cambridge University Press, London, ed. 2, 1992).
140. P. Lozano Sanchez, PhD Thesis, The University of Reading (2004).
141. C. T. Kresge, M. E. Leonowicz, W. J. Roth, J. C. Vartuli, J. S. Beck, *Nature* **359**, 710 (Oct, 1992).
142. J. S. Beck *et al.*, *J. Am. chem. Soc.* **114**, 10834 (1992).
143. J. C. Vartuli, K. D. Schmitt, C. T. Kresge, *Chemical Materials* **6**, 2317 (1994).
144. J. S. Beck, J. C. Vartuli, J. G. Kennedy, *Chemical Materials* **6**, 2317 (1994).
145. G. S. Attard, J. C. Glyde, C. G. Goltner, *Nature* **378**, 366 (1995).
146. J. M. Elliott *et al.*, *Chemistry of Materials* **11**, 3602 (Dec, 1999).
147. G. S. Attard, N. R. B. Coleman, J. M. Elliott, *Stud. Surf. Sci. Catal.* **117**, 89 (1998).
148. G. S. Attard *et al.*, *Science* **278**, 838 (Oct, 1997).
149. J. M. Elliott *et al.*, *Journal of New Materials for Electrochemical Systems* **2**, 239 (Oct, 1999).
150. S. Chen *et al.*, *Journal of the American Chemical Society* **130**, 13818 (Oct, 2008).
151. H. A. Gasteiger, S. S. Kocha, B. Sompalli, F. T. Wagner, *Applied Catalysis B-Environmental* **56**, 9 (2005).
152. M. Lanqun, G. Feng, Y. Yiming, S. Lei, W. Lun, *Electrochemistry Communications*, 989 (2007).
153. A. Yaropolov *et al.*, *Bioelectrochemistry* **70**, 199 (2007).
154. J. M. Hoare, *The Electrochemistry of Oxygen* (Interscience, New York, 1968).
155. E. Yeager, *Electrochimica Acta* **29**, 1527 (1984).
156. E. J. M. O'Sullivan, E. J. Calvo, in *Comprehensive Chemical Kinetics* R. G. Compton, Ed. (Elsevier, Amsterdam, 1987), vol. 27, pp. 247.
157. A. N. Frumkin, L. N. Nekrasov, *Dokl. Akad. Nauk. SSSR* **126**, 115 (1959).
158. L. Muller, L. N. Nekrasov, *Electrochimica Acta* **9**, 1015 (1964).
159. C. M. Sanchez-Sanchez, J. Rodiriguez-Lopez, A. J. Bard, *Analytical Chemistry* **80**, 3254 (2008).

160. V. S. Bagotzky, M. R. Tarasevich, V. Y. Filinovskii, *Elektrokhimiya* **5**, 1218 (1969).
161. A. Damjanovic, M. A. Genshaw, J. O. M. Bokris, *The Journal of Chemical Physics* **45**, 4057 (1966).
162. A. Damjanovic, M. A. Genshaw, J. O. M. Bokris, *Journal of Electrochemical Society* **114**, 466 (1967).
163. V. S. Bagotzky, M. R. Tarasevich, V. Y. Filinovskii, *Elektrokhimiya* **8**, 84 (1972).
164. H. S. Wroblowa, Y. C. Pan, G. Razumney, *Journal of Electroanalytical Chemistry* **69**, 195 (1976).
165. D. Pletcher, S. Sotiropoulos, (1993).
166. P. B. Balbuena, S. R. Calvo, E. J. Lamas, P. F. Salazar, J. M. Seminario, *J. Phys. Chem. B* **110**, 17452 (2006).
167. R. W. Zurilla, R. K. Sen, E. Yeager, *Journal of the Electrochemical Society* **125**, 1103 (1978).
168. M. R. Miah, T. Ohsaka, *J. Electrochem. Soc.* **154**, F186 (2007).
169. Y. Takasu *et al.*, *Electrochimica Acta* **41**, 2595 (1996).
170. M. Watanabe, H. Sei, P. Stonehart, *Journal of Electroanalytical Chemistry* **261**, 375 (1989).
171. G. Couturier, D. W. Kirk, P. J. Hyde, S. Srinivasan, *Electrochimica Acta* **32**, 995 (1987).
172. P. R. Birkin, J. M. Elliott, Y. E. Watson, *Chemical Communications*, 1693 (2000).
173. J. Jiang, A. Kucernak, *J. Electroanal. Chem.* **520**, 64 (2002).
174. J. Jiang, A. Kucernak, *Journal of Electroanalytical Chemistry* **533**, 153 (2002).
175. A. E. Zonst, *Understanding the FFT. A tutorial on the Algorithm & Software for Laymen, Students, Technicians and Working Engineers.* (Citrus Press, Titusville, Florida, 1995), pp. 180.
176. A. Scoog, D. M. West, *Principles of Instrumental Analysis* (Rhinehart and Winston, Philadelphia, 1980).
177. L. Bede, C., in *Spectroelectrochemistry. Theory and practice.* R. J. Gale, Ed. (Plenum, New York, 1988).
178. J. R. Macdonald, *Impedance Spectroscopy. Emphasizing Solid Materials and Systems.* (John Wiley & Sons New York, 1987), pp. 346.
179. T. J. S. o. m. engineers, Ed., *Visualized flow. Fluid motion in basic and engineering situations revealed by flow visualization.* (Pergamon Press), pp. 137.
180. A. J. Smits, T. T. Lim, Eds., *Flow Visualization: Techniques and examples* (Imperial College Press, London, 2000), pp. 396.
181. O. Reynolds, *Phil. Trans. Roy. Soc.* **174**, 935 (1883).
182. T. J. Mueller, in *Fluid Mechanics Measurements* R. J. Goldstein, Ed. (DC:Taylor & Francis, Washington, 1996) pp. 367-450.
183. P. Freymuth, W. Bank, M. Palmer, in *Flow Visualisation III* W. J. Yang, Ed. (Hemisphere, New York, 1985) pp. 99-105.
184. G. J. F. van Heijst, R. C. Kloosterziel, *Nature* **338**, 567 (1989).
185. R. M. Kelso, T. T. Lim, A. E. Perry, *Album of Visualization* **9**, 30 (1992).
186. H. T. Kim, S. J. Kline, W. C. Reynolds, *Journal of Fluid Mechanics* **50**, 133 (1971).

187. S. J. Kline, W. C. Reynolds, F. A. Schraub, P. W. Runstadler, *Journal of Fluid Mechanics* **95**, 741 (1967).
188. S. Trasatti, O. A. Petrii, *Journal of Electroanalytical Chemistry* **327**, 353 (1992).
189. C. Beriet, D. Pletcher, *Journal of Electroanalytical Chemistry* **361**, 93 (1993).
190. Q. Fulian, K. A. QGooch, A. C. Fisher, *Analytical Chemistry* **72**, 3480 (2000).
191. J. H. Scofield, *American Journal of Physics* **62**, 129 (1994).
192. J. L. Melville *et al.*, *Journal of Physical Chemistry B* **107**, 379 (Jan, 2003).
193. A. D. Skoog, D. M. West, F. J. Holler, *Fundamentals of Analytical Chemistry* (Saunders College Publishing, ed. Sixth), pp. 892.
194. http://www.dnr.state.wi.us/org/es/science/lc/OUTREACH/-Publications/LOD%20Guidance%20Document.pdf.
195. E. W. Weisstein, *"Volume." From MathWorld--A Wolfram Web Resource. http://mathworld.wolfram.com/Volume.html*

196. J. Hellemans, P. Forrez, R. Dewilde, *American Journal of Physics* **48**, 254 (1980).
197. H. J. Lugt, *Vortex Flow in Nature and Technology* (John Wiley & Sons, 1983), pp. 297.
198. S. Ilo, T. Kawamura, M. Matsubara, T. Yoshida, T. Ikeda, *Jsme International Journal Series B-Fluids and Thermal Engineering* **49**, 988 (Nov, 2006).
199. T. Seno, S. Kageyama, R. Ito, *Journal of Chemical Engineering of Japan* **20**, 128 (Apr, 1987).
200. S. E. Widnall, *Ann. Rev. Fluid Mech.* **7**, 141 (1975).
201. T. Maxworthy, *Journal of Fluid Mechanics* **81**, 465 (1977).
202. T. Kambe, Y. Oshima, *J. Phys. Soc. Japan* **38**, 271 (1975).
203. J. K. Harvey, *AIAA* **9**, 1659 (1971).
204. U. Boldes, J. C. Ferreri, *The Physics of Fluids* **16**, 2005 (1973).
205. T. Langkau, H. Baltruschat, *Electrochimica Acta* **44**, 909 (1998).
206. H. Angersteinkozlowska, B. E. Conway, B. Barnett, J. Mozota, *Journal of Electroanalytical Chemistry* **100**, 417 (1979).
207. D. Armand, J. Clavilier, *Journal of Electroanalytical Chemistry* **263**, 109 (1989).
208. K. Kunimatsu, M. G. Samant, H. Seki, *Journal of Electroanalytical Chemistry* **272**, 185 (Nov, 1989).
209. P. W. Atkins, *Physical Chemistry* (Oxford University Press, Oxford-Melburne-Tokyo, ed. 6th, 1998), pp. 1014.
210. M. L. Hitchman, *Measurement of Dissolved Oxygen*, Chemical Analysis (A Wiley-Interscience Publication, New York-Chichester-Brisbane-Toronto, 1978), pp. 255.
211. Y. F. Yang, G. Denuault, *Journal of Electroanalytical Chemistry* **418**, 99 (Nov, 1996).
212. Y. F. Yang, G. Denuault, *Journal of the Chemical Society-Faraday Transactions* **92**, 3791 (Oct, 1996).
213. Y. F. Yang, G. Denuault, *Journal of Electroanalytical Chemistry* **443**, 273 (Feb, 1998).
214. D. Pletcher, S. Sotiropoulos, *Journal of the Chemical Society-Faraday Transactions* **90**, 3663 (Dec, 1994).
215. K. Franaszczuk, J. Sobkowski, *Journal of Electroanalytical Chemistry* **261**, 223 (Mar, 1989).

216. A. N. Frumkin, O. A. Petry, *Electrochimica Acta* **15**, 735 (1970).
217. E. Gileadi, S. D. Argade, J. O. M. Bockris, *The Journal of Physical Chemistry* **70**, 2044 (1966).
218. S. A. G. Evans *et al.*, *Analytical Chemistry* **74**, 1322 (Mar, 2002).
219. A. Schneider *et al.*, *Physical Chemistry Chemical Physics* **10**, 1931 (2008).
220. W. J. Albery, A. R. Hillman, S. Bruckenstein, *Journal of Electroanalytical Chemistry* **100**, 687 (1979).
221. A. Ambari, C. Deslouis, B. Tribollet, *International Journal of Heat and Mass Transfer* **29**, 35 (1986).
222. K. Tokuda, S. Bruckenstein, B. Miller, *Journal of the Electrochemical Society* **122**, C110 (1975).
223. B. Tribollet, J. Newman, *Journal of the Electrochemical Society* **130**, 822 (1983).
224. B. Tribollet, J. Newman, *Journal of the Electrochemical Society* **130**, 2016 (1983).
225. *Instrumental Methods in Electrochemistry. Southampton Electrochemistry Group.* (Ellis Horwood Limited, Chichester, 1985), pp. 439.
226. N. V. Rees, R. G. Compton, *Russian Journal of Electrochemistry* **44**, 368 (Apr, 2008).
227. M. Thompson, O. V. Klymenko, R. G. Compton, *Journal of Electroanalytical Chemistry* **575**, 329 (Feb, 2005).
228. I. Streeter, M. Thompson, R. G. Compton, *Journal of Electroanalytical Chemistry* **591**, 133 (Jun, 2006).
229. W. J. Blaedel, C. L. Olson, L. R. Sharma, *Analytical Chemistry* **35**, 2100 (1963).
230. S. Silva-Martinez, University of Southampton (1997).
231. G. C. Bond, C. Louis, D. T. Thompson, *Catalysis by Gold* (Imperial College Press, 2006), pp. 366.
232. L. D. Burke, D. T. Buckley, J. A. Morrissey, *Analyst* **119**, 841 (1994).
233. M. E. Orazem, B. Tribollet, *Electrochemical Impedance Spectroscopy* (John Wiley & Sons, Inc., Hoboken, New Jersey, 2008), pp. 523.
234. W. J. Albery, M. L. Hitchman, *Ring-disc electrodes* (Clarendon Press, 1971).